Phase behaviour of macromolecular liquid crystlline materials: computational studies at the molecular level

Lorna M. Stimson

Phase Behaviour of Macromolecular Liquid Crystalline Materials: Computational Studies at the Molecular Level

Lorna M. Stimson

Department of Chemistry
University of Durham
England

January 2003

Submitted in partial fulfillment of the requirements for the degree of
Doctor of Philosophy

You have riches and freedom here,
but I feel no sense of faith or direction.
You have so many computers,
why don't you use them in the search of love?

Lech Wałęsa, Polish trade unionist,
statesman & president.

Abstract

Phase Behaviour of Macromolecular Liquid Crystalline Materials: Computational Studies at the Molecular Level

Lorna M. Stimson

Molecular simulations provide an increasingly useful insight into the static and dynamic characteristics of materials. In this thesis molecular simulations of macromolecular liquid crystalline materials are reported.

The first liquid crystalline material that has been investigated is a side chain liquid crystal polymer (SCLCP). In this study semi-atomistic molecular dynamics simulations have been conducted at a range of temperatures and an aligning potential has been applied to mimic the effect of a magnetic field. In cooling the SCLCP from an isotropic melt, microphase separation was observed yielding a domain structure. The application of a magnetic field to this structure aligns the domains producing a stable smectic mesophase. This is the first study in which mesophases have been observed using an off-lattice model of a SCLCP.

The second material that has been investigated is a dendrimer with terminal mesogenic functionalization. Here, a multi-scale approach has been taken with Monte Carlo studies of a single dendrimer molecule in the gas phase at the atomistic level, semi-atomistic molecular dynamics of a single molecule in liquid crystalline solvents and a coarse-grained molecular dynamics study of the dendrimer in the bulk. The coarse-grained model has been developed and parameterized using the results of the atomistic and semi-atomistic work. The single molecule studies showed that the liquid crystalline dendrimer was able to change its structure by conformational changes in the flexible chains that link the mesogenic groups to the core. Structural change was seen under the application of a mean field ordering potential in the gas phase, and in the presence of liquid crystalline solvents. No liquid crystalline phases were observed for the bulk phase studies of the coarse-grained model. However, when the length of the mesogenic units was increased there was some evidence for microphase separation in these systems.

Declaration

The work in this thesis is based on research carried out at the University of Durham. The Material contained in this thesis has not been submitted for any other degree or qualification at the University or Durham or any other university. The research in this thesis has been conducted by the author unless indicated otherwise.

Acknowledgments

Firstly, I must express my thanks to the Engineering and Physical Sciences Research Council for funding the grant that supported this work and subsequent grants that provided the computing resources essential to this kind of research. As with most individuals working as part of an organisation, within the Durham University Chemistry department there are countless people, to whom I am indebted, who work hard in a range of different ways to ensure the smooth running of the department and create a friendly, comfortable and productive working environment.

From a technical perspective, I must thank those people who have provided IT support over the last three years. The assistance of Dr. Lydia Heck in my first couple of years was invaluable and her friendship simply a pleasure. In the university IT service, among others I must thank Dr. Karen Brazier and Dr. Duncan Rand who have always provided excellent support for the high performance computing service and have dealt with and provided solutions to a multitude of problems. In the production of this thesis I acknowledge M. Imran for the LyX template, Dr. Michael Leech for assistance with printing, and Alison Stoddart and David Earl for correcting some of the early drafts.

My supervisor, Dr. Mark Wilson, is someone to whom I owe a great debt of gratitude. Academically and scientifically, Mark has always provided a stimulating environment in which to learn, study and develop ideas. I am grateful to him for allowing me the freedom to ask questions no matter how trivial or convoluted they may have been; for providing me with the opportunity to attend a number of meetings in the U.K. and further afield; and for giving me the chance to talk to and participate in discussions with a range of inspiring scientists. On a more personal note I feel I must also thank Mark for the great gift of his friendship. (Football matches, art galleries, lots of good food, many a game of backgammon, a fair few pints at the Vic', many conversations serious and otherwise, and a lot of laughs!)

From my arrival in Durham as an undergraduate to the present day, Prof. Judith Howard has never failed to be a source of advice and support.

I thank those with whom I have worked including Giusy, (Puppy-) Dave, Phil, Jaroslav and most of all (Cuddly-) Dave. (Who has been a great friend to me.)

I am fortunate to have some very special friends who have been a great source of support, laughter and love during my PhD: Charlie, Eleanor, Ian, Kerry, Richard, Stephanie and especially Alley and (Kev-) Dave who have never failed to demonstrate that they have faith in me.

I would like to thank my family, especially Mum, Dad and Martyn for their love and support. Finally, I would like to mention my Aunt and Uncle for the colour that they added to our childhood.

Contents

List of Figures

List of Tables

List of Abbreviations

DPD	Dissipative Particle Dynamics
EIS	Equivalent Inertia Spheriod
Et	Ethyl (C_2H_5)
GB	Gay-Berne (potential)
K	Crystalline
LC	Liquid Crystal
LCD	Liquid Crystal Display
LCDr	Liquid Crystal Dendrimer
LCP	Liquid Crystal Polymer
LJ	Lennard-Jones (potential)
MC	Monte Carlo
MCLCP	Main Chain Liquid Crystal Polymer
MD	Molecular Dynamics
Me	Methyl (CH_3)
MSD	Mean square displacement
N	Nematic
OEt	Oxyethyl (OC_2H_5)

OMe	Oxymethyl (OCH_3)
PDLCP	Polymer Dispersed Liquid Crystal Polymer
PAMAM	Polyamidoamine
PDMS	Polydimethylsiloxane
Ph	Phenyl
SCLCP	Side Chain Liquid Crystal Polymer
S / Sm	Smectic Phase
S_A / Sm_A	Smectic A Phase
S_B / Sm_B	Smectic B Phase
S_C / Sm_C	Smectic C Phase
S_X / Sm_X	Unclassified Smectic Phase
SC	Spherocylinder (potential)
SRS	Soft-Repulsive Spherocylinder
g	Glass
i	Isotropic phase

Chapter 1

Introduction to Liquid Crystalline Materials

1.1 Liquid Crystal Phases

Liquid crystal phases are mesophases which may exist between the liquid and solid states. There are a wide variety of such phases; however, they all exhibit certain similarities such as anisotropic ordering and relatively free movement at the molecular level.[1–3]

In solid crystalline phases there is a high degree of both positional and orientational order. The constituent molecules sit on lattice points, which form a repeat pattern and the direction of the molecular axes are dictated by this arrangement. In an isotropic liquid phase there is random diffusion of molecules and rapid molecular tumbling that eliminate the positional and orientational order respectively. However, in liquid crystalline materials it is possible to observe phases that retain a degree of order after a melting transition has taken place. These systems are now less dense than the solid and can be considered as liquid in some respects as they can flow and share some other fluid-like properties. However, they may still be considered crystalline as some order has been retained. Such systems are therefore called 'liquid crystals'

1.2 Historical Context

Liquid crystal phases are considered to have been discovered in 1888[4] when an Austrian botanist, Friederich Reinitzer, observed the formation of a cloudy fluid, before a transition to a clear liquid, whilst trying to determine the melting point of cholesteryl benzoate.[5] Two melting points had been observed for similar structures prior to this observation. Reinitzer made contact with German physicist, Otto Lehman, who had been intrigued by such effects before but had not identified it as evidence of the presence of a new phase. Lehman performed optical investigations on some of Reinitzer's samples and observed polarization effects and properties such as birefringence which are not seen in isotropic systems such as liquids.[6–8] This anisotropic 'translucent liquid' was seen to undergo another transition at a higher temperature to form a clear isotropic liquid. It took many years for these new systems to be truly recognised and detailed classification of the phases was made by Georges Friedel in 1922.[9]

1.3 Classification

An overview of the classification of the main categories of liquid crystal phases is illustrated in Figure 1.1 on the following page. The majority of liquid crystals fall into two classes: thermotropic and lyotropic.[10] It is possible for some compounds to be both lyotropic and thermotropic, such systems are known as amphotropic.[11]

1.3.1 Thermotropic Liquid Crystals

Most early studies of liquid crystalline systems involved thermotropic liquid crystals. These materials display thermotropic mesomorphism, i.e. the phase transitions are temperature induced. Thermotropic phase transitions can either be monotropic or enantiotropic. Monotropic phase transitions are those in which a phase may only be reached by super-cooling and enantiotropic phase transitions are transitions that occur reversibly with increasing and decreasing temperature.

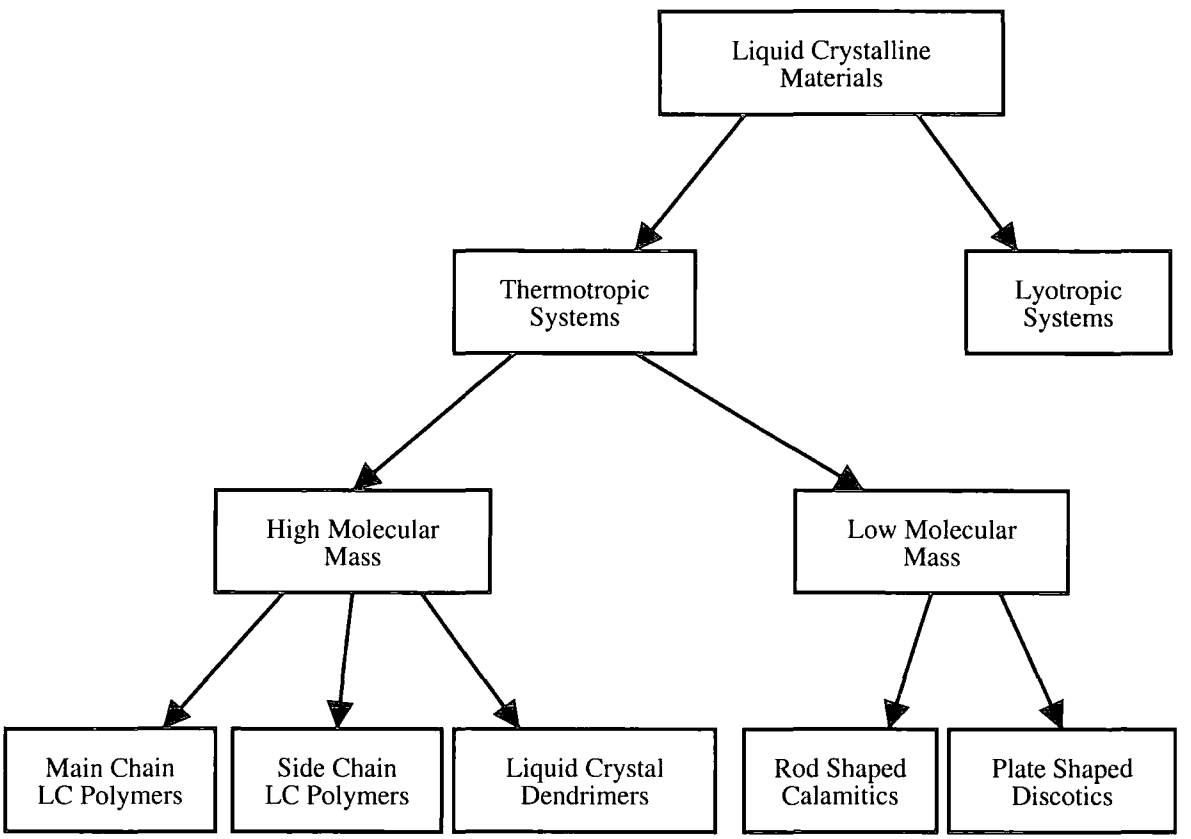

Figure 1.1: Overview of liquid crystal classification.

Thermotropic liquid crystal phase formation is enhanced by certain molecular structural features.[12,13] Favourable characteristics include rod like cores with aromatic character; cylindrical or disc shapes with high shape anisotropy; strong polar terminal groups; and a central constituent which allows conjugation with the aromatic groups. The structure of a typical mesogen can be seen in Figure 1.2.

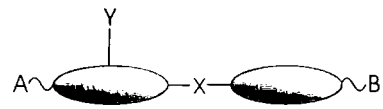

Figure 1.2: Generalized mesogenic structure.

There are many possible examples of terminal groups, A and B, *e.g.* Me, Et, OMe or OEt. At least one of these terminal groups is usually attached by a longer alkyl chain. Terminal groups which increase the length and not the breadth lead to increased thermal stability and anisotropy. The flexible alkyl chains temper this effect by reducing the stability of the crystalline phase. If either A or B is a phenyl or a similar group then they are especially efficient for promoting mesophase stability because of the additional conjugation. The least efficient groups are those such as fluorine or hydrogen, which are small. The group represented by X is a central group *e.g.* –N=C–, –C=C–, or $-CO_2-$. Such linkages are not always found, but these bridging groups can be useful to promote anisotropy and maintain linearity. The inclusion of a lateral substituent, Y, can be used to modify the morphology and the physical properties of the system. Lateral groups often have the effect of reducing the clearing point, as they make mesophases less thermally stable as a consequence of a reduction in translational order.[14]

All the work in this thesis involves materials that include thermotropic mesogenic groups. Therefore, the emphasis in the introductory chapters will be on thermotropic systems. Thermotropic mesophases can be further subdivided into three basic classes; nematic (from the Greek 'nematos ' meaning thread like), cholesteric, and smectic (from the Greek 'smectos' meaning soapy).

Nematic Liquid Crystals

Nematic liquid crystals are ordered with respect to their orientation but not to their position. This often results from rod-like molecules aligning to point, on average, in a uniform direction. The molecules can still move freely, but will maintain the same general direction, thus the fluidity of the liquid is maintained. A simple representation of a nematic can be seen in Figure 1.3. Some other nematic liquid crystals form from disc-like molecules that still maintain short range orientational order but orientate according to their short axes. These systems are known as discotics. The molecular arrangement in a nematic discotic is illustrated in Figure 1.4 on the next page.

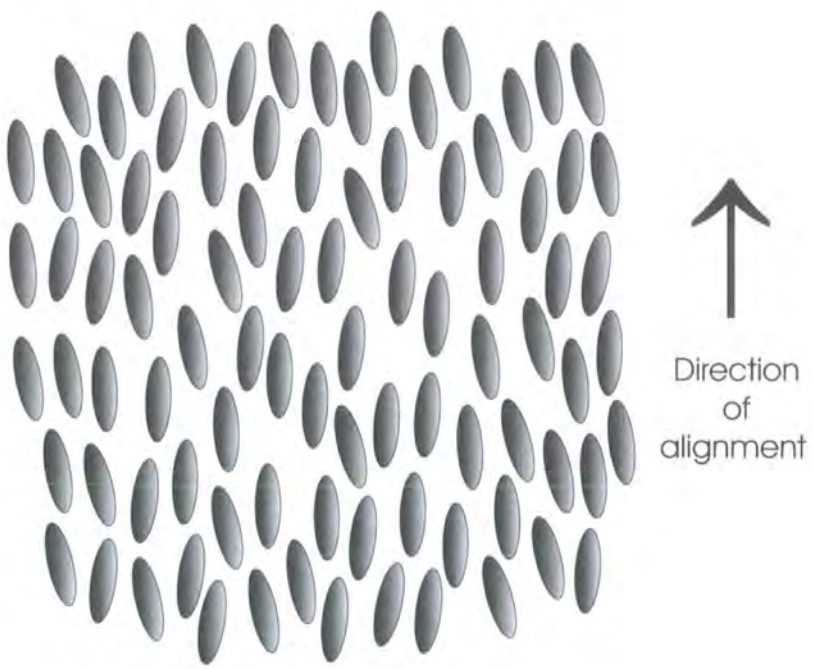

Figure 1.3: Molecular order in a nematic phase.

Smectic Liquid Crystals

Smectic liquid crystals exhibit not only one-dimensional order, like nematics, but are also stratified and therefore have two dimensional order.[15] There are many different molecular arrangements which may fit this general description. Consequently, smec-

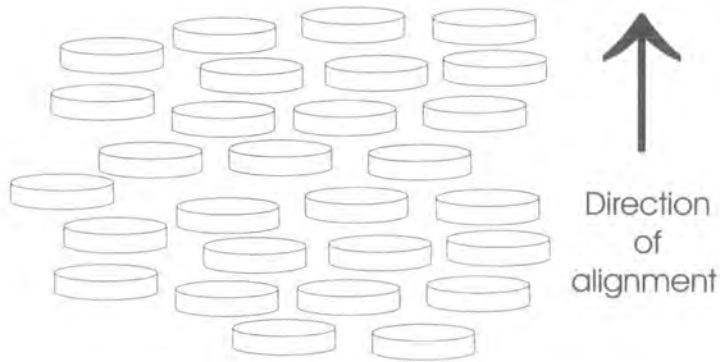

Figure 1.4: Molecular order in a discotic phase.

tic systems can be further classified according to the specific type of order involved. Simple representations of two important smectic phases can be seen in Figure 1.5 on the following page. In the smectic A phase we see layers orthogonal to the direction of alignment. In the smectic C phase, the molecules are tilted with respect to the layer normal.

Cholesteric (or Chiral Nematic) Liquid Crystals

The cholesteric mesophase exhibits the same local structure as the nematic phase but in addition molecular chirality induces a macroscopic twist about an axis that is normal to the director. The cholesteric phase is therefore optically active and left-handed or right-handed helices form from opposite enantiomers. The macroscopic helical pattern makes these phases non-superimposable.

1.3.2 Lyotropic Liquid Crystals

Lyotropic liquid crystal phases are formed by the mixing of two or more components. The phase behaviour is still influenced by temperature, but it is mainly changes in solvent concentration that lead to phase transitions. The importance of the delicate ordering of these systems in nature cannot be overestimated, as it controls the formation of cell membranes, organelles and, as a result, all living things.

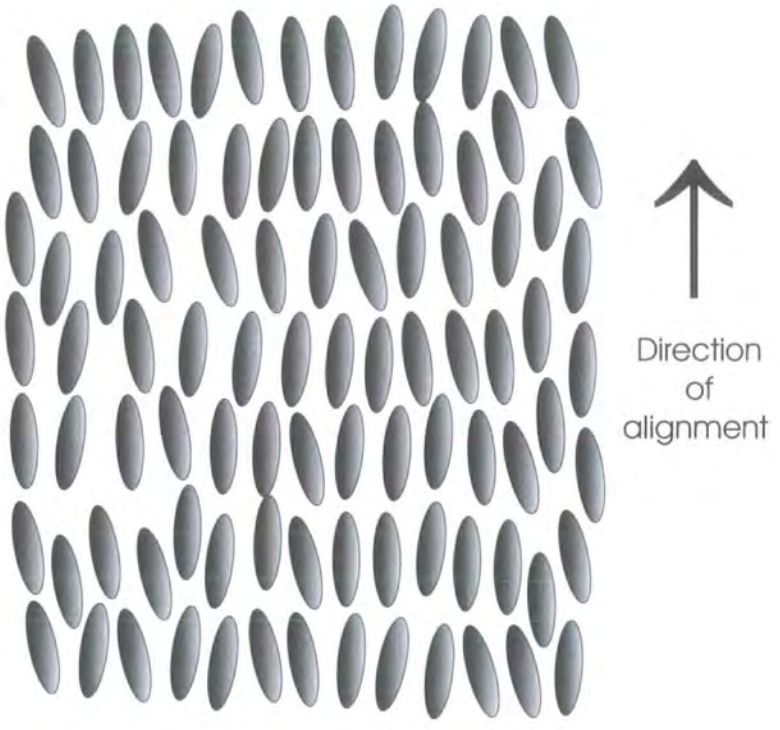

(a) Smectic A phase

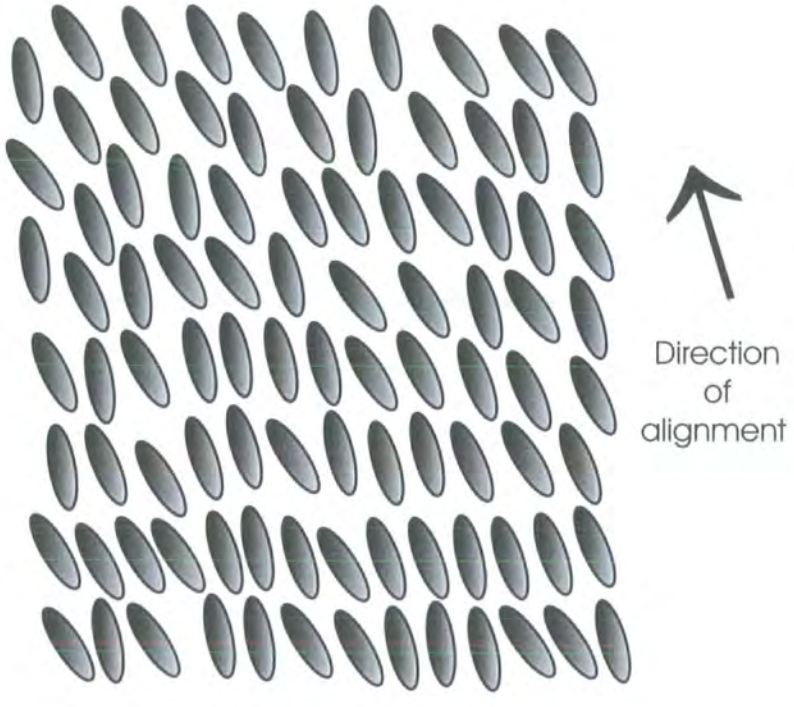

(b) Smectic C phase

Figure 1.5: Molecular order in smectic phases.

The molecular structure of lyotropic liquid crystals can vary.[16] However, a typical motif would be an amphiphilic molecule with a polar head and a hydrocarbon tail (depicted in Figure 1.6). These molecules can arrange in a number of ways, for example, in layers (lamellar phases) or in micelles as illustrated in Figure 1.7. Other arrangements include columnar phases, where all molecular tails point inward and arrange in a tubular fashion and inverted phases where molecular tails point outward into a hydrocarbon solvent. There is also variation in the packing of the columns or micelles, which may lead to cubic or hexagonal phases. If we consider a number of these molecules in a water solvent, the driving force for the formation of such a phase is the difference in hydrophilicity between the two parts of the molecule. The head groups line up to maximize contact with the solvent, while the tails group together and avoid contact with the solvent.

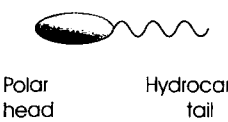

Figure 1.6: Amphiphilic molecule.

1.3.3 Other Liquid Crystals

There are a variety of liquid crystalline materials that incorporate mesogenic moieties into a larger structure or have mesogenic substituents. Such systems include liquid crystal polymers (LCPs),[17,18] elastomers and structures in which mesogens are not bonded to the main material, but are present along side, such as polymer dispersed liquid crystals. These systems will be discussed in the next chapter.

Another type of system that includes liquid crystal units in a macromolecular structure is the liquid crystalline dendrimer.[19] Here mesogenic units are attached to the ends of the branches of these molecular trees. A range of these structures have been probed and a number of mesophases reported.[20–23]

A major influence in the structure of liquid crystal dendrimers, especially for higher generations, is the large number of the mesogenic units, of which there may

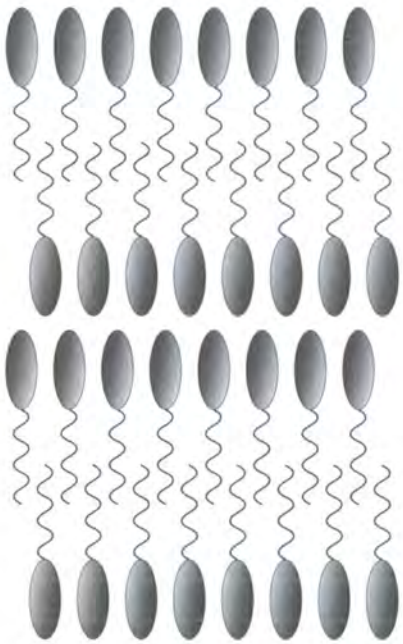

(a) cross section through strata in a layered lamellar phase.

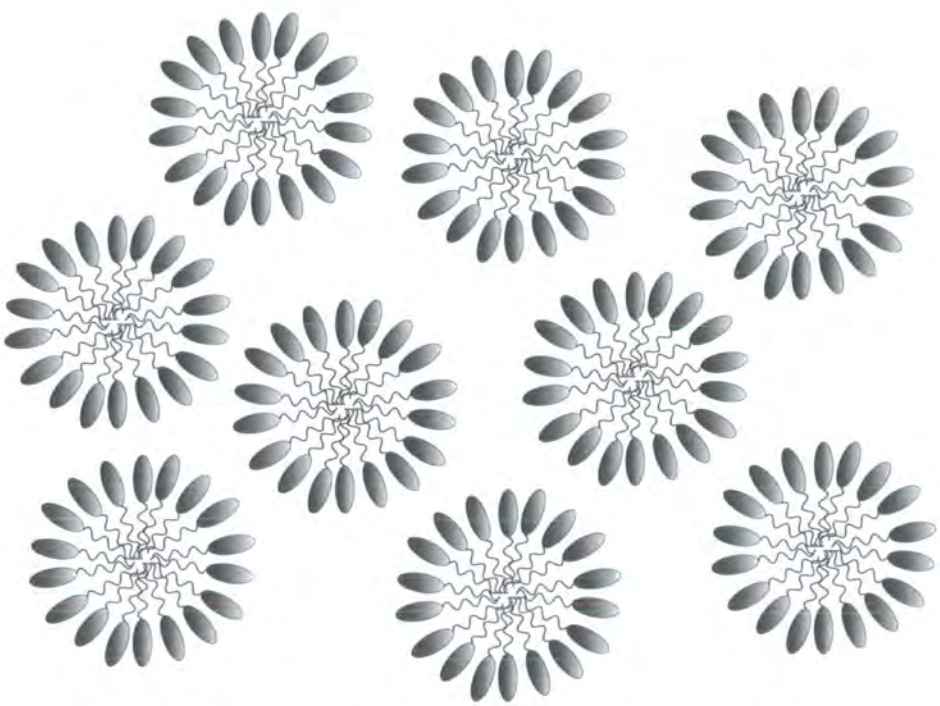

(b) Cross section through spherical micelles.

Figure 1.7: Lyotropic liquid crystal phases.

be hundreds, all joined at one central core. The phases formed can be thought of as analogous to those described for lyotropic liquid crystals, where the dendrimer is similar to a micelle. Also under the correct conditions, layered phases may also form.[24] Here the molecular order is analogous to that seen in lamellar phases.

A more thorough account of dendrimers and dendrimer liquid crystals may be found in Chapter 3.

1.4 Important Parameters

Regardless of whether liquid crystals are being studied from an experimental or a theoretical perspective there are certain key parameters that may be monitored to provide an insight into the behaviour of the system.

1.4.1 The Director

A quantitative description of the degree of orientational order in a system is often required and as the order is long range and not influenced by local short range fluctuations, this description needs to be based upon an average over many configurations of the system. To aid us with this description we define the director, $\underline{\mathbf{n}}$, as the preferred direction of alignment of the molecules in the system. This director is in effect the average direction of the molecular axis over all the configurations in question. If the system were perfectly ordered, the molecular axes of all molecules would point along the director.

1.4.2 The Order Parameter, S_2

The value we use to quantify the degree of orientational order in a given system is the order parameter, S_2. To calculate S_2 we define an angle, θ, as the angle between the director and the molecular axis of a specific molecule. This relationship is seen in Figure 1.8. Then we calculate the average,

$$S_2 = \left\langle \frac{3\cos^2\theta - 1}{2} \right\rangle . \tag{1.1}$$

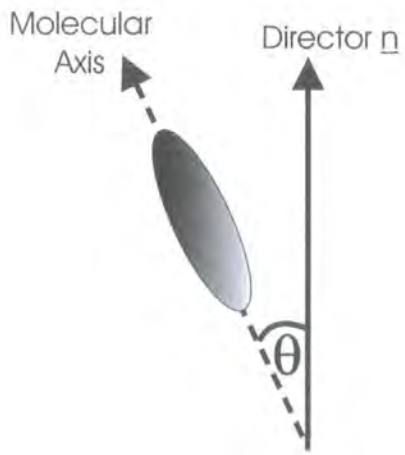

Figure 1.8: Relationship between the director and molecular axis.

The squaring of the $\cos\theta$ term leads to a lack of differentiation between a system in which all the molecules are pointing in parallel directions and one where some molecules are pointing anti-parallel.

By inspection we see that the value of S_2 has a range between -$\frac{1}{2}$ and +1 corresponding to $\theta = 90°$ through to $\theta = 0°$ respectively. It is obvious that in the case where $S_2 = -\frac{1}{2}$ that the system is highly ordered, but has aligned with the short molecular axis pointing along the director (i.e. it is a discotic nematic phase). For classic nematics, a value of S_2 in the range 0.4 to 0.8 is expected. The value tends to drop as the temperature increases and the phase transition to an isotropic liquid is approached. The nematic-isotropic phase transition is first order and consequently is shown by a discontinuous drop in the order parameter to a value of zero at the clearing point T_{NI}. An example of such a phase change can be seen in Figure 1.9.

1.5 Applications

Liquid crystalline materials are used in a wide variety of applications. The most familiar and well established use for liquid crystalline materials is in display technologies. Liquid crystalline displays range from simple monochromatic devices, that have been used in calculators, wrist watches and other appliances for many years, to more cutting edge devices such as flat panel displays with a full chromatic range

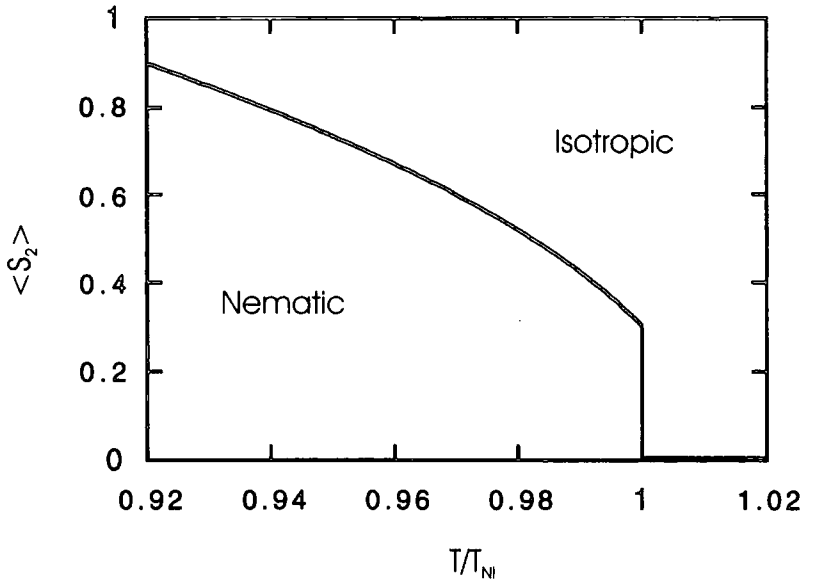

Figure 1.9: Change in order parameter, S_2, with increasing temperature.

The change occurs with a discontinuous drop in the order parameter to zero at $T/T_{NI} = 1$ (reproduced from[2]).

and little gray-scale inversion at wide viewing angles that are prevalent in laptop and desktop computers, televisions and even mobile phones.

Other areas of application that take advantage of the optical and electrical properties of these mesophases include non-linear optical devices, pyroelectric detectors and erasable optical storage disks.

With so much attention paid to the field of liquid crystal displays and other electro-optical devices it is easy to overlook the variety of other applications that utilize the unique properties of liquid crystalline materials. The delicate balance of ordering in these systems allows some materials to act as sensors. For example, the helical twist of the chiral nematic phases described in Section 1.3.1 is optically active and temperature dependent, therefore as the temperature changes so does the pitch and also the colour. This property is even more useful as it may be tailored for a desired temperature range. Among other applications thermographical technology of this kind is used for relatively inexpensive medical diagnosis where the liquid crystal can be painted onto the skin to check for abnormal temperature regions that

may be indicative of tumours or as a simple forehead thermometer to monitor a fever.

As well as the applications described above, which take advantage of properties arising from the ordering of the individual molecules in these systems, there are also applications in which the order itself is the important factor. Liquid crystalline materials may form high strength fibres or provide molecular scale templates for building specific architectures such as molecular sieves.

1.6 Computer Simulation of Liquid Crystals

Liquid crystals have been studied for many years using a wide range of computational techniques. The methodologies used in these studies range over many time and length scales; continuum theory has been well developed and is reviewed by Leslie;[25] lattice models in the spirit of the classical Ising model have been developed by Lebwohl, Lasher and others;[26–28] a variety of coarse grained models often using one site per molecule or mesogen have been studied in detail;[29–36] and more detailed fully atomistic and semi atomistic representations have been explored.[37–41] These techniques allow molecular potentials to be formulated that may be used within a simulation in order to probe the structure and structural changes that occur in a liquid crystalline material.

1.7 Scope

The work presented in this thesis concentrates on macromolecular liquid crystalline materials that incorporate thermotropic mesogens. In the next two chapters macromolecular systems are addressed. The next chapter introduces a range of polymeric materials with liquid crystalline constituents and Chapter 3 deals with dendromesogens, including some introductory information about dendrimers and properties of dendrimers that may be pertinent to the phase behaviour. In Chapter 4 the variety of models and simulation techniques used in this work and the structural properties that may be calculated from the these studies are explained.

A semi atomistic study of the phase behaviour of a side chain liquid crystal polymer is presented in Chapter 5. Using the techniques described in Chapter 4 it has been possible to characterize the phases formed by the system and transitions between structures. The model has been simulated, over a range of temperatures, with and without an external electric field.

A multiscale study of a carbosilane liquid crystal dendrimer using molecular dynamics and Monte Carlo simulations is reported in Chapters 6 and 7. In Chapter 6, the system has been investigated using a fully atomistic model, employing Monte Carlo techniques. The simulations have been carried out on single molecules using a variable strength mean field potential to represent the influence of surrounding molecules in a nematic phase, the chapter continues to describe work in which a semi-atomistic model, of the same LC dendrimer, has been studied in the presence of a Gay-Berne solvent. To complete the multiscale study, Chapter 7 details the formulation of a coarse-grained representation of the LC dendrimer that incorporates structural information obtained from the earlier studies. This model has been studied in the bulk.

Finally the various aspects of this research have been drawn together and summarized in Chapter 8.

Chapter 2

Introduction to Liquid Crystal Polymers

This chapter provides a short introduction to polymeric liquid crystalline materials. There is considerable interest in the systems described in this chapter, which contain mesogenic groups as part of a larger structure. These materials include liquid crystal polymers, liquid crystal elastomers and polymer dispersed liquid crystals. As Chapter 3 will concentrate on dendritic and hyperbranched materials, they will not be included in this discussion.

2.1 Liquid Crystal Polymers (LCPs)

Liquid crystal polymers fall into two broad classes: main chain LCPs and side chain LCPs.[42] This classification depends on the location of the mesogen within the polymer structure.

2.1.1 Main Chain Liquid Crystal Polymers (MCLCP)

In this class of LCPs the mesogens are incorporated into the backbone.[43,44] They are synthesized by condensation of mesogenic bifunctional monomers to yield low molecular weight MCLCPs. Figure 2.1 shows a cartoon of a typical MCLCP. These were first type of liquid crystal polymers to be discovered and a range of nematogenic and smectogenic polymers have been known for many years.[45]

Figure 2.1: Main chain liquid crystal polymer motif, showing the mesogens embedded in the backbone.

Figure 2.2: Alternative MCLCP motifs. (a) laterally embedded mesogens, (b) MCLCP with side groups, (c) rigid MCLCP.

There are many different structural variations possible for MCLCPs. These include; different orientations of mesogenic groups within the polymer; attachment of side groups; incorporation of non-rod shaped mesogens such as pear, disc or bent 'banana' shape moieties; and exclusion of the flexible chains between mesogens to form more rigid chains. Schematic diagrams of polymers with these structural features have been sketched in Figure 2.2.

Many MCLCPs have aromatic groups in the backbone. Simple examples of aromatic MCLCP structures are depicted in Figure 2.3. The rigidity of the polymer often depends on the linkage between aromatic units.[46] The linking groups shown are quite short, and may even be absent from some polymers. Therefore, these polyaromatic systems are likely to resemble the structure in Figure 2.2(c). Structures that contain flexible spacers between mesogenic groups, like the polymers studied by Lenz, are less rigid.[47] Table 2.1 shows the structure of one of these polymers and

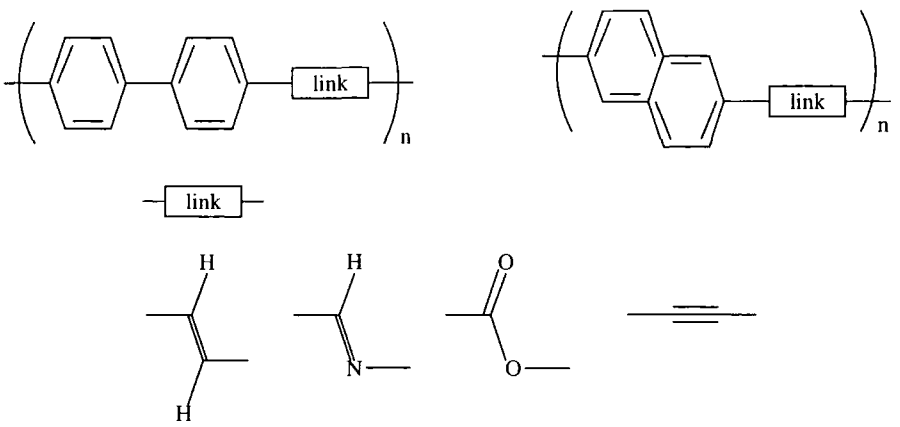

Figure 2.3: Examples of MCLCP monomers. Two aromatic backbones and some possible linkage groups for these aromatic polymers are shown.

transition temperatures for a homologous series of that polymer functionalised in different ways. Greater flexibility of the substituents lowers transition temperatures as the phases become less thermally stable. This loss in thermal stability is greater for the more condensed phases. This results in a broadening temperature range for liquid crystal phases. The reason for this change in phase behaviour is that the flexible side groups disrupt the close contacts of the polymer chains.

As we have seen, the character of the side group will have an influence on the phase behaviour of the polymer. If a group is bulky it will increase the glass transition temperature of the polymer. If the group is a flexible side chain it will depress the glass transition temperature and the material becomes more ductile. In effect the flexible side group acts as an internal plasticizer. This can be illustrated by considering a common group thermotropic MCLCPs, the substituted poly-(*p*-phenyleneterepthalate)esters. With Table 2.2 is a figure showing the structure of the polymer, which may be substituted at the sites labeled as X and Y. The effect of these substituent groups on phase transition temperatures is shown in Table 2.2. For the series of alkyl chain substituents the same overall trend that was observed in Table 2.1 is evident. For bulkier groups such as phenyl, chloro- and bromo- substituents we see a similar effect with the smallest chlorine group depressing T_m the least and phenyl having the greatest effect. It is interesting to see that if both sides

R	T_g (°C)	T_m(°C)	T_c(°C)
H	340	509	540
Methyl	317	427	463
Ethyl	308	344	400

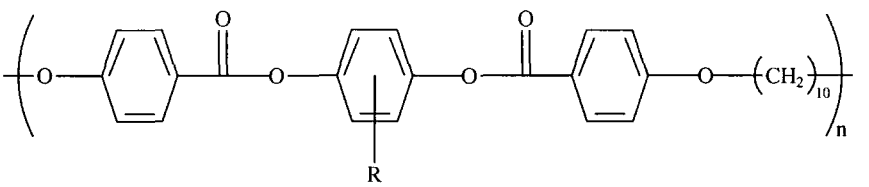

Table 2.1: Comparison of Glass transition temperature, T_g, melting temperature, T_m, and clearing temperature, T_c, of a series of MCLCPs. R is the substitution site.

are substituted with bulky phenyl groups crystallization is suppressed. Here the glass formed retains nematic order from the mesophase.

2.1.2 Side Chain Liquid Crystal Polymers (SCLCP)

An alternative structural motif for liquid crystal polymers has the mesogenic units attached as side chains, which hang from the polymer backbone (see Figure 2.4). The first attempts to synthesize these polymers produced molecules that did not form liquid crystal phases, as the tendency for the backbone to adopt a random coil conformation was dominant over the mesogens preference for orientational order. In 1978 Ringsdorf *et al.* used a short flexible carbon chain to link the mesogens to the backbone.[50] This spacer group enables the mesogens to arrange anisotropically as they are now less hindered by the backbone conformation; however, the backbone still exerts a significant influence on mesomorphism. Such systems usually include thermotropic mesogens that form smectic and nematic phases.[51] The mesogens in such systems are usually attached terminally as illustrated in Figure 2.4, but can be attached laterally or in both directions as in Figure 2.6.

X	Y	T_g (°C)	T_m(°C)	T_c(°C)	Source
n-hexyl	H	-	277	323	[48]
n-heptyl	H	-	257	302	[48]
n-octyl	H	-	257	307	[48]
n-nonyl	H	-	237	291	[48]
n-undecyl	H	-	228	292	[48]
Cl	H	220	372	510	[49]
Br	H	-	353	475	[49]
Phenyl	H	170	346	475	[49]
H	Cl	220	402	475	[49]
H	Br	-	353	475	[49]
H	Phenyl	130	265	343	[49]
Phenyl	Phenyl	122	-	231	[49]

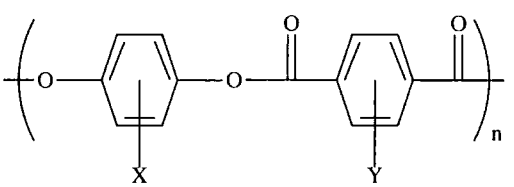

Table 2.2: Comparison of Glass transition temperature, T_g, melting temperature, T_m, and clearing temperature, T_c, of substituted poly-(p-phenylene terepthalate) esters,where X and Y are sites for substitution.

Figure 2.4: Side chain liquid crystal polymer with mesogens terminally attached to flexible spacers.

(a) (b)

Figure 2.5: SCLCP with (a) lateral side groups, (b) lateral and terminally attached mesogens.

In addition to the morphologies discussed in the last chapter, liquid crystalline polymers with side chain mesogens lead to an additional consideration of the smectic phase: mesogen units from different layers may interdigitate or remain separate.

Tables 2.3, 2.4, 2.5 and 2.6 respectively show the influence on the phase behaviour of SCLCPs, of the polymer backbone, molecular weight, tacticity and flexible spacer length.

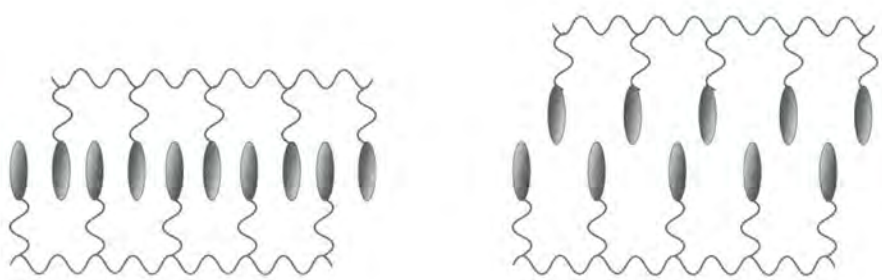

(a) (b)

Figure 2.6: SCLCP layer. (a) interdigitated side groups, (b) non-interdigitated side groups.

Polymer	Transitions (°C)	ΔT
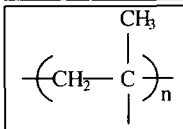	g $\xrightarrow{96}$ N $\xrightarrow{121}$ i	25
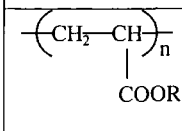	g $\xrightarrow{47}$ N $\xrightarrow{77}$ i	30
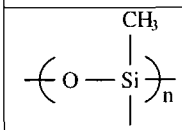	g $\xrightarrow{15}$ N $\xrightarrow{61}$ i	46

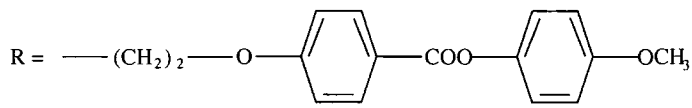

Table 2.3: Effect of the backbone in a SCLCP. Showing the phase transitions of polmethacrylate, polyacrylate and polysiloxane. Reproduced from[52]

Polymer Backbone

In Table 2.3 the phase behaviours of polymethacrylate, polyacrylate and polysiloxane backbones functionalised with a side chain containing a common mesogen are reported. Polysiloxane has the most flexible backbone of these polymers, polymethacrylate has the least flexible. Greater flexibility of the polymer backbone leads to more freedom of movement and position for the mesogen; it is more decoupled from the backbone. This decoupling allows more ordering to take place and the temperature range of the mesophase increases.

Molecular Weight

In Table 2.4 a comparison of three systems of the same polymer, differing only by molecular weight is reported. This polyacrylate side chain liquid crystal polymer was studied by Portugall *et al.* and shown to exhibit a nematic phase.[53] There is a clear trend for longer polymer chains to result in greater thermal stability and therefore

$\bar{M}_n$	degree of polymerisation	Transitions (°C)	ΔH
4500	13	g $\xrightarrow{53}$ N $\xrightarrow{100}$ i	0.6
14000	41	g $\xrightarrow{59}$ N $\xrightarrow{114}$ i	0.6
39000	114	g $\xrightarrow{62}$ N $\xrightarrow{116}$ i	0.9

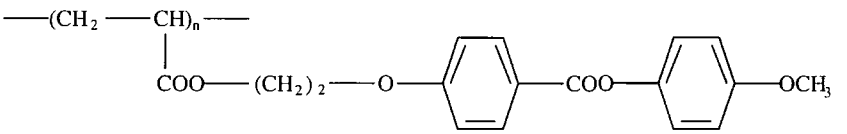

$\bar{M}_n$ is the number average molecular mass of the polymer.

Table 2.4: Effect of molecular mass on phase behaviour of a liquid crystalline polyacrylate.[54]

a rise in the temperature of the transitions. The rise in T_g is less than that of T_c leading to an increased range for the mesophase. The enthalpy of transition also increases with $\bar{M}_n$, which may indicate that there is more order in the systems with greater molecular mass. This increase in order of the mesophase may be because there is less coupling of the mesogens in longer chains.

Tacticity

Although the influence of tacticity on LCPs has not been extensively investigated, it seems likely that some stereochemical configurations place mesogens in positions which are favourable for crystallization. Therefore the tendency for mesophase formation is reduced. In addition, atactic configurations tend to increase chain flexibility.

Tacticity	Transitions (°C)
Atactic	K $\xrightarrow{117}$ S $\xrightarrow{127-131}$ i
Isotactic	K $\xrightarrow{131}$ S $\xrightarrow{135}$ i

Table 2.5: Effect of the Tacticity in a SCLCP.

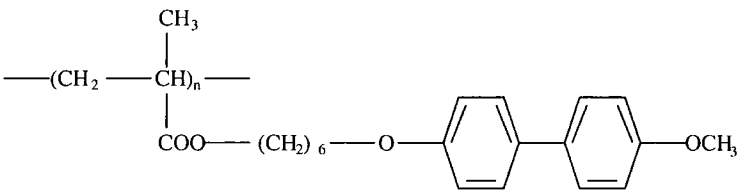

Hahn *et al.* studied the effect of the tacticity for the LCP poly[6-(4'-methoxy-4-biphenyloxy)hexy]methacrylate.[55] As can be seen in Table 2.5, the more flexible atactic polymer is the one which shows a mesophase. The more regular isotactic polymer is the one which exhibits a higher melting point.

Flexible Spacer Length

The flexible spacer plays a crucial role in decoupling the order of mesogenic groups from the LCP backbone. Extensive flexibility in the spacer leads to phase behaviour that closely resembles the low molecular weight mesogenic analog.

In Table 2.6, an increase in spacer length leads to a larger number of mesophases, enhanced thermal stability of the phases and an increased temperature range over which mesophases occur.

2.1.3 Combination LCPs

In some liquid crystal polymers both main chain and side chain motifs are combined to produce a polymer that has mesogenic units as side groups and as part of the polymer backbone as shown in Figure 2.7. Combination main chain and side chain

Spacer length	Transitions (°C)
0	$S \xrightarrow{255} i$
2	$g \xrightarrow{120} N \xrightarrow{152} i$
6	$K \xrightarrow{119} S \xrightarrow{136} i$
11	$g \xrightarrow{54} S_C \xrightarrow{87} S_A \xrightarrow{142} i$

Table 2.6: Effect of the flexible spacer length in a SCLCP.

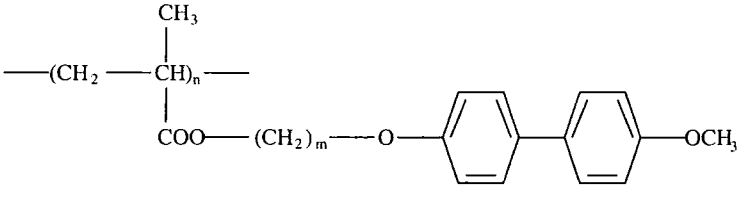

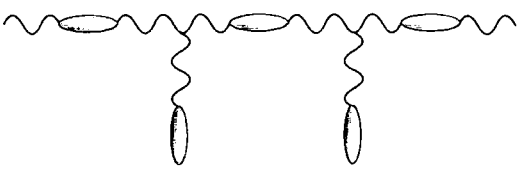

Figure 2.7: Liquid crystal polymer with main and side chain mesogens.

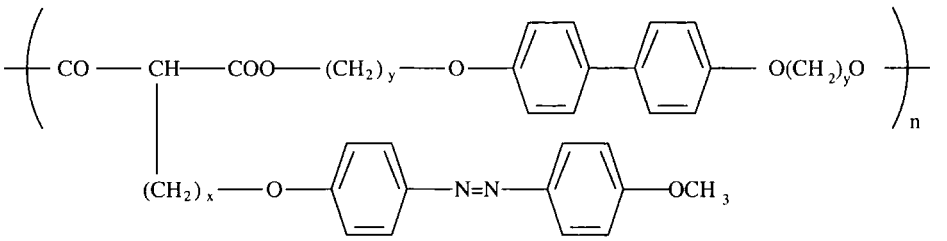

Figure 2.8: Example of a combination liquid crystal polymer.

LCPs were initially investigated as a possible route to a biaxial phase.[56] However, much work has shown that combination polymers are not biaxial, but do have interesting phase behaviour.[57,58] The mesophases formed by combination polymers generally have all mesogens, from the main and side chains, aligning in a common direction. The phases often have wide temperature ranges and sometimes more than one phase may exist in the material at the same time.

In Figure 2.8, a combination polymer from an early study is shown.[56] Here the phase behaviour is quite dependent on the lengths of the flexible spacers in the side group and in the backbone, x and y respectively, as this determines the ease with which the two mesogen types can line up to form smectic layers. The influence of spacer lengths is depicted in Figure 2.9. The relative lengths of the mesogens will also influence whether a smectic or nematic phase is prevalent. If the main chain and side chain mesogens are the same or of similar dimensions, then smectic and nematic phases are likely. Nematic phases will prevail if there is a difference in sizes between the types of mesogen.

The morphology of combination phases will also be influenced by differences in the strengths of interaction between mesogens. If the mesogens favour interaction with other mesogens of the same type, their may be some degree of microphase separation. Otherwise, if interactions between mesogenic moieties from different parts

Figure 2.9: Influence of main and side chain spacers on phase formation.

(Reproduced from[59])

of the polymer are strongest then a mixed phase may form. Again the difference in spacers will have a bearing on these phases.

A comprehensive account of the field of combination polymers can be found in the Handbook of Liquid Crystals, Volume 3.[60]

2.2 Liquid Crystal Elastomers

Mesogenic moieties in side chain liquid crystals polymers may span two polymer backbones creating a crosslink as shown in Figure 2.10. Polymers which are highly crosslinked are known as elastomers. Therefore, these crosslinked LCP materials are known as liquid crystal elastomers. Crosslinks may also be introduced between chains of MCLCPs or SCLCPs or between mesogenic groups as shown in 2.11. Combination polymers may also be cross-linked to form elastomers.

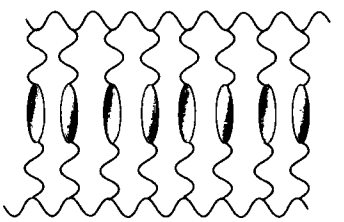

Figure 2.10: Liquid crystal polymer with crosslinks.

As with other polymer liquid crystals, elastomers, combine mechanical properties of the polymeric network with the phase behaviour of the liquid crystalline constituents. For an elastomer, the important mechanical characteristics are elasticity and shape retention. Liquid crystal elastomers show phase behavior which resemble that of low molecular weight liquid crystals. A feature of great interest in

Figure 2.11: Liquid crystal elastomer.

these systems is the possibility of shifting a phase transition temperature by exploiting the mechanical properties, for example, by applying a force. The macroscopic motion of the chains is greatly reduced, but the most microscopic motion of chain segments is unaffected. This microscopic motion allows movement, and alignment, of mesogenic units.

2.3 Polymer Dispersed Liquid Crystals

Droplets of a low molecular weight liquid crystal may be embedded into a solid polymer. This creates a malleable plastic material with liquid crystalline domains as shown in Figure 2.12. The small nematic domains will point in random directions. Application of a field to the polymer will line up these domains. In the absence of a field the material will scatter light. When the domains are aligned the scattering is reduced.

2.4 Application of LCPs

Liquid crystal polymers are used in many applications. The liquid crystalline characteristics provide interesting electro-optical properties, which, together with the advantages of polymeric materials such as processability and weight make a powerful combination.

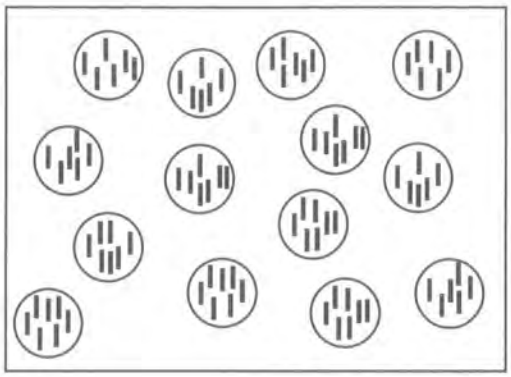

Figure 2.12: Polymer dispersed liquid crystal with aligned domains.

Side chain liquid crystal polymers may be used as thermal recording media. A polymer film of homotropically aligned SCLCP can be subjected to a laser that may heat a small, well-defined area causing the mesogens in that region to disorder. When the film is lowered to a temperature below the glass transition if the region realigns, it is likely to form domains and the director will not concur with that of the rest of the film. This region will no longer transmit light but will appear opaque. If cholesteric liquid crystals are used it is possible to achieve holographic data storage, which may be reversible.

Display applications of SCLCPs are not usually viable owing to the high viscosity and therefore long switching times. However, doping may provide a solution to this problem. Other liquid crystal polymers that have been tailored for faster switching times, for example by lowering T_g to allow more molecular motion, may be used as an alternative, low weight, flexible display material.

Main chain liquid crystal polymers may be spun to produce high strength fibres such as Kevlar®. Extended polymer chains can be aligned in a common direction with the aid of the liquid crystalline order making a reasonably light fibre extremely strong.

Polymer dispersed liquid crystals may be used to form optical devices which are flexible and bright, as light does not need to be polarized, but do not need well defined optics. One potential application is switchable windows that are transparent when a field is applied and when the field is removed scatter the light strongly so appear opaque.

Like their low molecular weight analogs, polymer liquid crystals have a variety of other uses including use as sensors, optical devices and molecular templates.

Chapter 3

Introduction to Liquid Crystal Dendrimers

This chapter provides a brief introduction to the broad area of dendritic systems, concentrating on the factors that effect dendromesogens and the phases they form. The field of dendrimers research is both extensive and prolific; there is a large selection of literature available including many thorough reviews of the subject.[61,62] It is obvious that to produce an exhaustive account of even just the liquid crystalline side of dendritic research is far beyond the scope of this work. Therefore, the aim of this chapter is to highlight key considerations for mesophase formation and to provide a few examples of molecules and morphologies that have been studied in this field. The work of Goodby *et al.*[11,63] is extremely useful in bridging the gap between understanding the behaviour of low molecular weight liquid crystals and larger oligiomeric and dendritic liquid crystals.

3.1 Historical Perspective

In 1944, during his delivery of a paper to the Faraday society,[64] Harry Melville stated:

> High Polymer molecules consist not only of long single strings of atoms united by primary valences, but also of such strings linked together at

> one point, that is the branched chain molecule, or at several points giving rise to a three dimensional network.
>
> ... up to the present such molecules have not been prepared, and thus no information about their behaviour is available.

Indeed, it was to be over thirty years until the first reported synthesis of dendritic molecules was published.

During the 1970s the groups of Vögtle and Newkome were working on complexation and guest/host systems with multidentate ligands.[65] So it was in search of a macromolecular selective substrate that Vögtle *et al* performed the first 'cascade' synthesis[66] in 1978. Since then this area of polymer science has become more and more popular, with many reviews published.[19,67,68] The first of these reviews[69] was where Tomalia coined the phrase 'Dendrimer' which originates from the Greek term 'dendra' meaning tree.

3.2 Molecular Structure

3.2.1 Dendrimers

Ideally, dendrimers are monodisperse, perfectly branched polymers, where each branching unit is identical to the other units. Therefore, dendrimers have fractal symmetry. An example of a dendrimer is shown in Figure 3.1. The main parts of a dendritic structure are the core, the branching points and the terminal groups. These aspects have been highlighted Figure 3.2. The surface groups are extremely important as they may be functionalised, to give a desired character to the molecule. It is important to note that there is a certain amount of free space between branches, these inner-cavities increase as the generation number increases. The surface groups, on the contrary, become more tightly packed as the generation number increases.

Melville's paper, from which the extract in Section 3.1 is taken, begins with a more fundamental statement about polymer science.

> Nearly every important property, and especially mechanical characteristics of a high polymer, is dependent on the molecular weight; therefore

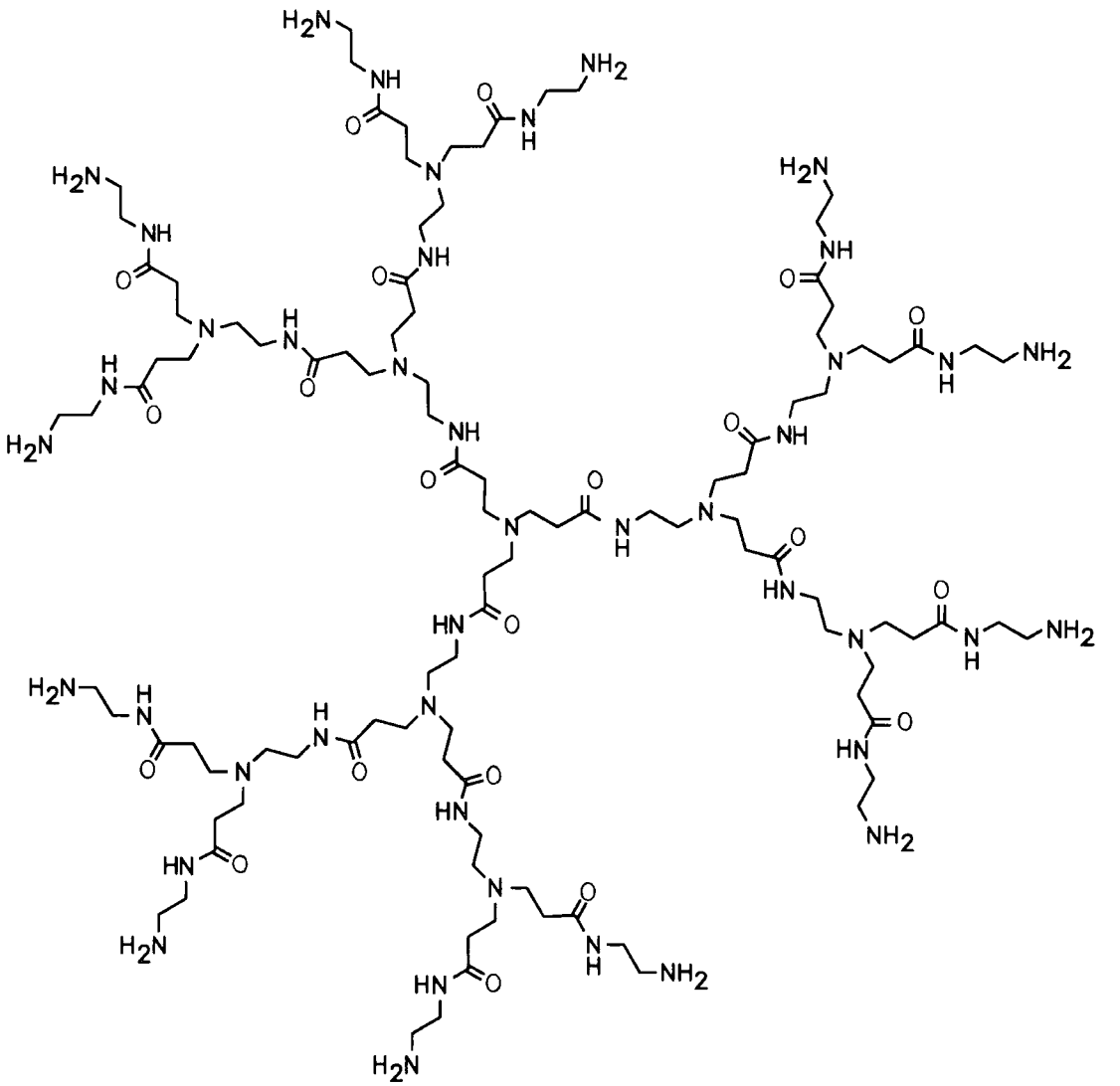

Figure 3.1: Molecular structure of a second generation poly(amidoamine) dendrimer.

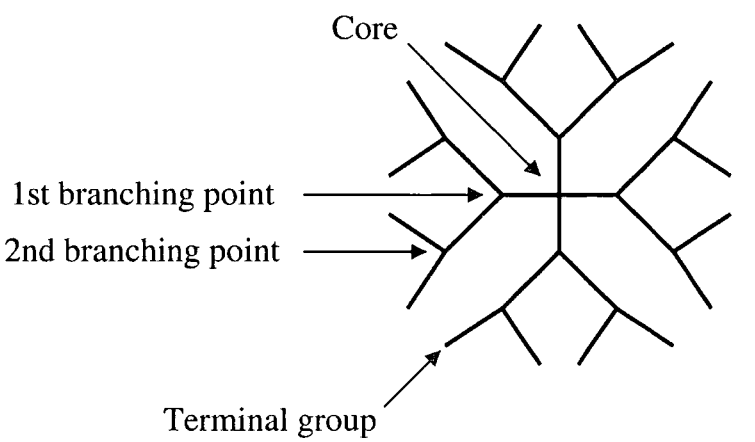

Figure 3.2: Schematic of a second generation dendrimer.

it's accurate determination is a prerequisite to advances in this branch on chemistry.

Calculation of average molecular weight for a polymer depends on the molecular weight distribution. As the molecular weight is not a single value the properties mentioned above do not have one specific value either. In the case of dendrimers, which are monodisperse, these properties are more sharply defined. This increased specificity of structure is desirable when tailoring molecular properties to applications.

Another class of dendritic molecules, often without fractal symmetry are arborols.* Arborol molecules are highly branched structures with surfaces functionalised by the hydroxide group. Often arborol molecules have different branching units in each layer. An examples of an arborol molecular structure is found in Figure 3.3, taken the early work of Newkome *et al.*[70] This molecule was synthesised and studied to investigate its suitability as a micelle analogue. In some ways, such molecules are analogous to the block copolymers that are studied in the field of linear polymers.

3.2.2 Hyperbranched Polymers

Despite feverish interest in dendritic structures, branched polymers as Melville suggested can take a number of different patterns. The term "Hyperbranched polymer" is used to refer to polymers in which the branching structure is random. Hyperbranched molecules can be made by simpler synthetic routes than the dendrimers, which require full conversion at each step to maintain their perfect structures. The randomness of hyperbranched polymers means that they are not monodisperse in there size or structure.

3.2.3 Dendrons

Classification of dendritic molecules is often quite complex. The term "dendron" is often used to describe a dendritic structure that is not a full spherical dendrimer,

*From the Greek word 'arbor' meaning branch.

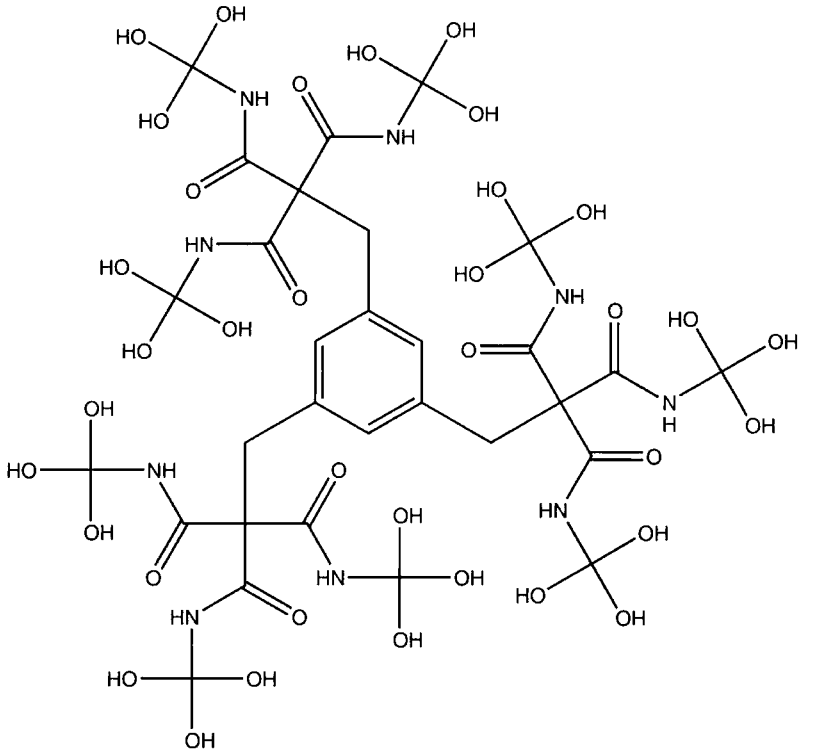

Figure 3.3: Arborol structure with an aromatic core, amide links in the first generation and alcohol groups on the surface.

but is a branch or wedge of a dendrimer. These dendrons may be attached to a central core to make a dendrimer or coupled to other groups to provide a wider range of molecular shapes. Such structures expand the variety of motifs that are available from branched molecular structures.

3.3 Geometrical Considerations

One of the most important mathematical concepts to be considered with dendritic growth is that of the starburst limit. If we consider that the sphere of space available to a dendrimer increases as a cube of the generation number, but that the number of monomer units within the structure increases by an exponential factor, a point will arise where there is simply insufficient space to move to the next generation. The point when the space available for growth becomes inadequate is known as the starburst limit and at this stage in dendrimer growth a high level of steric crowding causes the molecule to adopt a globular configuration.

The starburst limit may be calculated mathematically, along with density functions and crowding factors. Such calculations require some molecular details: the number of the number of branches on the core or core multiplicity; the number of branches at the branch point or branch multiplicity; the length and volume of the branching unit; and the core volume. We consider the total molecular volume, V_{tot}, as calculated in Equation 3.1 and the conformationally available volume, V_{ca}, as shown in Equation 3.2 and hence calculate a crowding factor f_{cr} as defined in Equation 3.3.

$$V_{tot} = \nu_c + \nu_s \left(n_c n_b^g\right) - \frac{\nu_b n_c}{n_b} + \sum_{x=0}^{g} \nu_b n_c n_b^{(x-1)}, \tag{3.1}$$

$$V_{ca} = \frac{4}{3}\pi \left(r_c + g l_b + l_s\right)^3, \tag{3.2}$$

$$f_{cr} = \frac{V_{tot}}{V_{ca}}. \tag{3.3}$$

In these equations ν_c, ν_b and ν_s are the volumes of the core, branch and surface moieties respectively, n_c and n_b are the multiplicities of the core and branching units, g is the generation number, r_c is the core radius, and l_b , l_s are the lengths of branches and surface groups.

If Equation 3.3 is expanded using Expressions 3.1 and 3.2 we see

$$f_{cr} \approx \frac{k\left(n_b^g - 1\right)}{g^3\left(n_b - 1\right)}, \tag{3.4}$$

where $k = \frac{3\nu_b n_c}{4\pi l_b^3}$. This simplified expression facilitates the plotting of the graph in Figure 3.4. It is shown in Figure 3.4 that a branch multiplicity of two leads to a series of generations where the second generation is approximately as crowded as the seventh. This indicates that generation seven is below the starburst limit. Therefore, there is reason to expect that, if efficient methods of preparation are used, the formation of such a dendrimer to at least generation seven is sterically feasible.

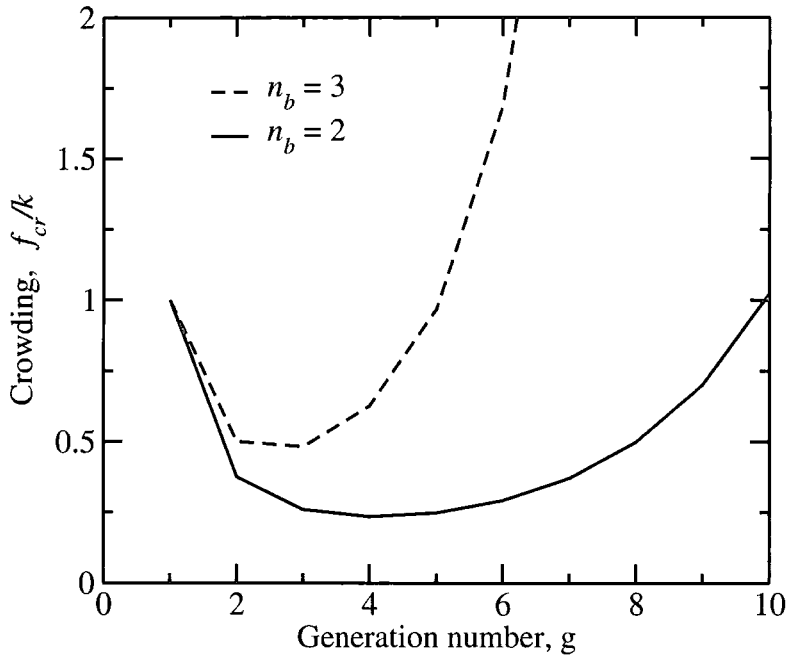

Figure 3.4: Relative crowding in terms of the crowding factor, f_{cr}, and the constant k with increasing generation, g. Branch multiplicities, n_b, of 2 and 3 have been plotted.

3.4 Dendromesogens

In recent years the emphasis of dendritic research has changed. As this branch of polymer science has become more mature, the motivation behind the work has become more application orientated. Dendrimers have possible applications for a range of applications in a variety of areas including medical engineering, agrochemistry, imaging, cosmetics and pharmaceuticals.

Functionalisation of dendritic molecules to expand the range of molecular characteristics available has led to the exploration of dendrimers that exhibit liquid crystalline characteristics. Such dendrimers have been called dendromesogens.

Liquid crystalline effects in branched macromolecules arise in three different ways: the whole molecule may act as a mesogen, the internal structure of the dendrimer may contain mesogenic moieties or the surface of the dendrimer may be functionalised with mesogenic groups. Each of these possibilities can lead to a number of possible morphologies.

3.4.1 Whole Molecules as Mesogens

When a whole molecule is behaving as a mesogenic unit it may form an overall rod or disc shape. These large mesogens can then pack together, for example discotic systems may pack in columns. A schematic representation of a columnar phase is depicted in Figure 3.5. Arrangement of columns can be random or they may pack into a number of patterns as is shown in Figure 3.6. An example of this type of ordering in discotic systems has been reported by Meier *et al.*[71] In this work the whole molecule acts as a large discotic mesogen. Hexagonal disordered, rectangular disordered and oblique phases are observed in these stilbenoid dendritic systems. The mesomorphism is only observed up to the third generation after which there is much greater steric hindrance to prevent mesophase formation. Pesak and Moore found that the first three generations of a phenylacetylene dendritic structure with peripheral ether chains also displayed this type of phase behaviour forming discotic mesophases.[72] Here the molecules form a anisotropic disc shape as they are relatively small and the crowding factor is low.

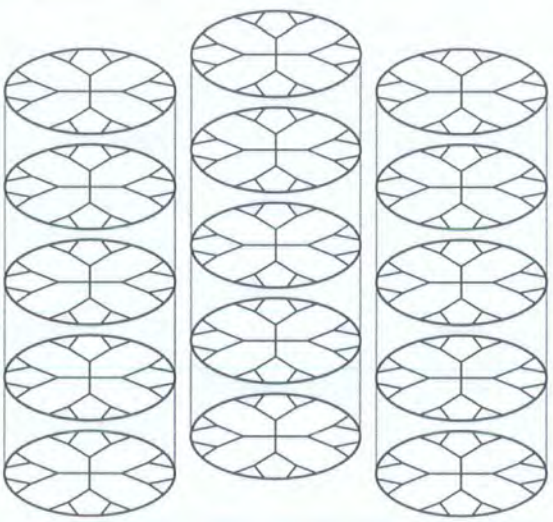

Figure 3.5: Whole dendrimer molecules may act as mesogens to form a columnar phase.

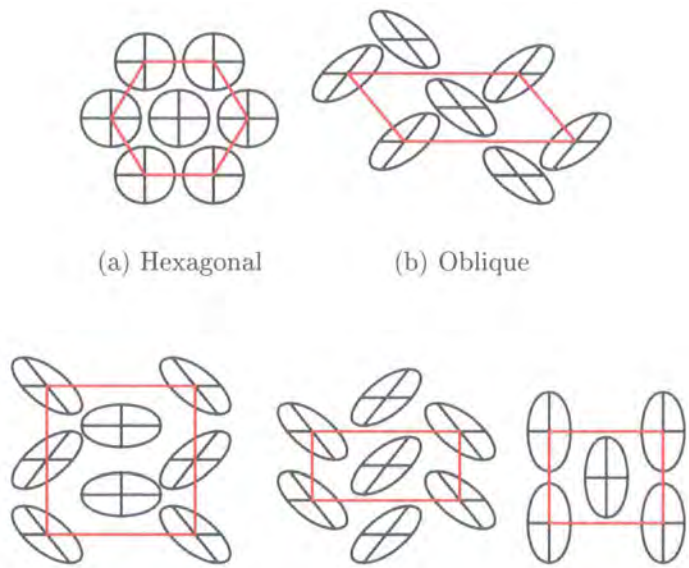

(a) Hexagonal (b) Oblique

(c) Rectangular

Figure 3.6: Schematic representation of a number of possible columnar morphologies.

Here the spoked ellipses and circles represent columns viewed from above.

3.4.2 Mesogens in the Interior of the Dendrimer

Dendritic structures with thermotropic mesogenic moieties forming the branched structure are generally found to have nematic and smectic phases in a similar way to their low molecular weight analogues. Figure 3.7 shows how this type of dendromesogens form nematic and smectic mesophases.

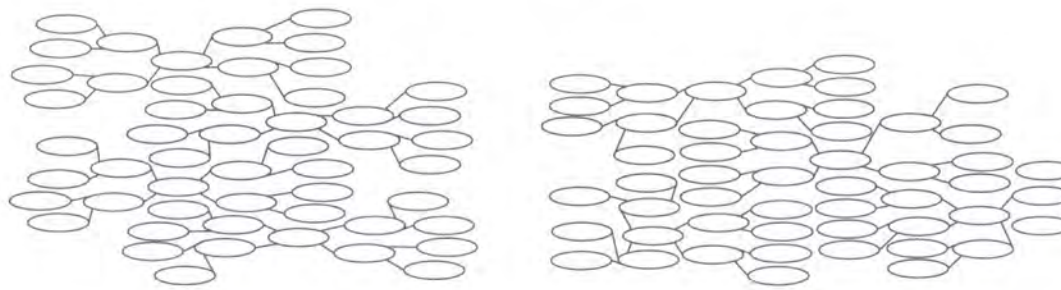

(a) (b)

Figure 3.7: Dendrimers with mesogens incorporated in their internal structure forming a) nematic and b) smectic phases.

There a many examples of calamitic systems with mesogenic moieties incorporated as an integral part of the core[73,74] including the work of Percec *et al.*[75] Here a rod-like AB_2 mesogenic monomer is used as the starting point in a convergent synthesis to form monodendrons and dendrimers, which systems were shown to be monodisperse. Within the range of dendrimers and dendrons that were synthesized a number of liquid crystal phases were observed. The first generation dendron molecule displayed a monotropic nematic with a small temperature range. For the second generation the mesophase temperature range expanded and the transition became enantiotropic and for the third and fourth generations nematic and smectic phases were seen. By connecting a number of the first generation dendrons together to form a dendrimer, again, the mesophase temperature range expanded and became enantiotropic. In the first generation dendrimer a smectic phase is also observed and higher generation dendrimers also have nematic and smectic mesophases.

Lyotropic systems of this kind have also been studied. Hyperbranched polymers studied by Kim[76] exhibit lyotropic mesomorphism as a result of the highly branched spheroid structure interacting with a solvent in differing concentrations. No crys-

tallinity had been previously detected in the polymer, but birefringence structure was observed.

3.4.3 Mesogens on the Surface of the Dendrimer

One of the valuable attributes of dendritic molecules is the potential for surface group functionalisation. The majority of investigations of liquid crystalline dendrimers study dendritic systems with the mesogenic groups attached to terminal groups There is a delicate balance between the mesogenic group preference for alignment into liquid crystalline morphologies and the entropy driven isotropic arrangement favoured by the core. This balance is modified by flexible spacers, which, like in side-chain liquid crystal polymers, decouple mesogens from the core. Figure 3.8 is a schematic representation of a nematic and a smectic phase formed by this type of molecule. These phases are analogous to those described in the previous section shown in Figure 3.7.

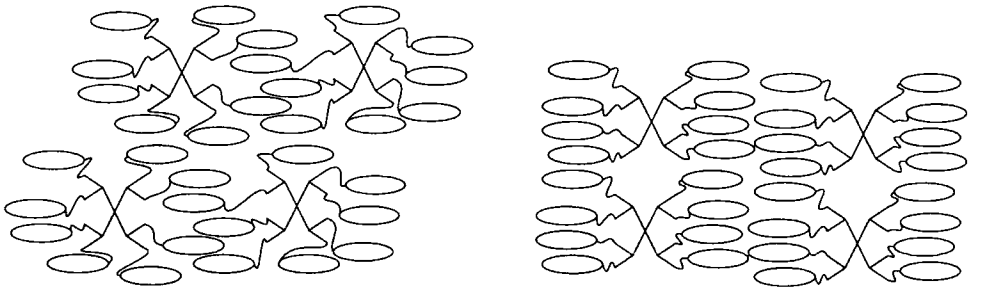

(a) (b)

Figure 3.8: Dendrimers with mesogens attached to surface groups forming a) nematic and b) smectic phases.

The molecules represented in Figure 3.7 form liquid crystalline morphologies that are extremely similar to low molecular weight mesogens. However, this class of the strength of the liquid crystalline characteristics of dendrimers that have peripheral mesogenic groups are greater than would be expected from low molecular weight mesogens tethered to a core. As with the dendrimers described in Section 3.4.1, the whole macromolecule may behave as a mesogen. Figure 3.9 is a schematic

representation of such a dendromesogen forming a rod and a disc conformation. Although this figure shows a a low generation dendrimer these conformations are not restricted to small dendromesogens.

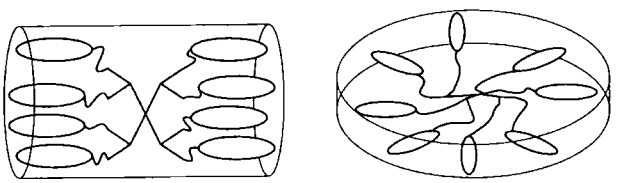

(a) (b)

Figure 3.9: Schematic diagram of a surface functionalised dendromesogen forming an overall a) rod and b) disc shape.

Barberá *et al.* have also studied dendromesogens with peripheral functionalisation.[24,77] Poly(amidoamine) dendrimers with mesogenic esters attached to the surface, in this work mesogens formed rods which aligned to form smectic layers as illustrated in Figure 3.10. They showed that with increasing generation number, and so number of mesogens, the diameter of the rod increases. However, the length of the rod changes very little. These combined effects result in a more disc-shape mesogen in larger generations. Therefore, the radial conformation (Figure 3.9b) is more likely for the larger generations, leading to columnar morphologies as illustrated in Figure 3.11.

Other studies of this class of dendromesogens show similar trends for generation dependent morphologies. For example, carbosilanes functionalised with peripheral mesogens show smectic morphologies for the first four generations, with a change to what is thought to be a columnar morphology in the fifth generation.[78–83]

3.5 Assemblies

Dendritic systems that consist, not of whole dendrimer molecules but, of assemblies of highly branched constituents like those shown in Figure 3.12 are the subject of a great deal of research. Percec *et al.* have synthesized a number of systems in which dendritic wedges come together to form columns or, for highly crowded

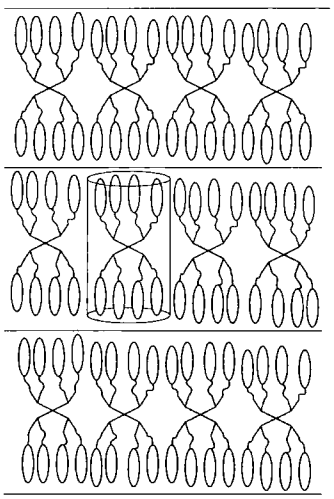

Figure 3.10: Diagram depicting smectic layer formation from rod-shape dendromesogens.

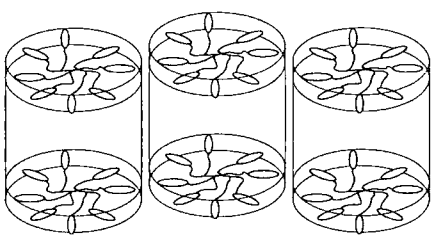

Figure 3.11: Diagram showing column formation from disc-shape dendromesogens.

three dimensional wedges, spheres.[21,22,75,84,85] The great range of possible morphologies that may arise from this range of systems has been studied and reviewed by Tschierske.[86–88]

3.6 Computational studies

The complex nature of dendritic and hyperbranched polymers makes simulation studies of such systems dependent on available computational resources. As increasingly powerful computers have come on-line dendritic systems have, over the last couple of years, become the focus of a number of studies. However, such studies are computationally expensive at the atomistic level because of the large number of sites required for a typical dendromesogen. These constraints mean there has been interest in exploring models that contain less detail.

Studies of dendrimers, that do not contain liquid crystalline moieties include; atomistic molecular dynamics studies;[92,93] pair potential calculations;[94] freely jointed bead spring models;[95] semi-empirical calculations to determine conformations;[96] and Monte Carlo studies both on and off lattice.[97–99] Computer simulation studies of dendrimers that have peripheral mesogenic groups are quite scarce, the most notable work is that of Photinos *et al.* In these studies the most likely molecular conformations are calculated and used to parameterize a description of the bulk system in terms of a "deformable continuum" that allows molecular sites to change between rod and disc conformations and so form ordered phases.[100,101]

3.7 Applications

Liquid crystalline dendrimers represent systems which are well defined in terms of symmetry, arrangement and molecular mass. Such high definition is extremely beneficial when coupled to the desirable electro-optical properties of liquid crystals systems. The intrinsic viscosity of a dendromesogen is much less than that of a liquid crystal polymer owing to a reduction in entanglements. This reduced viscosity results in a faster response to external stimulation. Therefore, dendritic systems

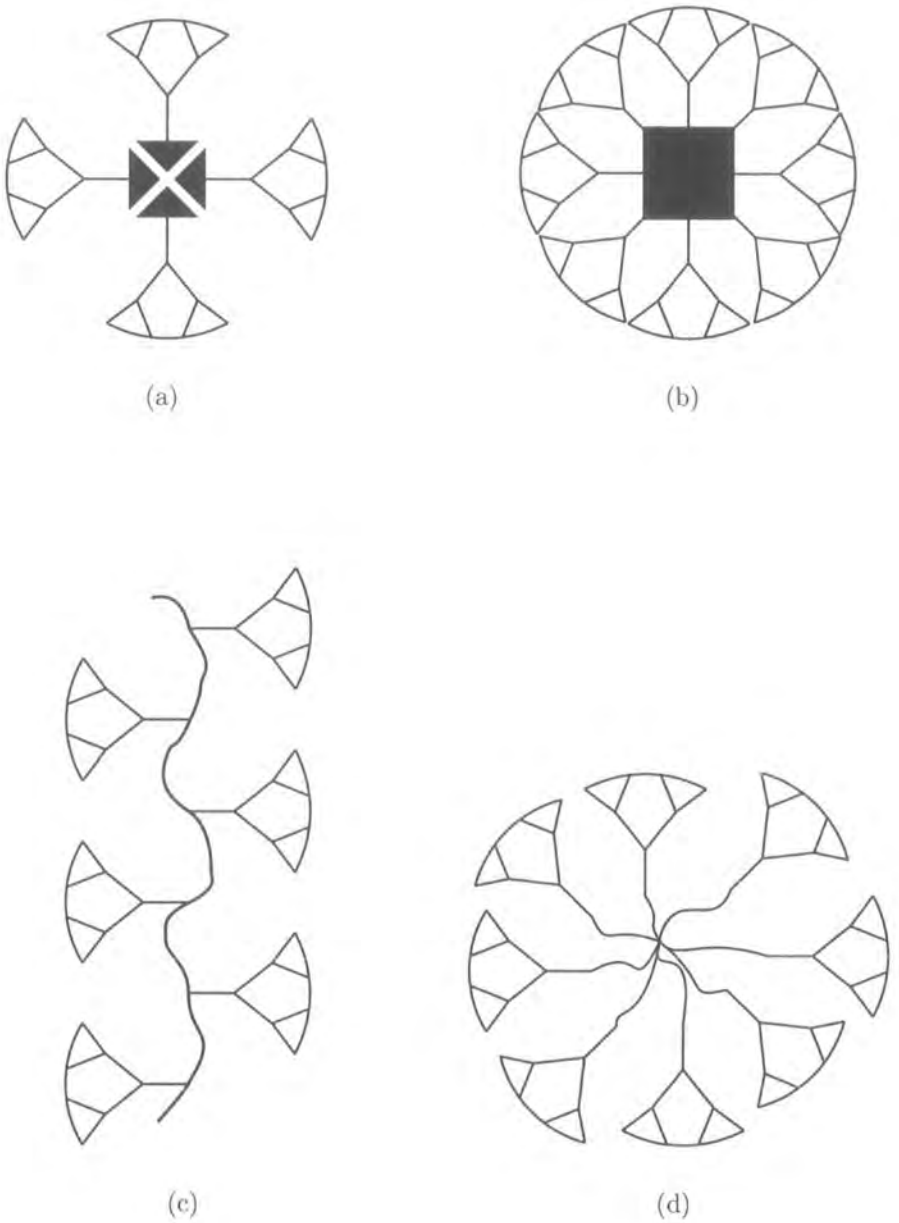

Figure 3.12: Schematic representations of dendritic assemblies.

a) dendrons held together by non-bonding interactions,[85,89] b) dendrons attached to a central structure,[89,90] c) polymer with side chain dendrons,[91] d) a star polymer with dendritic terminal groups.[21]

can be used to dope liquid crystal displays in order to decrease the switching time. Self assembly of dendritic systems can be useful for the design of liquid crystalline templates for microporous systems. This combination of high order and specialty effects makes dendromesogens very useful materials in many areas such as light modulation, lubrication and drug delivery agents.

Chapter 4

Computational Techniques

This chapter provides a background to the computational techniques that have been used in this research. For any simulation study, the basic methodology can be divided into three parts:

- Constructing a model that describes the system under investigation, often starting with a description of one molecule before moving on to a model that may be used for a bulk system.
- Implementing the model in a simulation.
- Using output to monitor the progress of the simulation and to calculate macroscopic properties.

4.1 Simulation Models

The modelling of molecules and materials may be achieved by employing a variety of techniques that simulate a range of time and length scales. In constructing a model it is important to consider the level of detail that is to be used. The time and length scales of any simulation should reflect the scale of the phenomenology that is under investigation. Initially, it is sometimes informative to undertake a smaller scale, more detailed study to gain information that may be useful to parametrize a new model.

At their most detailed, computational studies include only a handful of atoms, at a single point in time. These single point calculations are useful for the investigation of intermolecular forces and the calculation of very accurate potential energy surfaces. However, this level of theory can only examine a snapshot of a single configuration and not probe dynamic properties of a system.

Quantum molecular dynamics, using schemes like the Car-Parinello technique,[102] are able to investigate more atoms over a short amount of time. A typical scale for a quantum molecular dynamics study would be to investigate 64 water molecules for 100 ps. Here, structural properties and short timescale dynamic effects, like the fluctuation of hydrogen bonds in a system of water molecules can be investigated.

Atomistic studies, in which each atom is represented by a single site, may be employed over longer timescales; tens of thousands of atoms may be explored over nanosecond timescales. At this level it is possible to simulate a small protein and witness phenomena such as solvation, phase transitions and molecular motion at active sites.

To look at larger systems over longer times, coarse grained approaches have been developed. Here groups of atoms are represented by specially tailored potentials. Using coarse grained models, it is possible to examine hundreds of thousands of atoms over hundreds of nanoseconds.

It is important to realize that these classifications are not discrete methods, but may be used in combination. For example, an accurate description of an active site may be combined with a coarser representation of the periphery of the molecule. In this way the important factors influencing the phenomenon under investigation are included, but computationally expensive aspects, that may have little bearing on the behaviour of the active site, may be neglected. This broad outline of simulation scales is by no means exhaustive, theoretical methods provide other techniques, like density functional theory and continuum theories, on-lattice methods and other more specialised models.

As outlined in Section 1.6 on page 13, over the last thirty years, liquid crystalline materials have been modelled using a range of techniques. These studies encompass a range of scales and levels of detail. The characteristics and level of detail of a

model must be taken into account when conclusions are drawn from the results of a computational study. To exemplify this point one may consider the case of a simulation of a mesophase formed by a low molecular weight molecule where each molecule is represented by one potential site. A large amount of research has been conducted using single site potentials such as the Gay-Berne potential and hard and soft spherocylinder potentials. (Details of these potentials are found in Section 4.1.1.) These models have been useful in exploring the nature of liquid crystalline phases. However, as with any model, it is important to consider fully the limitations that these single-site potentials introduce and the effect of those limitations on the behaviour of the system. When a mesogenic molecule is represented by a simple single site there is no conformational freedom; the molecule has a fixed shape and invariant dimensions and therefore describes a rigid molecule. Real mesogens are not completely rigid, but rather have both a flexible and a rigid part. This difference between the real system and the model has a profound effect on the formation of ordered phases because the packing of rigid particles is less efficient. The effect of this discrepancy is seen in the difference between the change in density at the phase transition in the real and model systems. This does not invalidate the model, but it does restrict the information that can be gained from the study.

In essence any computational study must balance the constraints, that the physics of the system under investigation creates, with the availability of computer time. For this research the main considerations when deciding upon a model are: the macromolecular nature of the systems which necessitates large system sizes; the need for a mixture of rigidity and flexibility; and long time scales that may be required to observe annealation.

4.1.1 Potentials

Potential functions are the building blocks that make up a molecular model. These may be used, as described above, to represent a whole molecule or may only represent a small part of that model. This section describes some common potential forms that are used in liquid crystal simulations.

Figure 4.1 shows four different pair potentials that may be used in molecular simulation. Figures 4.1(a) and 4.1(b) are hard potentials, whereas 4.1(c) and 4.1(d) are soft potentials as they change smoothly.

Hard potentials

The form of the hard wall potential in Figure 4.1(a) is purely repulsive and extremely simple. The only interaction is the prevention of inter-penetration of particles. Particles do not contribute to the energy of other particles unless they overlap when they have infinite energy. Therefore the only influences on phase behaviour are shape and density. The value of the potential for two hard particles that have a separation distance that is greater than σ is zero. If they move together and the separation becomes less than σ then the potential value immediately rises and so the particles are forced apart. The simplest hard body is the hard sphere, although other shapes are possible. Liquid crystalline models of hard particles are often rods or discs that represent calamitic and discotic mesogens respectively.

The square well potential in Figure 4.1(b) is also quite simple as it has discrete values. Beyond r_2 there is no energetic contribution from the interaction of the particles. Between r_1 and r_2 an attractive interaction is incorporated as the potential has a negative value. At closer separation distances the energy rises sharply and there is a large repulsive force.

Soft potentials

The purely repulsive potential in Figure 4.1(c) is a soft wall. At separations of more than r_2 the potential is zero, between r_1 and r_2 there is a slowly increasing repulsive force between the sites and when sites are closer than r_1 there is a large force to push them apart. Potentials that smoothly change with separation, are more expensive as they require calculation of the potential for each separation. However, soft potentials are easier to simulate in a molecular dynamics study as repulsive forces rise gradually and prevent a particle from suddenly having an extremely large velocity. Examples of purely-repulsive soft potentials include some cut and shifted Lennard-Jones potentials and the soft-repulsive spherocylinder that are used to model isotropic and

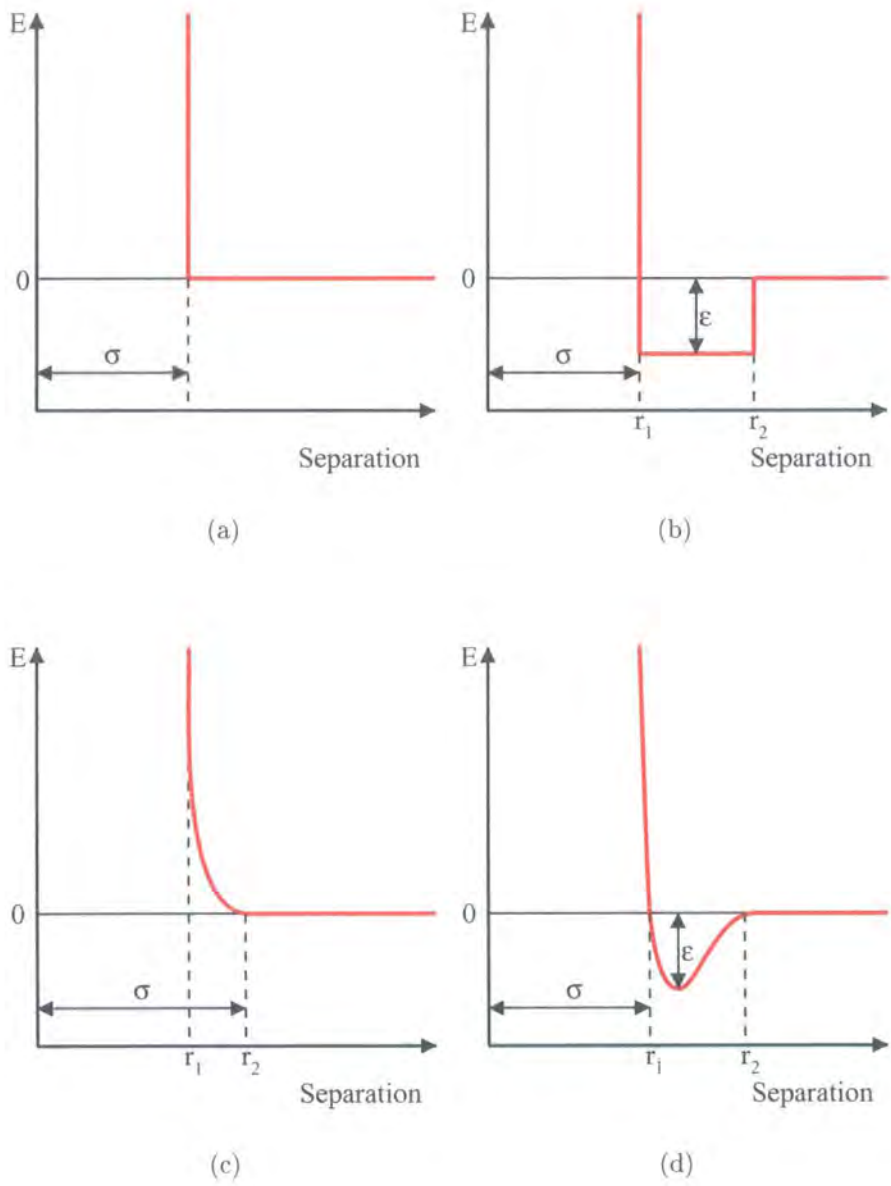

Figure 4.1: Pair potentials, where E is the energy of the interaction as a function of the separation distance between sites. (a) Hard repulsive (b) Square well (c) Soft repulsive (d) Soft repulsive and attractive.

anisotropic sites respectively. Chapter 7 describes the use of specific forms of these soft-repulsive potentials.

Depicted in Figure 4.1(d) is a smooth potential which is soft and has both a long range attractive interaction and a short range repulsive part. In this form, the gradient of the potential closely matches the van der Waals forces which exist between molecules. Example of such potentials include the Lennard-Jones potential for isotropic sites and the Gay-Berne potential for anisotropic sites.

i) Lennard-Jones

The Lennard Jones potential is an isotropic potential that may be used to model spherical atoms. The basic form of this potential is

$$V_{LJ}(r) = 4\epsilon \left[\left(\frac{\sigma}{r}\right)^{12} - \left(\frac{\sigma}{r}\right)^{6} \right], \tag{4.1}$$

where $V_{LJ}(r)$ is the Lennard-Jones potential at a position r, and ϵ and σ are respectively the well depth and distance at which $V_{LJ}(r) = 0$, which characterize the potential. These parameters can be seen in Figure 4.2 on the next page which shows a Lennard Jones potential plot for a dinitrogen system. The separation of the atomic centres at the potential minimum is referred to as r^*. In a simple system of two atoms of the same type, as in Figure 4.2, r^* approximates the diameter of the atoms.

The r^{-12} term represents short range repulsion and the r^{-6} term represents a long range attractive force.

ii) Gay-Berne

The Gay-Berne potential is an anisotropic potential that may be used to model groups of atoms.[104,105] Gay-Berne units are often used to represent mesogenic units.[30] The rationale behind the development of this potential was that the Lennard Jones potential is a good model for non-bonding interactions and so would be a good form for a new orientation dependent potential. In order to formulate this potential a shape anisotropy parameter, χ, must be defined.

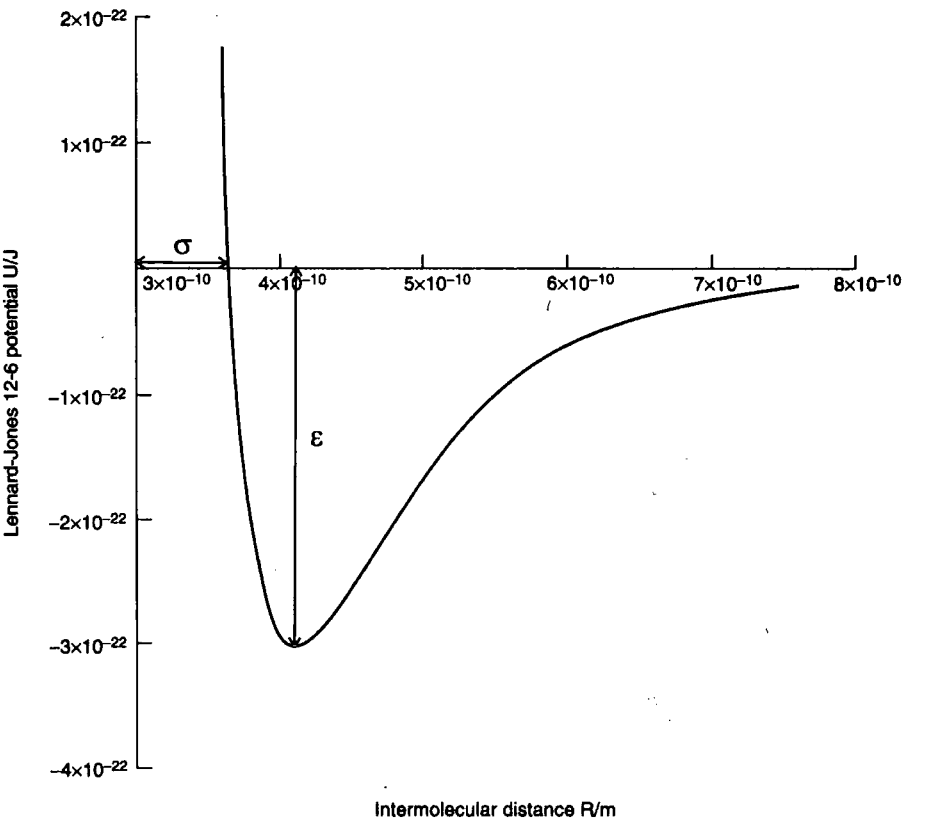

Figure 4.2: Lennard-Jones potential for dinitrogen (reproduced from[103]).

This plot shows the potential energy between two nitrogen atoms as a function of their separation distance.

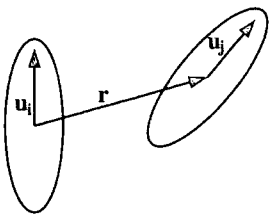

Figure 4.3: Diagram defining the orientation vectors for two adjacent molecules.

$$\chi = \frac{(\sigma_e/\sigma_s)^2 - 1}{(\sigma_e/\sigma_s)^2 + 1}. \tag{4.2}$$

The shape of the ellipsoid may vary from oblate to problate by changing the end-to-end and side-by-side parameters, σ_e and σ_s. When σ_e and σ_s are equal, $\chi = 0$ and the potential is spherical. As χ approaches 1 the potential tends toward an infinitely long rod and as χ tends toward -1 the potential tends toward an infinitely thin disc. Such manipulation allows the shape of the potential to be tailored to suit a specific mesogen.[106,107]

The Gay-Berne potential takes the form

$$V_{GB}\left(\hat{\mathbf{r}}, \hat{\mathbf{u}}_1, \hat{\mathbf{u}}_2\right) = 4\epsilon\left[\left(\frac{\sigma_0}{r - \sigma\left(\hat{\mathbf{r}}, \hat{\mathbf{u}}_1, \hat{\mathbf{u}}_2\right) + \sigma_0}\right)^{12} - \left(\frac{\sigma_0}{r - \sigma\left(\hat{\mathbf{r}}, \hat{\mathbf{u}}_1, \hat{\mathbf{u}}_2\right) + \sigma_0}\right)^{6}\right], \tag{4.3}$$

where the well depth is given by

$$\epsilon = \epsilon_0 \epsilon\left(\hat{\mathbf{u}}_1, \hat{\mathbf{u}}_2\right)^{\nu} \epsilon'\left(\hat{\mathbf{r}}, \hat{\mathbf{u}}_1, \hat{\mathbf{u}}_2\right)^{\mu} \tag{4.4}$$

with

$$\epsilon\left(\hat{\mathbf{u}}_1, \hat{\mathbf{u}}_2\right) = \left[1 - \chi^2\left(\hat{\mathbf{u}}_1 . \hat{\mathbf{u}}_2\right)^2\right]^{-\frac{1}{2}} \tag{4.5}$$

and

$$\epsilon'\left(\hat{\mathbf{r}}, \hat{\mathbf{u}}_1, \hat{\mathbf{u}}_2\right) = 1 - \left(\frac{\chi'}{2}\right)\left[\frac{\left(\hat{\mathbf{r}} . \hat{\mathbf{u}}_1 + \hat{\mathbf{r}} . \hat{\mathbf{u}}_2\right)^2}{1 + \chi'\left(\hat{\mathbf{u}}_1 . \hat{\mathbf{u}}_2\right)} + \frac{\left(\hat{\mathbf{r}} . \hat{\mathbf{u}}_1 - \hat{\mathbf{r}} . \hat{\mathbf{u}}_2\right)^2}{1 - \chi'\left(\hat{\mathbf{u}}_1 . \hat{\mathbf{u}}_2\right)}\right], \tag{4.6}$$

and the anisotropic contact distance is given by

$$\sigma\left(\hat{\mathbf{r}}, \hat{\mathbf{u}}_1, \hat{\mathbf{u}}_2\right) = \sigma_0 \left\{ 1 - \frac{\chi}{2} \left[\frac{\left(\hat{\mathbf{u}}_1.\hat{\mathbf{r}} + \hat{\mathbf{u}}_2.\hat{\mathbf{r}}\right)^2}{1 + \chi\left(\hat{\mathbf{u}}_1.\hat{\mathbf{u}}_2\right)} + \frac{\left(\hat{\mathbf{u}}_1.\hat{\mathbf{r}} - \hat{\mathbf{u}}_2.\hat{\mathbf{r}}\right)^2}{1 - \chi\left(\hat{\mathbf{u}}_1.\hat{\mathbf{u}}_2\right)} \right] \right\}^{-\frac{1}{2}}. \tag{4.7}$$

Here, $\hat{\mathbf{r}}$ is the unit vector that connects the centres of mass of the two ellipsoids, r is the distance between those centres of mass, $\mathbf{u}_1$and $\mathbf{u}_2$ are molecular axis vectors that are illustrated in Figure 4.3, σ is the intermolecular separation at which the attractive and repulsive terms cancel and the potential is zero, σ_0 is a scaling parameter and the shape anisotropy, χ, is given in Equation 4.2. The related parameter χ' is given by

$$\chi' = \frac{\left[1 - \left(\frac{\epsilon_e}{\epsilon_s}\right)^{\frac{1}{\mu}}\right]}{\left[1 + \left(\frac{\epsilon_e}{\epsilon_s}\right)^{\frac{1}{\mu}}\right]}. \tag{4.8}$$

Instead of χ and χ' it is often more useful to define the ratios $\kappa = \sigma_e/\sigma_s$ and $\kappa' = \epsilon_e/\epsilon_s$, which are the shape anisotropy and attractive anisotropy respectively. Thus, Equations 4.2 and 4.8 become

$$\chi = \left(\frac{\kappa^2 - 1}{\kappa^2 + 1}\right) \tag{4.9}$$

and

$$\chi' = \left(\frac{\kappa'^{\frac{1}{\mu}} - 1}{\kappa'^{\frac{1}{\mu}} + 1}\right) \tag{4.10}$$

respectively.

In order to uniquely describe any Gay-Berne potential we must set four quantities: the exponents μ and ν and the ratios κ and κ'. When the ratios κ and κ' go to unity, the potential may be simplified to the Lennard-Jones potential. Variation in these parameters results in a change in relative well depths and the corresponding separation distances (Figure 4.4). Variation in μ and ν change the orientation dependence of the relative well depths and so control rod and disc-like characteristics of the potential. These parameters may be phenomenologically fitted to suit a particular shape. It is possible to model a range of mesogens with the Gay-Berne potential from calamitic to discotic.[31,108–111] In this work we use $\mu = 2$ and $\nu = 1$,

which were parameterized to fit a linear array of four Lennard-Jones sites and have been studied extensively elsewhere.[112,113]

iii) Mixing GB and LJ sites

In the preceding two descriptions we have treated pair potentials of isotropic and anisotropic sites. However, to make full use of Lennard-Jones and Gay-Berne sites it is necessary to define a hybrid potential to describe the interaction between them. Therefore, Cleaver *et al.* proposed an extension to the Gay-Berne potential to describe the interaction of two different sites.[109] The Cleaver potential for the interaction of a spherical site with an ellipsoidal site takes the form

$$V_{GB/LJ}\left(\hat{\mathbf{r}},\hat{\mathbf{u}}_1\right)=4\epsilon\left[\left(\frac{\sigma_0^{GB/LJ}}{r-\sigma^{GB/LJ}\left(\hat{\mathbf{r}},\hat{\mathbf{u}}_1\right)+\sigma_0^{GB/LJ}}\right)^{12}-\left(\frac{\sigma_0^{GB/LJ}}{r-\sigma^{GB/LJ}\left(\hat{\mathbf{r}},\hat{\mathbf{u}}_1\right)+\sigma_0^{GB/LJ}}\right)^{6}\right], \tag{4.11}$$

where

$$\epsilon=\epsilon_0^{GB/LJ}\left[\epsilon\left(\hat{\mathbf{r}},\hat{\mathbf{u}}_1\right)^{GB/LJ}\right]^{\mu}=\epsilon_0^{GB/LJ}\left[1-\chi'\alpha'^{-2}\left(\hat{\mathbf{r}},\hat{\mathbf{u}}_1\right)^2\right]^{\mu} \tag{4.12}$$

with

$$\chi'\alpha'^{-2}=1-\left(\frac{\epsilon_e}{\epsilon_s}\right)^{\frac{1}{\mu}} \tag{4.13}$$

and

$$\sigma^{GB/LJ}\left(\hat{\mathbf{r}},\hat{\mathbf{u}}_1\right)=\sigma_0^{GB/LJ}\left[1-\chi\alpha'^{-2}\left(\hat{\mathbf{r}},\hat{\mathbf{u}}_1\right)^2\right]^{-\frac{1}{2}} \tag{4.14}$$

with

$$\chi\alpha'^{-2}=\left(\frac{l_1^2+d_1^2}{l_1^2+d_2^2}\right). \tag{4.15}$$

In Equations 4.11-4.15, $V_{GB/LJ}\left(\hat{\mathbf{r}},\hat{\mathbf{u}}_1\right)$ is the ellipsoid-sphere pair potential for a system where site 1 is ellipsoidal and site 2 is spherical; l_1,d_1 and d_2 are the lengths of the ellipsoid, the diameter of the ellipsoid and the diameter of the sphere respectively; and other parameters take the same meanings as in the Gay-Berne potential.

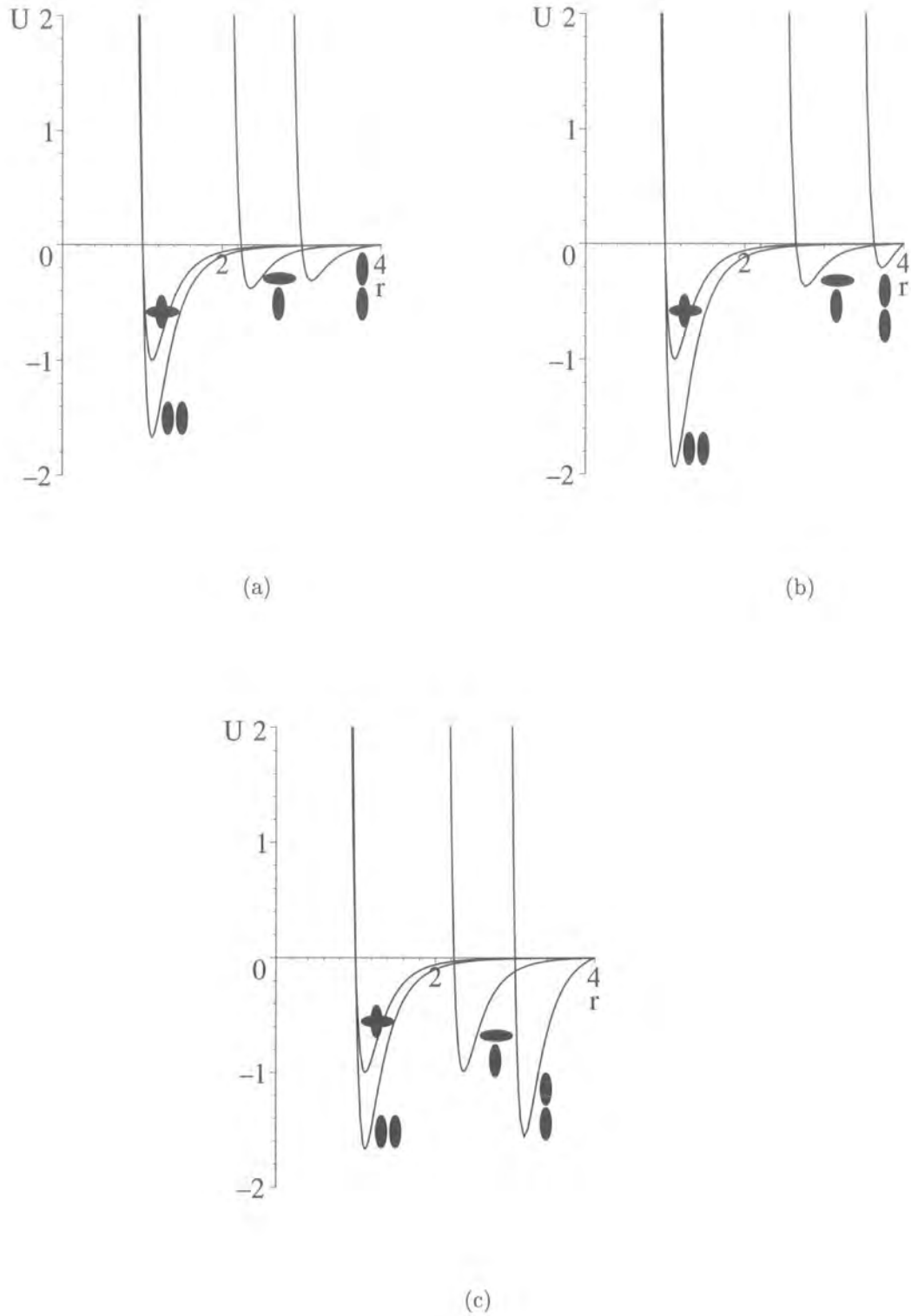

Figure 4.4: Three forms of the Gay-Berne potential plotted as function of fixed orientation, where U is the value of the interaction potential and r is the separation distance between sites, both in reduced units. All potentials have $\mu = 2$, $\nu = 1$, but vary in κ and κ'. a) $\kappa = 3$, $\kappa' = 5$, b) $\kappa = 3.6$, $\kappa' = 5$, c) $\kappa = 3$, $\kappa' = 1$.

4.1.2 Molecular Mechanics Force Fields

A molecular mechanics force field can be used to model all the interactions within a molecule. These include both the non-bonding interactions described in Section 4.1.1 and the strain energy associated with changes in internal molecular structure. Often formulating an accurate description of the interactions of one molecule is a useful first step to force field generation. Once this initial step is successful, intermolecular effects can be included in a description of the bulk system.[114]

In order to build a model of a molecule, we consider a classical total energetic description of all the intra-molecular interactions. There are many forms which this expression may take. Each one the treats the various energetic components in a slightly different way. One simple form for the total energy of a molecule can be obtained by considering the distortion energy of bonds, bond angles and dihedral angles within a molecule. In this description

$$E_{Total} = \sum_{bonds} E_{Bonds} + \sum_{angles} E_{Angles} + \sum_{dihedrals} E_{Dihedrals} + \sum_{<ij>} E_{Electostatic} + \sum_{<ij>} E_{VdW}, \tag{4.16}$$

where E_{Total} is the total energy of the system and E_{Bonds}, E_{Angles}, $E_{Dihedrals}$, $E_{Electostatic}$, E_{VdW} are the contributions to the total energy from bond stretching, angle bending, dihedral angle rotations, electrostatic forces and Van der Waals forces respectively. These energetic components may be calculated by the following potentials.

$$\sum_{bonds} E_{Bonds} = \sum_{bonds} K_b \left(r - r_{eq}\right)^2. \tag{4.17}$$

Equation 4.17 is the energy associated with the bonds in the system. K_b is a force constant, r is the actual bond length and r_{eq} is the natural bond length. Thus the bond energy is dependent on the distortion from the equilibrium position, with the bond being treated like a 'Hookean' spring linking two masses.

$$\sum_{angles} E_{Angles} = \sum_{angles} K_a \left(\theta - \theta_{eq}\right)^2. \tag{4.18}$$

Equation 4.18 is the energy associated with the bond angles in the system. K_a is again a force constant, θ is the actual bond angle and θ_{eq} is the natural bond angle. This expression is analogous to the bond energy in 4.17 and the energy is again dependent on the distortion from the equilibrium position.

$$\sum_{dihedrals} E_{Dihedrals} = \sum_{dihedrals} \sum_{n=1}^{n=3} \frac{K_{\phi n}}{2} (1 + \cos(n\phi - \gamma)). \tag{4.19}$$

Equation 4.19 is the energy associated with the dihedral angles in a system. ϕ is the dihedral angle, γ is the phase angle and $K_{\phi n}$ are force constants.

$$\sum_{<ij>} E_{Electrostatic} = \sum_{<ij>} \frac{q_i q_j}{4\pi\epsilon_0 r_{ij}}. \tag{4.20}$$

Equation 4.20 is the the electrostatic part of the non-bonding component of the energy, which is given by Coulomb's law. The interaction of point charges q_i and q_j representing atoms i and j respectively, and r_{ij} is the atomic separation. The sum in Equation 4.20 is taken over all pairs of atoms $< ij >$.

The final term in Equation 4.16 models the Van der Waals non-bonding interaction between sites.

There are a number of good literature force fields that are currently available. Many of the more sophisticated ones use additional cross-terms in Equation 4.16. These force fields have been incorporated into a number of commercially available software packages that perform molecular mechanics calculations.

4.1.3 Further Considerations

Once a satisfactory force field is found, then a simulation box is constructed and a number of the molecules placed in it. At this stage it is important to address a number of considerations regarding the simulation model as a whole.

Ensemble

Statistical mechanics provides a link between individual molecular properties and those of the bulk. When setting up an experiment an ensemble must be cho-

sen. In each ensemble a set of thermodynamic parameters are held constant and these parameters control the other macroscopic parameters for the system. Fixed macroscopic parameters are used to label the system. Principle ensembles used are NVE (micro-canonical), NVT (canonical), μVT (grand canonical) and NpT (isobaric/isothermal) or NpH (isobaric/isoenthalpic). N is the number of atoms or molecules; V is the volume of the simulation box; p is the pressure; T is the temperature; E is the total energy; H is the enthalpy; and μ is the chemical potential.

If we use an isobaric ensemble the volume of the simulation box may change, this adds additional degrees of freedom to the system. Coordinates in such a system are specified relative to the box and will vary with changes in volume. Details of an NpT ensemble have been documented by Andersen in 1980.[115]

Boundary conditions

To simulate the bulk properties of a system, periodic boundaries are used. In a periodic system, a molecule which moves out of one side of the box reappears on the other side, as shown in Figure 4.5. Figure 4.5 also depicts the nearest neighbour convention whereby molecules interact with their nearest periodic neighbour in space.

Cut-offs

In this thesis, cut and shifted forms of the potentials detailed in Section 4.1.1 are used. To increase the efficiency of the model it is possible to avoid calculating all the interactions in the system, but rather calculate only those which make a significant contributions to the energy.

The cut-offs used are, for the Lennard-Jones pair potential, $2.5\sigma_0^{LJ}$; for the Gay-Berne pair potential, $4\sigma_0^{GB}$; and for the GB/LJ potential, $4\sigma_0^{GB/LJ}$. For the GB/LJ and GB potentials to overcome the slight discontinuity in the potential at the cutoff distance the value of the energy at the cutoff is added to all parts of the curve. This technique avoids any impedance to the integration of the equations of motion that may have occurred owing to the discontinuity. The LJ potential is truncated at the cut-off but long-range corrections are calculated to compensate for this.

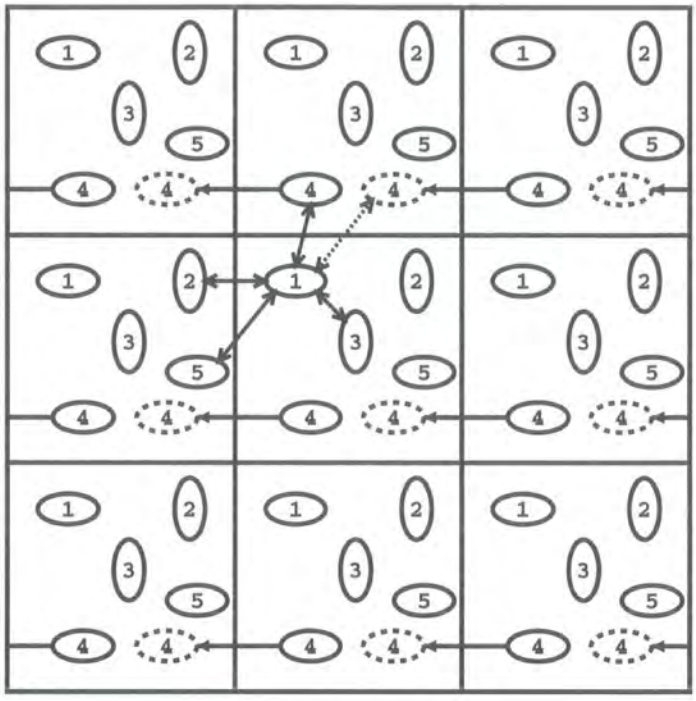

Figure 4.5: Periodic boundary conditions and the nearest neighbour convention. Molecule 4 is shown leaving across one edge and entering across another. For molecule 1, in the central box, the nearest image of each molecule is connected by a double ended arrow.

4.1.4 Techniques for Coarse Graining Molecular Models

The term coarse graining may be used to describe the process in which molecular detail is removed from a model. The principle behind coarse graining is to create a simplified model of the system without loosing the physics which is guiding the phenomenology that is being investigated. As polymers consist of many identical repeat units, they have been the subject of a great deal of research at the mesoscale level.

Formulating a semi-atomistic model from an atomistic model can be thought of as coarse graining. The semi-atomistic models used in this work use united atoms and Gay-Berne sites. The use of united atoms incorporates hydrogen sites into the heavy atoms to which they are attached; one Lennard-Jones site is used to model a CH_3 or CH_2 group. The elliptical Gay-Berne potential, which is described in Section 4.3, is used to model a whole mesogen. The Gay-Berne sites may be parameterized to model a specific molecule of molecular fragment by adapting the exponents μ and ν and anisotropy parameters κ and κ'.

At the opposite end on the coarse graining spectrum is the use of effective pair potentials. Here, a whole molecule that may contain hundreds or thousands of atoms are represented by one site. Typically effective pair potentials are parameterized by measuring the energy of interactions between two molecules as a function of their separation. A potential, such as the Morse potential is then fitted to the energy profile.

Between the semi-atomistic and effective pair regimes there are a vast number of mesoscale approaches that may be adopted to model a system. The scale and approach chosen often depends on the details of the system being investigated. Figure 4.6 illustrates four different scales that may be used.

In Figure 4.6(a) soft ellipsoids are used to represent whole chains. Murat and Kremer explore this scale in modelling melts of a pure polymer and a binary mixture.[117] Here the potentials are very soft and allow overlapping as is observed with real polymer chains. The beads were parameterized for different chain lengths to match distribution functions from other experiments. In the binary mixture of polymeric units A and B, $\sigma_{AA} = \sigma_{BB} = \sigma_{AB}$. Therefore the beads have the same effective

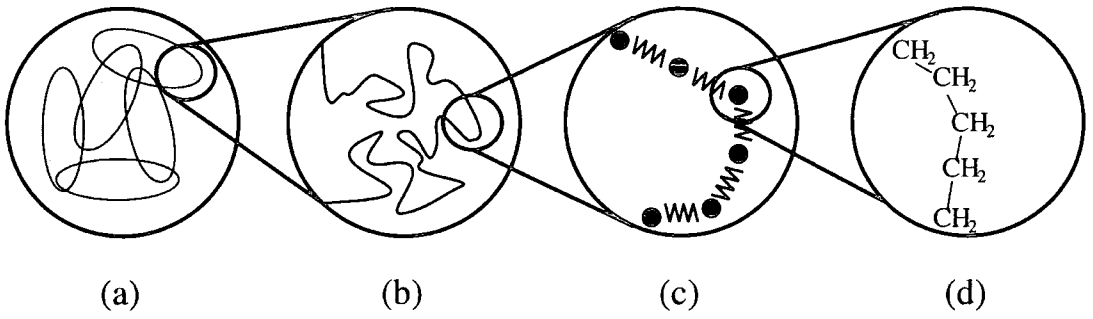

Figure 4.6: Mesoscale modelling of polymers: Four length scales for polyethylene. Adapted from.[116]

sizes. However, $\epsilon_{AA} = \epsilon_{BB} \neq \epsilon_{AB}$ so that the interaction for unlike polymers can be tailored to make them more or less repulsive than for like polymers.

Figure 4.6(b) illustrates a single bead representing a three dimensional Gaussian random walk. Such beads may be connected to one another at their centres of mass. Therefore, each bead models a large number of monomers, The scale of the beads means that the chemical detail of the polymer is not included in the system. This approach was used by Laso *et al.* to model a polymer.[118]

Figure 4.6(c) depicts the bead and spring model, with a few monomers represented by each bead. This approach was used by Fukunga *et al.* to model polyethylene.[119] In that work a 3:1 one mapping regime was employed, *i.e.* three monomers were represented by one bead. Bond lengths, angular and torsional potentials were parameterized from a united atom study. The bonding point was chosen as the centre of mass of each bead. Agreement was found for quantities such as the radius of gyration between the coarse grained approach and an united-atom study. A number of other groups have explored this approach, notably Hahn *et al.* in which bis-phenol-A-polycarbonate chains were modelled.[116,120,121] Here polymer chains were represented by two bead types to reflect the polymer structure. In initial work the two bead types were treated as spherical, later more detail was incorporated by representing one of the beads with an ellipsoid.

4.2 Simulation Techniques

Molecular dynamics (MD) and Monte Carlo (MC) have been employed in this research. Both methods enable the phase space of the system to be explored. If this exploration is ergodic, the portion of phase space that has been sampled will be representative of the entire system. The path through phase space that is explored using molecular dynamics evolves over time according to the solution of the classical equations of motion that describe the particles in the system. Monte Carlo methods select a path through phase space using a statistical methodology.

4.2.1 Molecular Dynamics

Historical Perspective

Molecular dynamics is a long established simulation technique. One of the first uses of this technique was documented by Alder and Wainwright in 1957.[122] This research simulated liquid and solid phases using a simple hard sphere model of an atom. Later, in 1964 Rahman used Lennard-Jones potentials to describe a system of 864 liquid argon atoms.[123] By 1967, phase diagrams of Lennard-Jones systems were being studied using MD.[124,125] By 1969, phase transitions were also under investigation.[126]

Simulation Technique

If molecules within a simulation box are considered to be subject to the laws of Newtonian mechanics, then their motion may be described by Equations 4.21, 4.22 & 4.23. To describe such a system, at a given point in time, the relative positions, velocities and energies of the atoms are required.

$$\frac{d\mathbf{r}_i}{dt} = \mathbf{v}_i' \tag{4.21}$$

$$\frac{d^2\mathbf{r}_i}{dt^2} = \mathbf{a}_i' \tag{4.22}$$

$$\mathbf{F}_i = m_i\mathbf{a}_i = -\nabla E_i. \tag{4.23}$$

In these equations, $\mathbf{r}_i$, $\mathbf{v}_i$, $\mathbf{a}_i$, m_i and $\mathbf{F}_i$ are respectively the position, velocity, acceleration, mass, and force experienced by atom i, and E_i is the energy of that atom.

To find the position of the atoms as a function of time, t, Equation 4.22 must be integrated. This may be achieved approximately with finite difference algorithms. Finite difference algorithms divide the integration into a number of steps at time intervals of length δt and calculate new values for the forces, velocities and positions of the atoms at each time interval. There are a number of algorithms can be used to integrate the equations of motion. In this work we use the Leapfrog algorithm.

The leapfrog algorithm considers the movement of an atom, i, and the resultant position and acceleration of that atom at integer time-steps of length δt. However, the velocities are evaluated at half-integer time-steps. Hence, the atomic velocities leapfrog over the positions and vice versa to give the relationships

$$\mathbf{r}_i(t+\delta t) = \mathbf{r}_i(t) + \delta t \mathbf{v}_i\left(t+\tfrac{1}{2}\delta t\right) \tag{4.24}$$

and

$$\mathbf{v}_i\left(t+\tfrac{1}{2}\delta t\right) = \mathbf{v}_i\left(t-\tfrac{1}{2}\delta t\right) + \mathbf{a}_i\delta t = \mathbf{v}_i\left(t-\tfrac{1}{2}\delta t\right) + \left(\frac{\mathbf{F}_i(t)}{m_i}\right)\delta t, \tag{4.25}$$

which describe the approximate time evolution of the system. This evolution is portrayed in Figure 4.7. This depiction shows how, in the first step positions are used, with the aid of the force field, to calculate accelerations; in the second step the new accelerations are used in combination with the old velocities to give new velocities (Equation 4.25); and in the third step the new velocities are used with the old positions to calculate new positions (Equation 4.24).

As the velocity at a time $t+\delta t$ may be approximated to the average of $\mathbf{v}_i\left(t+\frac{1}{2}\delta t\right)$ and $\mathbf{v}_i\left(t-\frac{1}{2}\delta t\right)$ this approach facilitates the calculation of instantaneous potential and kinetic energies.

A flow chart showing the practical implementation of this algorithm is presented in Figure 4.8. The algorithm is used to create a history file describing the movement of the atoms in the system and their relative positions and energies. These data can

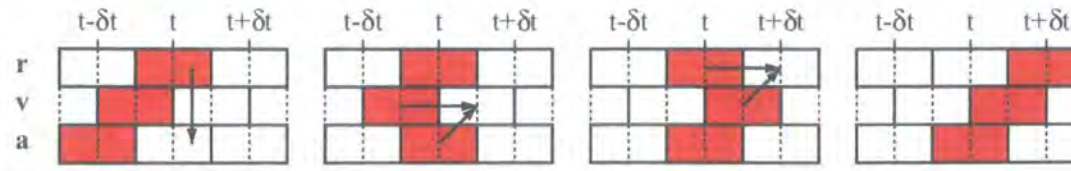

Figure 4.7: Leapfrog algorithm, showing progress along a trajectory. The shaded boxes indicate the most recent know values for the position, velocity and acceleration of an atom. The arrows show the variables that are used to calculate the next unknown quantity.

then be analyzed to obtain further information about the system as described in Section 4.3.

The methods outlined so far consider translational motion. However, when anisotropic particles are considered, extra degrees of freedom that relate to rotational motion must be addressed. For linear particles with only two degrees of rotational freedom, Equations 4.24 and 4.25 are still used to integrate the translational motion. However, we must consider an additional set of finite difference equations to integrate the rotational equations of motion:

$$\mathbf{u}_i(t+\frac{1}{2}\Delta t) \approx \mathbf{u}_i(t-\frac{1}{2}\Delta t) + \Delta t\left(\frac{\mathbf{g}_i^{\perp}}{I_i} + \lambda(t)\widehat{\mathbf{e}}_i(t)\right), \tag{4.26}$$

$$\widehat{\mathbf{e}}_i(t+\Delta t) \approx \widehat{\mathbf{e}}_i(t) + \Delta t\mathbf{u}_i(t+\frac{1}{2}\Delta t) \tag{4.27}$$

and

$$\Delta t\lambda_i(t) = -2\mathbf{u}_i(t-\frac{1}{2}\Delta t)\cdot\widehat{\mathbf{e}}_i(t). \tag{4.28}$$

These are formulated by considering the torque, $\mathbf{T}_i$ acting upon an ellipsoid in terms of the unit vector along the molecular axis $\mathbf{e}_i$, its time derivative $\mathbf{u}_i$ and the force applied $\mathbf{g}_i$. Hence,

$$\mathbf{T}_i = \mathbf{e}_i \times \mathbf{g}_i. \tag{4.29}$$

Here,

$$\mathbf{g}_i = \sum_j \mathbf{g}_{ij} = -\sum_j \nabla_{e_i} U_{ij} = -\sum_j \left(\frac{\partial U_{ij}}{\partial e_{xi}}, \frac{\partial U_{ij}}{\partial e_{yi}}, \frac{\partial U_{ij}}{\partial e_{zi}} \right). \tag{4.30}$$

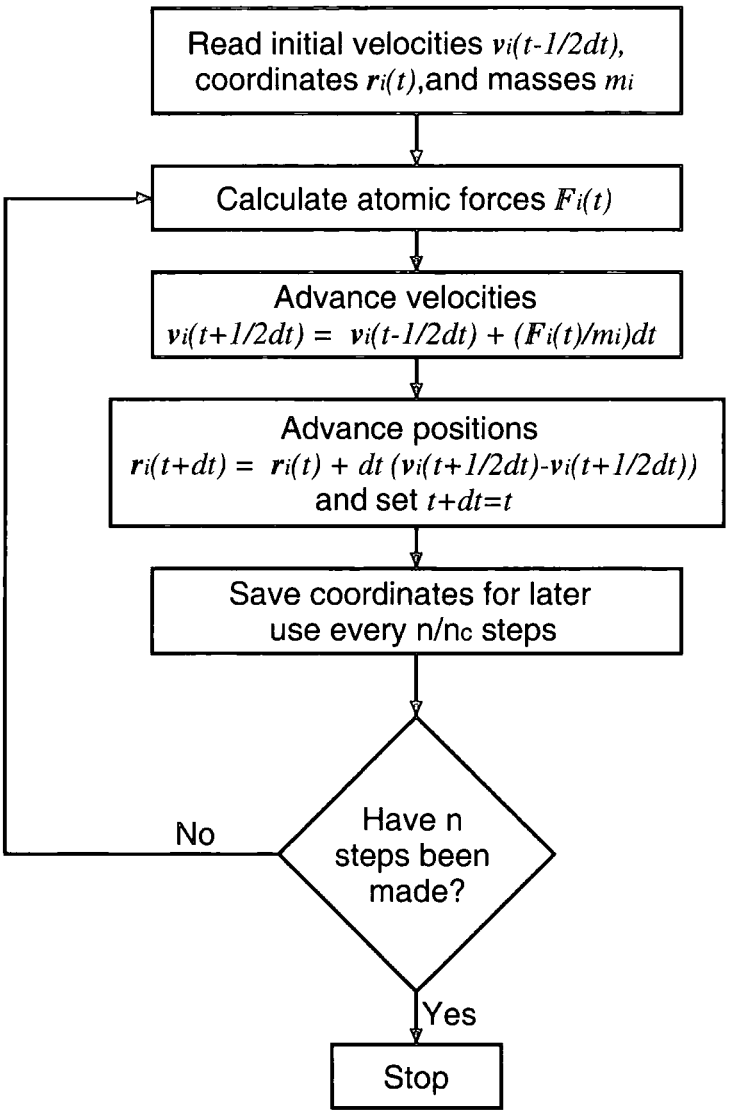

Figure 4.8: Flowchart of the iterative procedure of the leap frog finite difference algorithm that is used to solve equations of motion in a molecular dynamics simulation.

It is conventional to take the component of $\mathbf{g}_i$ perpendicular to $\mathbf{e}_i$,

$$\mathbf{g}_i^{\perp} = \mathbf{g}_i - (\mathbf{g}_i \cdot \mathbf{e}_i)\mathbf{e}_i, \tag{4.31}$$

so that Equation 4.29 becomes

$$\mathbf{T}_i = \mathbf{e}_i \times \mathbf{g}_i^{\perp}. \tag{4.32}$$

For this system the equations that are equivalent to Equations 4.21 and 4.22 for rotational motion are

$$\frac{d\hat{\mathbf{e}}_i}{dt} = \mathbf{u}_i \tag{4.33}$$

and

$$\frac{d^2\hat{\mathbf{e}}_i}{dy^2}\frac{d\mathbf{u}_i}{dt} = \frac{\mathbf{g}_i^{\perp}}{I_i} + \lambda e_i \tag{4.34}$$

where λ is an undetermined Lagrange multiplier as used in Equation 4.26, and I is the moment of inertia.

The starting point for a MD simulation is a model system for which the positions and velocities of each particle are known. From the initial positions the potential energy, and therefore the force acting on the particle, may be calculated from the expression that describes the force field.

Ensembles

There are number of practical considerations that must be addressed before running an MD simulation these include the choice of ensemble. There must be a way of adjusting the macroscopic parameters of the system to ensure that the appropriate variables are maintained at a fixed value for the chosen ensemble. Of the ensembles described on page 58, the NVE and NpT have been used in molecular dynamics studies in this work. In this classical framework the total number of particles within the system is invariant.

Newtonian mechanics in the absence of friction implies an NVE ensemble with conservation of energy and a fixed volume. The transition from a micro-canonical to

a canonical ensemble is relatively straight forward owing to the close link between energy and temperature.

However, implementation of the NpT ensemble requires some sort of barostat and thermostat. There are a number of thermostats and barostats from literature sources.[127,128] In this thesis two thermostat/barostat combinations have been used: the Nosé-Hoover thermostat with corresponding Hoover barostat and the Andersen thermostat in combination with a Monte Carlo barostat.

Nosé-Hoover methods introduce new degrees of freedom to the system corresponding to the volume of the simulation box and the temperature. The average temperature and volume are now conserved quantities and the simulation may be performed in the micro-canonical ensemble and result in a canonical distribution.[129]

The second thermostat used is a form of the Andersen thermostat[115] in which the whole system collides with a heat bath on a regular basis, this scales the velocities of all the particles, as the heat bath temperature is fixed it acts as a heat sink for the system.

The Monte Carlo method makes trial changes in the simulation box volume.[30] A more detailed account of Monte Carlo methodology is found in Section 4.2.2. The acceptance of the changes in volume are governed by a random number, δ, that has a range ($-\delta_{max}$, δ_{max}) chosen to give 35-50% acceptance. The new volume, V_{new} is calculated from the old volume, V_{old} using

$$V_{new} = V_{old} \exp(\delta). \tag{4.35}$$

Trial moves are accepted with a probability of the minimum of $(1, \exp(-\beta \Delta H))$, where

$$\beta \Delta H = \beta \Delta E + \beta p \Delta V - (N_m + 1)\, \delta.$$

Here $\beta = \frac{1}{kT}$, ΔE is difference in potential energy, $E_{new} - E_{old}$, for a trial move, p is pressure, V is volume and H is enthalpy.

4.2.2 Monte Carlo Techniques

Monte Carlo (MC) techniques are the second type of simulations that have been used in this research. MC differs from MD as it involves a stochastic methods using probabilities derived from statistical mechanics to screen trial moves.

Historical Notes

The term Monte Carlo* is used to refer to a range of problem solving techniques that use random numbers and statistical sampling to examine mathematical and physical situations. Such techniques have been used for well over a century. The development of statistical sampling techniques was closely entwined with the invention and improvement of the first mechanical calculators and computers. Much of this initial work was based at the Los Alamos National Laboratory during the period of the second work war and the years that followed. The development of the Metropolis algorithm in 1953[131] allowed for thermal importance sampling and therefore was instrumental in the installation of MC as one of the most popular techniques for molecular simulation. In some early studies Metropolis *et al.* and other groups examined the interactions, in two and three dimensional systems of hard sphere and disc potentials. Over the following years phase transitions, radial distribution functions and other macroscopic properties of gases were being addressed.[132]

Sampling

Usually the aim of Monte Carlo is to make an accurate prediction of the expectation value, $\langle A \rangle$, of an observable, A, of a system. One way to calculate $\langle A \rangle$ is to average A for each state weighted with its Boltzmann probability, so

$$\langle A \rangle = \frac{\sum_n A_n e^{-\beta E_n}}{\sum_n e^{-\beta E_n}}, \tag{4.36}$$

where there are n states, E is the energy of the state and $\beta = \frac{1}{kT}$, where k is Boltzmann's constant and T is the temperature. Calculating $\langle A \rangle$ from Equation 4.36

*The name "Monte Carlo" was first used by Metropolis in 1947, it parallels the use of random numbers in these methods to the gambling in Monacan casinos.[130]

is impossible for anything but a very small system. Therefore, it is more practical to sample a subset of the total number of states. Selection of an appropriate subset is crucial for calculating an accurate expectation value. It is useful to consider an experimental measurement of an observable property in laboratory conditions; again only a subset of states are sampled as a great deal of phase space corresponds to extremely high energy configurations which are physically unlikely. If a subset were to be chosen at random, the proportion of states that correspond to high energy would too large. Therefore, the expectation value would be far from the observable value. The methodology involved in choosing an appropriate subset is named importance sampling.

Markov chains

Movement through phase space via this series of states requires careful navigation to ensure that all states occur with appropriate probability. This navigation may be exacted by what is known as a Markov process. With a Markov chain of states, a system in a state, μ, going to a proposed new state, ν, has a probability of acceptance of $P_{\mu\to\nu}$. To generate the Markov chain, $P_{\mu\to\nu}$ must not vary over time, should only depend on states μ and ν, and must comply with the condition

$$\sum_{\nu} P_{\mu\to\nu} = 1. \tag{4.37}$$

For a Markov process to be successful, it should also satisfy two further constraints: detailed balance[†] and ergodicity.

Detailed balance ensures that a simulation has reached equilibrium. Equilibrium is a situation in which the rate of moving into and out of a state are equal. This is called microscopic reversibility and means

$$\sum_{\nu} p_{\mu} P_{\mu\to\nu} = \sum_{\nu} p_{\nu} P_{\nu\to\mu} \tag{4.38}$$

[†]As Manousiouthakis and Deem have shown, the condition of detailed balance is not strictly necessary. However, if detailed balance is vigorously enforced it will ensure that the true requirement of "balance" is satisfied.[128,133]

where p_μ and p_ν are the probability distributions of the the states μ and ν respectively.

Ergodicity implies that for every state the probability distribution is non-zero. Therefore, all states of the system are feasible and given infinite sampling would be visited. If a system is ergodic then a time average, of an observable quantity, will be equal to the ensemble average. Moreover, as an ensemble average is time independent, a time average from an ergodic Markov chain is uncorrelated with the starting state.

The Metropolis algorithm

The most prevalent technique for importance sampling in a molecular system is the Metropolis method. Metropolis MC generates configurations "randomly" but in such a way that they occur with the correct Boltzmann weights. With this method the total energy as described in Equation 4.16 is calculated directly from the atomic coordinates. Random changes are made in the molecular structure and the difference in energy between the old and new configurations is calculated. The moves are then accepted with a Boltzmann probability. This acceptance is achieved by requiring that $e^{-\beta\Delta E}$ is greater than a random number between 0 and 1, where ΔE is the difference between the energy of the trial state and the old state. The Metropolis algorithm may be seen in Figure 4.9.

Ensembles

In the Monte-Carlo study reported in Chapter 6, an isolated molecule is studied. Therefore, it is not necessary to consider which ensemble is to be employed. However, generally when employing MC techniques, all the ensembles described in Section 4.1.3 are possible, even those like the grand canonical ensemble that are not possible using MD methodology. The Metropolis algorithm classically samples the canonical ensemble. The use of alternate ensembles requires adaptation of the MC algorithm. An example of one such adaptation is the MC box move described on Page 4.2.1 that ensures constant pressure, which may be incorporated into a Monte Carlo scheme.

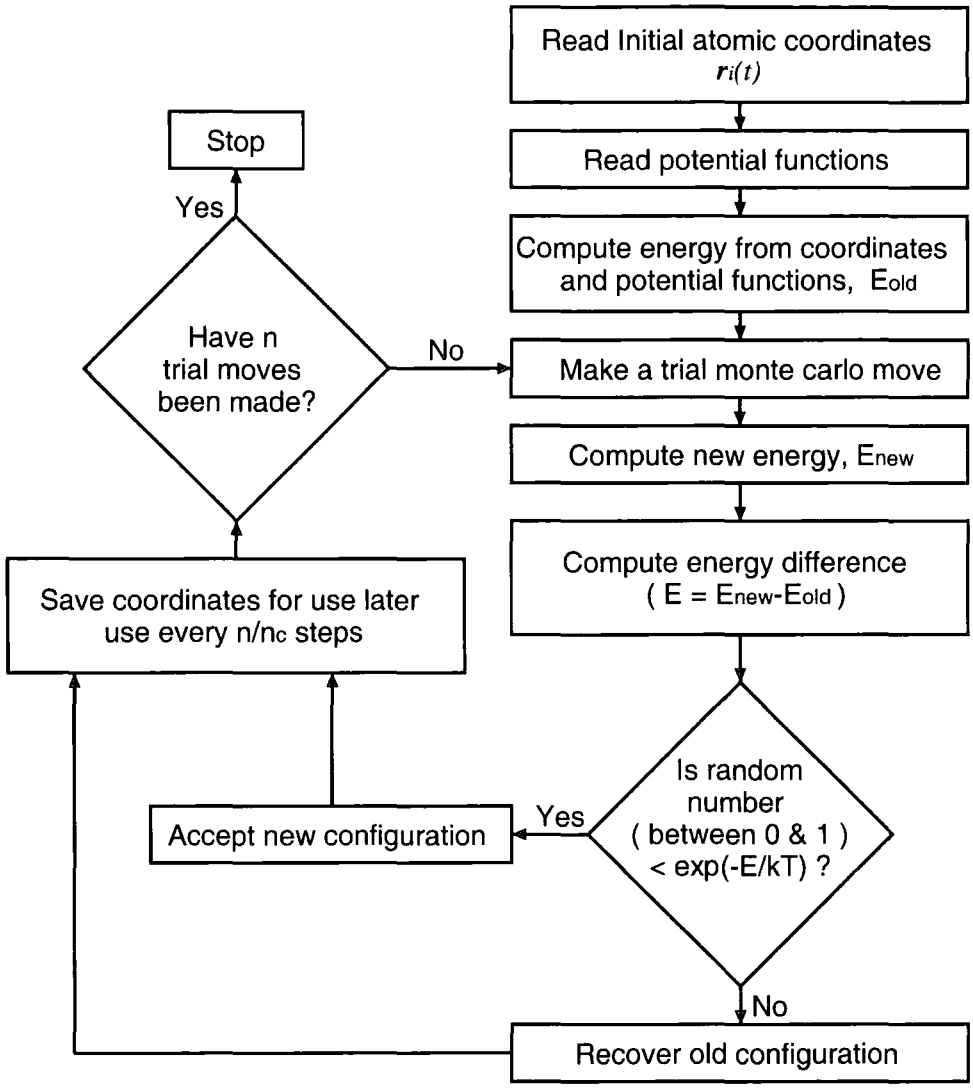

Figure 4.9: The Metropolis algorithm.

When implementing such adaptations it is important to ensure that the principles of ergodicity and balance via microscopic reversibility are obeyed.

4.3 Macroscopic properties

Simulation studies are, in some ways, able to provide more detail on a molecular scale than their experimental counterparts; it would be extremely difficult to monitor experimentally the positions and movement of every molecule within a real liquid. Nevertheless, the observable quantities that may be gleaned from examination of a real system may seldom be computed from these raw data without significant manipulation.

At each step of a MD simulation coordinates, velocities and energies of all the particles in the system are known. However, to be able to draw conclusions from these data, it is useful to have some mechanism to derive observable quantities that may be compared with experimental measurements. Extraction of characteristic quantities can also assist the understanding of the molecular structure of the simulated system. From the information gained in a molecular dynamics study it is possible to observe structural and dynamic effects.

For MC simulations, although coordinates and energies are accessible, there is no timescale. Therefore, there are no velocities or information relating to dynamic processes or effects.

In this section methods used to analyze raw simulation details are described.

4.3.1 Nematic order parameter, $< S_2 >$

In Sections 1.8 and 1.4.2, the concepts of a director and an order parameter were introduced. Here these concepts are expanded and a more in depth mathematical description is given.

To monitor the nematogenic, orientational, order in the system the particle coordinates may be used to calculate $< S_2 >$ for mesogenic units in the system. In an atomistic simulation a vector that is synonymous with the long axis of the molecule must be defined. For example, in the mesogenic compound 4-pentyl-4'-

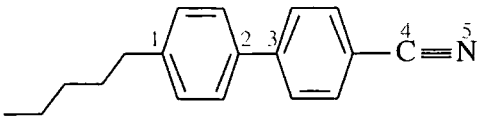

Figure 4.10: The structure of the mesogenic compound 5CB. Numbered atoms could define the end points of inter-atomic vectors, which approximate the long axis of the molecule.

cyanobiphenyl (5CB), an order parameter may be calculated for the C≡N bond (*i.e.* 4→5 in Figure 4.10), the inter-ring bond (*i.e.* 2→3 in Figure 4.10), a vector that spans the length of the rigid part of the molecule (*e.g.* 1→5 in Figure 4.10) or a vector representing the molecular long axis calculated from the molecular moment of inertia tensor. In semi-atomistic or coarser grained representation the orientation vector of the site representing the mesogen may be used. The orientations of the all the molecules may then be used to calculate the director, $\underline{\mathbf{n}}$, using the ordering tensor,

$$Q_{\alpha\beta} = \frac{1}{N}\sum_{i=1}^{N}\left(\frac{3}{2}\hat{\mathbf{e}}_{i\alpha}\hat{\mathbf{e}}_{i\beta} - \frac{1}{2}\delta_{\alpha\beta}\right), \qquad \alpha,\beta = x,y,z. \tag{4.39}$$

In this expression for the ordering tensor, N is the number of molecules in the system; $\hat{\mathbf{e}}_{i\alpha}$ and $\hat{\mathbf{e}}_{i\beta}$ are components of the unit vectors along the long molecular axes of molecule i; and $\delta_{\alpha\beta}$ is a Kronecker delta. Expansion of the ordering tensor, yields the the matrix

$$Q_{\alpha\beta} = \frac{1}{N}\sum_{i=1}^{N}\begin{bmatrix} \frac{3}{2}\hat{\mathbf{e}}_{ix}\hat{\mathbf{e}}_{ix} - \frac{1}{2} & \frac{3}{2}\hat{\mathbf{e}}_{ix}\hat{\mathbf{e}}_{iy} & \frac{3}{2}\hat{\mathbf{e}}_{ix}\hat{\mathbf{e}}_{iz} \\ \frac{3}{2}\hat{\mathbf{e}}_{iy}\hat{\mathbf{e}}_{ix} & \frac{3}{2}\hat{\mathbf{e}}_{iy}\hat{\mathbf{e}}_{iy} - \frac{1}{2} & \frac{3}{2}\hat{\mathbf{e}}_{iy}\hat{\mathbf{e}}_{iz} \\ \frac{3}{2}\hat{\mathbf{e}}_{iz}\hat{\mathbf{e}}_{ix} & \frac{3}{2}\hat{\mathbf{e}}_{iz}\hat{\mathbf{e}}_{iy} & \frac{3}{2}\hat{\mathbf{e}}_{iz}\hat{\mathbf{e}}_{iz} - \frac{1}{2} \end{bmatrix}. \tag{4.40}$$

The largest eigenvalue to result from the diagonalization of $Q_{\alpha\beta}$ corresponds to the order parameter, $\langle S_2 \rangle$, the director, $\underline{\mathbf{n}}$, is the eigenvector associated with this eigenvalue.

Once a director has been defined, S_2 may also be measured by taking an average of the second Legendre polynomial, P_2, of the product of the director and each of the unit vectors that describes the orientation of the mesogens, $\underline{\mathbf{e}}$. So

$$S_2 = \langle P_2\left(\underline{\mathbf{n}}.\underline{\mathbf{e}}\right)\rangle = \langle P_2\left(\cos\theta\right)\rangle = \left\langle \frac{3}{2}\cos^2\theta - \frac{1}{2} \right\rangle \tag{4.41}$$

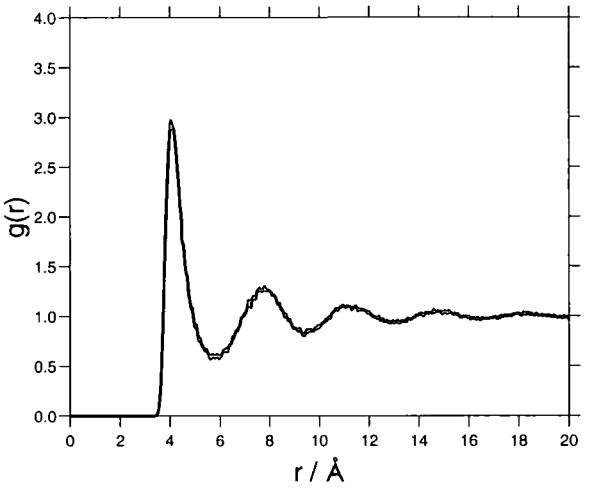

Figure 4.11: Example of the form of $g(r)$ for a system of Lennard-Jones sites.

as in Equation 1.1 from Chapter 1.

4.3.2 Distribution Functions

They are a number of distribution functions that may be calculated to describe translational order. The first such function is the pair or radial distribution function, $g(r)$, described by Expression 4.42,

$$g(r) = \frac{V}{[N]^2} \left\langle \sum_{i}^{N} \sum_{j \neq i}^{N} \delta(\mathbf{r} - \mathbf{r}_{ij}) \right\rangle, \tag{4.42}$$

where N is the number of sites, V is the volume and $\mathbf{r}_{ij}$ the vector between the centres of mass for the sites i and j. $g(r)$ measures the probability of finding a particle at a distance $\mathbf{r}$ from another particle. Figure 4.11 depicts the form of a radial distribution function for a system of Lennard-Jones sites. This figure can be thought of as a probability distribution for sites surrounding a central site at the origin. There is depletion next to the site and the first solvation shell is indicated by the peak at approximately 4 Å, outside this peak there are alternating troughs and peaks that are progressively smaller in magnitude until the function tails off to a limiting value of unity as $g(r)$ is measured relative to an ideal gas of the same density. The fading of the distribution shows there is no long range correlation in the system.

This distribution may be resolved into two components that are perpendicular and parallel to the director, denoted by $g_{\perp}(r)$ and $g_{\parallel}(r)$ respectively. A peak in $g_{\parallel}(r)$ is indicative of the formation of smectic layers, while a peak in $g_{\perp}(r)$ is a sign of 'in plane' order. For each of the distribution functions it is important to realize that when shells are examined at increasing distance, r, then their relative volume increases. So the probability must be normalized using these volumes.

The pairwise orientational correlation function, $g_2(r)$, as calculated from 4.43 provides further insight into the ordering within the layers. $g_2(r)$ measures the alignment of pairs of mesogens as a function of density.

$$g_2(r) = \langle P_2(\cos\theta_{ij}(r))\rangle_{shell}\,. \tag{4.43}$$

Here P_2 is the second Legendre polynomial term and θ_{ij} is the angle between the molecular axes of the Gay-Berne sites i and j. Therefore, $g_2(r)$ is similar to a distance dependent order parameter, that treats $\cos\theta$ rather that $\cos^2\theta$. The $\cos\theta$ term leads to differentiation between parallel and anti-parallel ordering, which is not available from the order parameter itself.

4.3.3 Diffusion Coefficient, D

Unlike the order parameter and radial distribution functions, diffusion is a dynamic property. Therefore, data from MC studies can not be used to calculate the diffusion of the system. Ultimately diffusion is a property of molecular mobility in a system. It may be measured by the diffusion coefficient, D. D is equivalent to three measurable quantities: the integral of the velocity autocorrelation function, the limiting long time correlation between velocity and displacement and the limiting long time mean square displacement gradient (Equation 4.44.)

In this work, D is calculated from the Einstein relation

$$D = \frac{1}{6t}\left\langle |\mathbf{r}_i(t) - \mathbf{r}_i(0)|^2 \right\rangle, \tag{4.44}$$

where $\mathbf{r}_i(t)$ is the molecular position vector at time t and $\mathbf{r}_i(t) - \mathbf{r}_i(0)$ is averaged over a number of time origins.

D is an important parameter of the system that allows us to monitor the molecular motion and therefore observe the onset of freezing. An increase in the orientational or translational order leads to a drop in D.

Chapter 5

Side Chain Liquid Crystal Polymer

This chapter details molecular dynamics studies of a side chain liquid crystal polymer in the NpT ensemble. The system has been modelled on a semi-atomistic scale, using Lennard-Jones sites to represent united atoms in the polymer and Gay-Berne sites to represent the mesogenic moieties. These studies simulate cooling of a SCLCP from the melt. To encourage a smectic liquid crystal phase to grow an external magnetic field has been applied. Structural analysis of the polymer over a range of temperatures is described.

5.1 Background

The simulations described in this chapter use a model SCLCP of the type described in Section 2.1.2, depicted in Figure 2.4 on page 20. The polymer which has been the subject of a number of experimental studies,[134,135] has a polydimethylsiloxane (PDMS) backbone, with a hexyl-chain flexible spacer attached to each silicon atom. At the end of the alkyl chain a mesogen is linked via an oxygen atom. This structure is shown in Figure 5.1. The flexibility of siloxane polymers is useful when designing a SCLCP as it restricts the mesogens less than other polymer backbones. A schematic representation of a monomer from this system is shown in Figure 5.2.

In experimental studies of SCLCPs a combination of techniques have been used to explore the nature of phases formed. Sarna *et al.* have investigated siloxane polymers in the biphasic region using differential scanning calorimetry and optical

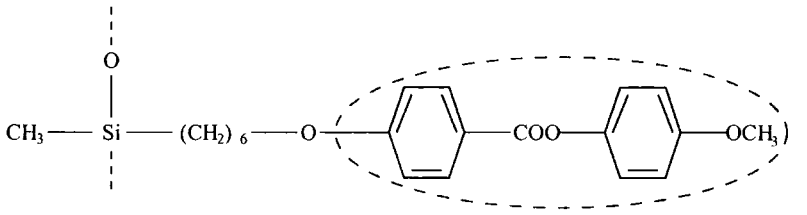

Figure 5.1: Chemical structure of the SCLCP with a PDMS backbone. The mesogenic moiety is encircled.

microscopy.[136] Here the polymer has undergone microphase separation and liquid crystalline phases have been observed for systems which retain a flexible backbone, until the temperature is reduced sufficiently for the polymer to undergo a glass transition. The polymers were annealed in the presence of a magnetic field to enhance alignment. The segregation leads to a splitting in the peaks obtained from differential scanning calorimetry. In these studies two smectic phases were observed, from examination of the optical textures of these mesophases one appeared to be well-formed and the other seemed to have less well developed smectic layers.

Other studies have used magnetic fields to control the orientation of the mesogenic units in SCLCPs.[137,138] Richardson *et al.* have reported a number of studies of SCLCPs in a magnetic field. These studies investigated the structure of four polymers using X-ray diffraction. In this work a polymer with a PDMS backbone functionalised with a chiral mesogenic unit through an undecyl alkyl chain has been studied whilst being cooled at 1°C/min in a 9.4 T field from an isotropic melt. This polymer had a degree of polymerisation of 14, the phase behaviour observed was (in °C)

$$\mathrm{g} \xrightarrow{12} \mathrm{S_X} \xrightarrow{22} \mathrm{S_C} \xrightarrow{152} \mathrm{i.}$$

In that work the smectic phases observed showed substantial disorder within the layers. It was shown that the PDMS backbone is flexible enough to allow the liquid crystalline order to predominate over the tendency of the polymer backbones to curl up into random coil conformations.[139]

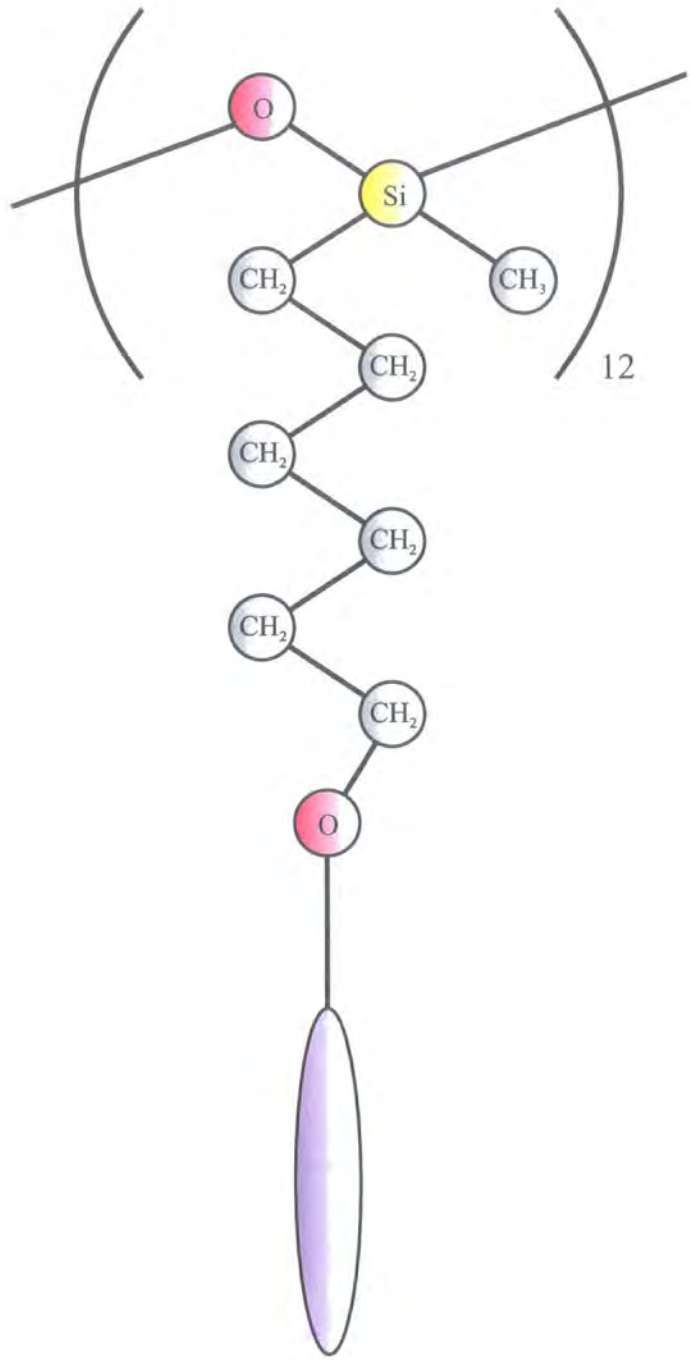

Figure 5.2: Schematic representation of the structure of a PDMS monomer. The ellipse that terminates the side chain represents a mesogenic moiety.

5.2 Model

Figure 5.2 provides a schematic representation of the model SCLCP used in this study.There are four different types of site representing; silicon atoms; oxygen atoms; carbon united-atoms, which are the same for the CH_2 as CH_3 groups; and an elliptical site representing the mesogenic unit. A whole molecule described in this way is shown in Figure 5.3.

The forcefield used to describe the system in these studies is of the form

$$\begin{aligned} E_{Total} = & \sum_{i=1}^{N_{angles}} \frac{k_i^{ang}}{2} \left(\theta_i - \theta_i^0\right)^2 + \sum_{i=1}^{N_{GB}} k_i^{GBang} \left(\upsilon_i - \upsilon_i^0\right)^2 \\ & + \sum_{i=1}^{N_{dihedrals}} \left[a_{1i}\left(1+\cos\phi_i\right) + a_{2i}\left(1-\cos\left(2\phi_i\right)\right) + a_{3i}\left(1+\cos\left(3\phi_i\right)\right)\right] \\ & + \sum_{i=1}^{N_{LJ}} \sum_{j>1}^{N_{LJ}} U_{LJ} + \sum_{i=1}^{N_{LJ}} \sum_{j=1}^{N_{GB}} U_{LJ/GB} + \sum_{i=1}^{N_{GB}} \sum_{j>i}^{N_{GB}} U_{GB} + U_{ext}, \end{aligned} \tag{5.1}$$

where N_{angles}, $N_{dihedrals}$, N_{LJ} and N_{GB} are the number of angles, the number of dihedral angles, the number of Lennard-Jones sites and the number of Gay-Berne sites respectively in the system. In Equation 5.1 a harmonic potential is used to model bond angle deformations, where k_i^{ang} is a bond angle force constant, θ_i is the actual bond angle and θ_i^0 is the equilibrium bond angle. The second term in Equation 5.1 represents the angle between the orientation of Gay-Berne site and the bond that connects it to the rest of the molecule. This angle is known as the Gay-Berne angle and is shown in Figure 5.4. The deformation of the Gay-Berne angle is modelled with a harmonic potential, with k_i^{GBang} as the angular force constant, υ_i as the actual Gay-Berne angle and υ_i^0 is the equilibrium Gay-Berne angle. The inclusion of a Gay-Berne angle term prevents free-rotation of the mesogen about its centre. Such a rotation would be an unphysical movement. The dihedral angle component of Equation 5.1 is the third term, where ϕ_i is the dihedral angle and a_1, a_2 and a_3 are constants that parametrize the form of the potential for each type of dihedral angle. The terms U_{LJ}, $U_{LJ/GB}$ and U_{GB} are the non-bonding interactions between each pair of sites. These non-bonding terms are described in detail in Section 4.1.1 on Page, 48 by Equations 4.1, 4.3 and 4.11. Thus, the expression

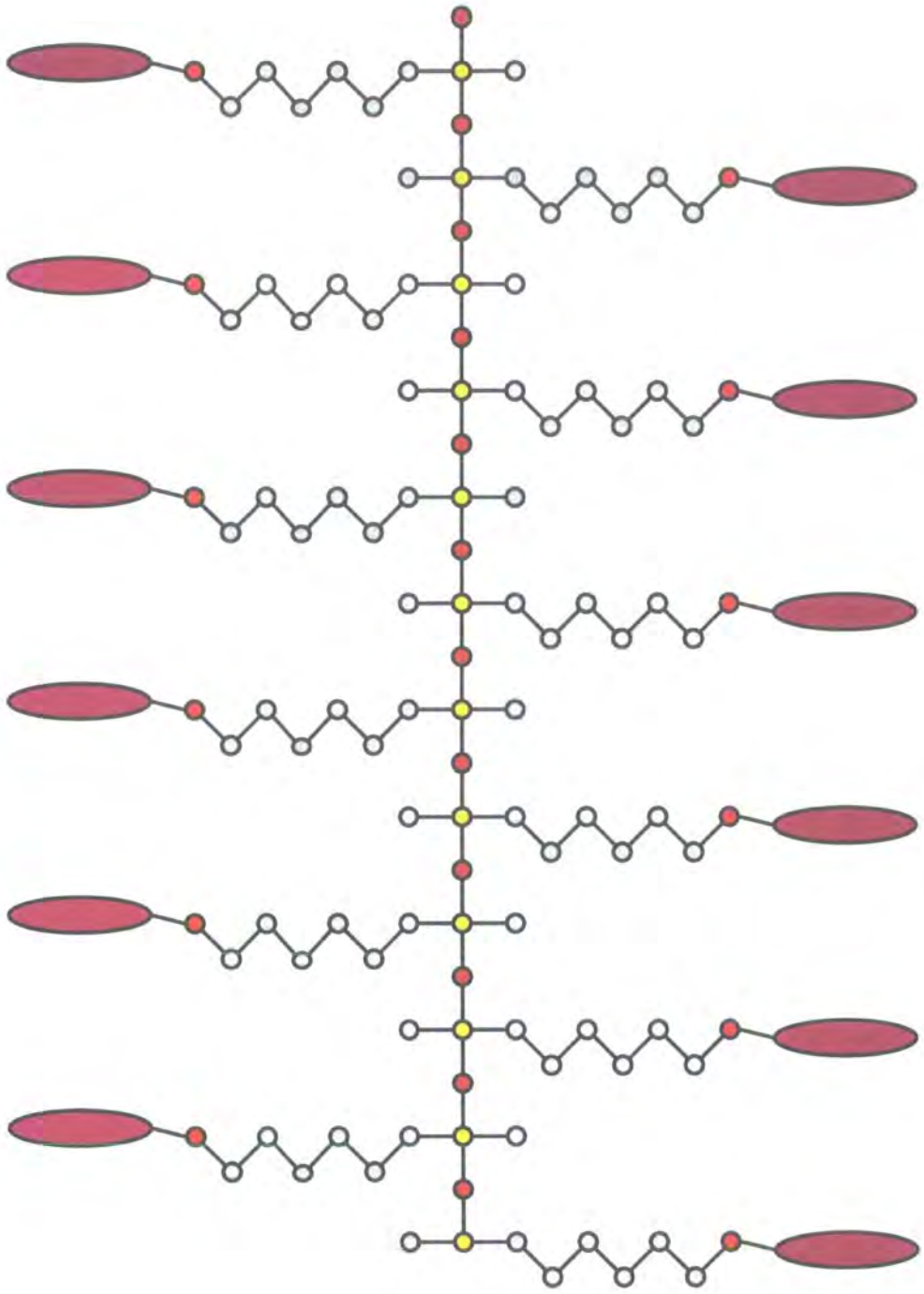

(a)

Figure 5.3: Schematic representation of the structure of one polymer chain formed from Lennard-Jones united atoms and Gay-Berne mesogenic sites.

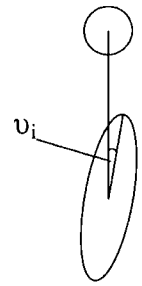

Figure 5.4: Illustration of the Gay-Berne angle, υ_i, between a Gay-Berne site and a Lennard-Jones site that are directly bonded.

accounts for pairwise interactions between sites which are considered to be additive. The final term in Equation 5.1, U_{ext}, is the interaction of the sites with an external magnetic field. The form and derivation of this field is discussed in Section 5.3.2 on page 87.

The forcefield parameters were obtained from previous hybrid GB/LJ studies of a liquid crystal dimer[30] and a mesogen with tails at both ends,[140] augmented by data from the MM2 forcefield for the siloxane part and updating the Ryckaert Bellemans potential (used in[30]) to the more recent work by Martin and Siepmann[141] and later Nath and Khare.[142] The full potential is specified by parameters in tables 5.1-5.4.

Dihedral Angle	Force constants /K			Source
ϕ	a_1	a_2	a_3	
Si-O-Si-O	0.0	0.0	0.0	Quantum Calculations
Si-O-Si-C	0.0	0.0	503.23	-
O-Si-C-C	0.0	0.0	84.03	[143]
C-Si-C-C	0.0	150.97	84.03	[143]
Si-C-C-C	355.04	-68.19	791.32	C-C-C-C from[141,142]
C-C-C-C	355.04	-68.19	791.32	C-C-C-C from[141,142]
C-C-C-O	355.04	-68.19	791.32	C-C-C-C from[141,142]
C-C-O-GB	355.04	-68.19	791.32	C-C-C-C from[141,142]

Table 5.1: Dihedral angle parameters.

In the forcefield there are no terms relating to bond stretching; the bond stretch terms are left out as the SHAKE procedure is used to constrain bond lengths.[146] The time-scale of the bond vibrations is much shorter than that of the movement

Bond angle	Eqm. angle /° θ^0	Source	Force constant k^{ang}/k_b /10^{-20} K rad^{-2}	Source
Si-O-Si	145.7	143	62500	141,142
O-Si-O	113.5	143	32580	143
O-Si-C	108.5	143	25340	143
Si-C-C	109.0	143	28960	143
C-Si-C	110.8	143	34750	143
C-C-C	114.0	141,142	62500	141,142
C-C-O	107.5	143	50680	143
C-O-GB	115.8	AM1*	62500	141,142

Table 5.2: Bond angle parameters.

*From the resultant structure of an AM1 energy minimization calculation for the the angle in a CH_2-O-Ph fragment.

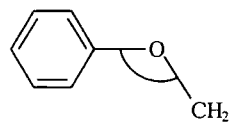

Atom	Mass /10^{-25} kg	ϵ/k_b /K	Source	σ /Å	Source
Si	0.4662965	72.0	144	3.932	30,140,145
O	0.2656794	72.0	144	3.923	30,140,145
CH_n	0.2329290	72.0	144	3.923	30,140,145

Table 5.3: Atom parameters.

Parameter	Value	Source
Mass (GB)	$2.9557968 \times 10^{-25}$ kg	30,140
Inertia (GB)	0.27305×10^{-23} kg rad^{-2}	30,140
$\epsilon_0^{GB}/k_b = \epsilon_{ee}/k_b$	406.51 K	30,140
$\epsilon_0^{GB/LJ}/k_b$	171.08 K	30,140
$\sigma_0^{GB} = \sigma_{ss}$	4.721 Å	30,140
$\sigma_0^{GB/LJ}$	4.117 Å	30,140
GB angle	0.0	-
GB angle force constant	86.4428656	141,142
$\chi\alpha^{-2}$	0.55279	109,140
$\chi'\alpha'^{-2}$	0.77027	109,140

Table 5.4: Other Parameters.

of bond angles etc. Therefore, if this degree of freedom is removed then a larger molecular dynamics time step may be used. Thus, longer timescale simulations become accessible without over-burdening computer resources. The bond lengths are constrained to the values given in Table 5.5

Bond	Length /Å	Source
Si-O	1.626	143
Si-C	1.880	143
C-C	1.523	143
C-O	1.402	143
O-GB	6.000	143

Table 5.5: Bond lengths.

In this model a variant of the Gay-Berne potential that has been studied by de Miguel *et al.* is employed.[110] In this form of the Gay-Berne potential, the exponents μ and ν are 2 and 1 respectively, the length to breadth ratio, σ_{ee}/σ_{ss}, is 3.0 and the ratio of well-depths, $\epsilon_{ee}/\epsilon_{ss}$ is 1/5. Additionally, $\sigma_0^{GB} = \sigma_{ss}$ and $\epsilon_0^{GB}/k_b = \epsilon_{ss}/k_b$ are set according to Table 5.4. This parameterization was devised by fitting to the mesogen in the PDMS polymer.

Spherical non-bonded cut-offs were employed throughout for U_{LJ}, $U_{LJ/GB}$ and U_{GB}. The GB and GB/LJ non-bonded potentials were shifted to ensure that the

Interaction	LJ/LJ	LJ/GB	GB/GB
Potential cutoff /Å	9.0	16.5	18.8
Verlet list cutoff /Å	12.0	17.7	20.3

Table 5.6: Potential and Verlet cutoffs.

interactions went smoothly to zero. Long-range corrections to the energy and virial were evaluated for the LJ potential. Separate Verlet neighbour lists were used for each of the three non-bonded cut-offs. These values are given in Table 5.6. In Equation 5.1, atoms that are bonded in 1-2, 1-3 or 1-4 patterns to each other are excluded for the non-bonded interactions as the influences are accounted for in the SHAKE procedure, the bond-angle potential and the dihedral-angle potential contributions.

5.3 Simulation

5.3.1 Procedure

The molecular dynamics studies were used to examine the phase behaviour of the polymer. The simulations were carried out using the anisotropic form of the leapfrog algorithm, as described in section 4.2.1 on page 65, to solve the equations of motion. The NpT ensemble was employed, at zero pressure with a 2 fs timestep. The Andersen thermostat[115] was implemented to allow the system to collide with a heat bath every 100 steps in order to maintain a constant temperature. The simulation box dimensions were allowed to vary using Monte Carlo moves, as described in section 4.2.2 on page 69, which were attempted every 10 time steps.

An array of 64 identical polymer molecules were placed in a simulation box and preliminary simulations were undertaken to relax the polymer configurations. These simulations were conducted at 600 K to ensure that the polymer was able to move freely and form a melt.

5.3.2 Magnetic field

Preliminary investigations suggested that the system was extremely viscous and accordingly the annealing process was very slow. Therefore, the simulations, like the real system described on page 78, would require a magnetic field to encourage liquid crystal phase formation. An external potential, used to represent a magnetic field, was applied to the system. This external potential was included in the calculation of torques acting on each mesogenic site and the calculation of the total energy of the molecule. This torque arises from the diamagnetic anisotropy of the mesogen, which makes orientations in which the liquid crystalline groups lie parallel to an external field favourable. Any nematic domains in a system will enhance this alignment as the collective effect of a bulk liquid crystal increases the influence of a magnetic field.

The form of the potential used to represent this force was

$$U_{ext} = \sum_{i=1}^{N_{gb}} -\epsilon^{field}\hat{\mathbf{u}}_{zi} \tag{5.2}$$

where, U_{ext} is the external potential (The final term in Equation 5.1), ϵ^{field}, is the field strength, N_{gb} is the number of Gay-Berne sites and $\hat{\mathbf{u}}_z$ is the z component of the Gay-Berne orientational vector. This potential models a field parallel to the z axis.

The magnetic field strength was set to align nematic domains in a common direction without interfering with the degree of order in the system or the resultant phase. It has been shown by Luckhurst *et al.* that if a sufficiently large magnetic field is applied to a nematic liquid crystal, the system will undergo a phase transition to a smectic phase.[147] In the work of Luckhurst values for ϵ^{field} of 0.5 ϵ_0^{GB}, 5.0 ϵ_0^{GB} and 8.0 ϵ_0^{GB} were used and phase transitions to the smectic were observed for the two larger field strengths, while the system with $\epsilon^{field} = 0.5\,\epsilon_0^{GB}$ remained nematic. In this simulation study potentials of $\epsilon^{field} = 0.36\ \epsilon_0^{GB}$ and $0.89\ \epsilon_0^{GB}$, respectfully 0.2×10^{-20} J and 0.5×10^{-20} J were employed.

To ensure that the aligning potentials used to represent magnetic fields in this work were not large enough to disrupt the phase behaviour they have been applied

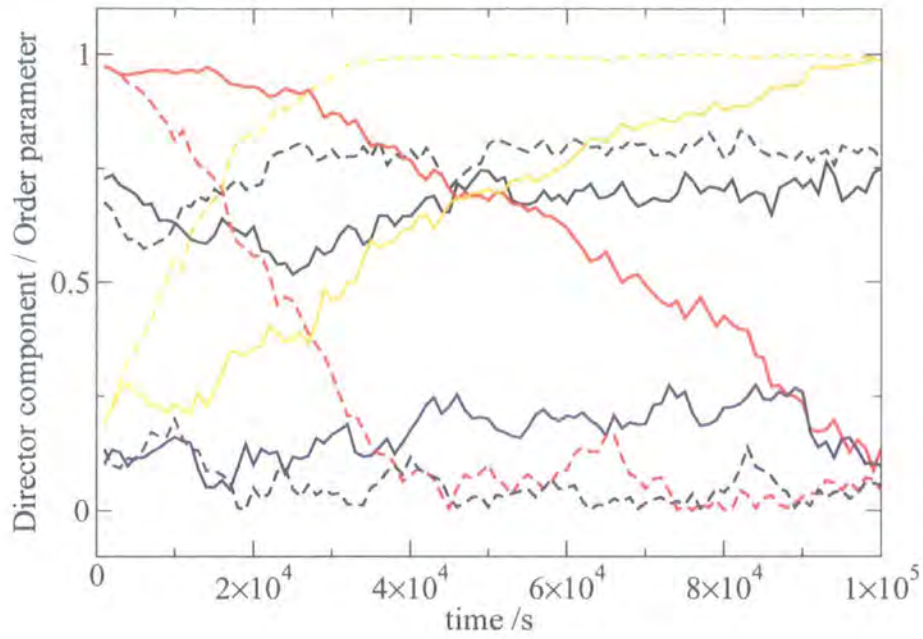

Figure 5.5: Reorientation of the director due to a magnetic field.

Black is the order parameter and red, blue and orange the x, y, and z components, respectively, of the orientation of the director. Solid lines represent a system under a field of 0.2×10^{-20} J and dashed lines represent a system under a field of 0.5×10^{-20} J

to a test system. This test system consists of 256 Gay Berne sites, parameterized to match the ones in the SCLCP. The test simulation was conducted at 400 K, with a 10^{-15} s timestep. The potential cut-off radius was 18.88 Å and the Verlet neighbour list cut-off was 20.30 Å. At the start of the simulation the Gay-Berne sites were in a nematic phase with the director along the x axis.

Figure 5.5 shows how aligning potentials of strength 0.2×10^{-20} J and 0.5×10^{-20} J induce a change in the director as the phase re-orientates to be aligned along the z axis, parallel to the magnetic field. However, the order parameter at the start and end of the runs is not effected by the aligning potential.

5.3.3 Cooling runs

To observe the phase behaviour of the model a sample was cooled slowly from the melt over 35 ns with no external potential. These runs are summarized in Table 5.7.

Field Strength /$\times 10^{-20}$ J	Temperature /K	Time /ns
0.0	600	1
0.0	500	4*
0.0	450	4
0.0	400	6
0.0	350	8
0.0	300	6
0.0	250	6

Table 5.7: Cooling runs in the absence of an external field. The end of the 500 K runs (marked*) is the starting point for the runs in Tables 5.8, 5.9 and 5.14.

Field Strength /$\times 10^{-20}$J	Temperature /K	Time /ns
0.2	450	4
0.2	400	6
0.2	350	6
0.2	300	6
0.2	250	6
0.2	200	6

Table 5.8: Cooling runs in a field of strength 0.2 $\times 10^{-20}$ J, started from 500 K melt with no field.

From the isotropic melt at 500 K a further two sets of runs were started. In these two simulations a magnetic field was modelled by an external potential. The summaries of these simulations are given in Tables 5.8 and 5.9 on the following page.

The configurations of the system at each temperature, for each set of simulations were analyzed by calculating order parameters, radial distribution functions and diffusion constants. The methods for calculating these values are outlined in Section 4.3 on page 73. Also, the dimensions of the simulation box were monitored and snapshots were generated using AVS software,[148] to visualize the system and enable a qualitative assessment of the progress of microphase separation by eye.

Field Strength / $\times 10^{-20}$J	Temperature /K	Time /ns
0.5	450	6
0.5	400	4
0.5	350	6
0.5	300	6
0.5	250	6
0.5	200	6

Table 5.9: Cooling runs in a field of strength 0.5 $\times 10^{-20}$ J , started from 500 K melt with no field.

5.4 Results and discussion

5.4.1 Simulation Data

Table 5.10 contains a summary of the measurements of the simulation box volume and order parameter for all simulations that have been described.

5.4.2 Order parameter

The time evolution of the order parameter for the cooling runs without an aligning potential, with a 0.2 $\times 10^{-20}$ J and a 0.5 $\times 10^{-20}$ J field strength are plotted in Figure 5.6.

In the absence of an external potential (Figure 5.6a) the average order in the system does not change very much with cooling; there is very little overall orientational order at any point in these runs.

When the smaller aligning potential is applied to the system a large change in the order parameter develops. The system at higher temperatures has little overall orientational order. However, as the system is cooled the order parameter grows. The growth continues until 250 K, when a final value of approximately $\langle S_2 \rangle = 0.6$ is reached. This level of order persists even when the sample is cooled further to 200 K. This may indicate that the system is no longer fluid and could be frozen.

When a larger aligning potential is applied to the system molecules align to some degree even at high temperatures (Figure 5.6c). The potential is therefore

Temp. /K	Field $/\times 10^{-20}$J	Volume /Å$^3 \times 10^5(\pm 5\%)$	O.P. $< S_2 > (\pm 0.05)$
500	0.0	6.20	0.043
450	0.0	5.72	0.040
400	0.0	5.29	0.055
350	0.0	4.94	0.064
300	0.0	4.66	0.079
250	0.0	4.41	0.095
450	0.2	5.69	0.126
400	0.2	5.28	0.183
350	0.2	4.92	0.298
300	0.2	4.60	0.498
250	0.2	4.37	0.583
200	0.2	4.21	0.587
450	0.5	5.54	0.380
400	0.5	5.08	0.599
350	0.5	4.79	0.687
300	0.5	4.55	0.737
250	0.5	4.35	0.749
200	0.5	4.19	0.750

Table 5.10: Summary of simulation data. Values of order parameter and mean square diffusion are for Gay-Berne sites, averaged over the last 2 ns of the simulation.

strong enough to cause some spontaneous order in the melt. When the system is cooled a rapid increase in the order parameter is observed and the sample becomes well ordered with respect to orientation. A final value in the region $\langle S_2 \rangle = 0.75$ is reached. The system is well ordered at 300 K, after which there is little change in $\langle S_2 \rangle$ on further cooling.

5.4.3 Snapshots

Configurations of the system were extracted for each of the three cooling runs at a range of temperatures. In these snapshots the Lennard-Jones united atoms that make up the polymer are represented by white spheres and the Gay-Berne sites are represented by coloured ellipsoids. The colour of the ellipsoids shows the orientation. Red, green and blue ellipsoids represent mutually orthogonal directions.

Figure 5.7 shows the system with no external potential applied at 50 degree intervals between at 450 K and 250 K. The snapshots at 450 K and 400 K show an isotropic system with no orientational or positional order and full mixing between the polymeric parts of the molecule and the mesogens. When this sample is cooled some microphase separation is evident from the formation of mesogen-rich and polymer-rich regions.

The effect of the smaller aligning potential is seen in Figure 5.8, which show the system with a 0.2 $\times 10^{-20}$ J field applied at the same temperatures. At 450 K the fluid is isotropic and is quite well mixed. This mixing reduces a little at 400 K and there is some evidence of mesogen-rich areas forming. Cooling this system to 350 K results in more marked microphase separation. Although there are large mesogen rich domains, the order parameter is indicative of a system were the domains do not point in a common direction or that ordering within the domains is low. At 300 K the domains have aligned in a common direction. Further cooling to 250 K sees these domains forming layers. This effect is probably enhanced by the periodic box.

Finally, Figure 5.9 shows the system with an external potential of field strength 0.5 $\times 10^{-20}$ J applied. At 450 K the system is still mixed, but the larger potential has already induced some molecular alignment in the fluid. With this stronger field the

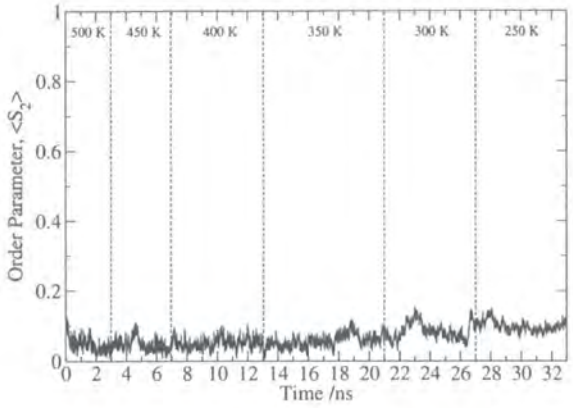

(a)

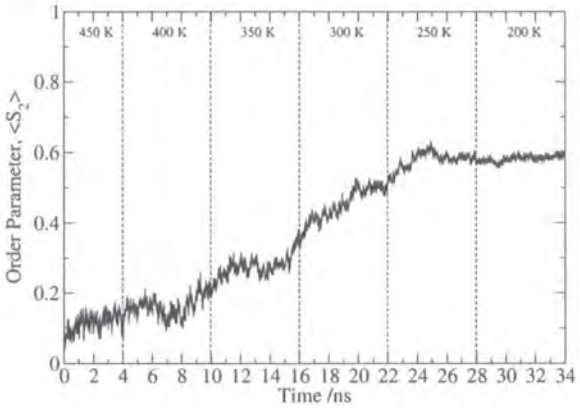

(b)

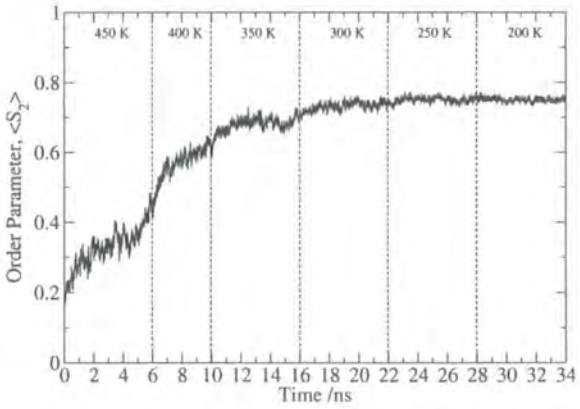

(c)

Figure 5.6: Order parameter for cooling, using an aligning potential with a field strength of (a) 0.0×10^{-20} J, (b) 0.2×10^{-20} J and (c) 0.5×10^{-20} J.

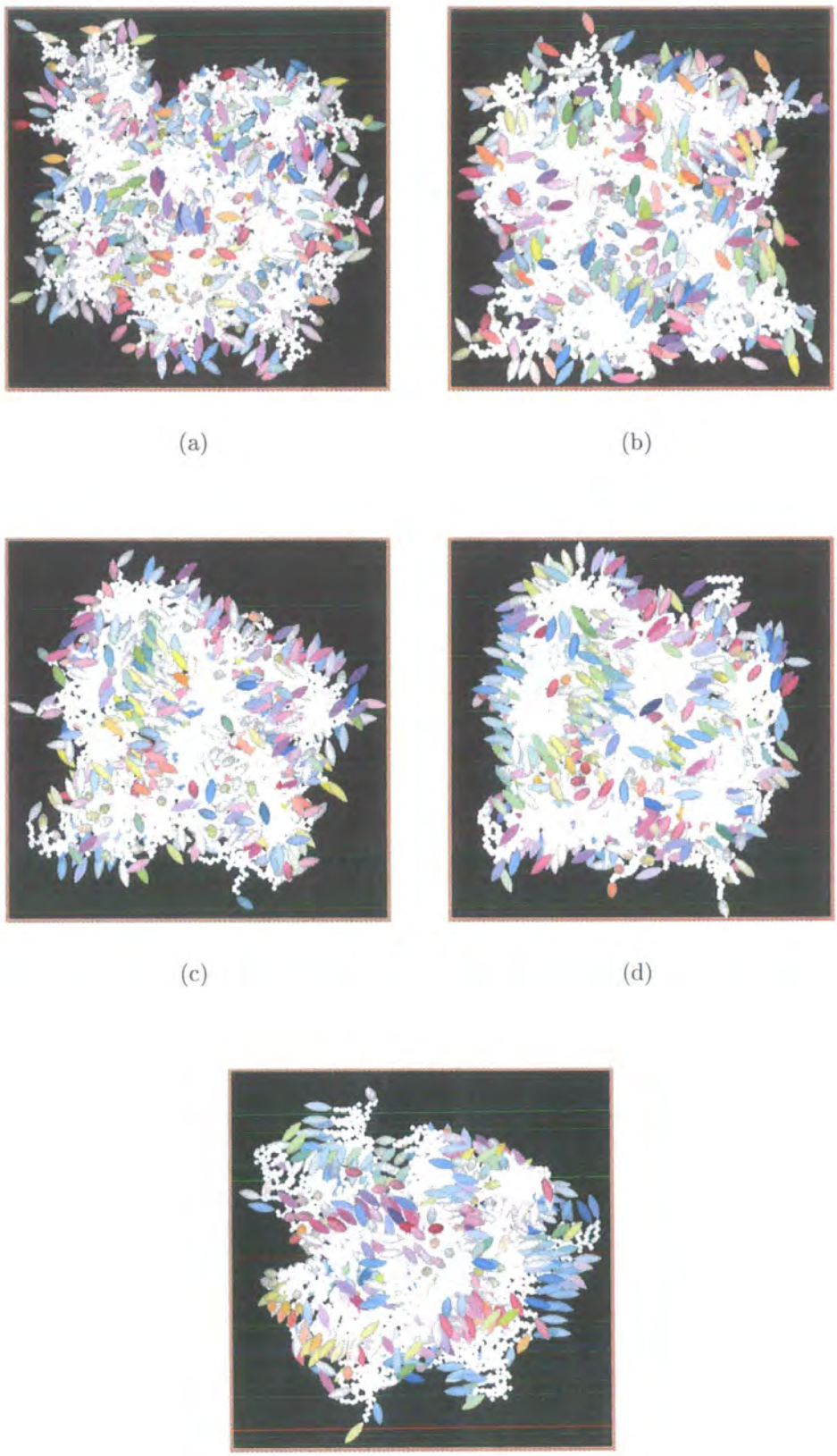

(a) (b)

(c) (d)

(e)

Figure 5.7: Snapshots of the SCLCP at (a) 450 K, (b) 400 K, (c) 350 K, (d) 300 K and (e) 250 K with no aligning potential applied.

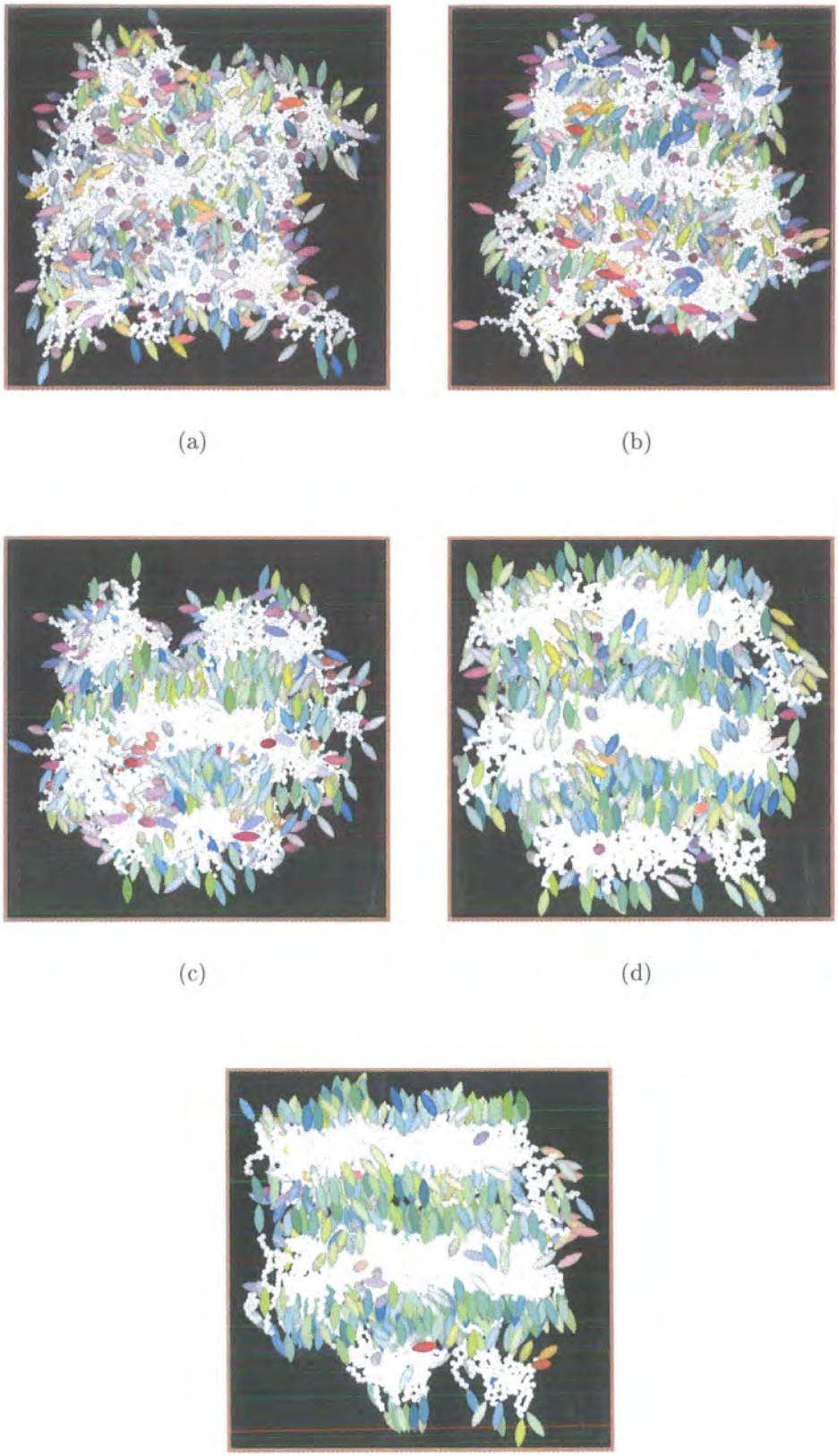

(a) (b)

(c) (d)

(e)

Figure 5.8: Snapshot of the SCLCP at (a) 450 K, (b) 400 K, (c) 350 K, (d) 300 K and (e) 250 K with a 0.2 $\times 10^{-20}$ J aligning potential applied.

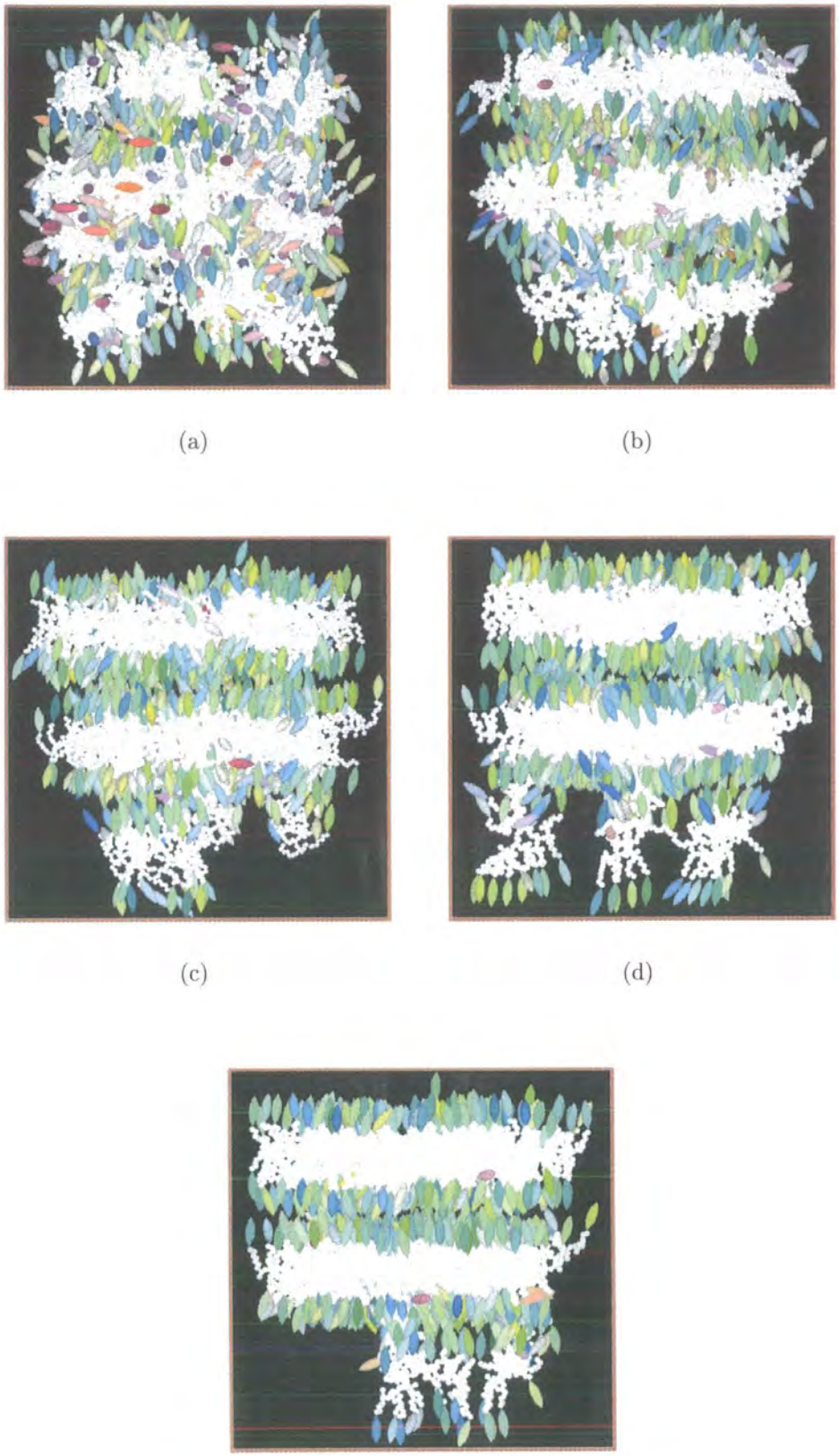

(a) (b)

(c) (d)

(e)

Figure 5.9: Snapshot of the SCLCP at (a) 450 K, (b) 400 K, (c) 350 K, (d) 300 K and (e) 250 K with a 0.5 $\times 10^{-20}$ J aligning potential applied.

system phase separates much sooner and layers can be seen even at 400 K. However, order within these layers appears nematic like. When the sample is cooled to 350 K the strata become well developed and a pattern with one polymer layer sandwiched between two mesogen layers emerges. The ordering inside the mesogenic layers still seems quite nematic at this stage. However when the system is cooled to 250 K the 2:1 morphology sharpens and smectic order within the mesogen layers is observed.

Each of the systems at 350 K show different morphologies. To illustrate this snapshots from each simulation have been colour coded to indicate the region of the molecule to which they belong, then disseminated into constituent parts in order to examine these morphologies further. In Figures 5.10, 5.11 and 5.12, the polymer backbone is coloured blue, the flexible spacers are red and the mesogens are white.

Figure 5.10 shows the SCLCP without a field at 350 K. Here the pictures confirm that the system has some fluctuation in proportion of mesogens and polymer in different areas of the polymer. However, there is still mixing in most areas and no obvious orientational ordering.

In Figure 5.11 phase separation becomes more obvious. Despite poor overall ordering the system does have large domains that appear to have some nematic character and are aligned with other domains.

In the system that is exposed to the larger external field, clear layers of mesogens and backbone are now evident. Figure 5.12a shows two layers of polymer backbone, each surrounded by flexible spacer chains between these layers a layer of mesogens is evident. This stratum seems to have divided into a double layer of mesogens. Figure 5.12b concurs with this description. In Figure 5.12c the backbone can be seen in distinct layers, with a defect allowing one chain to traverse the mesogen layer and reach a neighbouring layer.

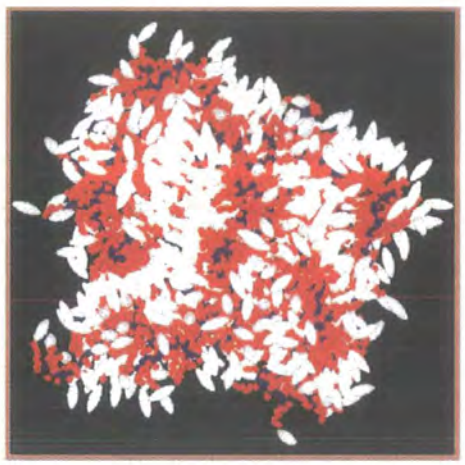

(a)

(b)

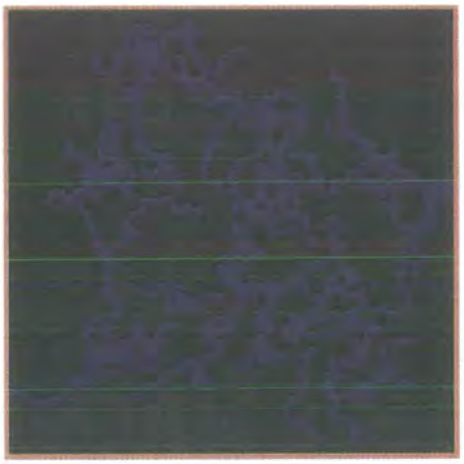

(c)

Figure 5.10: Snapshots of system without a field split into parts.
(a) the whole system, (b) the mesogenic units and (c) only the polymer backbone.

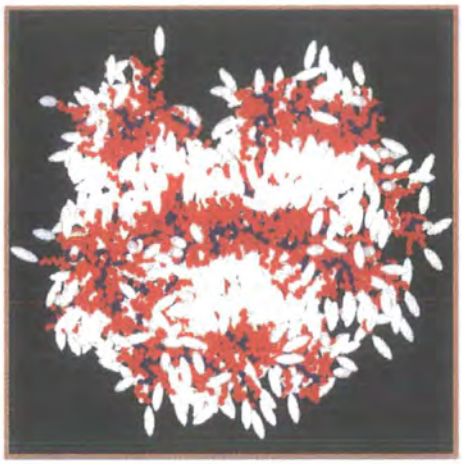

(a)

(b)

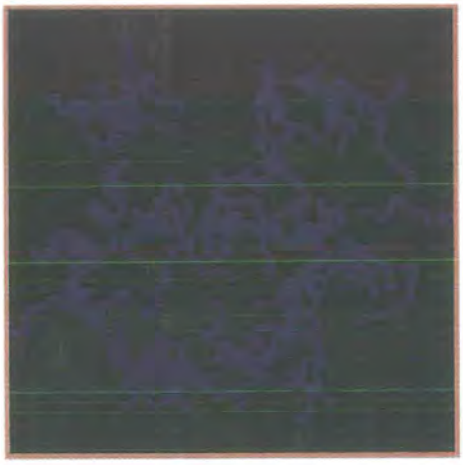

(c)

Figure 5.11: Snapshots of system with a 0.2 $\times 10^{-20}$ J field split into parts. (a) the whole system, (b) the mesogenic units and (c) only the polymer backbone.

(a)

(b)

(c)

Figure 5.12: Snapshots of system with a 0.5 $\times 10^{-20}$ J field split into parts. (a) the whole system, (b) the mesogenic units and (c) only the polymer backbone.

5.4.4 Radial distribution functions

Distribution functions were calculated for the system in each field at 450 K, 350 K and 250 K. The radial distribution of the Gay-Berne sites, $g(r)$ (Figure 5.13); and the components of $g(r)$ perpendicular to, $g_{\perp}(r)$ and parallel to the director, $g_{\parallel}(r)$ (Figures 5.15 and 5.16 respectively); and the orientational pair distribution function for Gay-Berne sites, $g_2(r)$ (Figure 5.14), are plotted for each of these three temperatures. The radial distribution functions are normalized with respect to an ideal gas of uniform density.

The radial distribution function, $g(r)$ at 450 K in, Figure 5.13a , shows all three systems to be liquid. Around each mesogen there is a region of depletion due to short-range repulsive forces preventing overlaps. Just after 5 Å there is a nearest neighbour peak that compensates for the depletion shell. After this the distribution flattens to a limiting value of unity.

In Figure 5.14a, $g_2(r)$ at 450 K also shows a depletion zone followed by a nearest neighbour peak. The value at long distances tends to $\langle S_2 \rangle^2$. The small amount of field induced order for the system with the larger aligning potential is evident.

At 450 K, the lack of structure in $g_{\parallel}(r)$ confirms that there are no layers or domains forming at this temperature.

When the system is cooled to 350 K, $g(r)$ for the system with no field applied remains the same; for the system in the small field, the nearest neighbour peak grows a little, indicating a small increase in the ordering of the mesogens in the system. For the system in the larger field the nearest neighbour peak is much more developed and there is some depletion just beyond this peak. Two other peaks are also evident at roughly two and three times the separation distance of the nearest neighbour peak. The three peaks are at approximately 5.5, 11.0 and 16 Å. These functions are plotted in Figure 5.13b.

$g_2(r)$ for the systems at 350 K is shown in Figure 5.14b. Here three distinct values are obtained as the limiting values for the curves at large r. Three solvation shells are again evident for the system in the larger field.

The perpendicular and parallel components at 350 K are plotted in Figures 5.15b and 5.16b. The perpendicular component for the highest field strength again shows

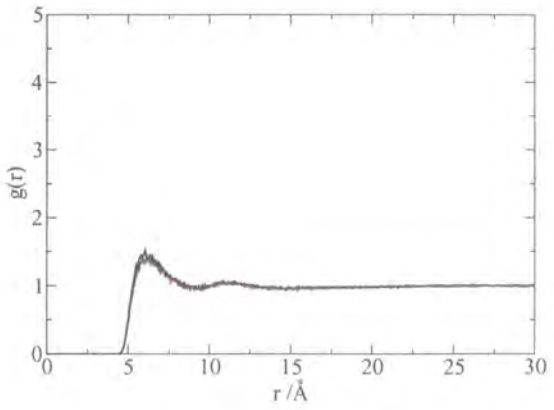

(a)

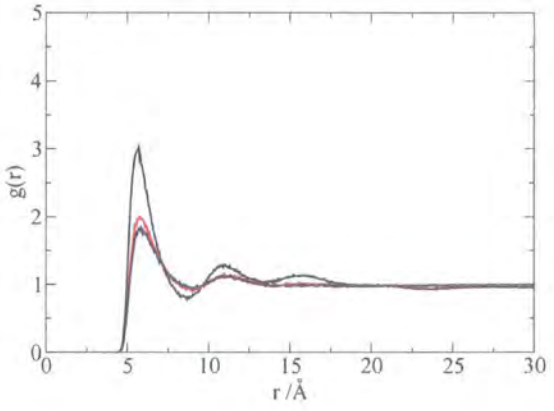

(b)

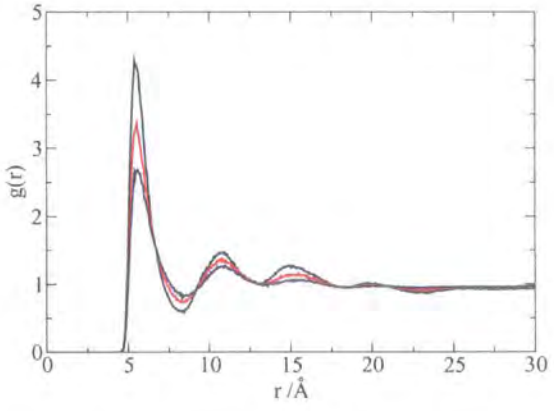

(c)

Figure 5.13: Radial distribution function, *g(r)* at (a) 450 K, (b) 350 K, (c) 250 K. The black, red and blue lines represent systems with 0.5×10^{-20} J, 0.2×10^{-20} J and 0.0×10^{-20} J aligning potentials applied.

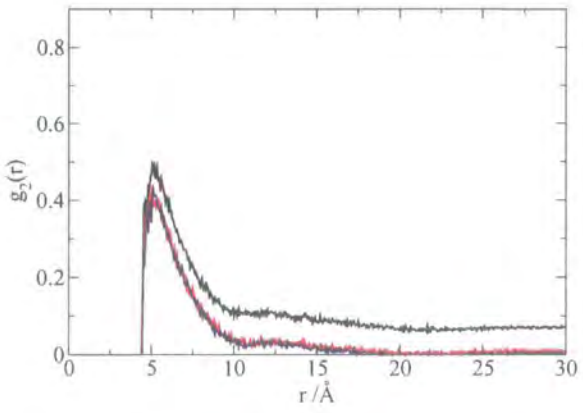

(a)

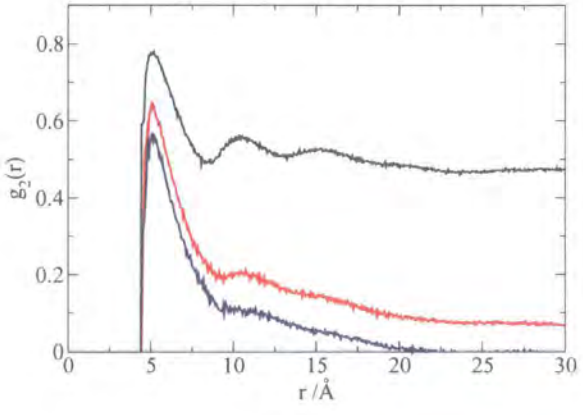

(b)

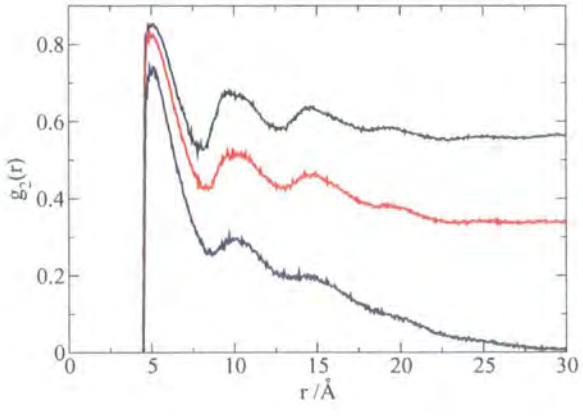

(c)

Figure 5.14: Orientational pairwise distribution function, $g_2(r)$ at (a) 450 K, (b) 350 K, (c) 250 K. The black, red and blue lines represent systems with 0.5×10^{-20} J, 0.2×10^{-20} J and 0.0 $\times10^{-20}$ J aligning potentials applied.

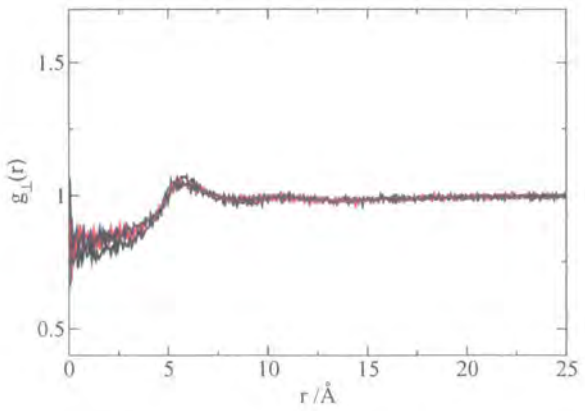

(a)

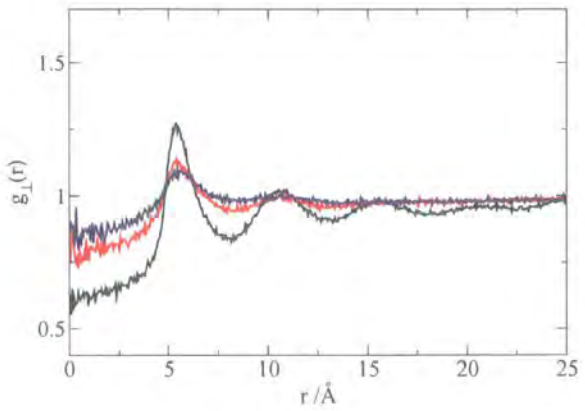

(b)

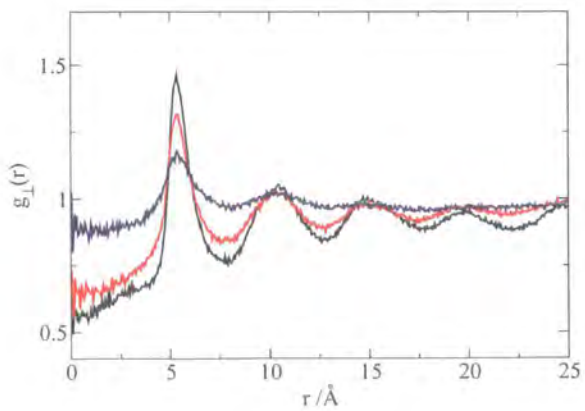

(c)

Figure 5.15: Perpendicular component of the radial distribution function, $g_{\perp}(r)$ at (a) 450 K, (b) 350 K, (c) 250 K. The black, red and blue lines represent systems with 0.5×10^{-20} J, 0.2×10^{-20} J and 0.0 $\times10^{-20}$ J aligning potentials applied.

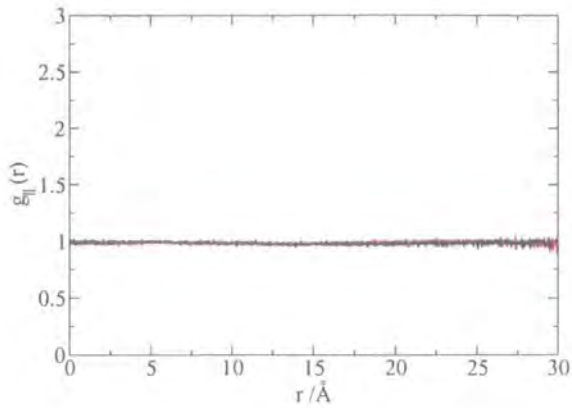

(a)

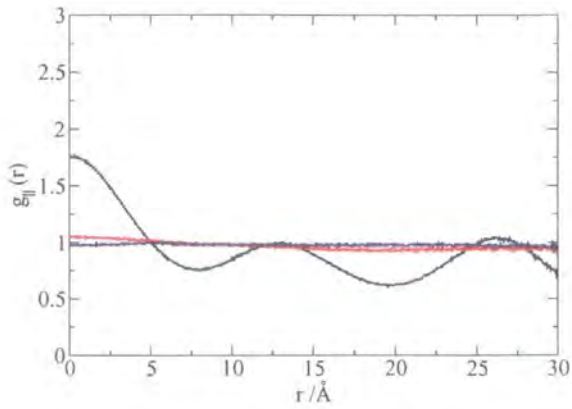

(b)

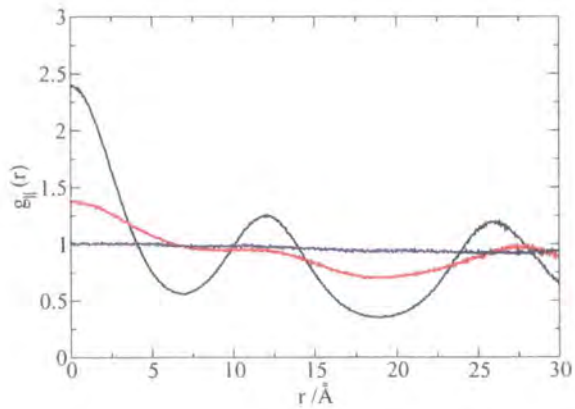

(c)

Figure 5.16: Parallel component of the radial distribution function, $g_{||}(r)$ at (a) 450 K, (b) 350 K, (c) 250 K. The black, red and blue lines represent systems with 0.5×10^{-20} J, 0.2×10^{-20} J and 0.0 $\times10^{-20}$ J aligning potentials applied.

three peaks and the parallel component clearly shows peaks and troughs, which are indicative of smectic layers. The lack of long range order in $g_{\perp}(r)$ and the typical "liquid-like" appearance of the curves suggests that the smectic is a fluid smectic, such as smectic A. No structure in $g_{||}(r)$ for the sample in the smaller magnetic field suggests that any order in this system is purely nematic; there are no smectic characteristics of domains forming. In the simulation with the larger field strength, 0.5 $\times 10^{-20}$ J, there are three distinct peaks: the peak at approximately $r = 0$ Å, which represents sites in the same layer, at approximately $r = 12$ Å, which represents neighbouring sites in the same mesogen-rich region but a different smectic layer and at about $r = 26$ Å, which is due to mesogens in the next mesogen-rich region down.

At 250 K the radial distributions are more structured for each system. In Figure 5.13(c), all three systems show three solvation shell peaks, there is also a possible fourth peak in the distribution for the sample in the external potential of 0.5 $\times 10^{-20}$ J.

In Figure 5.14c, $g_2(r)$, shows an increase in orientational order for the systems with an external potential applied. There is also more structure in these distribution functions with the peaks indicating strong orientational correlation between neighbouring molecules, out to the third nearest neighbour in each system. However, with the external potential switched off, the polymer still clearly has no long range order.

The perpendicular component of the radial distribution function for the 250 K systems is shown in Figure 5.15(c). In this distribution any order occurring within smectic layers would be evident. For the system with no aligning potential applied there is little structure, but for the samples in the magnetic field there are a number of peaks. The even distribution of these suggests that the phase does not have in-layer ordering and the decay in peak height is indicative of fluid-like order, as expected in a smectic phase.

Figure 5.16c shows that for the system in the smaller field some layers are present although they are less well formed than the those in the aligning potential. In this function we see three strong peaks for the system with the larger aligning potential, these are at the same distances as for the higher temperature seen in Figure 5.16b,

but they have a greater magnitude indicating a more well-structured system. For the system with the smaller aligning potential the peaks at approximately 0.0 Å and 27 Å correspond to two layers of mesogens. However, the presence of a small shoulder rather than a strong peak at about 10 Å is indicative that the mesogen regions are not split into two distinct smectic layers, but nematic like order exists within the mesogen rich regions.

5.4.5 Diffusion

The mean square displacement (MSD) of sites within the molecule has been calculated to compute diffusion coefficients. A typical form for the MSD plotted with respect to time is shown in Figure 5.17. The plot is non-linear at short times. However, a linear region is seen at long times, as depicted in the figure, from which diffusion data can be obtained. The diffusion coefficient, D, is directly linked to the MSD, by the Einstein relation

$$D = \frac{1}{6t} \left\langle |\mathbf{r}_i(t_2) - \mathbf{r}_i(t_1)|^2 \right\rangle, \tag{5.3}$$

where $\mathbf{r}_i(t_1)$ and $\mathbf{r}_i(t_2)$ are the molecular position vectors at times t_1 and t_2 respectively and the angular brackets denote an average over all molecules.

For this study the MSD displacement data is calculated for a number of time origins. An example of the mean square diffusion data for the Gay-Berne sites at range of temperatures is given in Figure 5.18. The linear region of each curve has been extracted and is shown in Figure 5.19. From this figure each data set can be fitted to a line of best-fit and the gradients of the lines extracted. The diffusion coefficients can be calculated from the gradient using Equation 5.3. In all, diffusion coefficients have been calculated for three sites in the molecule: all the Gay-Berne sites, the Lennard-Jones atom at the centre of each polymer chain and a Lennard-Jones atom at the end of each polymer. These coefficients can be found in Table 5.11.

Diffusion coefficients can be used to identify phase transitions in a simulation. If a system undergoes a transition to a liquid crystalline phase from a liquid there is a

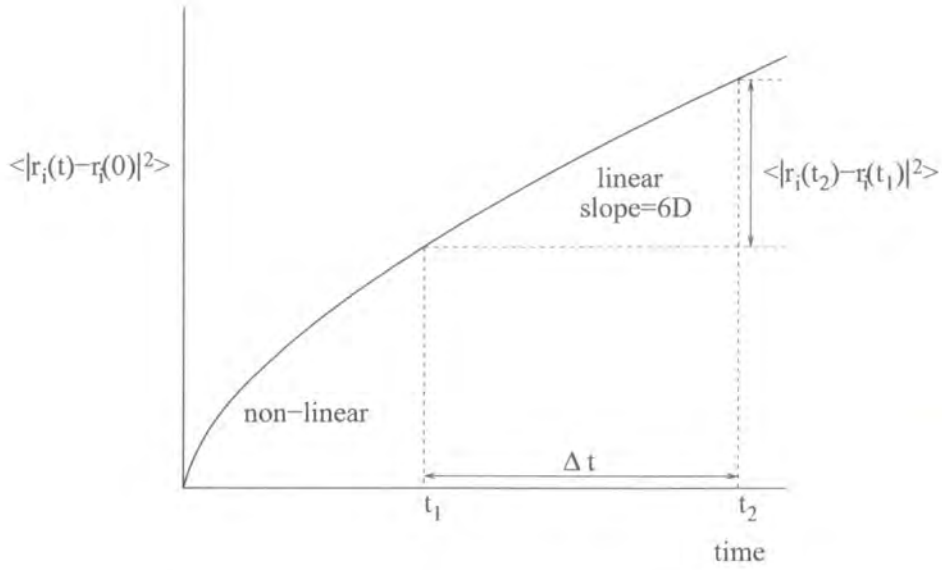

Figure 5.17: Schematic representation of the shape of a mean square displacement plot.

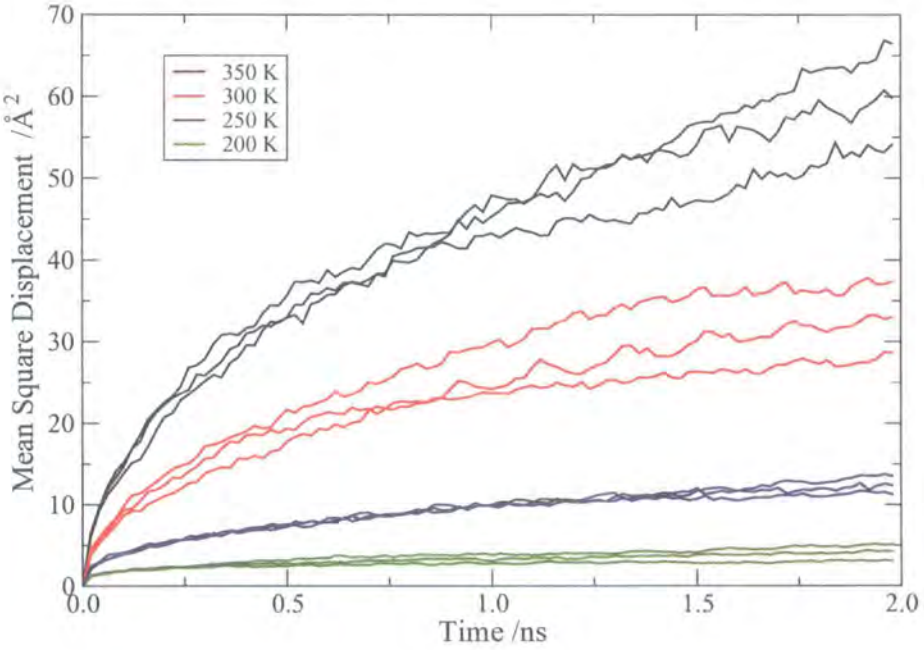

Figure 5.18: Example of mean square displacement data for Gay-Berne sites with an external potential of 0.5 $\times 10^{-20}$ J, over a range of temperatures.

Temp. /K	Field /$\times 10^{-20}$J	D (GB) /m^2 s^{-1}	D (LJ1) /m^2 s^{-1}	D (LJ2) /m^2 s^{-1}
500	0.0	$2.39 \pm 0.36 \times 10^{-10}$	$1.10 \pm 0.13 \times 10^{-10}$	$7.06 \pm 0.40 \times 10^{-11}$
450	0.0	$1.50 \pm 0.11 \times 10^{-10}$	$6.92 \pm 0.93 \times 10^{-11}$	$4.40 \pm 0.55 \times 10^{-11}$
400	0.0	$8.54 \pm 2.05 \times 10^{-11}$	$4.75 \pm 0.86 \times 10^{-11}$	$2.66 \pm 0.31 \times 10^{-11}$
350	0.0	$5.12 \pm 1.25 \times 10^{-11}$	$2.79 \pm 0.76 \times 10^{-11}$	$1.54 \pm 0.36 \times 10^{-11}$
300	0.0	$2.22 \pm 0.61 \times 10^{-11}$	$1.56 \pm 0.42 \times 10^{-11}$	$6.60 \pm 0.98 \times 10^{-12}$
250	0.0	$8.08 \pm 3.36 \times 10^{-12}$	$4.55 \pm 0.85 \times 10^{-12}$	$1.88 \pm 0.34 \times 10^{-12}$
450	0.2	$1.17 \pm 0.27 \times 10^{-10}$	$6.95 \pm 1.02 \times 10^{-11}$	$4.36 \pm 0.26 \times 10^{-11}$
400	0.2	$7.83 \pm 1.03 \times 10^{-11}$	$4.96 \pm 1.69 \times 10^{-11}$	$3.01 \pm 0.96 \times 10^{-11}$
350	0.2	$5.23 \pm 0.22 \times 10^{-11}$	$2.06 \pm 0.58 \times 10^{-11}$	$1.33 \pm 0.50 \times 10^{-11}$
300	0.2	$2.27 \pm 0.18 \times 10^{-11}$	$1.06 \pm 0.31 \times 10^{-11}$	$4.39 \pm 0.07 \times 10^{-12}$
250	0.2	$9.19 \pm 0.76 \times 10^{-12}$	$3.23 \pm 0.61 \times 10^{-12}$	$1.26 \pm 0.26 \times 10^{-12}$
200	0.2	$1.87 \pm 0.70 \times 10^{-12}$	$1.05 \pm 0.31 \times 10^{-12}$	$3.30 \pm 0.22 \times 10^{-12}$
450	0.5	$8.45 \pm 1.88 \times 10^{-11}$	$6.34 \pm 0.49 \times 10^{-11}$	$4.18 \pm 0.47 \times 10^{-11}$
400	0.5	$4.41 \pm 1.08 \times 10^{-11}$	$2.77 \pm 1.50 \times 10^{-11}$	$1.50 \pm 0.49 \times 10^{-11}$
350	0.5	$2.62 \pm 0.82 \times 10^{-11}$	$1.55 \pm 0.12 \times 10^{-11}$	$5.75 \pm 2.89 \times 10^{-12}$
300	0.5	$8.76 \pm 2.70 \times 10^{-12}$	$5.48 \pm 2.12 \times 10^{-12}$	$2.22 \pm 0.27 \times 10^{-12}$
250	0.5	$4.08 \pm 2.71 \times 10^{-12}$	$1.38 \pm 0.51 \times 10^{-12}$	$8.12 \pm 5.36 \times 10^{-13}$
200	0.5	$1.58 \pm 1.03 \times 10^{-12}$	$9.39 \pm 3.76 \times 10^{-13}$	$3.30 \pm 3.01 \times 10^{-13}$

Table 5.11: Summary of diffusion coefficients. Averages over the last 2 ns of the simulation. For the Gay-Berne sites (GB), a Lennard-Jones site at the end of the polymer (LJ1) and a Lennard-Jones site in the middle of the polymer (LJ2).

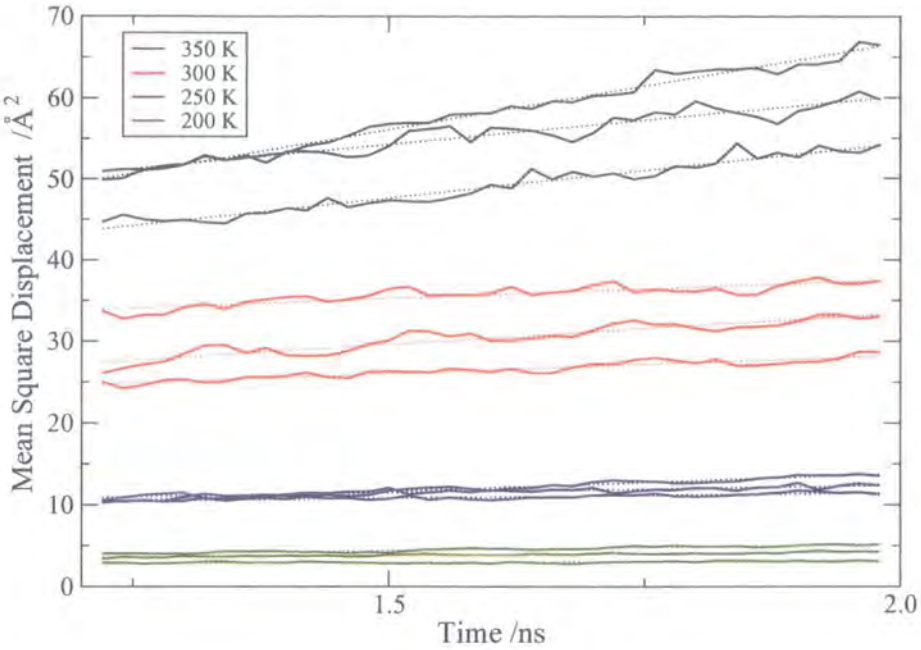

Figure 5.19: Mean square displacement data selected to give limiting slopes for Gay-Berne sites with an external potential of 0.5 $\times 10^{-20}$ J, over a range of temperatures.

large decrease in the diffusion co-efficient as the movement of the molecules is greatly impeded. Therefore, by looking for changes in the slope of $\log D$ with respect to the temperature phase transitions may be found. In Figure 5.20 the diffusion coefficients extracted from the MSD data in Figure 5.19 have been plotted in this way. Linear regression has been used to fit a series of straight lines to different parts of the data. By looking at the regression coefficients it is possible to judge which of these fits may be the closest fit.

This procedure has been used to fit all the diffusion coefficients. Figure 5.21 shows the best fits for the systems with no aligning potential, a 0.2 $\times 10^{-20}$ J external potential and a 0.5 $\times 10^{-20}$ J potential. Each of these figures show that the movement of the sites is as expected middle of backbone $<$ end of polymer chain $<$ mesogen. In the simulations without an external potential applied the most likely phase transition is at 350 K. In the simulations with the smaller field strength the most likely phase transition is at 300 K. In the simulations with the larger field strength the most likely phase transition is at 350 K.

This system exhibits complex phase behaviour, and there are a number of possible transitions: isotropic to nematic, nematic to smectic, glass transition, etc. How-

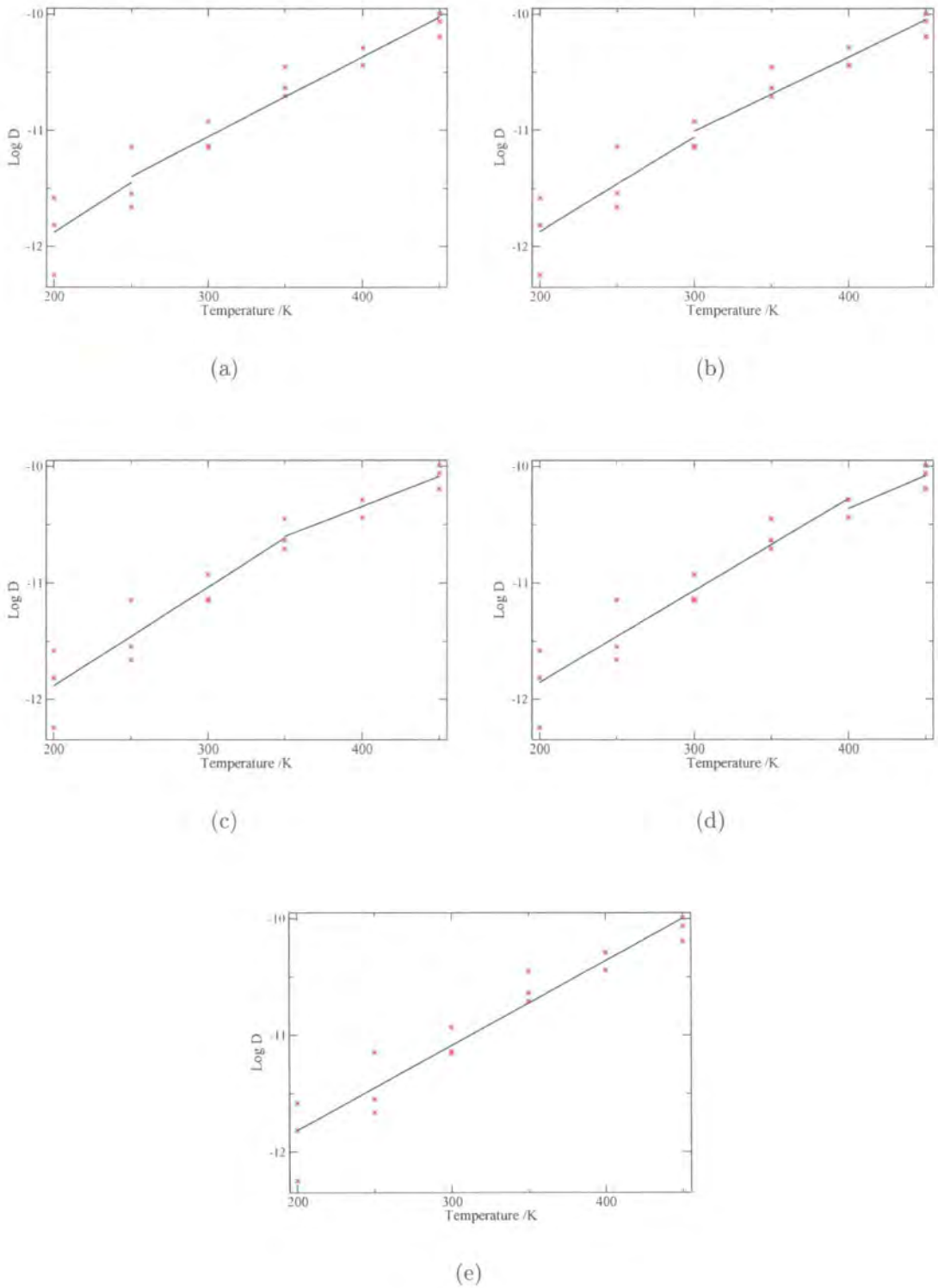

Figure 5.20: Linear regression fits for diffusion data.
(a) phase change at 250 K, (b) phase change at 300 K, (c) phase change at 350 K, (d) phase change at 400 K, (e) no phase change.

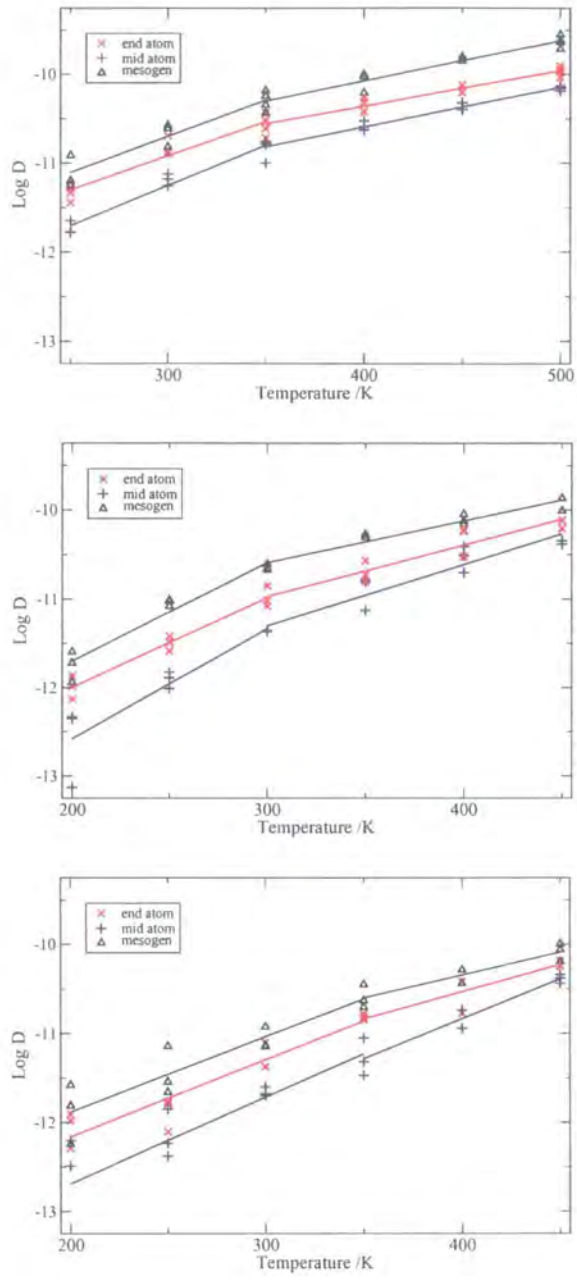

Figure 5.21: Plot of log D vs temperature fitted to show a possible phase transition for the SCLCP with an aligning potential of (a) 0.0 $\times 10^{-20}$ J, (b) 0.2 $\times 10^{-20}$ J, (c) 0.5 $\times 10^{-20}$ J applied.

ever, some insights into the phase behaviour are still gained from diffusion data. In the isotropic phase D values are comparable for systems with and without applied fields, but when cooled molecular alignment by a 0.5 $\times 10^{-20}$ J potential reduces D by an order of magnitude. In the 0.2 $\times 10^{-20}$ J potential alignment is slower and therefore this transition takes place at a lower temperature. Any transition for the sample with no field applied will be of a different kind owing to the lack of alignment in this system.

5.4.6 Comparison to Experimental Findings

The bilayer structure that has been observed differs from the findings of Ebbutt *et al.* for this SCLCP that indicate that a smectic phase with broad disordered monolayers with tilted Sm_C character forms direct from the isotropic melt.[139] However, the broad temperature range of the smectic mesophase found in that study (30 °C – 150 °C) is in agreement with the simulation results. One factor that shed light on this discrepancy is that Ebbutt *et al.* report that they were unable to align the polymer in a field. This may have reduced the opportunity for microphase separation on a bulk scale.

Another study of polysiloxane SCLCPs that was conducted without an aligning field is the work of Martinoty *et al.* that explored the effects of shearing and friction in the polymers, here finite clusters which formed as a result of nematic effects in the mesogenic groups.[135] This finding is in agreement with the simulations conducted with no field applied

A study on a number of homopolymeric SCLCPs by Fan *et al.* did find a bilayer structure and agreeable distribution functions.[138] Also the phase behaviour of these systems concurs with the conclusions of this simulation study with a narrow nematic range preceding a large smectic range.

5.5 Further Simulations

In the light of the results described in Section 5.4 some questions about the phase behaviour of this model remained:

Temp. /K	Potential /$\times 10^{-20}$J	Time /ns	Starting point	Volume /Å^3 $\times 10^5(\pm 5\%)$	$< S_2 >$ (± 0.05)
350	0.0	38	350 K, 0.0 $\times 10^{-20}$J	4.92	0.179
350	0.2	38	350 K, 0.2 $\times 10^{-20}$J	4.80	0.652

Table 5.12: Summary of simulation data for two state points. Values of order parameter are for Gay-Berne sites, averaged over the last 2 ns of the simulation.

- Would the level of order found in the system with the large field arise in the systems with a smaller field or no field if a long enough time frame was studied?
- Would the liquid crystalline phases formed in a magnetic field remain stable when the field was removed?
- Is the rate of cooling of the system related to the phase behaviour?

In an attempt to answer these questions further simulations were undertaken.

5.5.1 State Points

Two state points were chosen for further investigation. Table 5.12 shows the details of these state points. Configurations from previous runs were extracted and used to start new simulations. The volume and order parameter for these simulations indicate that, despite being at the same temperature the systems are in different phases.

The time evolution of the order parameter for these new simulations is shown in Figure 5.22. In the absence of a external potential the orientational order rises but remains low and the radial distribution functions (Figures 5.23 and 5.24) reveal little change. However, there is evidence that the structure has developed; snapshots of the system show signs of microphase separation (Figure 5.25). In the snapshots mesogens are shown to be pointing in two directions, one domain with its director pointing into the page and other domains with the domain directors pointing from left to right. This indicates that without a field to align the molecules, domains do form, but remain uncorrelated with other parts of the system.

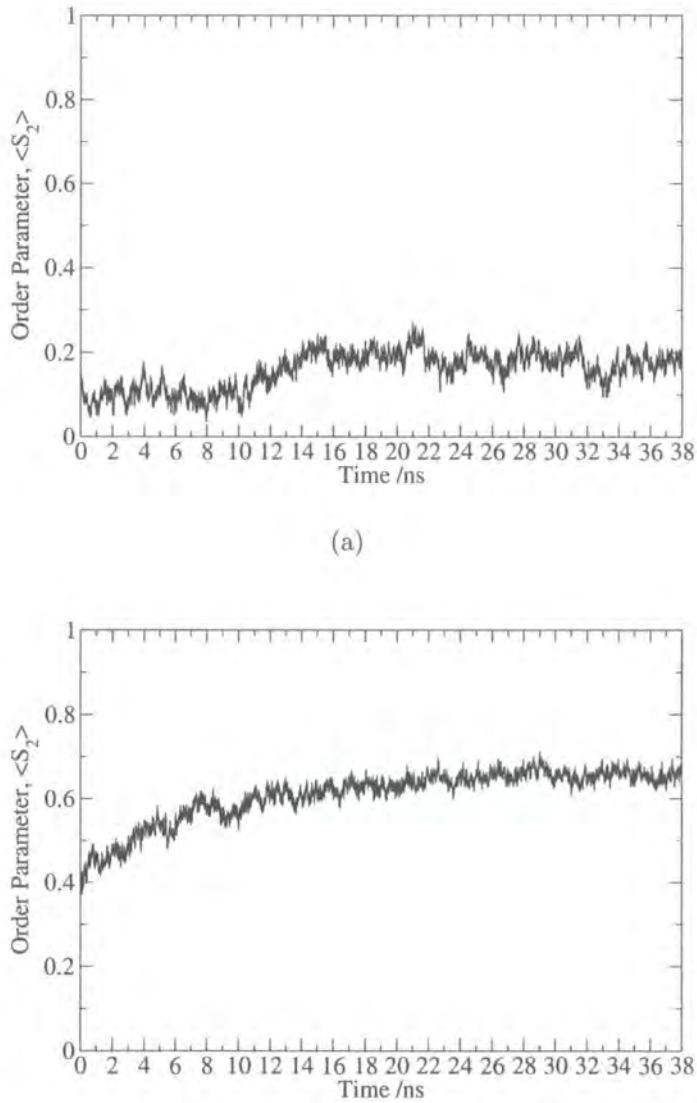

Figure 5.22: Order parameter for state point runs at 350 K with (a) no aligning potential and (b) 0.2 $\times 10^{-20}$J.

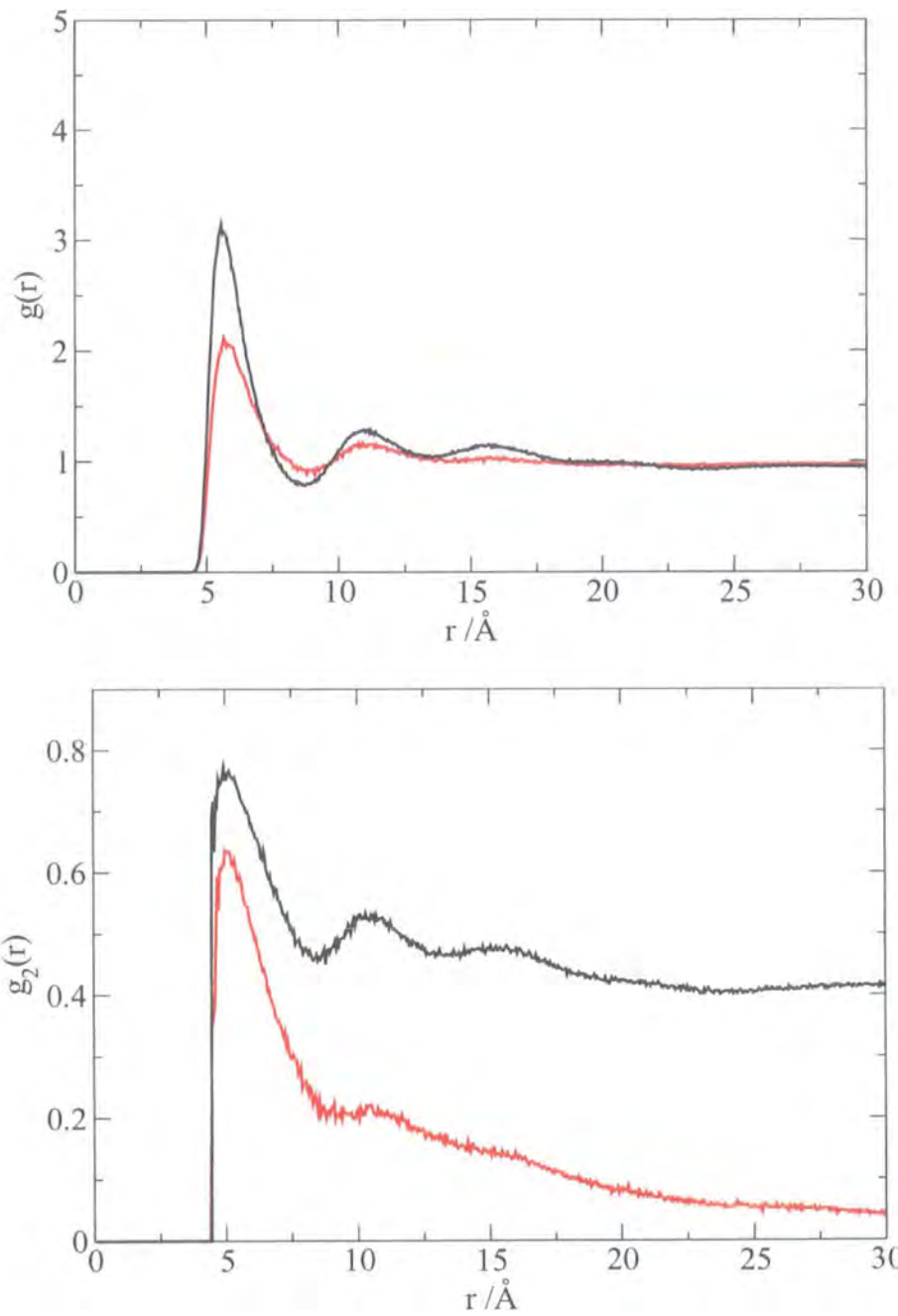

Figure 5.23: (a) Radial distribution function, $g(r)$ and (b) orientational correlation function, $g_2(r)$ for the state points at 350 K after annealing for 38 ns
The black line is the state point in the 0.2 $\times 10^{-20}$J potential and the red line is the state point without the external potential.

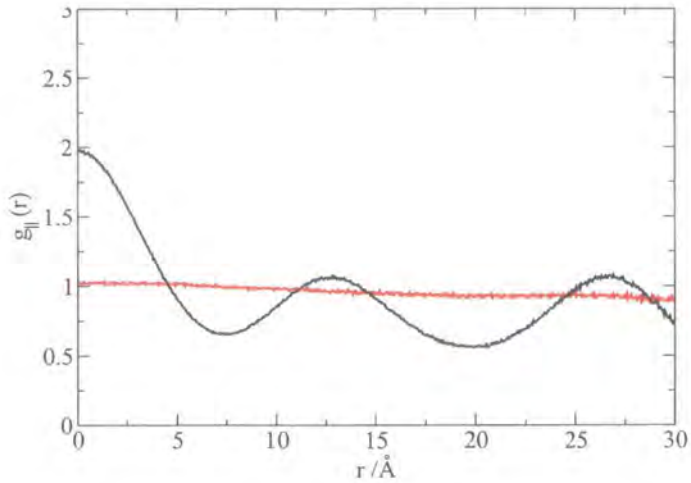

(a)

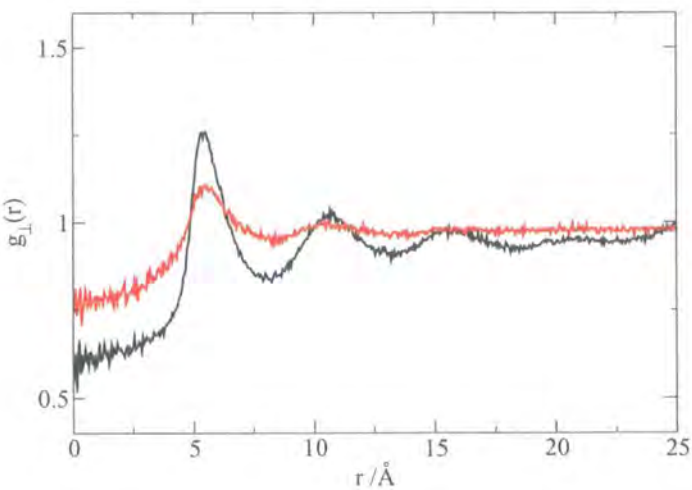

(b)

Figure 5.24: (a) Parallel and (b) perpendicular components of the radial distribution function, $g_{\parallel}(r)$ and $g_{\perp}(r)$ for the state points at 350 K after annealing for 38 ns. The black line is the state point in the 0.2 $\times 10^{-20}$J potential and the red line is the state point without the external potential.

(a)

(b)

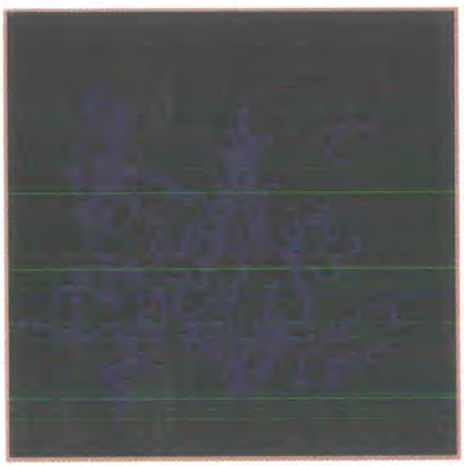

(c)

Figure 5.25: Snapshots of the 0.0 $\times 10^{-20}$J state point at 350 K split into parts. (a) the whole system, (b) the mesogenic units and (c) only the polymer backbone.

(a)

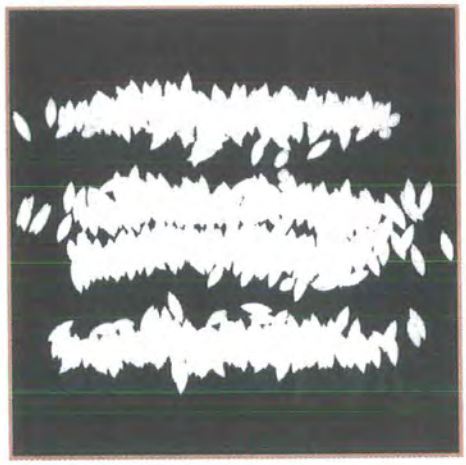

(b)

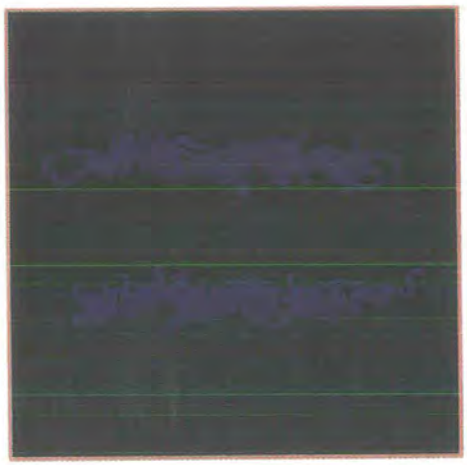

(c)

Figure 5.26: Snapshots of the 0.2 $\times 10^{-20}$J state point at 350 K split into parts. (a) the whole system, (b) the mesogenic units and (c) only the polymer backbone.

Temp. /K	Potential /$\times 10^{-20}$J	Time /ns	Starting point	Volume /Å^3 $\times 10^5(\pm 5\%)$	$< S_2 >$ (± 0.05)
300	0.0	28	300 K, 0.5 $\times 10^{-20}$J	4.55	0.616
350	0.0	34	350 K, 0.5 $\times 10^{-20}$J	4.79	0.614

Table 5.13: Summary of simulation data. Values of order parameter are for Gay-Berne sites, averaged over the last 2 ns of the simulation.

When the system is left at 350 K with a small field applied there is a significant rise in the order parameter. This suggests that there has been a change in the structure and that given a long enough time scale this small field causes the LC domains to align. The mesogens in these domains can be seen to stay in a nematic state rather than showing smectic ordering like the sample that was cooled in the larger field. Looking at radial distribution functions (Figures 5.23 and 5.24) and snapshots (Figure 5.26) together it is evident that polymer layers have formed, with a layer spacing of $\approx$ 2.6 Å. However, small peaks in $g_\perp(r)$ and the small peak in $g_\parallel(r)$ at 12.5 Å indicate that any smectic ordering within these layers is very weak. The structure of this phase is comparable with the phase formed in the larger field over a shorter timescale.

5.5.2 Switching the field off

To examine the stability of the phases formed and ensure that they are real mesophases and not merely artifacts of the applied fields further simulations were conducted with the field removed. A summary of these runs and their starting points is given in Table 5.13. These temperatures were chosen to ensure that there was still sufficient molecular movement to allow a relaxation of orientational order if desirable.

The order parameters over the course of the runs may be seen in Figure 5.27 for the 300 K and 350 K runs. In both simulations there is an initial drop in order parameter $\langle S_2 \rangle$ rapidly stabilizes at a value characteristic of a nematic liquid crystal (about 0.6). From these simulations it is clear that a stable orientationally ordered phase persists after the magnetic field is removed.

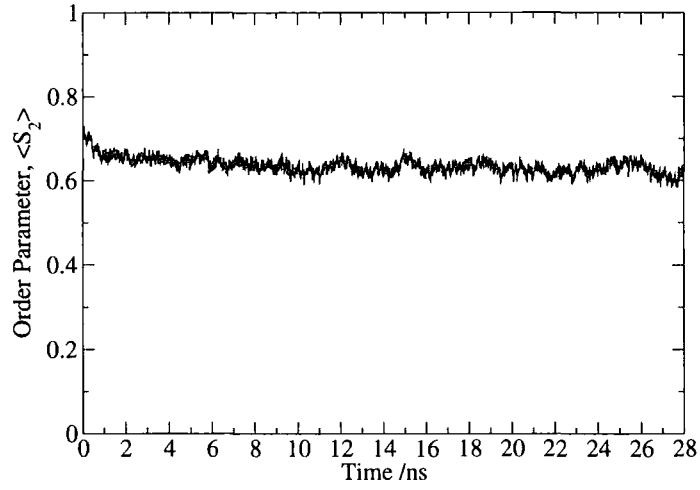

(a)

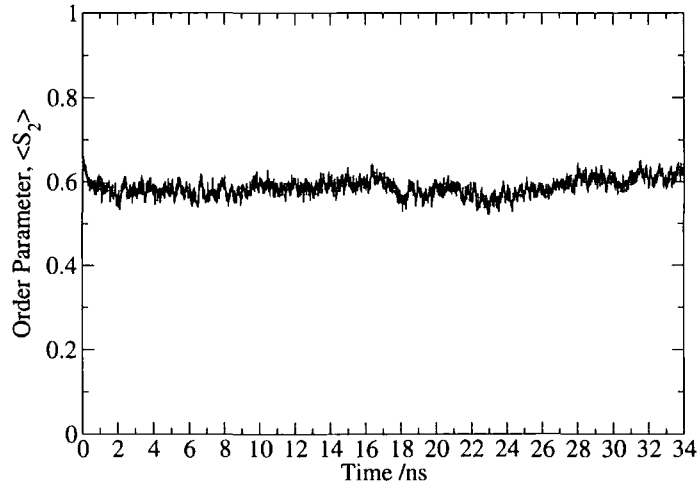

Figure 5.27: Order parameter at (a) 300 K and (b) for runs where the external potential is removed.

Temp. /K	Field /$\times 10^{-20}$J	Time /ns	Volume /Å^3 $\times$ 10^5($\pm$5%)	O.P. $< S_2 >$ ($\pm$0.05)
500	0.5	2	6.16	0.247
450	0.5	2	5.64	0.319
400	0.5	2	5.17	0.469
350	0.5	2	4.84	0.593
300	0.5	2	4.58	0.673
250	0.5	2	4.35	0.725
200	0.5	2	4.18	0.728

Table 5.14: Summary of simulation data for simulations cooled more rapidly. Values of order parameter are for Gay-Berne sites, averaged over the last 0.5 ns of the simulation.

The snapshots (Figures 5.28 and 5.28) reveal that the liquid crystal phase remains well-formed for both temperatures. At 300K the distinct smectic mesogenic bilayer persists. At 350K the ordering within the layers appears to be more nematic. The distribution functions in Figures 5.30-5.31 agree with these observations.

5.5.3 Increasing the Rate of Cooling

To investigate the influence of cooling rate, a further set of simulations was started from the isotropic melt at 500 K, cooling by 50 K each 2 ns. The value of the order parameter at each temperatures can be seen in Figure 5.32. The structure of the resultant phase is very similar to that in the earlier simulation that is cooled over a longer time.

The snapshots, in Figures 5.33 and 5.34, show similar stratified patterns emerging. However, the system has more defects and more nematic ordering seems to have been frozen in, in the cooling process. This causes the phases to be slightly less well aligned and less well ordered that in simulations that have been cooled more slowly. The distribution functions (Figures 5.35 and 5.36) show also that the system is more nematic in character. The parallel component of the radial distribution shows wider peaks and troughs, indicating that layers are less well formed, particularly at 350 K.

(a)

(b)

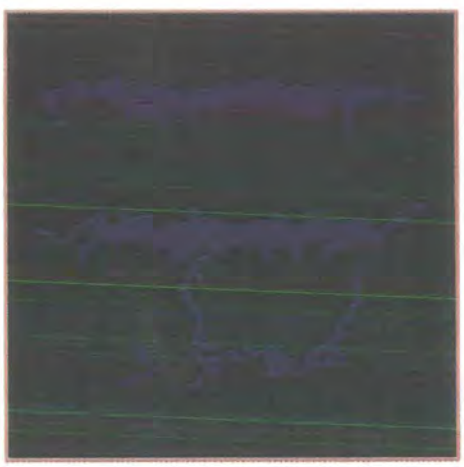

(c)

Figure 5.28: Snapshots of an aligned system after the field is removed at 300 K split into parts.
(a) the whole system, (b) the mesogenic units and (c) only the polymer backbone.

(a)

(b)

(c)

Figure 5.29: Snapshots of an aligned system after the field is removed at 350 K split into parts.
(a) the whole system, (b) the mesogenic units and (c) only the polymer backbone.

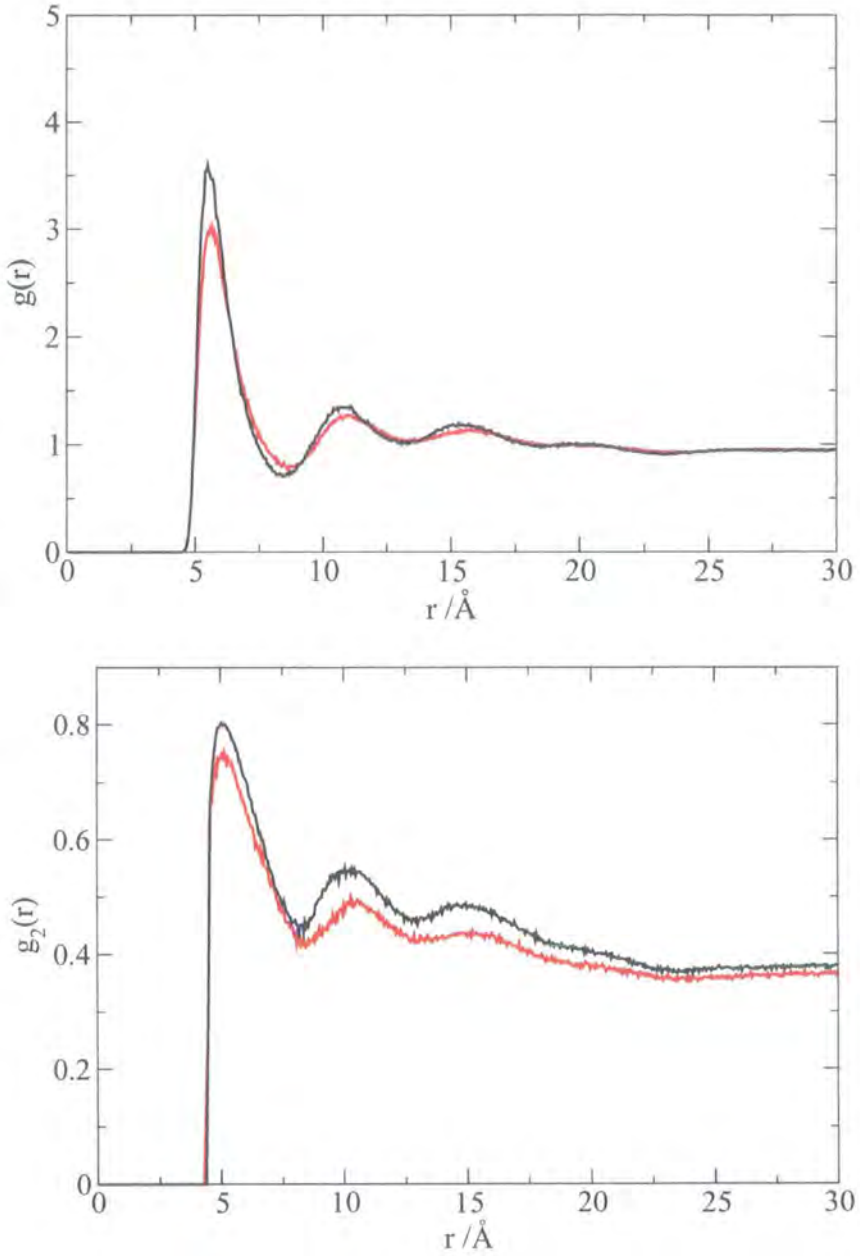

Figure 5.30: (a) Radial distribution function, *g(r)* and (b) orientational correlation function, $g_2(r)$ for simulations where the field has been removed.
The black line is the 300 K system. The red line is the 350 K system.

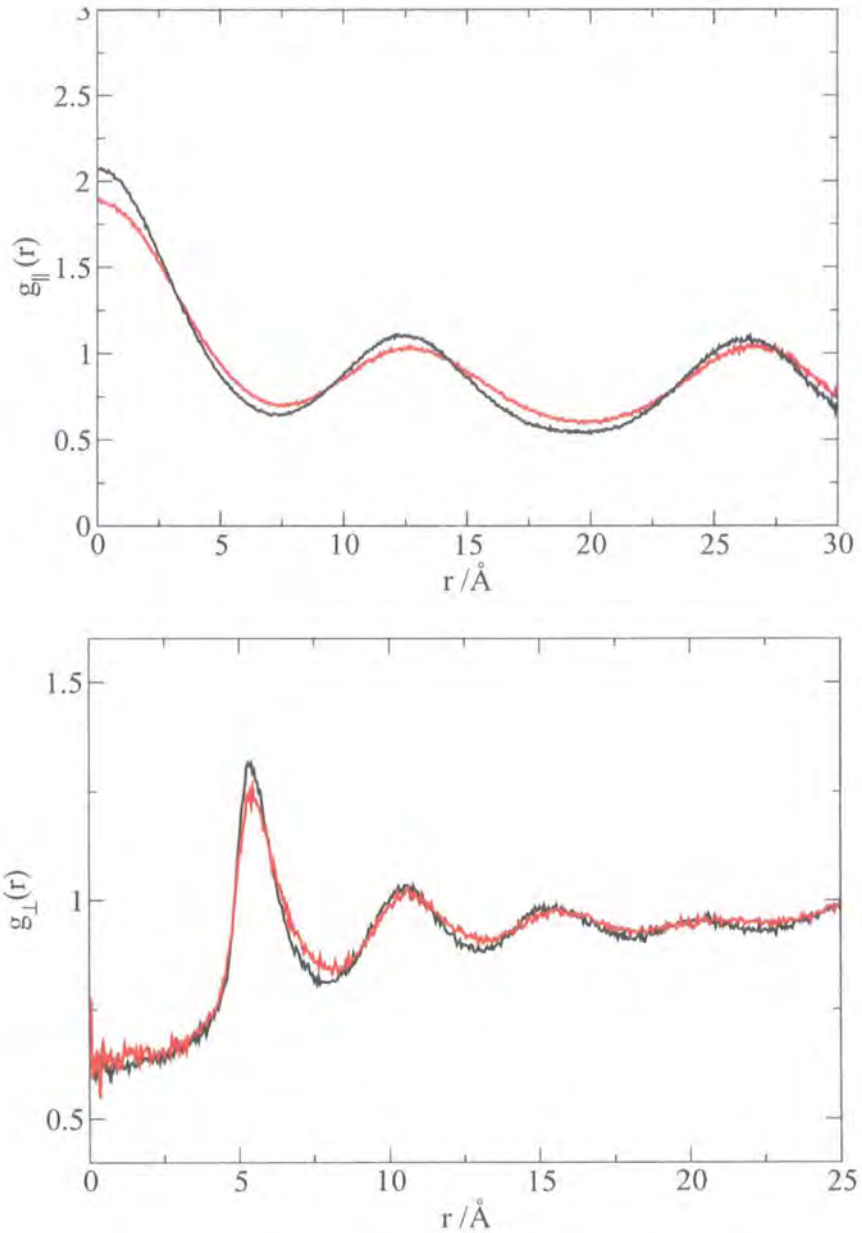

Figure 5.31: (a) Parallel and (b) perpendicular components of the radial distribution function, $g_{\parallel}(r)$ and $g_{\perp}(r)$ for a simulation where the field has been removed. The black line is the 300 K run and the red line is the 350 K run.

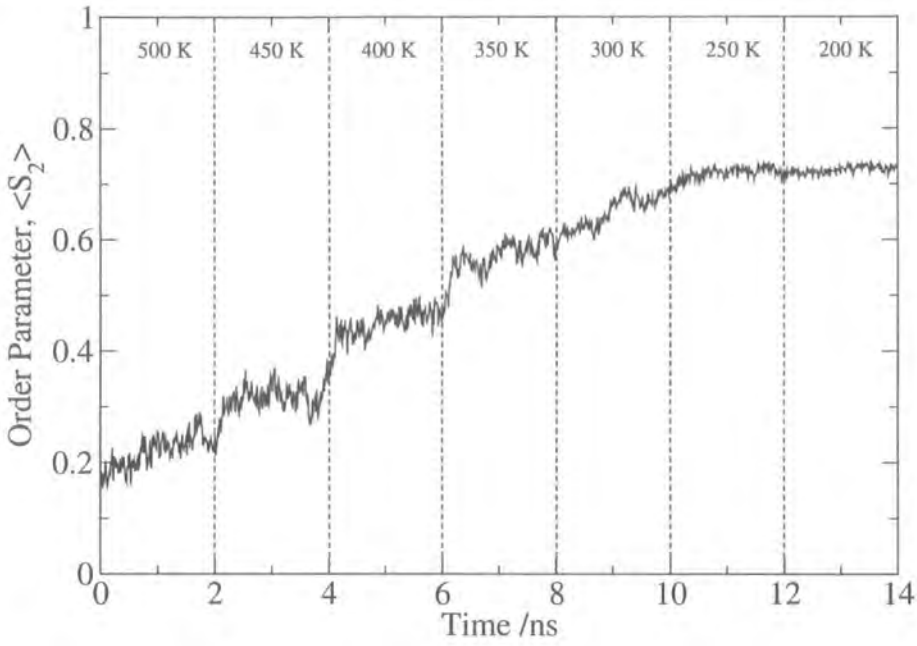

Figure 5.32: Order parameter for faster rate of cooling runs in a 0.2 $\times 10^{-20}$J potential.

However, the emergence of a series of peaks in $g_{\perp}(r)$ at 200 K indicates that at the lower temperatures smectic A ordering has started to emerge. It therefore seems that at low temperatures smectic ordering of the mesogens is preferred.

5.6 Conclusion

The work described in this chapter represents a detailed study into the phase behaviour of a SCLCP.

A number of phases have been observed: An isotropic liquid, an anisotropic liquid, and a phase separated LC phase. The LC structure seems to have taken two forms one in which the layers of mesogens have nematic order and another in which smectic layers are seen within the mesogen rich strata. All the systems show phase separation into mesogen rich and polymer rich regions prior to annealing. This separation leads to domains which have some nematogenic order, but these domains do not align to a common direction unless a magnetic field is applied. This microphase separation agrees with differential scanning calorimetry results from the

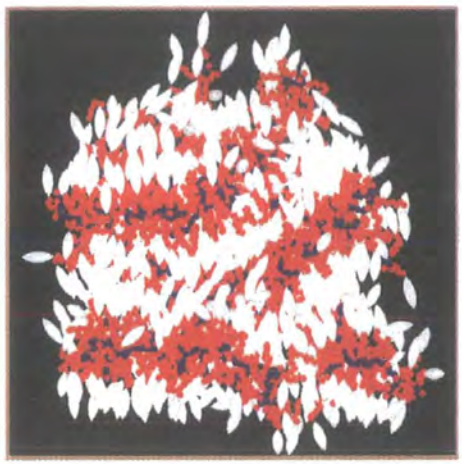

(a)

(b)

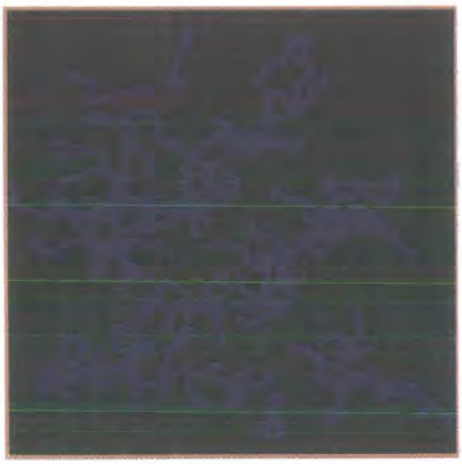

(c)

Figure 5.33: Snapshots of system cooled quickly with a 0.5 $\times 10^{-20}$J field at 350 K split into parts. a) the whole system, b) the mesogenic units and c) only the polymer backbone.

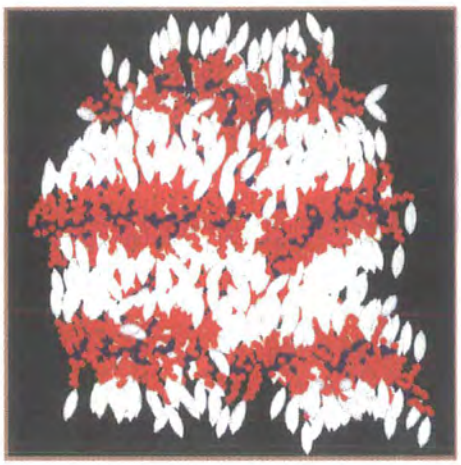

(a)

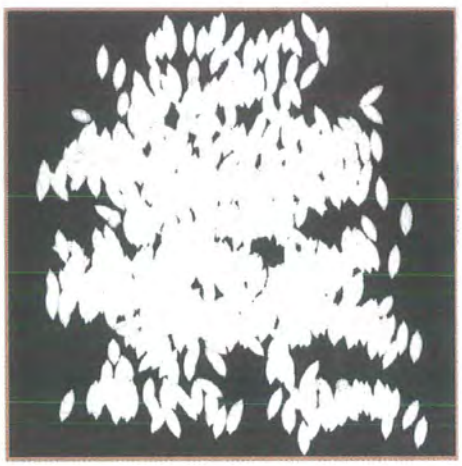

(b)

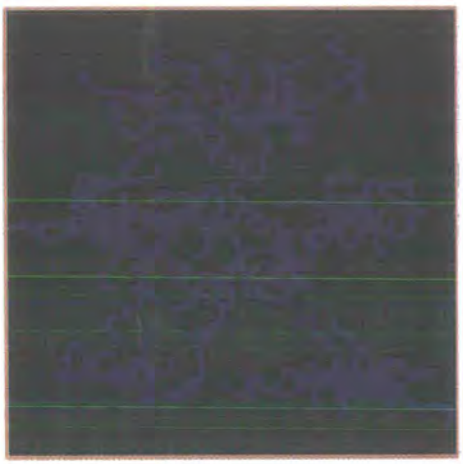

(c)

Figure 5.34: Snapshots of system cooled quickly with a 0.5 $\times 10^{-20}$J field at 200 K split into parts. a) the whole system, b) the mesogenic units and c) only the polymer backbone.

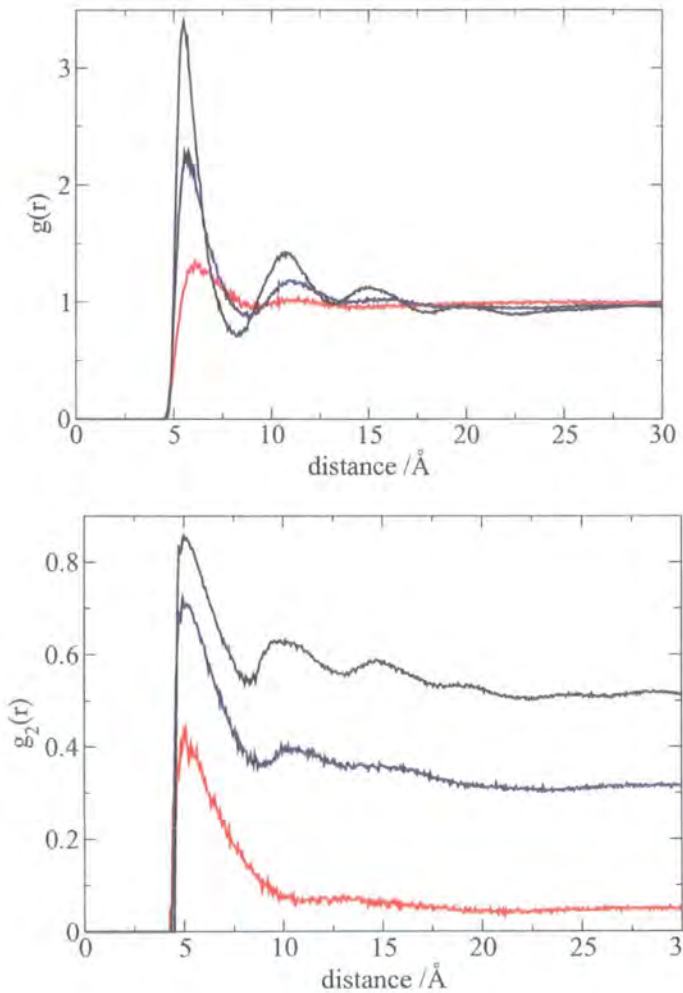

Figure 5.35: (a) Radial distribution function, *g(r)* and (b) orientational correlation function, $g_2(r)$ for the more rapidly cooled system.
The black line is the system at 200 K, the blue line is the system at 350 K and the red line is the system at 500 K.

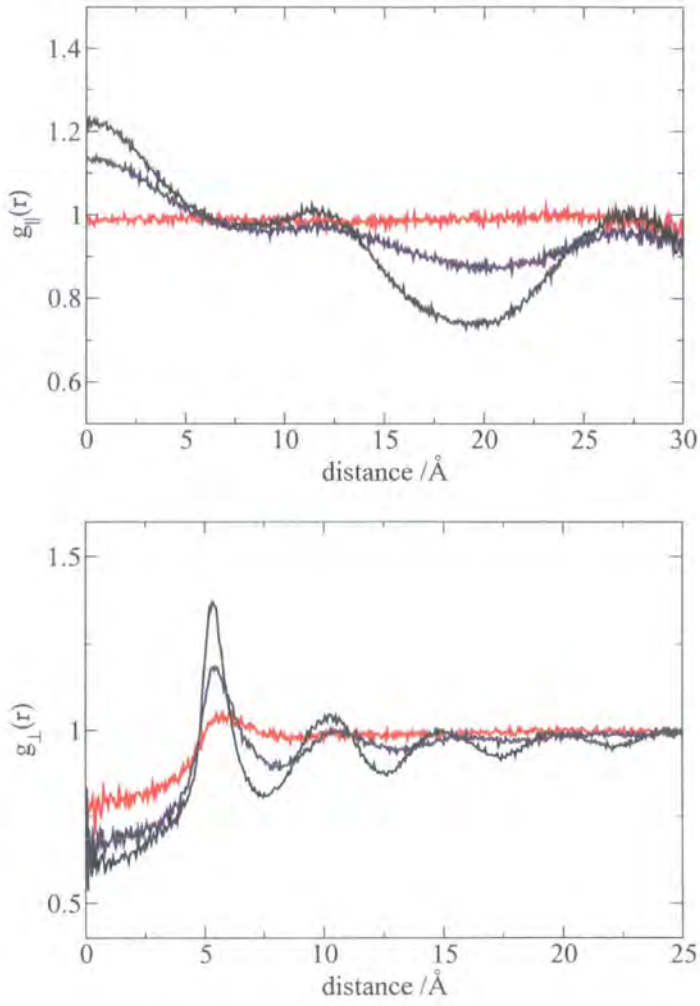

Figure 5.36: (a) Parallel and (b) perpendicular components of the radial distribution function, $g_{\parallel}(r)$ and $g_{\perp}(r)$ for the more rapidly cooled system.
The black line is the system at 200 K, the blue line is the system at 350 K and the red line is the system at 500 K.

work of Sarna *et al.* where SCLCPs were annealed over many hours and a splitting of the endotherm representing the transition to the mesophase was observed.[136]

Diffusion constant calculations show that diffusion is larger in the mesogenic domains. Unfortunately, the length of runs and the high viscosity of the mesophases means that it is difficult to cool the mesophases sufficiently slowly to measure the glass transition. If diffusion data were available for more temperatures it might be possible to see two slightly different transition temperatures to the glass: one for the polymer chains and the other for the mesogens.

On the application of a magnetic field the mesogenic domains align and a transition to a layered structure is observed. Some defects are possible with backbone chains spanning two layers. However, generally the ordering expels the polymer backbone from the mesogen rich regions. The exception is when a system is cooled quickly and the polymer is not able to be expelled quickly enough. These quickly cooled studies provide insight into the time frames in which the different parts of the system respond to the field. The need for this aligning potential agrees with the experimental observations of Ebbutt *et al.*[139] In this study a 9.4 T field was sufficient to align other polymer chains, but not a polysiloxane SCLCP with comparable degree of polymerisation to the simulation.

Two types of mesogenic ordering have been observed within the polymer layers. Nematic ordering of the mesogens occurs first on layer formation and nematic layers appear to be stable at higher temperatures in the stronger field. However, at lower temperatures smectic A ordering occurs and a mesogenic bilayer appears to be the stable structure.

From observing the phases formed from the state point studies, and the systems which are left for a long while with no field applied, it has to be noted that the phases formed in the first part of this study are probably not completely relaxed. For an accurate phase diagram to be mapped out (comparable to those now available for low molecular weight mesogens) simulations over longer times would need to be conducted. In this respect, the simulation problem is exactly analogous to the experimental problem where extremely viscous samples also require long times to relax (in some cases annealation times of several days are required). None the less,

the insights provided by this first simulation study of these polymers are extremely useful.

Chapter 6

Dendromesogen: Atomistic and Semi-Atomistic Studies

In this chapter a carbosilane dendrimer has been investigated in an attempt to understand its structure. Two models have been employed: a fully atomistic model, simulated using Monte Carlo techniques, in the gas phase with a nematic mean field applied. and a semi-atomistic model, which is similar in design to the model used in the SCLCP chapter. Gay-Berne sites are used to describe the mesogens and Lennard-Jones sites to describe the rest of the dendrimer. With the latter model we are able to investigate the changes in structure of the dendrimer as its molecular environment is changed by studying the dendrimer in a LC solvent.

6.1 Introduction

The series of dendrimers that are the focus of these studies consist of carbosilane cores with terminal alkyl chains that end in a cyanobiphenyl mesogens. The first five generations have been synthesized and the current understanding of the structure is based on characterization by X-ray diffraction studies. In Figure 6.1 the molecular structure of a first generation core and the terminal group that contains the mesogenic moiety are depicted. At the centre of these structures is a silicon atom with four branches coming off. These branches consist of three carbon alkyl chains that each connect to a silicon atom which becomes a new branch point. In Figure 6.1

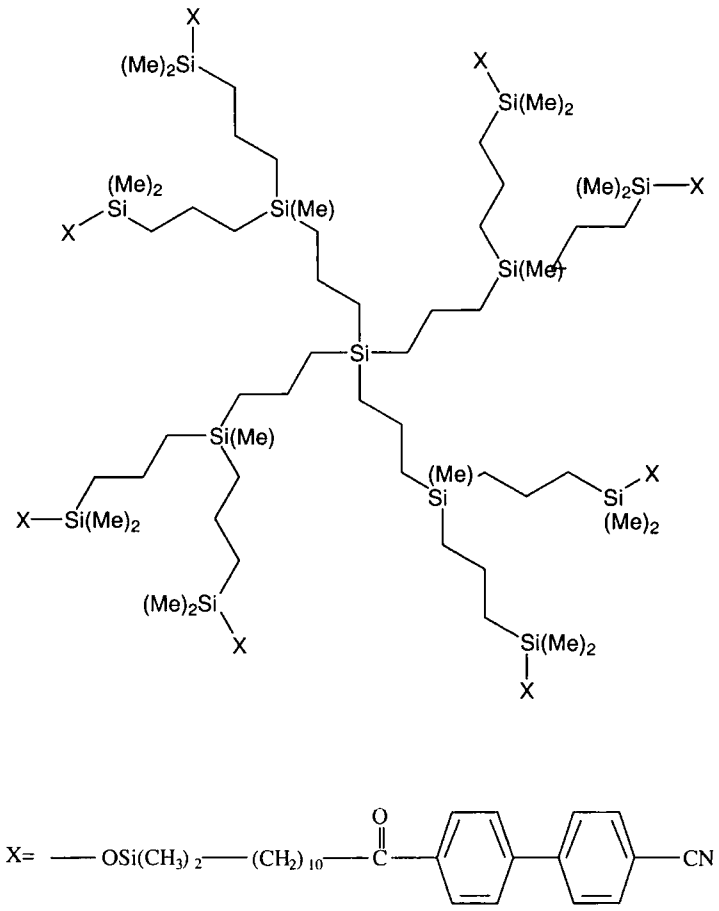

Figure 6.1: Molecular structure of a first generation carbosilane dendrimer.

X represents the sites where the terminal unit shown above is attached.

there is one layer of branch points as this is a first generation dendrimer. Therefore, the first generation has eight terminal groups. In the 2nd, 3rd, 4th and 5th generations there are 16, 32, 64 and 128 terminal groups respectively. A schematic representation of the generation three dendrimer is given in Figure 6.2.

It is evident that these dendrimer structures are very large. Table 6.1 records the numbers of atoms and bonds in each molecule of the first five generations. In this study the third generation of the dendrimer was chosen, as higher generations were considered too big to be studied at an atomistic level.

The experimental findings for these dendrimers suggested that they show interesting phase behaviour that has not been fully understood. As described in Section 3.4.3, the phases formed by dendromesogens are decided by the conforma-

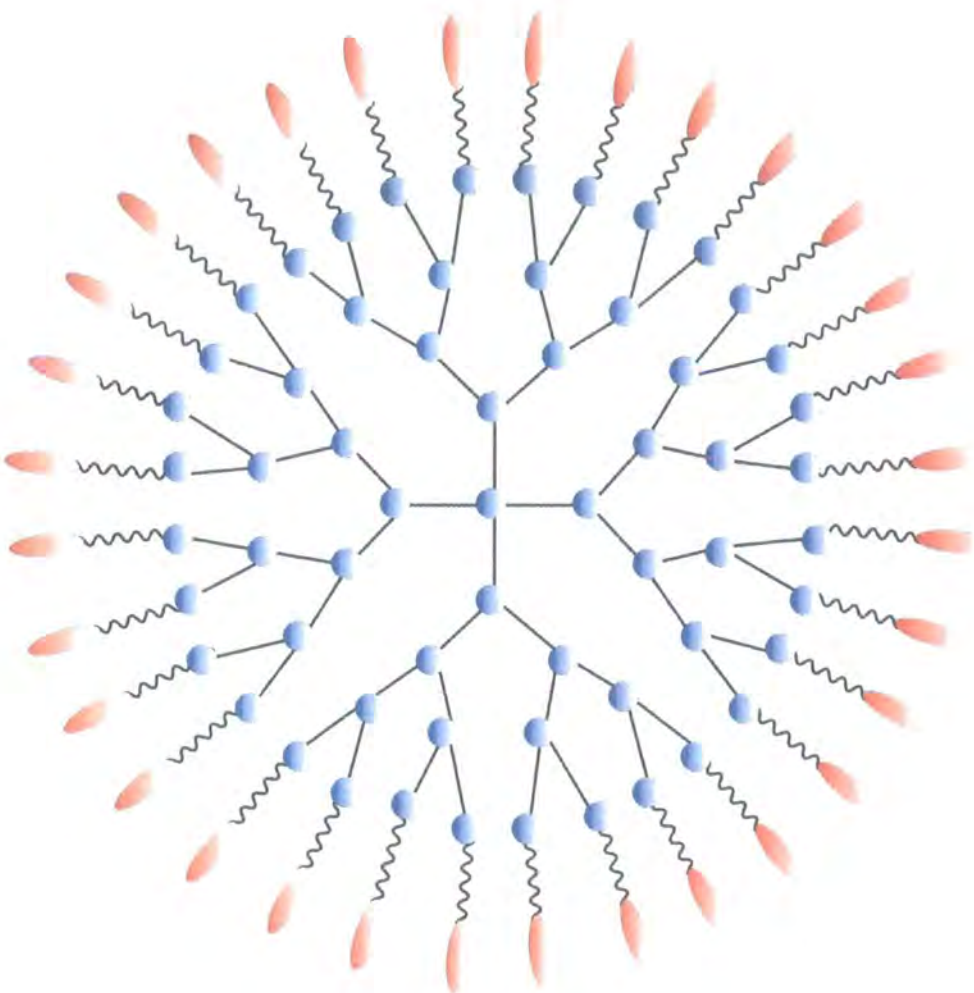

Figure 6.2: Schematic of the structure of a third generation dendrimer.

Generation	1^{st}	2^{nd}	3^{rd}	4^{th}	5^{th}
No. of atoms	721	1497	3049	6153	12361
No. of Bonds	736	1528	3112	6280	12616

Table 6.1: Number of atoms and bonds in each of the first five generations of the dendromesogen series.

tions adopted by individual molecules. The carbosilane systems studied herein are no exception; an interesting balance arises between the rod and disc based morphologies in these systems shown in Figure 6.3.[78,82] Richardson *et al.* characterized the first four dendrimers in the series by optical microscopy. The phase diagram, is shown in Figure 6.4.[80] The phases were characterized further by X-ray diffraction and differential scanning calorimetry. The samples were cooled in the presence of a 9.4 T magnetic field. Further work by Richardson *et al.* showed that for the 5th generation of the series the phase behaviour was different.[81] When cooled from the isotropic phase the following phases were observed,

$$\mathrm{Sm_A} \xrightarrow{40\,^\circ\mathrm{C}} \mathrm{D_{rec}} \xrightarrow{121\,^\circ\mathrm{C}} \mathrm{D_{hd}} \xrightarrow{126\,^\circ\mathrm{C}} \mathrm{i},$$

where, $\mathrm{D_{hd}}$ is a discotic phase with circular columns forming a hexagonal array, and $\mathrm{D_{rec}}$ has discotic columns that are ellipsoidal and so form a rectangular array. In the $\mathrm{Sm_A}$ the dendromesogen molecules are rod-shaped and form layers. Each of these phases is depicted in Figure 6.3, the smectic phases found can be interdigitated or non-interdigitated as shown. The interdigitation of mesogens was shown to increase with generation number. Later atomic force microscopy studies confirmed these morphologies.[79] The change that occurs between generation four and five that facilitates columnar phase formation is of great interest. The atomic force microscopy study indicated that the generation 5 morphology forms columnar domains. It has been suggested that the driving force for the formation of these columns is microphase separation and that there is a stronger interaction between mesogens in the same column than mesogenic units in different columns.

6.2 Atomistic Studies

This section describes a Monte-Carlo investigation of the LCDr structure using an atomistic model. Here every atom, including hydrogen atoms and those in the mesogenic groups, is represented by a Lennard-Jones site. The system investigated consisted of an isolated 3rd generation dendromesogen molecule in the gas phase.

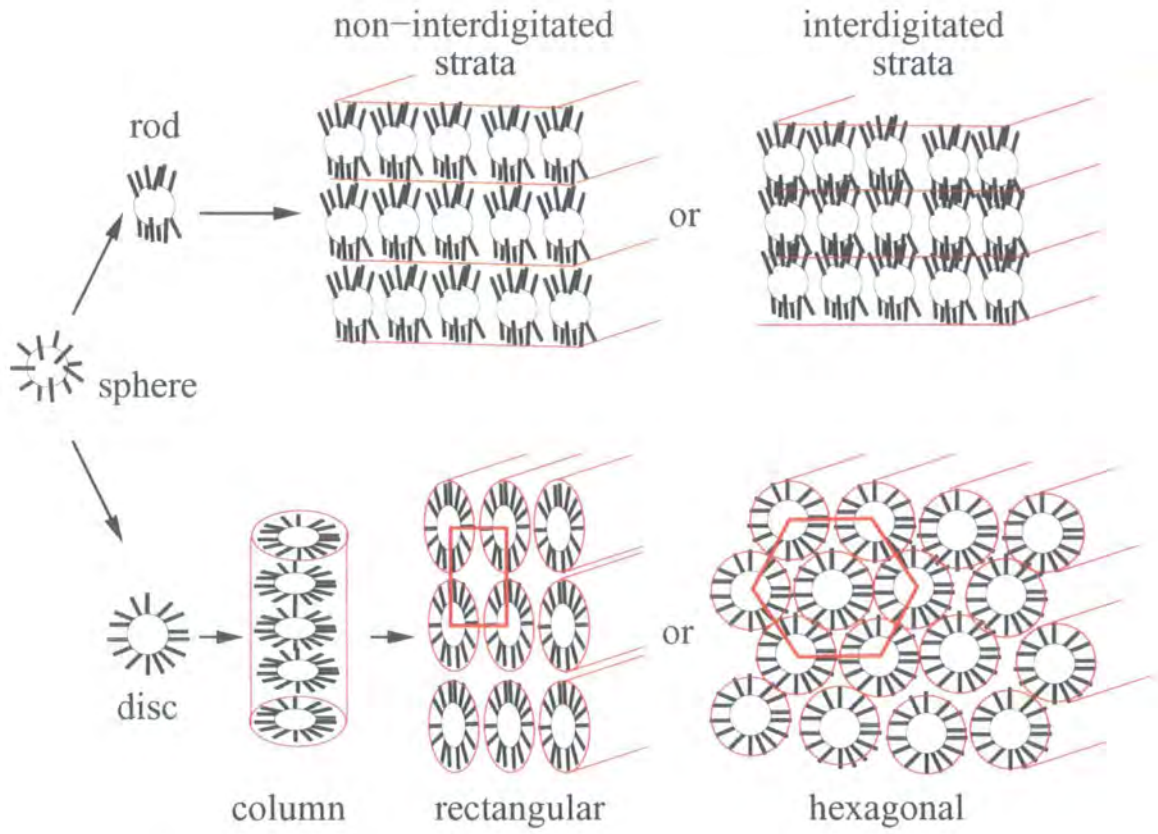

Figure 6.3: Schematic of possible conformational and morphological structures formed by the dendromesogens.

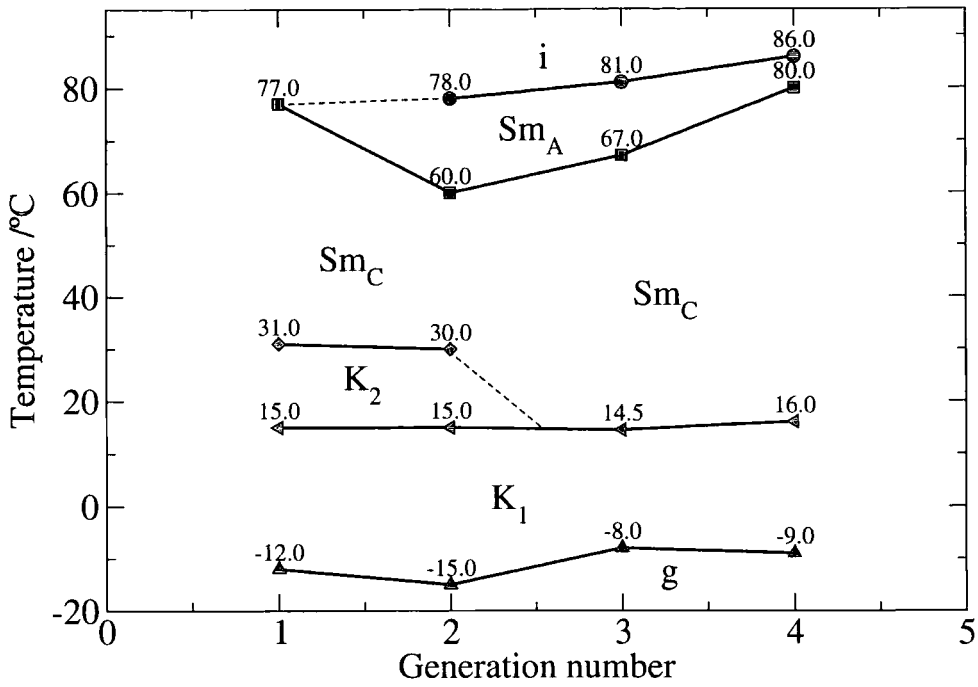

Figure 6.4: Phase diagram of a series of LCDrs.

K_1 and K_2 are crystalline phases (reproduced from[81]).

A mean field potential was applied to the mesogenic sites to emulate a nematic environment.

6.2.1 Building the Model

The structures were built using the Cerius[2] software. The cores were constructed first by fusing dendritic wedges together. When the structures were complete their energies were minimized, firstly using a specially adapted forcefield to expand the structure and make the interatomic spacing greater than necessary, then the universal forcefield was used to adjust the system back to a more realistic low energy configuration. In the specially adapted forcefield the mesogenic units are replaced by chlorine atoms with large van der Waals radii (14 Å) and large carbon-chlorine bond lengths of 5 Å. The chlorine radii and bond lengths subsequently changed back and further energy minimization performed. This expansion and contraction of the

Atom name	Mass /a.m.u.	σ_0 /Å	ϵ_0 /kcal mol^{-1}	Atom type
C	12.01	3.75	0.105	sp2 carbonyl carbon
CA	12.01	3.55	0.70	Benzene carbon
CT	12.01	3.50	0.066	Alkane carbon
CZ	12.01	3.65	0.15	Cyano carbon
HA	1.008	2.42	0.03	Benzene hydrogen
HC	1.008	2.5	0.03	Alkane hydrogen
HO	1.008	0.0	0.0	Mono-alcohol
NZ	14.01	3.20	0.17	Cyano nitrogen
O	16.00	2.96	0.21	Carbonyl oxygen
OS	16.00	2.9	0.17	Ester oxygen
OH	16.00	3.12	0.17	Mono-alcohol oxygen

Table 6.2: Key to atom types used in Tables 6.3 to 6.5 and non-bonding parameters.

molecular structure resulted in a structure with less overlaps and helped position the terminal groups at the surface of the dendrimer.

6.2.2 Parameterization

The atomistic model has been parameterized according to the liquid crystal force field (LCFF) proposed by Cook *et al.* based on the OPLS[149–151] force field. The atom types used are shown in Table 6.2. The silicon atoms in the carbosilane core were replaced with carbon atoms of the type found in alkanes (CT). Tables 6.3 to 6.5 show the bonding, angular and torsional parameters.

6.2.3 Simulation Procedure

The Monte Carlo simulations employed an internal co-ordinate approach in which the molecular geometry is stored in a Z-matrix. This method was detailed by Wilson in a study of low molecular weight liquid crystals.[152] The Z-matrix specifies the first atom (atom 1) at the origin of the coordinate frame; the second atom (atom 2) is then defined by its bond length to atom 1; the third atom (atom 3) by its bond length to atom 2 and the bond angle made with atoms 2 and 1; and the fourth atom (atom 4) in terms of a bond length to atom 3, an angle with atoms 3 and 2 and a dihedral atom with atoms 3, 2 and 1 . Subsequent atoms are defined by a bond

Bonding atoms		Length /Å
C	CA	1.490
C	O	1.229
CA	OS	1.364
C	OS	1.327
CA	CA	1.40
CA	CZ	1.451
CZ	NZ	1.157
CT	CT	1.529
CT	HC	1.09
CA	HA	1.08
CA	O	1.38
CT	OS	1.41
C	CT	1.522
CP	CP	1.40
CP	CA	1.40

Table 6.3: Bond lengths.

Atoms			Angle /°	K_θ /kcal mol^{-1}rad^{-2}
CA	CA	CZ	120.0	70.0
CA	CZ	NZ	180.0	150.0
CA	CA	OS	120.0	70.0
CA	CA	CA	120.0	63.0
CA	CA	HA	120.0	35.0
CT	CT	CT	112.7	58.35
CT	CT	C	112.7	58.35
CT	CT	HC	110.7	37.5
HC	CT	HC	107.8	33.0
O	C	OS	123.4	83.0
CA	OS	C	118.1	82.62
CT	C	O	120.4	80.0
CT	C	OS	120.4	80.0
C	CT	HC	109.5	35.0
OS	C	CT	111.4	81.0
CT	OS	CT	109.5	60.0
CT	CT	OS	109.0	50.0

Table 6.4: Bond angle parameters.

Dihedral				V_1	V_2	V_3
HC	CT	CT	HC	0.000	0.000	0.318
HC	CT	CT	CT	0.000	0.000	0.366
CT	CT	CT	CT	1.740	-0.157	0.279
C	OS	CA	CA	0.000	2.550	0.000
CA	CA	CA	CA	0.000	9.510	0.000
CA	CA	CA	HA	0.000	9.510	0.000
HA	CA	CA	HA	0.000	9.510	0.000
O	C	OS	CA	-0.635	3.681	1.529
CT	OS	CT	CT	0.650	-0.250	0.670
HC	CT	CT	OS	0.000	0.000	0.468

Table 6.5: Dihedral angle parameters in kcal mol^{-1}.

length, a bond angle and a dihedral angle to any three previously defined atoms. The construction of a Z-matrix is shown in Table 6.6.

Monte Carlo trial moves were generated by making a random change in an angle, θ_{bcn}, and a dihedral angle, ϕ_{abcn} to generate a new molecular geometry. The energies of these conformations are then compared and the move accepted or rejected according to the criteria set out in the Metropolis algorithm[131] (described in Section 4.2.2 and Figure 4.9 on Page 72).

In this work, for ease of calculation we constrain bond lengths. Also the ring structures have been frozen as changes in the angles and dihedral that define the rings result in severe disruption to the rest of the ring system. Furthermore, the cyano group which terminates each mesogenic moiety is frozen as depicted in Figure 6.5. The generation of the equilibrium should take into account any constraints on the system. However, the effect of the constraints is expected to be extremely small and therefore is not calculated.

The range of the changes made to the bond angles and dihedral angles to generate trial geometries was set to $-\theta^{max} < \theta_{\text{bcn}} < \theta^{max}$ and $-\phi^{max} < \phi_{\text{abcn}} < \phi^{max}$. The maximum displacements, θ^{max} and ϕ^{max} started as 5° and 10° respectively and were adjusted during the course of the simulation to ensure an acceptance ratio of between 35 and 50%. Ten percent of the trial moves were made so that the dihedral displacement was adjusted by ±60°. The energy change for trial movements in the core of the dendrimer means that they are much less likely than movements in

Atom no.	Bond length	Bond angle	Dihedral angle	Bonded atom	1,3 atom	1,4 atom
1						
2	l_{12}			1		
3	l_{23}	θ_{123}		2	1	
4	l_{34}	θ_{234}	ϕ_{1234}	3	2	1
⋮						
n	l_{cn}	θ_{bcn}	ϕ_{abcn}	c	b	a

Distances, l_{cn}, angles θ_{bcn} and dihedral angles ϕ_{abcn} are as shown:

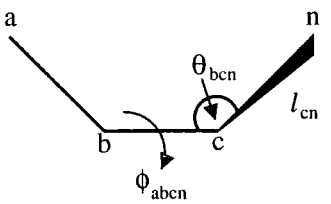

Table 6.6: Example of how a Z-matrix is constructed.

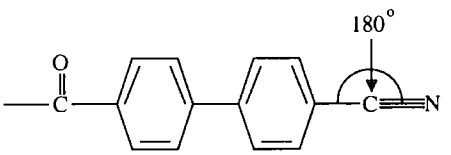

Figure 6.5: Cyano group constraint.

the rest of the molecule. However, this level of acceptance ratio was sufficient to guarantee some movement in the core.

The cartesian coordinates of any atom may be calculated from the coordinates of the preceding atom using the matrix equation

$$\begin{pmatrix} x_n \\ y_n \\ z_n \end{pmatrix} = \begin{pmatrix} x_c \\ y_c \\ z_c \end{pmatrix} + \mathbf{A}.\mathbf{T} \begin{pmatrix} l_{cn} \\ 0 \\ 0 \end{pmatrix}, \tag{6.1}$$

where the **T** matrix is defined in terms of the θ_{bcn} and ϕ_{abcn}

$$\mathbf{T}\left(\theta_{\text{bcn}}, \phi_{\text{abcn}}\right) = \begin{pmatrix} \cos\theta_{\text{bcn}} & \sin\theta_{\text{bcn}} & 0 \\ \sin\theta_{\text{bcn}}\cos\phi_{\text{abcn}} & -\cos\theta_{\text{bcn}}\cos\phi_{\text{abcn}} & \sin\phi_{\text{abcn}} \\ \sin\theta_{\text{bcn}}\sin\phi_{\text{abcn}} & -\cos\theta_{\text{bcn}}\sin\phi_{\text{abcn}} & \cos\phi_{\text{abcn}} \end{pmatrix}, \tag{6.2}$$

and **A** is a matrix that facilitates the rotation of the cartesian axes system onto the axis system that is defined in terms of atoms 1, 2, 3 and 4. This matrix is constructed in terms of the Euler angles θ, ϕ and ψ,

$$\mathbf{A}\left(\theta, \phi, \psi\right) = \begin{pmatrix} \cos\phi\cos\psi - \sin\phi\cos\theta\sin\psi & \sin\phi\cos\psi + \cos\phi\cos\theta\sin\psi & \sin\theta\sin\psi \\ -\cos\phi\sin\psi - \sin\phi\cos\theta\cos\psi & -\sin\phi\sin\psi + \cos\phi\cos\theta\cos\psi & \sin\theta\cos\psi \\ \sin\phi\sin\theta & -\cos\phi\sin\theta & \cos\theta \end{pmatrix}. \tag{6.3}$$

6.2.4 Nematic Mean Field

The size of the dendrimer molecule limits this atomistic simulation to one molecule, *i.e.* the gas phase. In an attempt to compensate for some of the influences of other molecules in the system the molecule has been coupled to a nematic mean field. This mean field is represented by a potential of mean torque that is conformationally dependent. The energy of a molecule in such a potential has been shown by Emsley *et al.* to be

$$U(\Gamma, \omega) = U_{int}(\Gamma) + U_{ext}(\Gamma, \omega), \tag{6.4}$$

where U_{int} and U_{ext} are the conformational energy and the energy due to the mean field respectively.[153] Γ describes a given configuration and ω is the orientation of the molecule. If Equation 6.4 is expanded in spherical harmonics, $C_{L,m}$,

$$U_{ext}(\Gamma, \beta\gamma) = -\sum{}' (-)^m \varepsilon_{L,m} C_{L,m}(\beta\gamma), \tag{6.5}$$

where $\varepsilon_{L,m}$ is an interaction tensor written in irreducible form, β and γ are spherical polar angles of the director and the prime denotes only even terms in the expansion

are kept. This expression truncated at $L = 2$ may be written as[154]

$$U_{ext}(\Gamma, \beta\gamma) = -\varepsilon_{2,0} P_2(\cos\beta) - \varepsilon_{2,2} \left(\frac{3}{2}\right)^{\frac{1}{2}} \sin^2\beta \cos 2\gamma, \tag{6.6}$$

where $\varepsilon_{2,0}$ and $\varepsilon_{2,2}$ can be related to the cartesian components of the interaction tensor such that,

$$\varepsilon_{2,0} = \left(\frac{2}{3}\right)^{\frac{1}{2}} \left(\varepsilon_{zz} - \frac{\varepsilon_{xx} - \varepsilon_{yy}}{2}\right), \tag{6.7}$$

and,

$$\varepsilon_{2,2} = \frac{\varepsilon_{xx} - \varepsilon_{yy}}{2}. \tag{6.8}$$

In this case only the $\cos\beta$ term is applied to the system. The calculation of the mean field potential is linked to the direction of the mesogens by the vector that lies along the C ≡ N bond. Potentials of $\epsilon = 0$, 5 and 10 kJ mol^{-1} were used in this study.

6.2.5 Experimental and Results

Simulations were conducted on the third generation LCDr at 400 K with potential strengths of 0, 5 and 10 kJ mol^{-1} and with a potential strength of 5 kJ mol^{-1} at 300 K, 350 K and 450 K.

Order parameter

The evolution of the order parameter for each system is given in Figures 6.6 and 6.7. It is evident that the mean field induces an increase in order parameter for the dendrimer. Statistically, as there are only 32 mesogens in this system, the order parameter of a randomly orientated system will be higher than for a larger size. Therefore, an order parameter of 0.2 for the system with no mean field applied effectively represents a randomly aligned system. For the largest field strength the mesogens have aligned to a level similar to a nematic liquid crystal system.

For a potential of 10 kJ mol^{-1} variation in temperature seems to have no great effect on the orientational order (Figure 6.7).

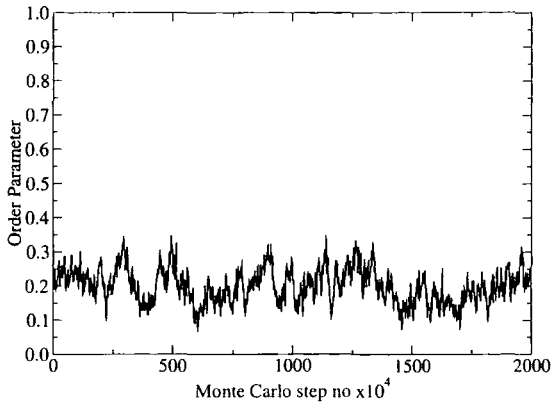

(a)

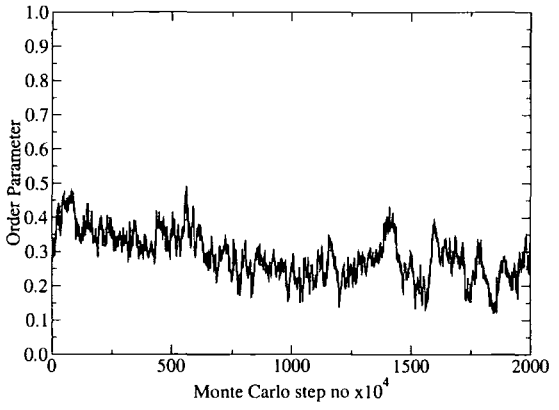

(b)

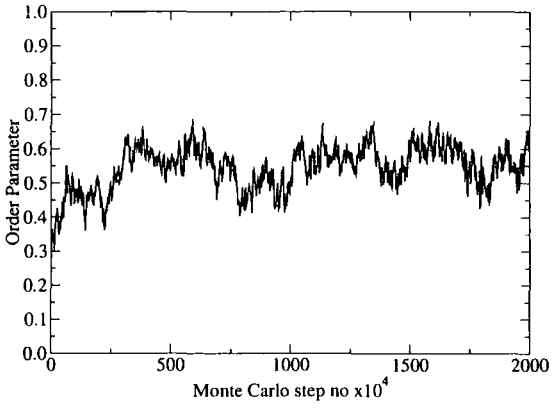

(c)

Figure 6.6: Evolution of order parameter for the dendrimer at 400 K, with a nematic mean field strength of (a) 0 kJmol^{-1}, (b) 5 kJ mol^{-1} (c) 10 kJ mol^{-1}.

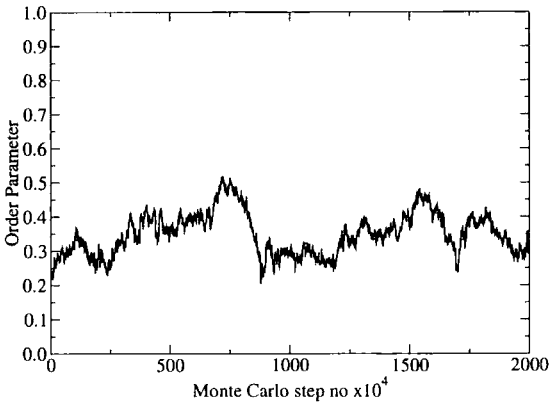

(a)

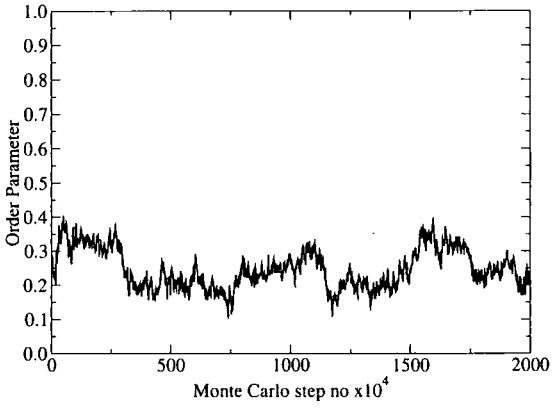

(b)

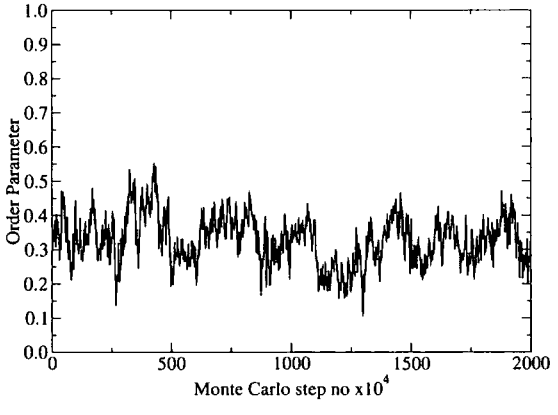

(c)

Figure 6.7: Evolution of order parameter for the dendrimer with a nematic mean field strength of 5 kJ mol^{-1} at (a) 300 K, (b) 350 K and (c) 450 K.

Equivalent Inertia Spheroid

The calculation of an equivalent inertia spheroid was used as a guide to the molecular shape of the dendromesogen. This spheroid has the same mass and moments of inertia as the molecule being investigated, but is of uniform mass density. For any molecule, an inertia tensor may be defined as

$$I_{\alpha\beta} = \sum_i m_i \left(r_i^2 \delta_{\alpha\beta} - r_{i\alpha} r_{i\beta} \right), \tag{6.9}$$

where $\alpha, \beta = x, y, z$, and m_i and r_i are the mass and distances, r_i are measured relative to the centre of mass. Diagonalization of this tensor gives the eigenvectors **a**, **b** and **c**, which correspond to the axes and eigenvalues I_{aa}, I_{bb} and I_{cc} which are the moments of inertia about those axes. A spheroid with axis lengths a, b and c and mass $M = \sum_i m_i$ has moments

$$I_{aa}/M = (b^2 + c^2)/5$$

and cyclic permutations thereof. Therefore,

$$a = \sqrt{[2.5\left(I_{bb} + I_{cc} - I_{aa}\right)/M]}, \tag{6.10}$$

$$b = \sqrt{[2.5\left(I_{aa} + I_{cc} - I_{bb}\right)/M]}, \tag{6.11}$$

and

$$c = \sqrt{[2.5\left(I_{aa} + I_{bb} - I_{cc}\right)/M]}. \tag{6.12}$$

Equations 6.10, 6.11 and 6.12 were used to calculate the molecular shape. The evolution of molecular axis lengths for each system are shown in Figure 6.8 and 6.9. The variation in the equivalent inertia spheroid with molecular shape is given in Table 6.7. In these figures there are regions that seem more prolate or oblate, but no overall pattern persists. There seem to be long time scale fluctuations between regions of different shapes. Table 6.8 shows the average values for the molecular axis lengths in each simulation. An example is seen in Figure 6.8c, where between 6×10^6 and 9×10^6 steps the molecule is disc-shape, but later, after 20×10^6 the

Shape	Condition
Sphere	a = b = c
Rod	a > b = c
Disc	a = b > c

Table 6.7: Relative molecular axis lengths for different molecular shapes.

Temp	Mean field potential	Molecular axes lengths /Å		
/K	ϵ /kJ mol^{-1}	a	b	c
300	5.0	25.70	22.74	19.14
350	5.0	26.11	27.75	19.25
400	0.0	25.66	23.21	20.20
400	5.0	24.83	23.00	21.52
400	10.0	26.59	22.42	19.57
450	5.0	27.02	23.34	19.19

Table 6.8: Summary of molecular axis lengths.

system switches to a rod-shape. As the axis lengths are similar, these rod and disc conformations are actually only slightly oblate or prolate.

Snapshots

Snapshots of the dendrimer at different stages of each simulation were made and compiled into movies, which allowed changes in conformation to be viewed as a function of simulation time. Example snapshots from these movies are given in Figures 6.10 and 6.11. The movies showed that the dendrimer was able to undergo rapid conformational change, with the mesogenic groups able to change orientation many times during the course of a simulation. In contrast to the central core of the dendrimer, the flexible chains had a high degree of conformational freedom, and this increased with temperature. Relatively small conformational changes in the chains

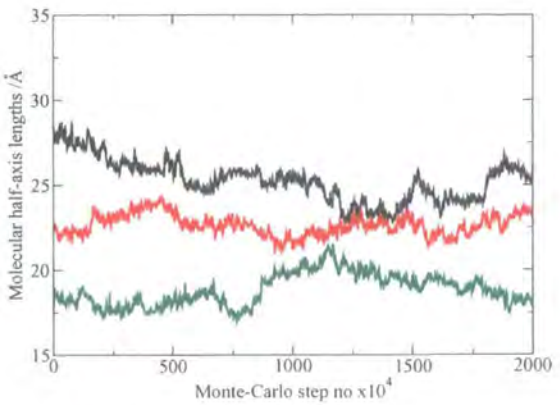

(a)

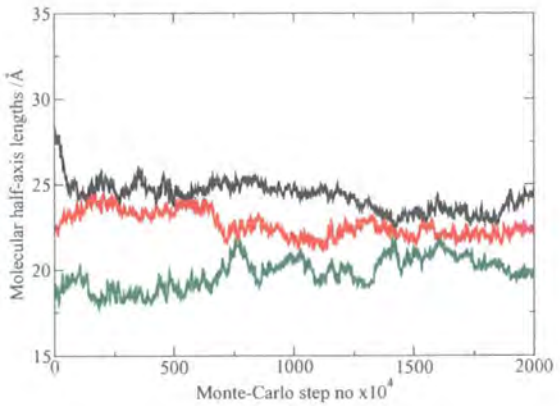

(b)

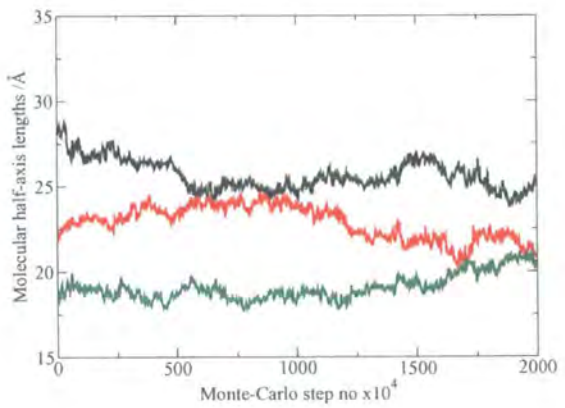

(c)

Figure 6.8: Evolution of molecular axis lengths for the dendrimer at 400 K, with a nematic mean field potential of (a) 0 kJmol^{-1}, (b) 5 kJ mol^{-1} (c) 10 kJ mol^{-1}.

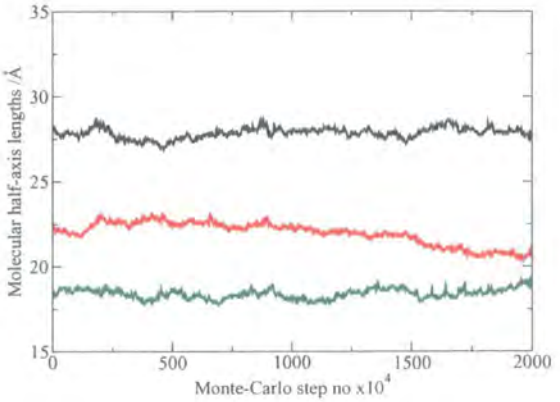

(a)

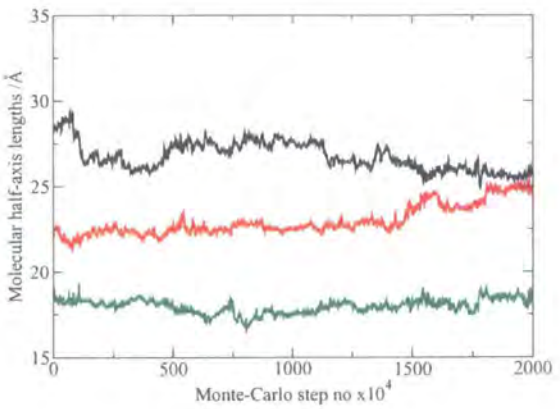

(b)

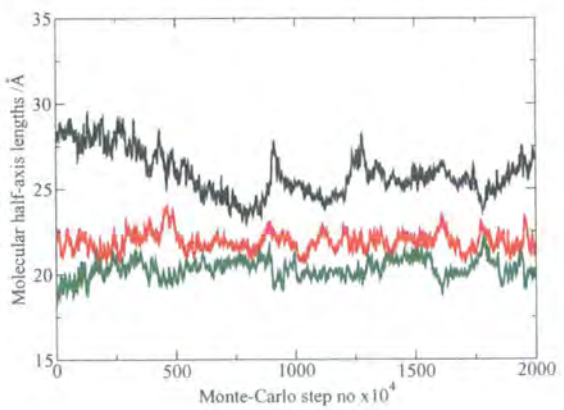

(c)

Figure 6.9: Evolution of molecular axis lengths for the dendrimer at with a nematic mean field potential of 5 kJ mol^{-1} at (a) 300 K, (b) 350 K and (c) 450 K.

were sufficient to transform the overall structure of the dendrimer from rod-shaped to a slightly flattened disc-shape.

The snapshot in Figure 6.10 is taken from the simulation in the largest mean field. This corresponds to a relatively large order parameter of $< S_2 >= 0.56$. The alignment of the cyanobiphenyl mesogenic groups is evident from the pictures. However, in the simulations there is no tendency for the dendrimer to form the characteristic rod shape that has been postulated as responsible for the formation of smectic layers in the bulk system (Figure 3.10 on Page 42).

6.2.6 Summary

In these atomistic simulations the conformations of the flexible spacers are able to rapidly change. Such effects cause changes in molecular shape. Despite alignment of mesogens in the $10\,\mathrm{kJ\,mol^{-1}}$ field this flexibility still allows the overall structure to fluctuate between slightly oblate and slightly prolate shapes. In addition to these fluctuations there are long time-scale changes. Therefore, regions of different molecular shapes occur during the course of the simulation. These long scale fluctuations mean that the lengths of simulation (20×10^6) are insufficient to get good averages for the semi-axis lengths a, b, and c. No evidence for the cylindrical rods, that are postulated to form smectic A layers, has been found.

6.3 Semi-Atomistic Studies

This work was carried out as part of a joint project with Dr. J. M. Ilnytskyi. All the initial work, model building and generation of starting co-ordinates was done by LMS and the the MD simulations were run by JMI.

6.3.1 Model

In order to reduce the computational demands of studying the dendrimer and thus facilitate simulations of a dendromesogen in a LC solvent a new model was generated on a semi-atomistic scale. On this scale hydrogen atoms can be neglected and mesogenic moieties replaced by single potentials. In this new model there were

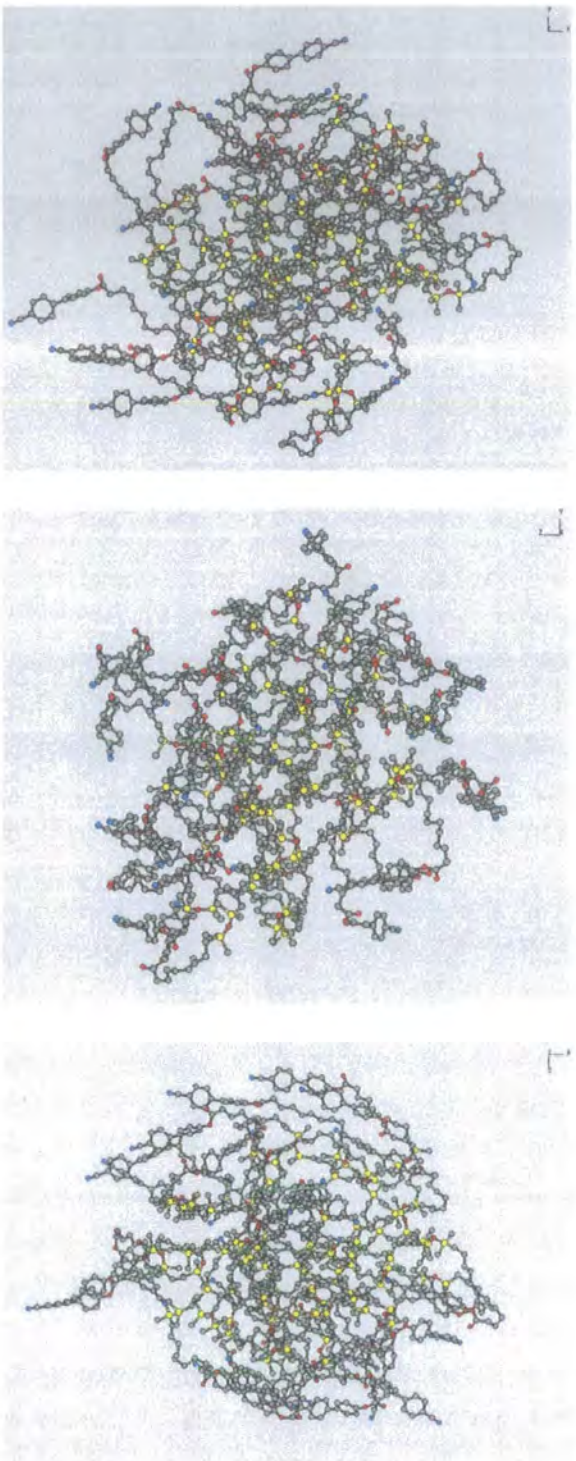

Figure 6.10: Snapshots from three orthogonal direction showing the LCDr, in a slightly oblate conformation, at 400 K with a 10 kJ mol^{-1}potential applied, after 7.50×10^6 MC steps.

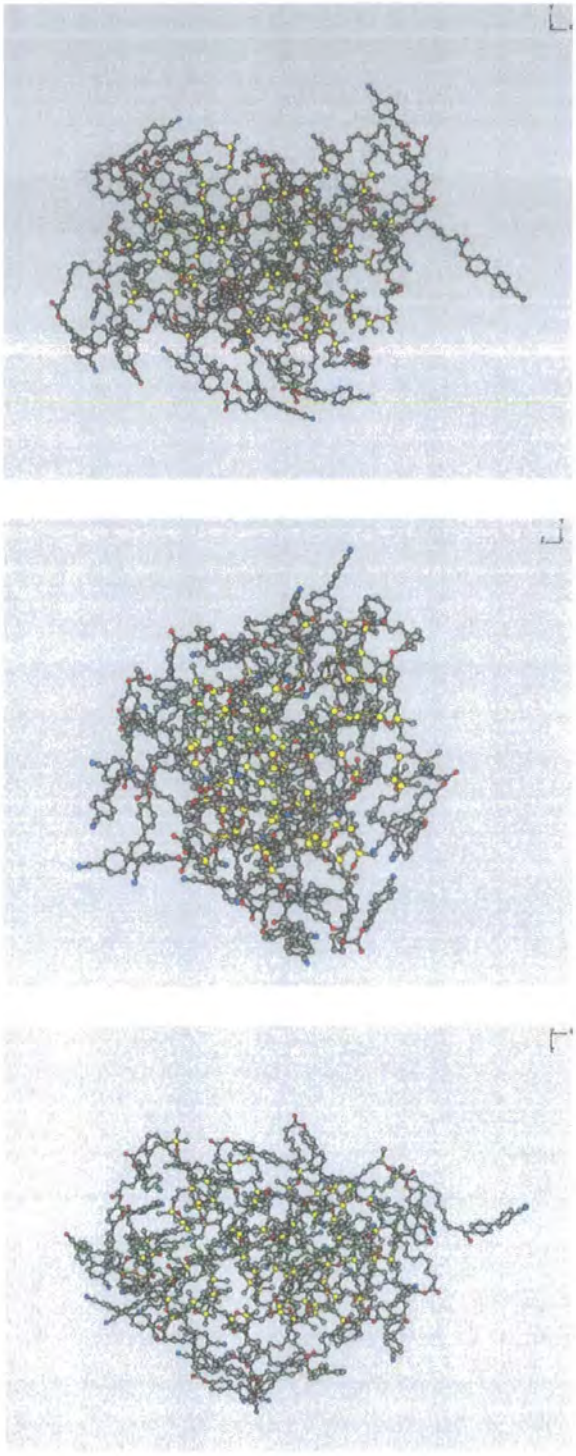

Figure 6.11: Snapshots from three orthogonal direction showing the LCDr, in a slightly prolate conformation, at 300 K with a 5 kJ mol^{-1}potential applied, after 20×10^6 MC steps.

781 united-atom Lennard-Jones sites and 32 Gay-Berne sites representing the 32 mesogenic groups. Figure 6.12 shows a schematic of the semi-atomistic dendrimer model.

The dendrimer was placed in a solvent modelled by 4732 GB sites. Although some of these molecules were removed before the dendrimer simulation runs commenced (as explained in Section 6.3.3). These sites were parameterized in the same way as the mesogenic moieties. A forcefield similar to that described in Chapter 5 for the SCLCP described in Section 5.2 on page 81, was used to describe the interactions of the molecule with itself and the solvent. However, the term relating to the contribution to the total energy from the dihedral angles was changed to the form,

$$E_{dihedrals} = \sum_{i=1}^{N_{dihedrals}} \left[a_{0i} + a_{1i}\cos\phi_i + a_{2i}\cos^2\phi_i + a_{3i}\cos^3\phi_i\right], \tag{6.13}$$

where ϕ_i is the dihedral angle and a_0, a_1, a_2 and a_3 are constants that parametrize the form of the potential for each type of dihedral angle.

The united atoms were represented by a Lennard-Jones site, all these sites were parameterized in the same way. All Gay-Berne sites had $\mu = 2$, $\nu = 1$, $\kappa = 3.5$, $\kappa' = 3$ and other parameters as shown in Table 6.9. Table 6.9 also contains parameters that describe the non-bonding, bonded, angular and torsional parameters. The two sets or torsional values refer to branched and non-branched torsions; the primes indicate a branched torsion. All these parameters are taken from the work of Vlugt *et al.* which calculated appropriate parameters for branched and non-branched alkanes.[155] Cut-offs for the potentials are given in Table 6.10.

6.3.2 Building the Model

Although it may have been possible to generate the semi-atomistic topology from the atomistic Monte Carlo Z-matrix by stripping hydrogen atoms and replacing mesogenic sites with one Gay-Berne site it is difficult to generate the correct topology information this way. Therefore, the molecular structure was rebuilt from scratch.

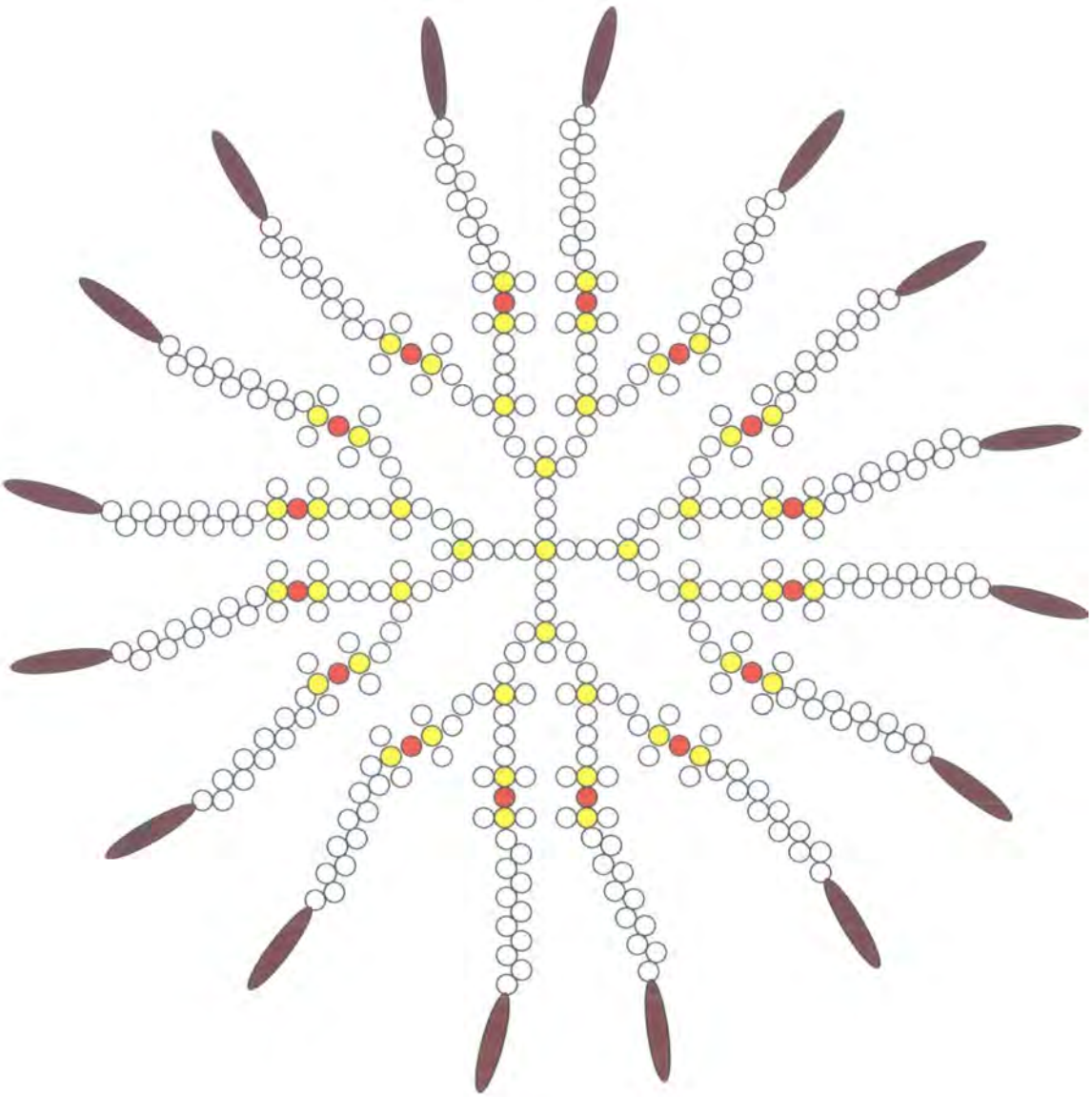

Figure 6.12: Schematic representation of a semi-atomistic dendrimer.
To simplify the picture a smaller 2nd generation is depicted. The circles represent LJ sites (grey for carbon, yellow for silicon and red for oxygen) and the ellipses GB sites.

Parameter	Value
Mass (GB)	$2.9557968 \times 10^{-25}$ kg
Inertia (GB)	0.27305×10^{-23} kg rad^{-2}
Mass (LJ)	$0.2324784 \times 10^{-25}$ kg
$\epsilon_0^{GB}/k_b = \epsilon_{ee}/k_b$	406.51 K
$\epsilon_0^{GB/LJ}/k_b$	138.37 K
ϵ_0^{LJ}/k_b	47.13 K
$\sigma_0^{GB} = \sigma_{ss}$	3.829 Å
$\sigma_0^{GB/LJ}$	3.88 Å
σ_0^{LJ}	3.93 Å
GB angle	0.0 °
GB angle force constant	86.44 J rad^{-2}
l_b^{LJ-LJ}	1.53 Å
$l_b^{LJ/GB}$	7.46 Å
k^{bond}	361.291 J Å^{-2}
θ_{eq}	113 °
k^{ang}	86.29 J rad^{-2}
a_0/k_b	1009.728 K
a_1/k_b	2018.446 K
a_2/k_b	136.341 K
a_3/k_b	-3164.52 K
a_0'/k_b	1.394 K
a_1'/k_b	2.787 K
a_2'/k_b	0.188 K
a_3'/k_b	-4.369 K

Table 6.9: Other Parameters.

Interaction	LJ/LJ	LJ/GB	GB/GB
Potential cutoff /Å	9.8	22.0	16.5
Verlet list cutoff /Å	10.8	24.2	18.15

Table 6.10: Potential and Verlet cutoffs.

Two useful characteristics for the numbering of atoms in the semi-atomistic topology are sequentially numbered branches to facilitate the analysis of molecular fragments and grouping of all mesogenic sites at the end of the topology. The mesogens must also be at the surface of the molecule to make replacement with Gay-Berne sites easier. The configuration was generated as a branched network, starting from a central tetrahedral silicon atom and using a geometric algorithm to build up a dendritic structure. This algorithm is summarized in the flow diagram in Figure 6.13.

Even with careful growth it proved impossible to completely eliminate close contacts between atoms. Consequently this input was used as a starting point for the Monte Carlo program. Monte Carlo runs were used to eliminate close contacts and overlaps. In these runs, a set of fused LJ sites was used to replace the Gay-Berne particle. A high negative charge on these sites ensured that the mesogens repelled each other to form a convenient spherical starting configuration for the dendrimer. Finally hydrogen atoms were stripped from the structure and the rod of LJs was replaced by a Gay-Berne site with the orientation vector of the Gay Berne taken from the direction of the LJ rod. Hence, a conveniently labeled topology file with GBs at the end was produced with suitable co-ordinates for input into the GBMOL-DD[156] program.

6.3.3 Molecular Dynamics Simulations

Procedure

The MD simulations for this model were carried out by JMI. Here the results are described briefly. The information gained from these studies was used to help design the coarse grain study in Chapter 7.

Two simulations of a solvated dendrimer molecule were conducted, one with the solvent in a nematic phase and one with the solvent in a smectic A phase. The nematic and smectic solvents were formed by MD simulations at 400 K and reduced density, $\rho^* = N\left(\sigma^{GB}\right)^3/V$, of 0.2505 and 0.2608 respectively. These equilibrations started from a lattice of the Gay-Berne sites and were achieved over 1 ns with a 3

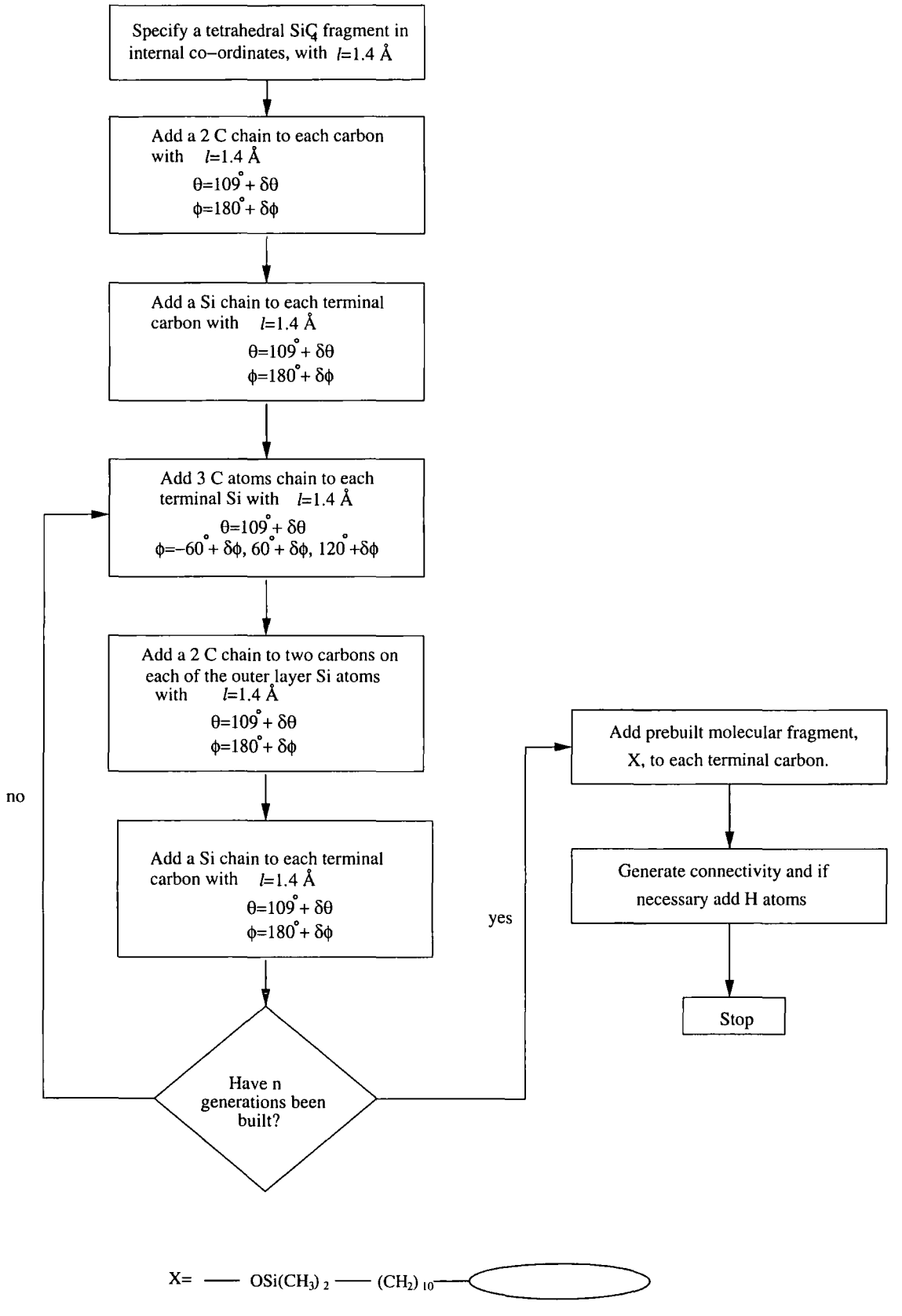

Figure 6.13: Flowchart showing the building of a LCDr. Here, $\delta\theta$ and $\delta\phi$ are random values that change at each step in the range 0 – 3° which prevent atomic sites from being co-incident with each other.

fs timestep. When the dendrimer was introduced to the simulation box any solvent molecules that overlapped with the dendrimer sites were removed. The simulations were then continued for a further 3-4 ns under the same conditions for the equilibrium of that solvent system.

Results

A number of order parameters for the nematic and smectic systems have been calculated:

- S_{solv}, the order parameter of the solvent.
- S_{mix}, the order parameter of the dendritic mesogens and the solvent.
- S_{den}, the order parameter of the dendritic mesogens relative to the director of the dendritic mesogens.
- $S_{\text{d/s}}$, the order parameter of the dendritic mesogens relative to the director of the solvent.

S_{mix} approximates to S_{solv} as the number of dendritic mesogens is very small compared to the solvent.

The evolution of these order parameters during the course of the experiments is shown in Figures 6.14 and 6.16. In each of these studies the dendrimer is introduced after 1 ns. Snapshots of the systems when the dendrimer is added, after a short time and when equilibrium is reached are shown in Figures 6.15 and 6.17.

In the nematic solvent, there is a small initial drop in the order parameter S_{solv} owing to disruption by the dendrimer. As the system re-equilibrates S_{solv} reaches a level just below that from before the solute molecule is added. $S_{\text{d/s}}$ and S_{den} gradually rise to a level approximately equal to that of S_{solv} (Figure 6.14). The process of the dendrimer aligning is seen in the snapshots. At first, the dendrimer has small gaps due to eliminated solvent molecules, then these are filled by the solvent and finally the dendrimer aligns. As well as the alignment of the mesogens it is evident that the whole dendrimer molecule changes from a more spherical shape (in isolation) to an elongated spheroid on immersion in the solvent (Figure 6.15).

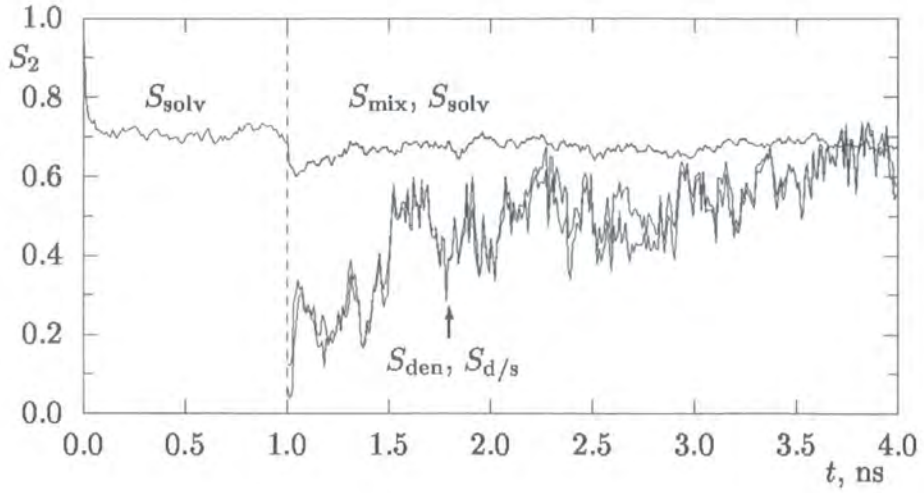

Figure 6.14: Evolution of the order parameter, S_2, for a dendrimer in a nematic solvent.
S_{solv}, S_{mix}, $S_{den}$and $S_{d/s}$ are the order parameters for the solvent molecules, all the GB sites, the dendrimer mesogens and the dendrimer mesogens with respect to the director of the solvent respectively.

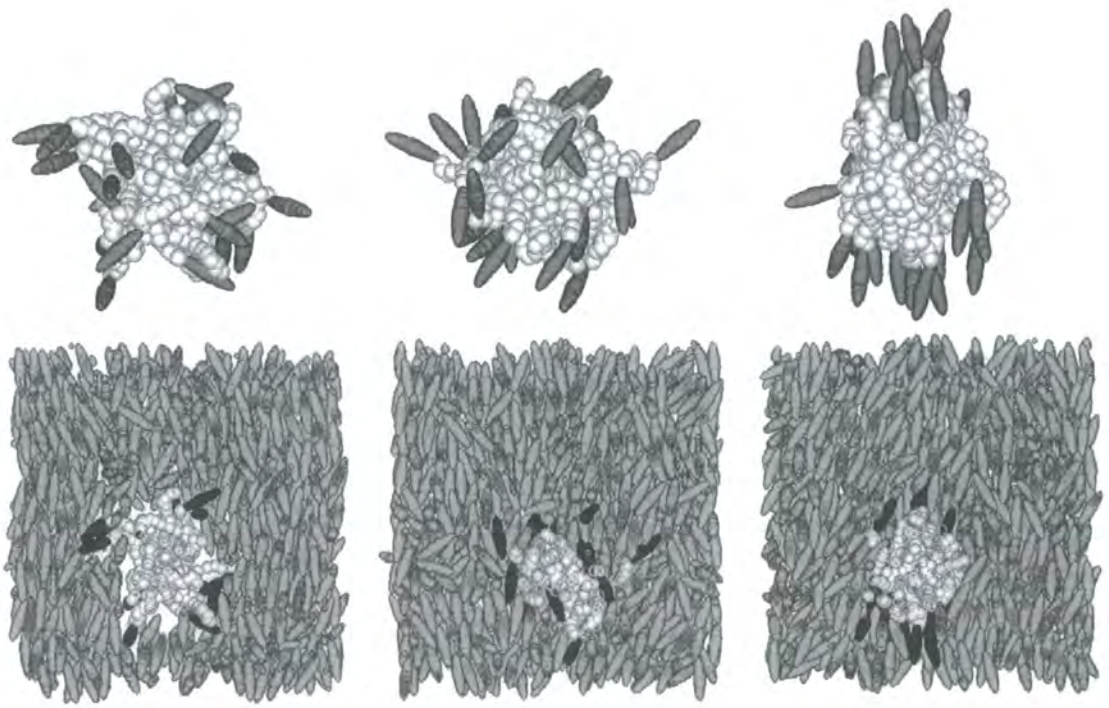

Figure 6.15: Snapshots of the dendrimer structure in a nematic solvent at t = 1, 2 and 4 ns.

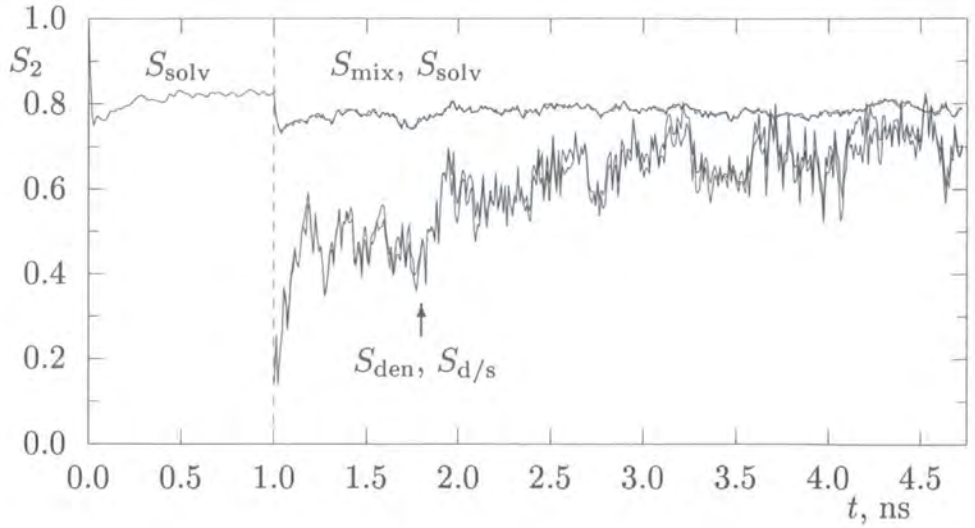

Figure 6.16: Evolution of the order parameter, S_2, for a dendrimer in a smectic solvent.
S_{solv}, S_{mix}, $S_{\text{den}}$and $S_{\text{d/s}}$ are the order parameters for the solvent molecules, all the GB sites, the dendrimer mesogens and the dendrimer mesogens with respect to the director of the solvent respectively.

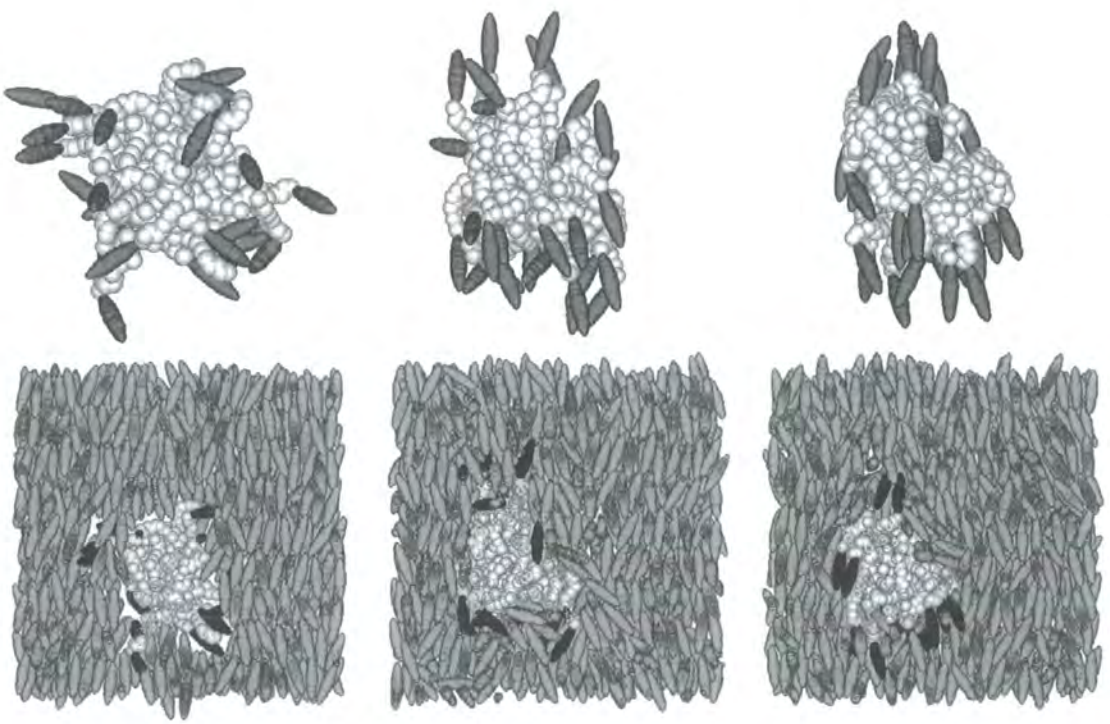

Figure 6.17: Snapshots of the dendrimer structure in a smectic solvent at t = 1, 2 and 4.5 ns.

Similar effects are seen in the smectic solvent. The initial rise in the order parameters of the dendrimer, $S_{d/s}$ and S_{den}, is slightly faster than that from the nematic solvent. However, equilibration takes slightly longer and results for $S_{d/s}$ and S_{den} are slightly lower than S_{mix} and S_{solv} (Figure 6.16). The snapshots in Figure 6.17 shed some light on these changes. Like the nematic system, the first pictures show the spherical dendrimer with some gaps from solvent molecules that have been removed. After some time the solvent fills in and the dendrimer seems to have become nematic-like, finally as the simulation continues the dendritic mesogens adjust such that they lie in the smectic layers. The mesogens attached to the dendrimer span five different smectic layers of the solvent.

In Figure 6.18 the various generations of the core are depicted along with a snapshot of the whole molecule. This figure also shows how much penetration of the solvent there is into different layers of the dendrimer. This shows how the solvent substantially penetrates the volume of the outer regions of the dendromesogen. However, the level of deeper penetration into the core of the dendrimer is very slight for the 3rd generation of core and minimal for the second generation of core. The levels of penetration do not alter much depending on the solvent.

6.4 Conclusions

From these studies of the LCDr important structural information has been obtained.

In atomistic studies of a single, gas phase dendromesogen flexibility in the alkyl spacers, which link the mesogens to the core, enable the structure to change rapidly. In mean fields this flexibility leads to alignment of mesogens. However, the overall molecular structure is still free to change between slightly oblate and prolate conformations.

In the semi-atomistic solution phase studies the dendritic mesogens seem to adopt the ordering of the surrounding solvent molecules. When the solvent is in a nematic phase the dendritic core becomes elongated and the mesogens align parallel to the director of the solvent. In a smectic solvent the mesogens align and then

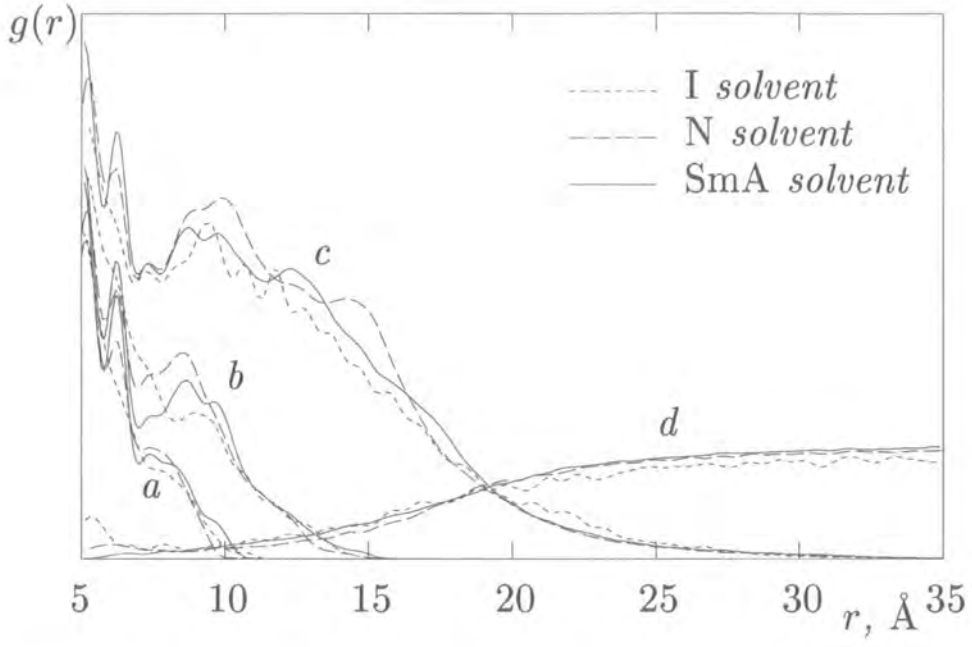

The sets of lines represent (a) second and (b) third generations of the core and (c) the whole dendrimer and (d) the solvent molecules. The relative sizes of the 1st, 2nd and 3rd generations of the core are shown with the whole dendrimer:

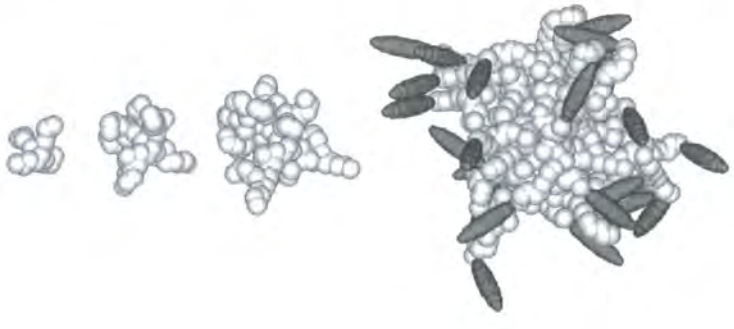

Figure 6.18: Distribution functions of solvent molecules relative to the core of the dendrimer.

later they settle into the smectic layers. The dendritic structure stretches across approximately five smectic layers.

Further information from these studies will be used in the following chapter to obtain structural information and to parameterize a coarse grained model.

Chapter 7

Dendromesogen: Coarse Grained Study

This chapter describes the formulation and study of a coarse grained model of a liquid crystalline dendrimer. The rationale behind the approach chosen is explained and the parameterization of the forcefield described. Molecular dynamics simulations using this model to explore the phase behaviour are reported. Finally the model is assessed to determine to what degree it has captured the essential physics of the system being studied.

7.1 Model Building

When formulating a coarse grained model which can be used to study the system described in Chapter 6 we must first decide a mapping regime and the nature of the interactions, then consider how to make the most of the information gained from the atomistic and semi-atomistic studies.

For this system the key points from the earlier studies that need to be incorporated into the coarse-grained model are:

- **A dendritic core** that is seemingly decoupled from the outer parts of the molecule. This does not undergo significant structural change during the course of the study. Penetration of the core by other parts of the system should be minimal.

- **Flexible chains terminating in mesogenic units**, that are able to change conformation depending on their environment. The overall molecular structure can change by rearrangement of the chains

7.1.1 Mapping

As described in Section 3.4 on Page 36, a liquid crystalline dendrimer consists of a rigid scaffolding at the core, surrounded by flexible branches which act as spacers and terminate in mesogenic functionalization.

A number of different approaches to coarse graining of molecular systems are described in Chapter 4 (Section 4.1.4), here we address the requirements of the core, the chains that acts as a flexible spacers and the mesogens. For this work one of the principal methods for determining particle size will be to maintain the excluded volume that each part of the system occupies in reality. In this study three particle types are employed to represent the system; a large spherical bead to represent the whole of the rigid core, a number of smaller spherical beads to represent a flexible spacer, and spherocylindrical sites representative of mesogenic moieties. In table 7.1 the atomistic detail represented by each bead is given. Figures 7.3-7.5 show the molecular structure included in each particle. The overall model shape can be seen in Figures 7.1 and 7.2, where a schematic of the dendrimer is shown.

Site	Molecular detail
Large sphere	
	$Si((CH_2)_3SiCH_3((CH_2)_3SiCH_3((CH_2)_3SiCH_3((CH_2)_3Si(CH_3)_2OSi(CH_2)_3)_2)_2)_2)_4$
Small sphere	$(CH_2)_3$
Mesogenic site	$COO(C_{12}H_8)CN$

Table 7.1: Mapping of molecular detail onto coarse-grained sites for a 3rd generation carbosilane dendrimer.

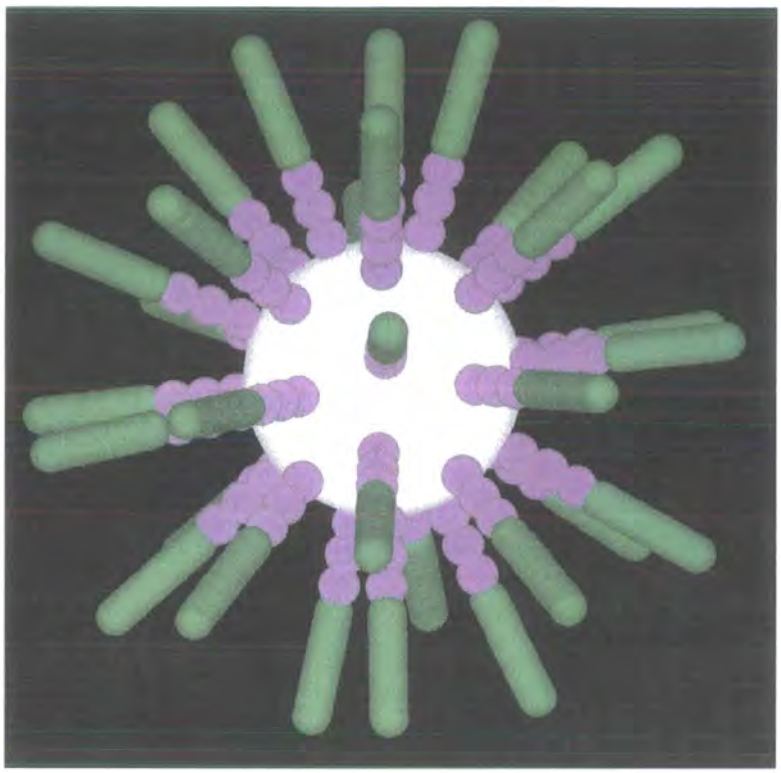

Figure 7.1: A 3rd generation LCDr molecule mapped as described in Section 7.1.1. Here the core is white, the smaller spheres make up the flexible chains are blue and the mesogenic sites are coloured green.

Label	Measurement	Equivalent parameter
L	Length of spherocylinder	-
D	Breadth of spherocylinder	$2^{\frac{1}{6}}\sigma_{sc}$
R_1	Radius of small sphere	$\frac{2^{\frac{1}{6}}\sigma_{small}}{2}$
R_2	Radius of large sphere	$\frac{2^{\frac{1}{6}}\sigma_{big}}{2}$
a	Large-small bond length	-
b	Small-small bond length	-
c	Small sphere-spherocylinder bond length	-

Table 7.2: Definition of model measurements shown in Figure 7.2. The equivalent parameters reflect how these measurements relate to the potentials described in Section 7.1.2. Further explanation is available in Section 7.1.4.

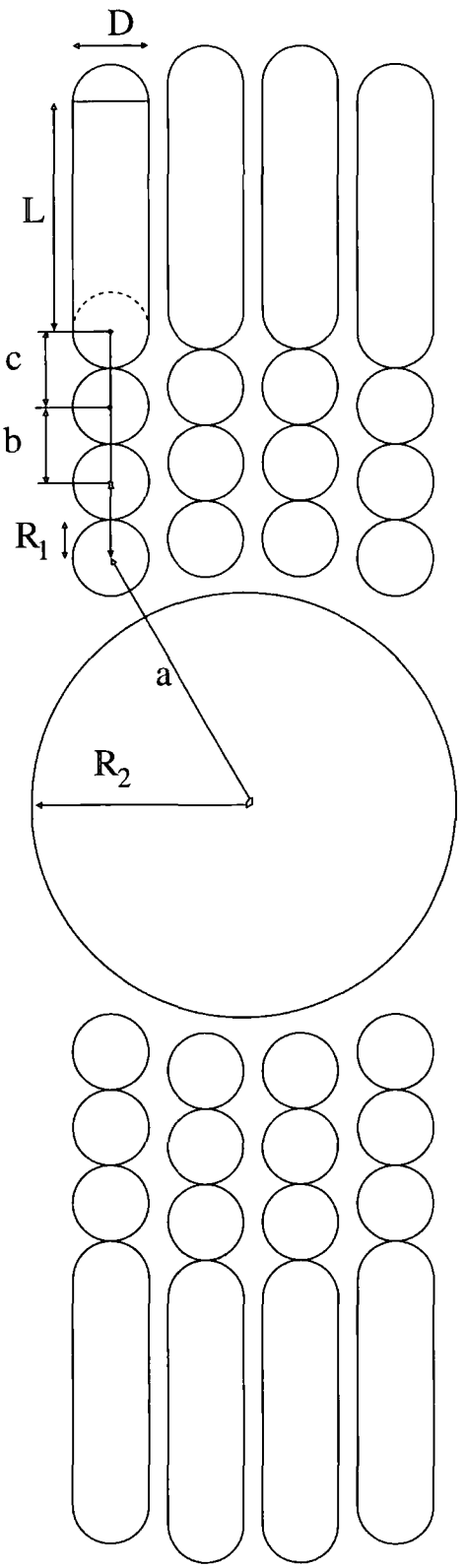

Figure 7.2: Mapping of a LCDr as described in Section 7.1.1, annotated measurements are defined in Table 7.2. The third generation molecule that is the subject of this work has thirty-two mesogenic branches rather than the eight seen here.

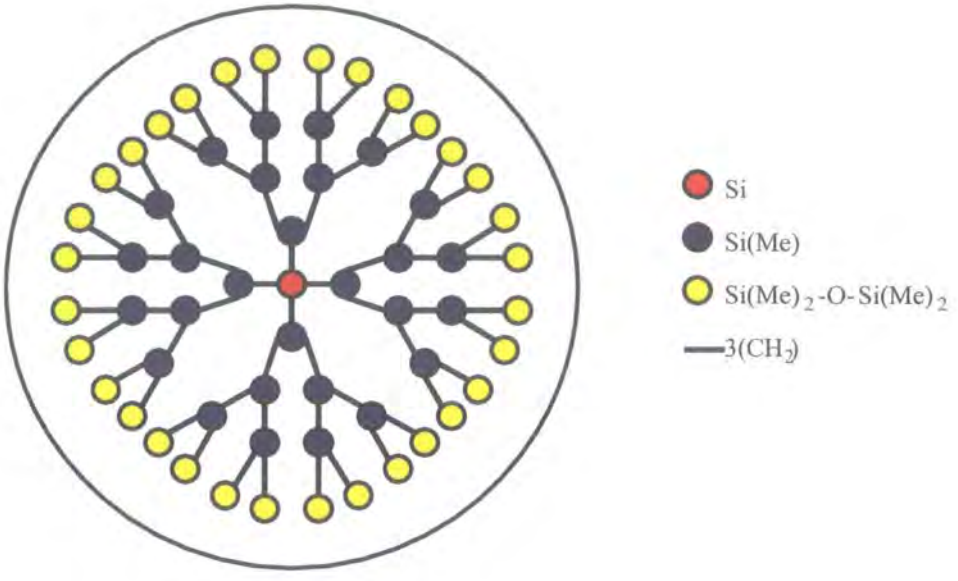

Figure 7.3: Molecular detail of the core particle.

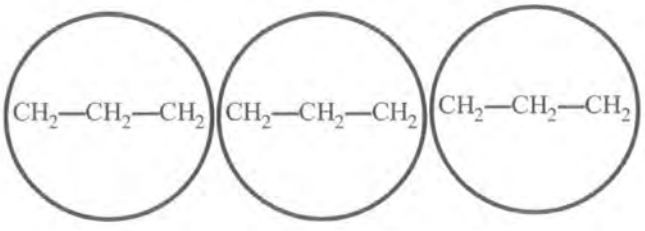

Figure 7.4: Molecular detail the three particles that make up the flexible spacer.

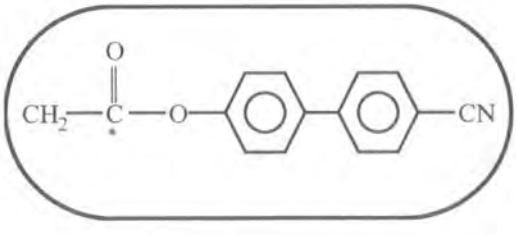

Figure 7.5: Molecular detail of the mesogen particle.

7.1.2 Potentials

Once a mapping regime is outlined, the form of potentials used to construct the model must be decided. This model includes two different potentials, both are purely repulsive. For the spherical sites the cut and shifted form of the Lennard-Jones potential Equation 7.1 is used.

$$U_{LJ}(r_{ij}) = \begin{cases} 4\epsilon\left[\left(\frac{\sigma}{r_{ij}}\right)^{12} - \left(\frac{\sigma}{r_{ij}}\right)^{6} + \frac{1}{4}\right], & r_{ij} < r_{cut}, \\ 0, & r_{ij} \geqslant r_{cut}, \end{cases} \tag{7.1}$$

where $U_{LJ}(r_{ij})$ is the Lennard-Jones potential at a position r_{ij} and ϵ and σ are respectively the well depth and distance of closest approach, which characterize the potential. For the mesogenic units the spherocylindrical potential,[36] Equation 7.2, is used.

$$U_{SC}(d_{ij}) = \begin{cases} 4\epsilon\left[\left(\frac{\sigma}{d_{ij}}\right)^{12} - \left(\frac{\sigma}{d_{ij}}\right)^{6} + \frac{1}{4}\right], & d_{ij} < d_{cut}, \\ 0, & d_{ij} \geqslant d_{cut}, \end{cases} \tag{7.2}$$

where $U_{SC}(d_{ij})$ is the potential at a minimum distance d_{ij}. This distance is not as easy to define as that for the spherical sites. It is defined as the shortest contact length between lines that run along the centres of the cylindrical region of the potential as shown in Figure 7.6. The form of this purely repulsive potential is plotted in Figure 7.7.

The potential defined in Equation 7.2 can be used also to describe the interaction of a spherocylinder with a Lennard-Jones site, by considering d_{ij} as the minimum separation between the centre point of the sphere and the line that runs along the centre of the spherocylinder. (This is equivalent to considering a sphere as a spherocylinder where $L = 0$.)

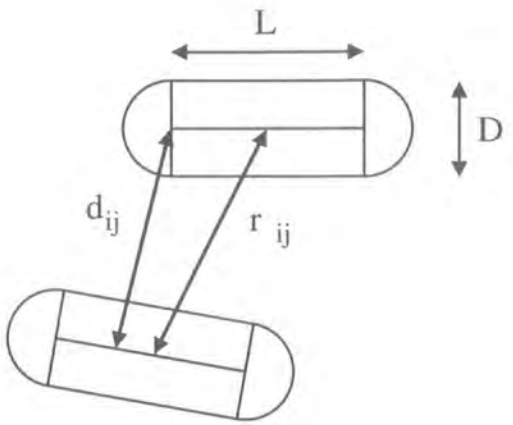

Figure 7.6: Schematic drawing to define the minimum separation, d_{ij}, and the distance between centres, r_{ij}, for a pair of spherocylindrical sites.

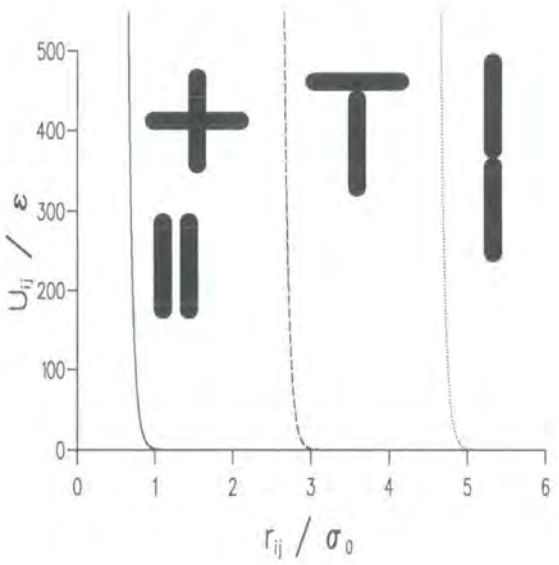

Figure 7.7: Spherocylinder potential plotted as a function of the distance of separation between the sites for three different orientations of approach.

7.1.3 Other Interactions

In addition to the non-bonded interactions described in Section 7.1.2, potentials must be included to define the behaviour of directly bonded sites. Also consideration must be given to the angular and torsional distributions.

A bonding potential which has been used in many studies is the FENE potential.[157] The FENE potential takes the form

$$U_{FENE}(r_{ij}) = -\frac{1}{2}k(l_{max} - l_0)^2 \ln\left(1 - \frac{(r_{ij} - l_0)^2}{(l_{max} - l_0)^2}\right), \tag{7.3}$$

wherein r_{ij} is the separation distance of the bonded sites, k is the bond strength and l_{max} and l_0 are the maximum and optimum bond lengths respectively. Owing to the symmetry of this expression there is no need to specify a value for the minimum separation. The FENE potential has been extensively used for coarse-grained polymer models (as detailed in Section 3.4 on Page 36). Some advantages of the FENE potential are evident from Figure 7.8; the potential has finite bounds that mean it will never move beyond a given minimum and maximum value (in Figure 7.8 the limits of the potential are shown at $r = 0.4$, 1.0); and the shallow bottom and steep walls allow relatively easy fluctuation of the bond length between those bounds. These features are favourable for a bonding potential used with coarse-grained beads as the distribution of bond lengths is wider than that of an atomistic bond. There are however practical problems with the finitude of the FENE potential which may necessitate a shorter time step than would otherwise be desirable. Such problems arise from the fact that unless a time step is sufficiently small it may be possible for a bond length to go beyond the finite bounds during integration of the equations of motion and therefore cause the bond to break effectively.

When considering a bonding potential it was important to keep some of the key qualities of the FENE potential, but if possible to modify it to overcome some of its less favourable characteristics.

The bonding potential that has been chosen for this model is the potential

$$U_{bond}(r_{ij}) = \frac{1}{2}k(r_{ij} - l_0)^{12}, \tag{7.4}$$

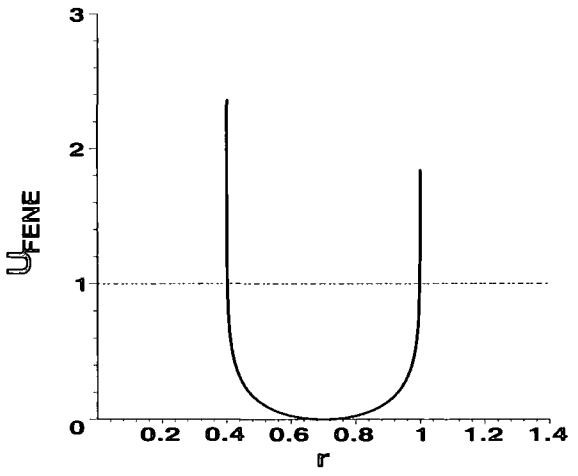

Figure 7.8: FENE potential as a function of bond length using $l_{max} = 1.0$, $l_0 = 0.7$, $\sigma = 1.0$, $\epsilon = 1$ (plotted as a dashed line) and $k = 5.0$.

where r_{ij}, k and l_0 take there usual meanings. In Figure 7.13 U_{bond} is plotted as a function of separation of bonding sites, this shows that the potential is shallow at the bottom with steep walls. However, unlike the FENE potential, this potential is no longer finite and thus a larger timestep can be used. The bond constant, k, has been chosen to make the potential sufficiently soft in comparison with the non-bonding interactions so as not to impede the timestep, yet stiff enough that the range of accessible bond lengths at a reasonably energy (below ϵ) will not be too wide as to allow particles to pass between a bonding pair.

For a spherical site the usual bonding point is the centre of the sphere; however, for a spherocylinder there are a number of points where the site may be bonded. In this system the spherocylinders are bonded at the centre of one of the hemispheres. (Shown in Figure 7.9.)

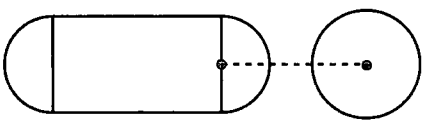

Figure 7.9: Bonding between a spherocylinder and a sphere. The bonding point is shown as black dot, the bond as a dashed line.

One last technical point about bonding that needs to be addressed is whether to include a non-bonding interaction for bonded pairs. In this work parameterization using data from the atomistic simulations provides values such as l_0, it would therefore be inconsistent to impose non-bonded forces on bonded pairs and thus shift the equilibrium bond length away from the desired one. Also the bonding potential was chosen for its shape and to add to it a non-bonding term would completely change that shape. For these reasons bonded pairs have been excluded from non-bonding interactions.

7.1.4 Parameterization of Model.

From the work in Chapter 6 we already have a lot of information which may be incorporated into the coarse-grained model. This section describes the way in which information particularly from those studies has been used in the parameterization of the force field for the coarse-grained model.

A model forcefield needs to include all the initial information about the system. In the case of this study we will need to parameterize the masses and moments of inertia (for non spherical sites); dimensions such as length, breadth and radii; values of σ and ϵ, as detailed in Section 7.1.2, for each particle; bond lengths and bond strength, k, parameters; potential cut-off distances; and geometrical parameters such as angular and torsional constraints or potentials.

Dimensions

There are a range of possible methods to decide the size of each site and its potential that are to be used in the simulations. In formulating this model a number of possible approaches were initially considered. One approach, which was not finally used, was to calculate the distribution functions of centres of atoms from the centre of the molecule and from other atoms during the coarse of the atomistic simulations described in Chapter 6. These distributions could then be combined with van der Waals radii to get an idea of how large a coarse-grained site might be. Eventually however the methodology chosen was to have an equivalence of excluded volumes between the actual molecular structure and the coarse-grained sites. This approach

has been used by Kremer *et al.* to parameterize models used to study the dynamics of polycarbonate melts.[116,158]

The volumes of spherical beads can be used to calculate directly the radii, which are easily translated into values for σ as $r^* = 2^{\frac{1}{6}}\sigma$, where r^* is equivalent to the diameter of the bead as it is the closest distance of separation of two sites. (i.e. when the two hard walls are touching). For the spherocylindrical sites this process is not so straight forward and the length of the site must be measured in order to calculate σ.

To measure the molecular volume of each fragment the smooth invariant molecular surface (SIMS) method was used.[159] The SIMS method calculates a molecular surface by simulating the rolling of probe spheres over the inside and outside of a molecular structure to produce a solvent excluded region, which represents the molecular volume.* The volumes of the whole molecule, a mesogen and a the flexible spacer were 20571.42, 204.41 and 151.99 Å^3 respectively, leading to a core volume of 9166.62 Å^3 and a volume for the smaller spheres of 50.63 Å^3. From these volumes the radii of the small spherical site, R_1, was calculated as 2.30 Å and larger sphere radii, R_2, as 12.98 Å. Therefore the values of σ_{small} and σ_{big} were determined to be 23.13 and 4.09 Å.

For the spherocylinder a value for L must be determined before D and therefore σ_{sc} can be determined. For this model L was calculated from the assumption that the total length of the spherocylinder including the hemispherical caps, $L + D$, is equal to the sum of the distance between the terminal nitrogen atom in the mesogen and the carbon atom which connects the mesogen to the flexible spacer, plus the van der Waals radii of nitrogen and carbon. The nitrogen-carbon distance was calculated from the average of this interatomic distance in the atomistic simulations. The variation of this length during the course of an atomistic simulations has been plotted in Figure 7.10 and the distribution of this parameter over time is shown in Figure 7.11. The average value was found to be 12.89 Å. The van der Waals radii of nitrogen and carbon are 1.55 and 1.70 Å respectively.[160] Therefore $L+D = 16.14$ Å.

*The program used to implement the SIMS method was written by Dr. Yury N Vorobjev and obtained from the URL *http://femto.med.unc.edu/People/vorobjev/SIMS.html.*

This may be used with the standard equation for the volume of a spherocylinder, $Volume = \frac{4}{3}\pi\left(\frac{D}{2}\right)^3 + L\pi\left(\frac{D}{2}\right)^2$, to give just one real solution for L and D. In this case $L = 11.93$ Å and $D = 4.20$ Å. Using this value for D, $\sigma_{sc} = 3.74$ Å.

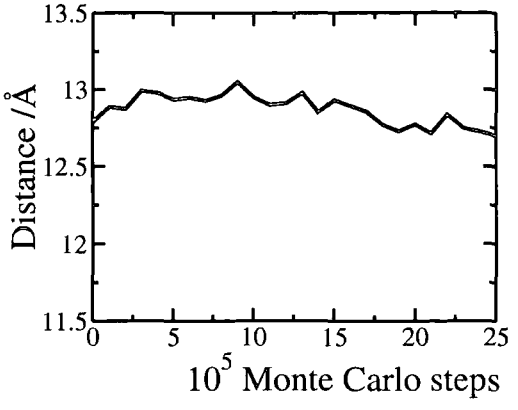

Figure 7.10: Variation in the interatomic distance between the terminal nitrogen and the carbon that joins the mesogen to the rest of the molecule over the course of the simulation. These data were extracted from the coordinates acquired in the atomistic studies described in Chapter 6.

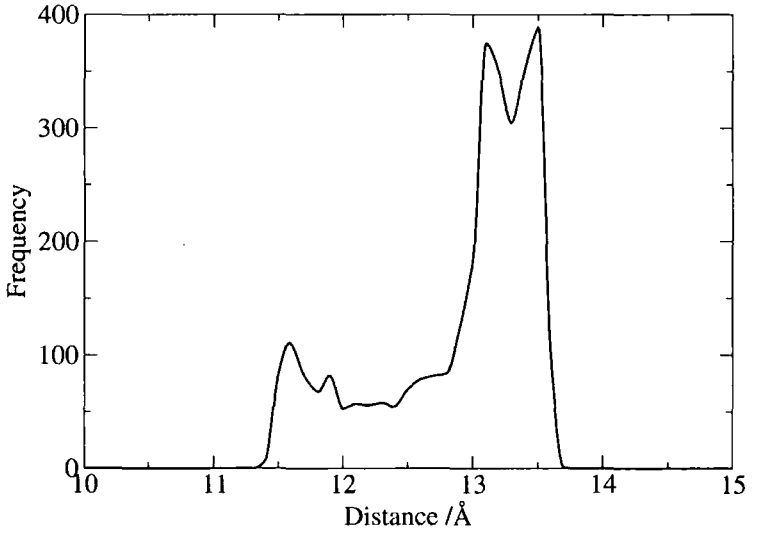

Figure 7.11: Distribution of interatomic distances between the terminal nitrogen and the carbon that joins the mesogen to the rest of the molecule.

With σ values determined, the other parameter that must be specified is ϵ, the depth of the potential. For this study ϵ for each of the sites was taken as the same value of 0.247×10^{-20} J. This value of ϵ is from studies using hybrid Lennard-Jones/Gay-Berne models.[30]

Bond Parameters

From Figure 7.2 it is evident that there are three bond lengths that need to be considered: a, b, and c. Each of these was determined from atomistic coordinates in the same way as the interatomic distance was in the previous section, using appropriate atoms that were considered to be at the centre of the site. For the large spherical bead the central atom was considered to be the central silicon atom, where the four initial branches join. For the smaller sphere the middle of the three carbon atoms in the $3(CH_2)$ chain was defined as the central atom. As described in Section 7.1.3, bonding of the spherocylinder is from the centre of one of the hemispherical caps.

To determine force constants for the bonding potentials a comparison between the Lennard-Jones potential and the bonding potential curves was made. The force constant was chosen such that the gradient of the bonding potential in the region where the energy is below ϵ is comparable to that using the Lennard-Jones potential. Hence, the equations of motion may be integrated without requiring a smaller timestep. This comparison of gradients was made for the bonded and non-bonded interaction of a small spherical site with a spherocylinder as this represents the steepest Lennard-Jones curve gradient.

Figure 7.12 shows the distribution of bond lengths for distances a and b. Table 7.3 shows the resultant bond lengths, with the corresponding bond strength. The potential that these parameters lead to are shown in Figure 7.13. These potentials, and therefore the bond strengths, were chosen to be steep so like the FENE potential they have a restrained length, but not to exceed the gradient of the Lennard-Jones potential in the region $0 < U/\epsilon < 1$.

bond	length /Å	K_θ /$\times 10^{-20}$ J rad^{-2}
a	16.680	60
b	3.617	60
c	2.979	60

Table 7.3: Bond parameters.

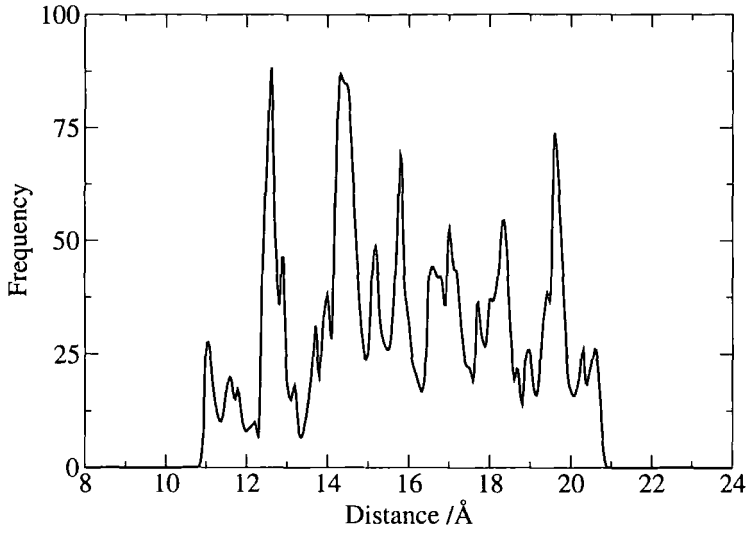

(a) Bond length between large and small spherical sites.

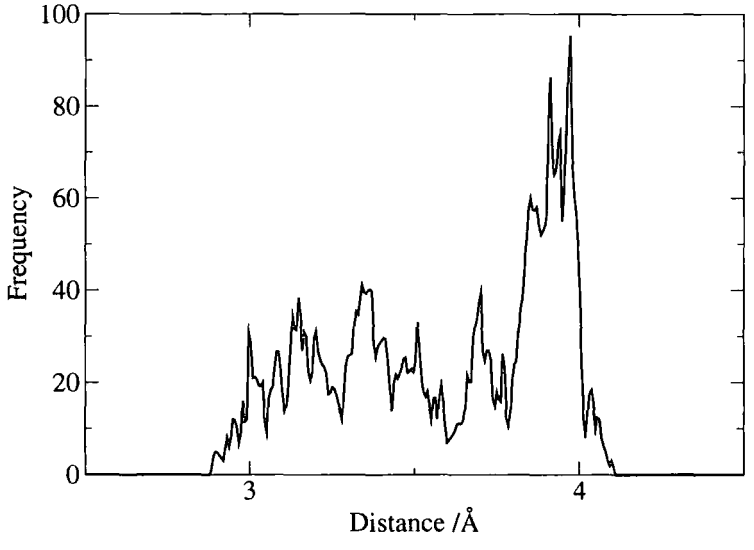

(b) Bond length between two smaller spherical sites that form the flexible spacer.

Figure 7.12: Distributions of bond lengths for distances between spheres. Lengths correspond to distances a and b in Figure 7.2. These measurements were extracted from an atomistic simulation at 400 K with no mean field applied.

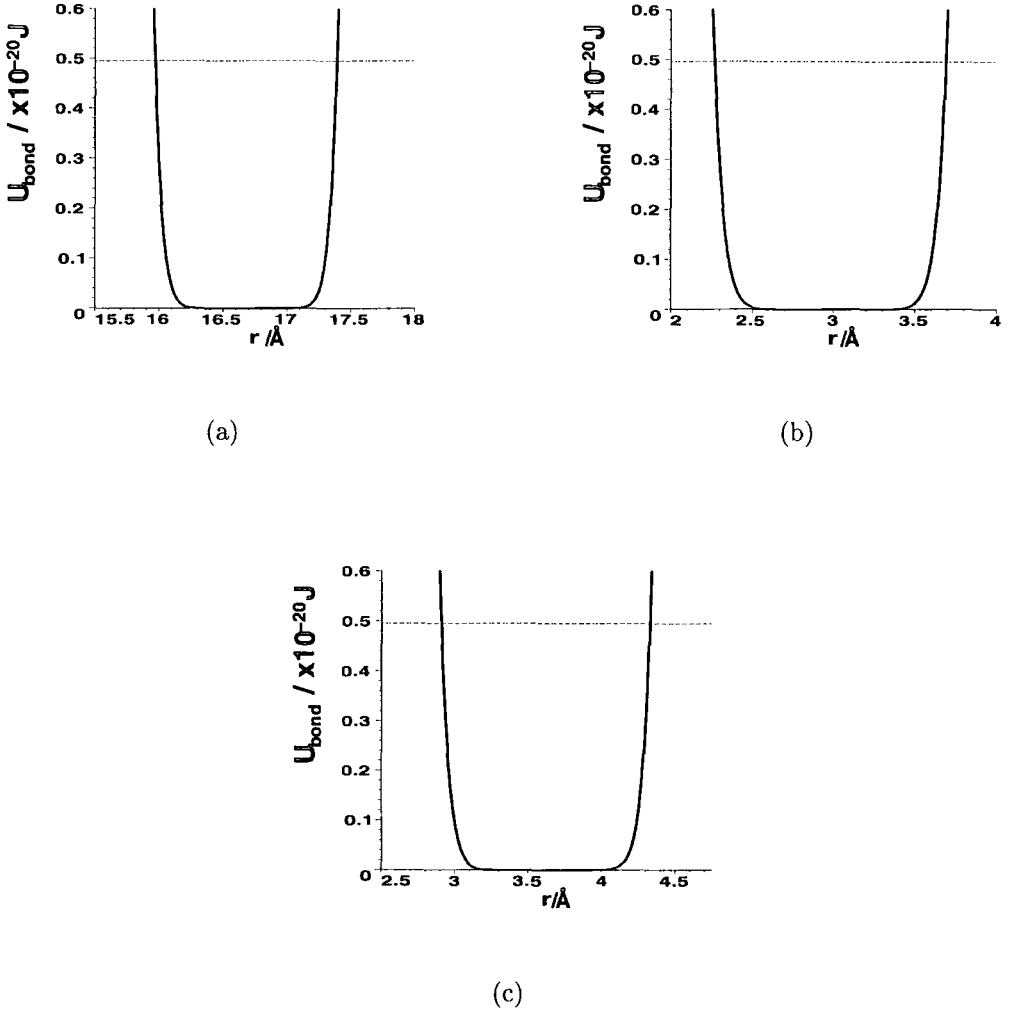

Figure 7.13: Bond potentials for bonds a, b, c as described in Figure 7.2.

Angular and Torsional Parameters

Distribution functions for angular and torsional potentials (labled in Figure 7.14) were extracted from the atomistic coordinates, these can be seen in Figure 7.15. The broadness and lack of strong peaks at particular angles means that additional angular and torsional potentials were not required in the model.

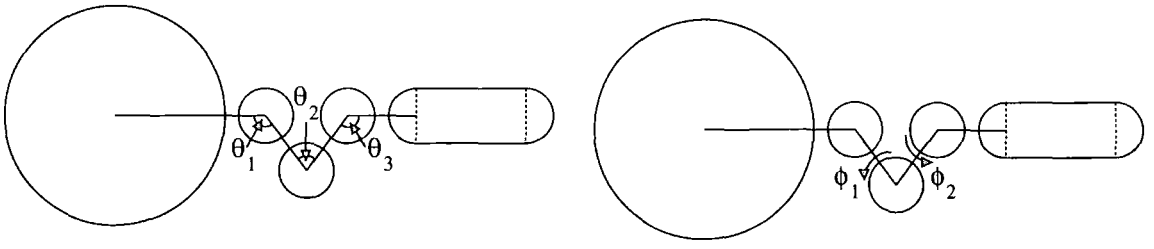

Figure 7.14: Schematic diagram showing the bond angles and torsion angles in the coarse-grained model.

Mass and Inertia

The masses of the sites have been calculated in the usual way and are shown in Table 7.4. For the non-spherical site it is important to account for the inertia of the spherocylinder. Figure 7.16 shows the reduction of the mesogen to a rod. In Figure 7.16a the mesogen has 3 degrees of freedom relating to rotational motion, which have moments of inertia I_x^a, I_y^a, I_z^a about the x, y and z axes respectively. In Figure 7.16b the the equivalent rod can be resolved into two degrees of freedom relating to rotational motion, which have moments of inertia, I_x^b and I_y^b. Symmetry about the rod leads to $I_x^b = I_y^b$.

The rotational kinetic energy of a molecule is given by,

$$K = \frac{1}{2}\left(I_x\omega_x^2 + I_y\omega_y^2 + I_z\omega_z^2\right), \tag{7.5}$$

where, I_x, I_y, I_z, and ω_x, ω_y, ω_z are moments of inertia and angular velocities about x, y and z. For a rod of circular cross-section if there is rotational motion about the z direction, there will be no contribution to the molecular rotational kinetic energy arising from this. Equation 7.5 can be reduced in this case to

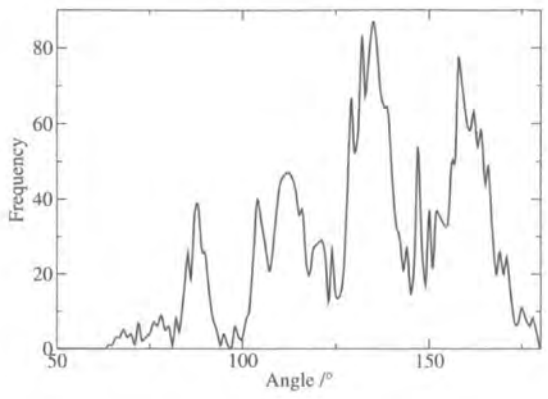

(a)

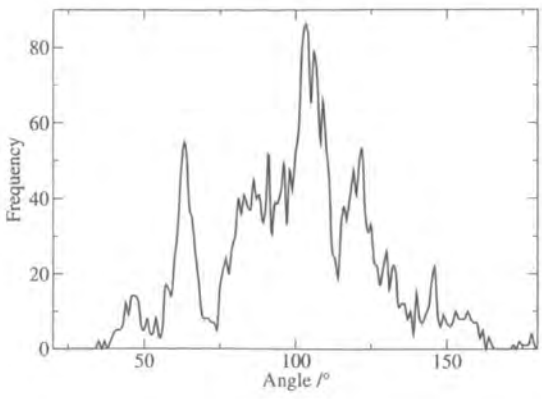

(b)

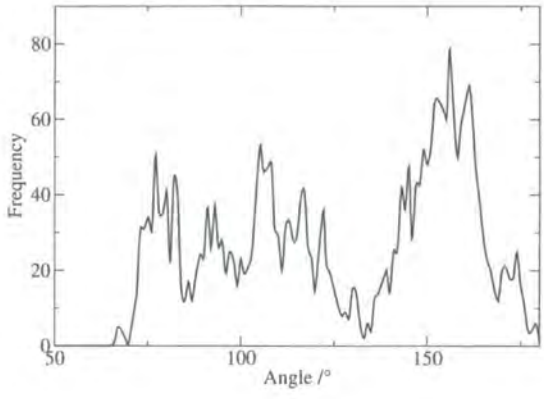

(c)

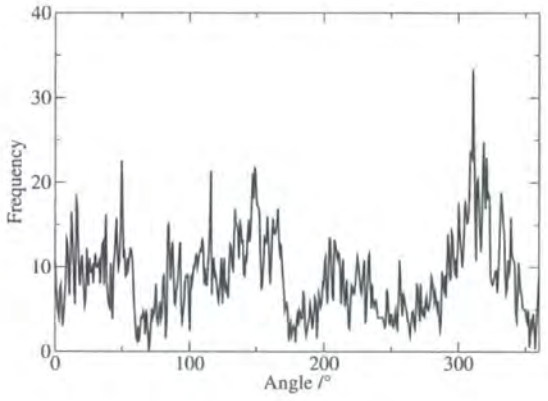

(d)

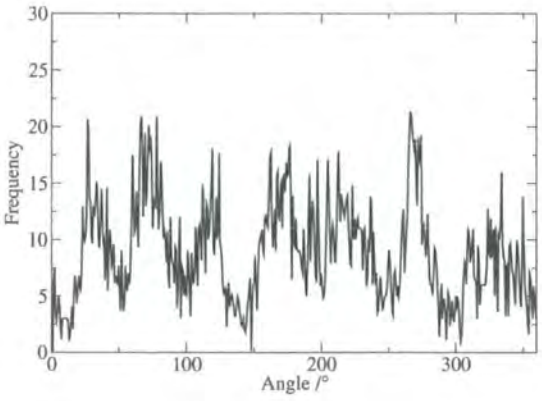

(e)

Figure 7.15: Distributions of angles and torsional angles extracted the atomistic simulations. Data corresponds to the angular measurements (a) θ_1, (b) θ_2, (c) θ_3, (d) $\phi_1$and (e) ϕ_2 shown in Figure 7.14. These measurements were extracted from an atomistic simulation at 400 K with no mean field applied.

$$K = \frac{1}{2}\left(I_x^b\omega_x^2 + I_y^b\omega_y^2\right) = I_{xy}^b\left(\omega_x^2 + \omega_y^2\right), \tag{7.6}$$

where $I_{xy}^b = \frac{\left(I_x^b + I_y^b\right)}{2}$, which is the overall effective moment of inertia. So in order to calculate an overall moment of inertia for the spherocylinder we initially calculate the three moments of inertia for the mesogen from the atomic coordinates and masses. One moment which corresponds to the z direction will have a much smaller moment and can be ignored. The two components for the x and y directions are averaged to give the effective moment of inertia of the rod.

Site	Relative Molecular Mass /a.m.u.	Mass /$\times 10^{-25}$Kg
Large sphere	7994.10	132.75
Small sphere	42.08	0.69878
Mesogenic site	236.24	3.9393
	Relative Molecular Mass /a.m.u.	Effective moment of inertia /$\times 10^{-24}$Kg m^2
Mesogenic site	3608.95	5.9930

Table 7.4: Masses and moments of inertia of coarse-grained sites.

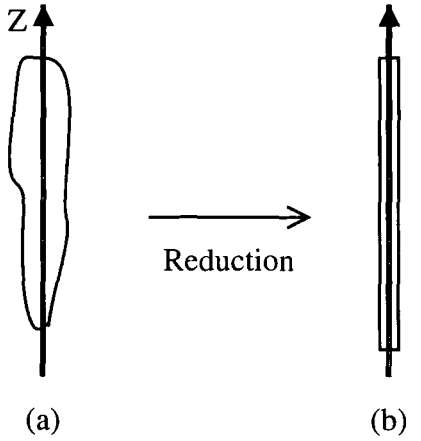

Figure 7.16: Sketch to show the reduction of a three-dimensional shape such as a mesogen, (a), to a rod, (b), in order to simplify the calculation of the moment of inertia.

7.2 Simulation Procedure

Phase changes with density are classically considered to be representative of lyotropic liquid crystals. However, as the potentials described in this study are purely repulsive, temperature is less important than density and the phase behaviour of the system is considered in terms of its changes in the latter. A simulation box was constructed with 100 molecules, each described by the model in the previous section. Bonded sites were excluded in the calculation of non-bonding interactions. A timestep of 7.5×10^{-15} s was used throughout these studies.

Compression from the gas phase lattice at an extremely low density of 40.55 kg m^{-3}. of 100 molecules gradually to a range of higher densities was achieved by applying an NpT ensemble and gradually increasing the pressure. Configurations were extracted at each density for study in the NVT ensemble.

7.3 Results

7.3.1 Phase Diagram

A phase diagram for the dendrimer is shown in Figure 7.17. This figure shows the change in pressure as a function of density. As the pressure rises the phase density increases. A phase transition would be see as a discontinuity in this graph. Here, there is no phase transition, only a gradual condensing of the system.

7.3.2 Correlation times

One of the problems of looking for liquid crystal phases starting from the isotropic liquid, is that growth of orientation order can take a long time. Correlation functions that measure the relation between the orientation of a system over time may be used to detect changes in orientational ordering that might signal the onset of liquid crystal phase formation. In this work the first-rank autocorrelation function C_1 has been calculated from

$$C_1 = \langle P_1 (\cos \delta\gamma (t)) \rangle = \langle \cos (\hat{\mathbf{u}} (t) \cdot \hat{\mathbf{u}} (0)) \rangle , \tag{7.7}$$

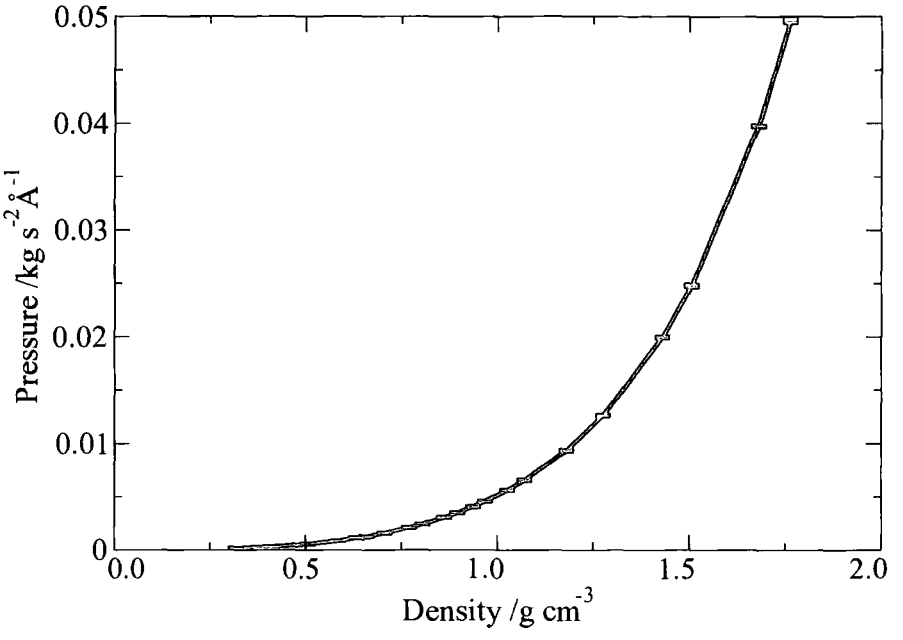

Figure 7.17: Phase behaviour of the bulk dendrimer.

where P_1 is the first Legendre polynomial and $\delta\gamma(t)$ is the change in orientation over time, t. An auto-correlation function will start at a value of unity and decay to zero in an isotropic or a nematic phase. However, in the nematic phase this decay takes longer. The onset of a transition to a liquid crystal phase would be marked by a rapid slow down in the decay of C_1.

The orientation correlation function, which may be considered analogous to the diffusion for translational motion is plotted in Figure 7.18. A number of densities are shown. As the system is compressed the time for the reorientation of the spherocylinders increases. However, given a longer time the functions will fade to a limit of zero, and there appears to be no evidence for a possible phase change.

7.3.3 Order Parameter

The evolution of the order parameter with compression is shown in Figure 7.19. The value of the order parameter is very small. Therefore the phase is isotropic with respect to molecular orientation. These data are taken for the average of the last 10^5 molecular dynamics steps from an NVT simulation lasting 10^6 for each density.

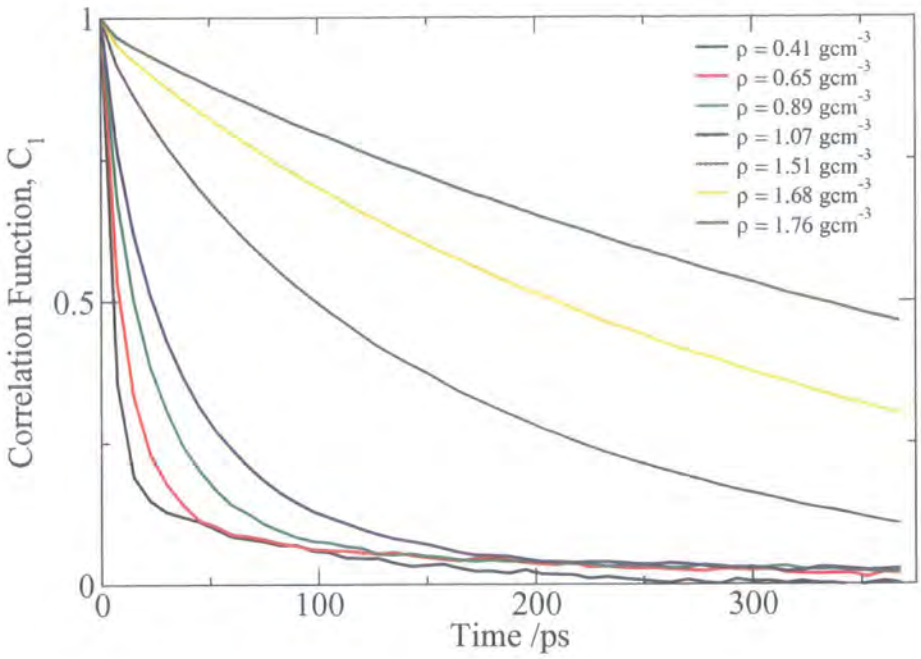

Figure 7.18: Correlation functions for a range of densities over the course of 375 ps.

There is a slight rise in the order for the more condensed systems. However, the magnitude remains negligible.

7.3.4 Snapshots

Snapshots of the system at a low and high density are shown in Figure 7.20. These snapshots concur with the conclusion that no liquid crystalline phases are being formed. Even at high density the system remains fully mixed and isotropically orientated. In particular there is no evidence for microphase separation and alignment of spherocylinders in "clumps" as was seen in the SCLCP system in Chapter 5.

7.3.5 Application of an Aligning Field

In order to try and induce a liquid crystalline phase, a magnetic field was applied to the system at high density (1.76 g cm^3). This field, which was applied to the spherocylinders, is of the same form that was applied to the Gay-Berne sites in the SCLCP work (Chapter 5). The magnitude of the field was larger than in the earlier work, with a field strength of 2.0×10^{-20} J. The time evolution of the order

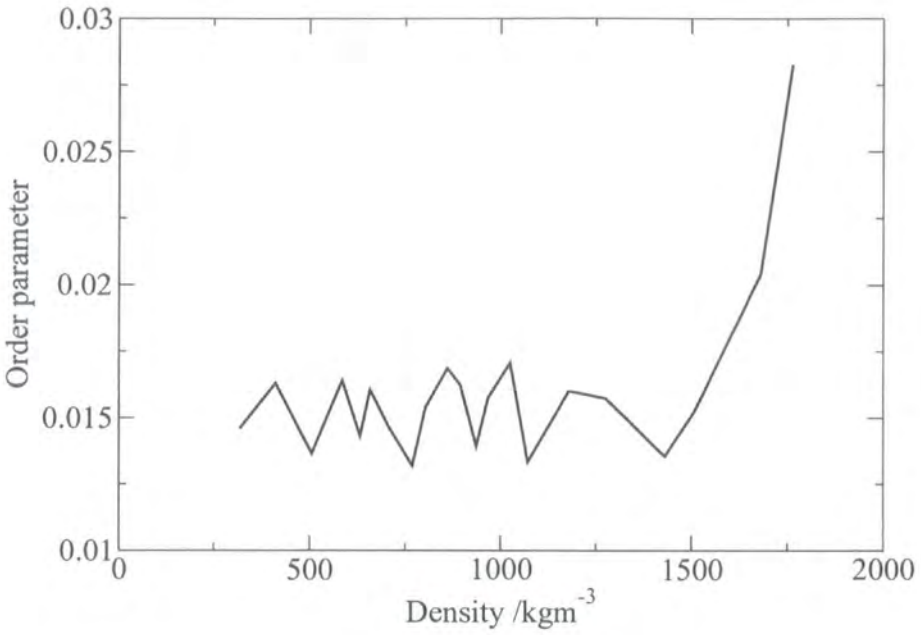

Figure 7.19: Order parameter evolution with density.

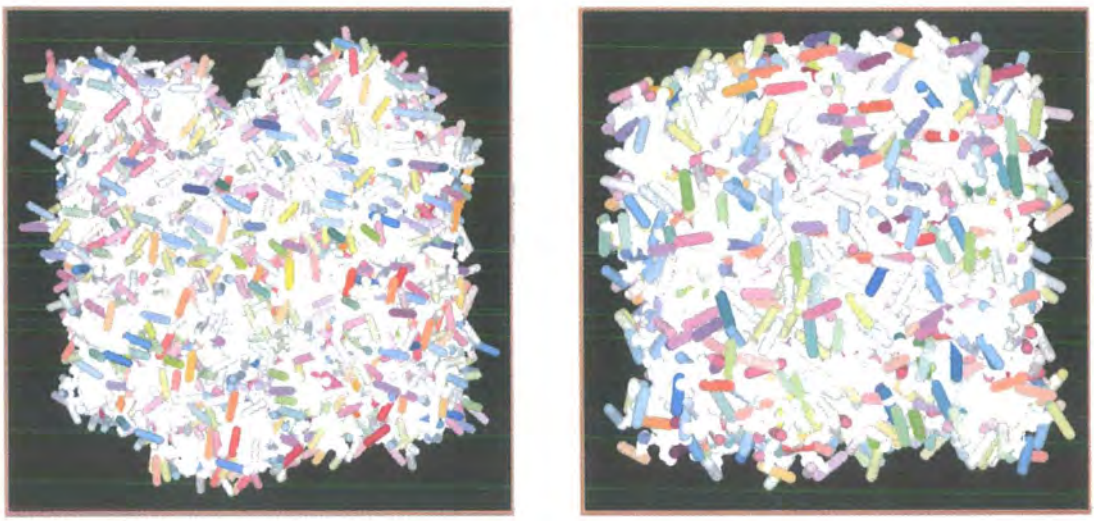

(a) (b)

Figure 7.20: Snapshots of the system at (a) 0.63 g cm^{-3} and (b) 1.76 g cm^{-3}.

parameter of this system is shown in Figure 7.21. The field was applied for 0.75 ns and then removed and the system monitored for another 0.75 ns. The application of the magnetic field leads to a rise in the order parameter. However, on removal of the field, marked with a dashed line, the system relaxes to a disordered configuration. This is also shown in the snapshots in Figure 7.22. The loss of order when the field is removed shows that there is no liquid crystal phase formation.

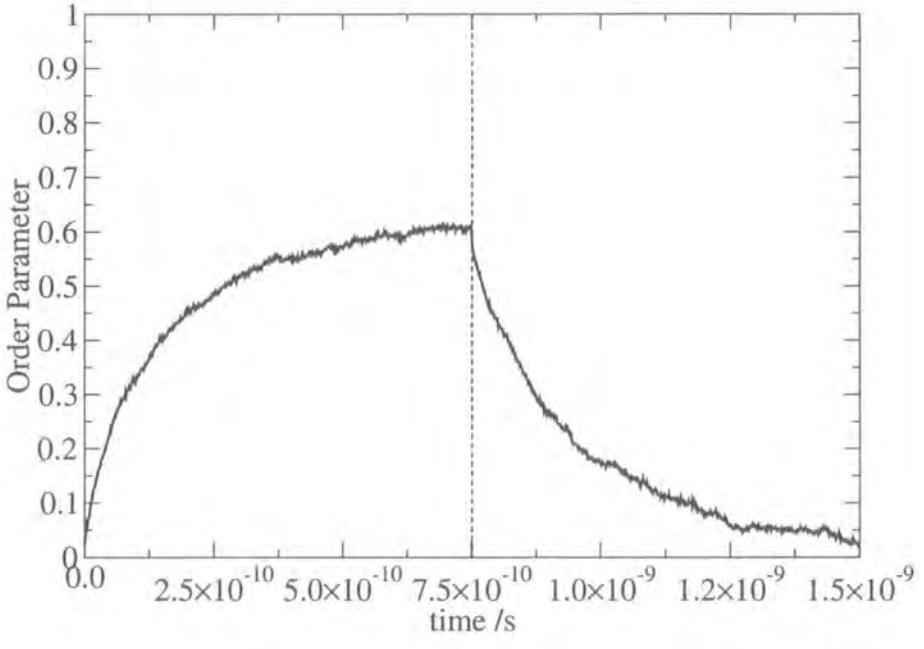

Figure 7.21: Time evolution of the order parameter of a system at high density exposed to and removed from an external field.

7.4 Use of Longer Spherocylinders

Looking at the information presented so far and considering the phase behaviour expected from a system of spherocylinders it seemed that the L/D ratio may be too small to induce liquid crystal phases. In particular, no evidence for microphase separation was seen even under the application of an aligning potential. In this system, where there are no attractive interactions between particles, microphase separation can only occur due to entropic effects (competition between rotational and translational entropy as described in detail in Section 7.5.2) . Use of longer spherocylinders would increase the entropic driving force for microphase separation.

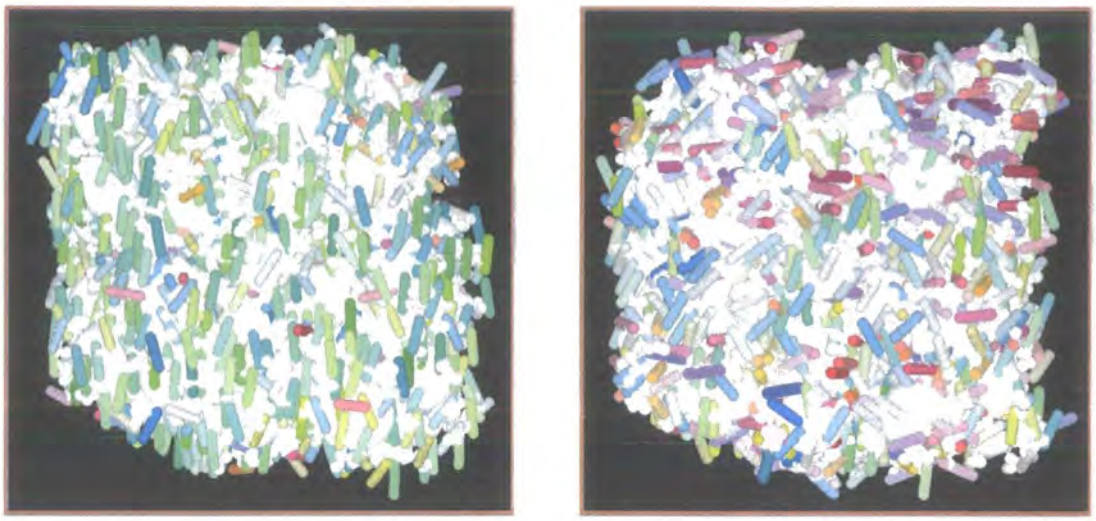

(a) (b)

Figure 7.22: Snapshots showing (a) the system in a magnetic field, (b) the relaxed system with the field removed.

Therefore, further simulations were conducted with the same model, but with $L/D = 6.0$

The phase diagram of this new system is presented in Figure 7.23. Here the density is less than for the previous studies owing to the increase in molecular volume of the sites. Simulations have been conducted in the same way as for the previous system.

7.4.1 Correlation Times

The correlation functions for the new system are presented in Figure 7.24. The correlation functions decay more slowly for this system with longer spherocylinders. The slowness in the decay of C_1 at $\rho = 1.09$ g cm^{-3} is comparable to that seen in a liquid crystal phase. However, no abrupt change in the decay of C_1 occurs with density. The latter might have indicated a change in local orientational ordering heralding the growth of an orientationally ordered phase.

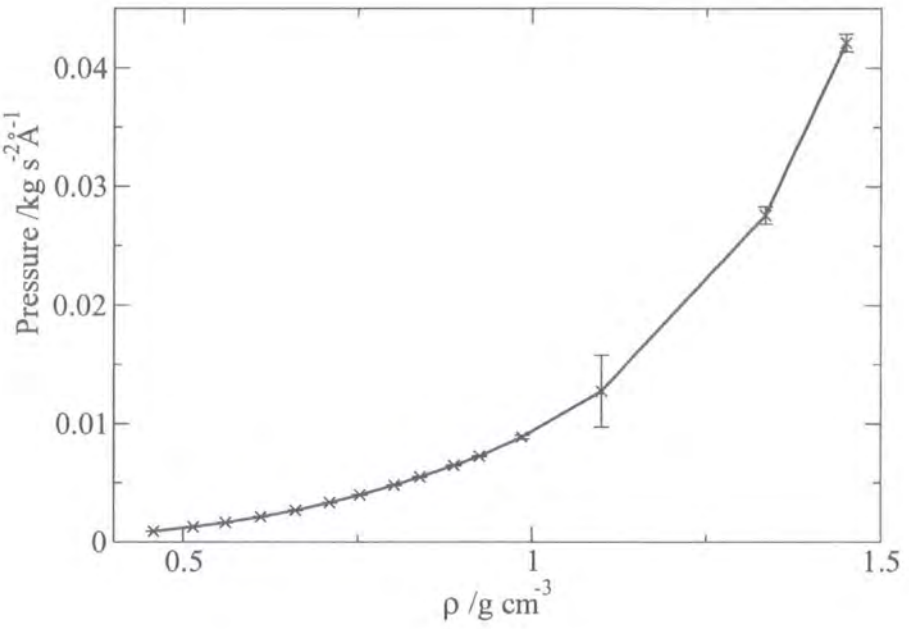

Figure 7.23: Phase diagram for the bulk dendrimer with $L/D = 6.0$ spherocylinders.

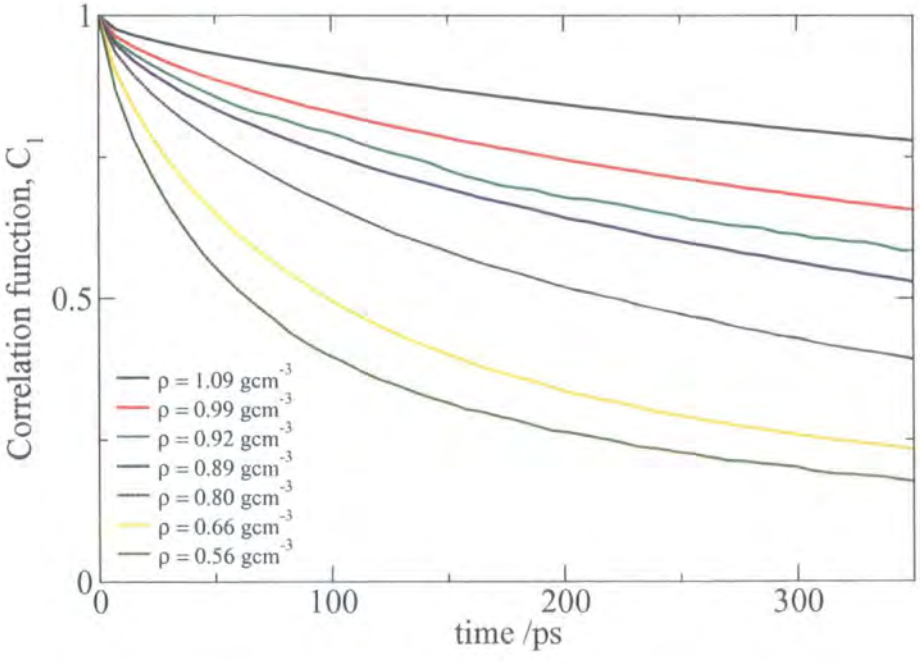

Figure 7.24: Correlation functions for the system with L/D = 6.0.

7.4.2 Order Parameter

The order parameter of the system at a range of densities is given in Figure 7.25. This graph shows that the system is isotropic, with respect to orientation, at all densities.

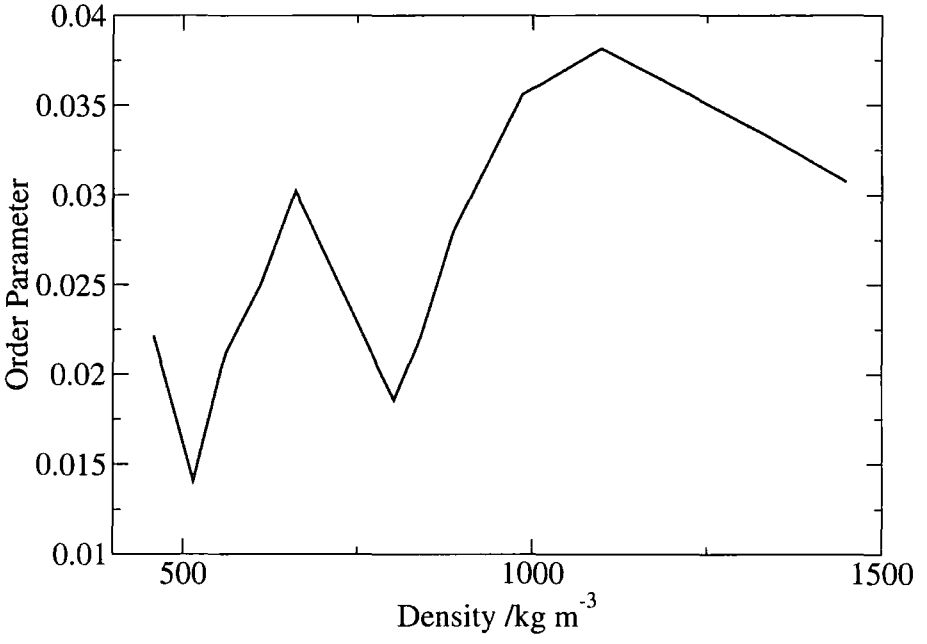

Figure 7.25: Order parameter evolution with density for the dendrimer with longer mesogenic sites.

7.4.3 Snapshots

Snapshots for the system at 3 densities are shown in Figure 7.26. As the system is compressed to 1.09 g cm^{-3} there appears to be some "clumping" together of mesogenic units. Within the clumps there is clear evidence for local orientational order of the individual spherocylinders. However, the "director" for each group of spherocylinders points in a different direction. The extent of the microphase separation appears to be relatively small and most of the groups of spherocylinders possess less than 10 particles. From the snapshots there appears to be no evidence for the extended domains that might lead to the formation of a smectic phase.

The driving force for the formation of spherocylinder clusters is space filling. At high densities the spherocylinders are able to pack more efficiently when orientationally ordered (see Section 7.5.2).

7.4.4 Diffusion Data

In Figure 7.27 the translational diffusion of the spherocylinders is plotted for each density. This diffusion data has been calculated from mean square diffusion data in the same way as for the SCLCP in Section 5.4.5 on page 107. We see that there is a dramatic change in the rate of diffusion with increasing density, suggesting that a 2nd order phase transition is occurring and a frozen glass is forming at above 1 g cm^{-3}. Decay of orientational order is also slow at this density, and the formation of orientationally ordered domains suggests this may be the region to look for the formation of mesophases. Therefore, a density close to this transition has been selected for the application of a magnetic field.

7.4.5 Application of an Aligning Field

Two state points at $\rho = 1.09$ gcm^{-3} and $\rho = 1.33$ gcm^{-3} were selected to study under the application of an external field. Following the procedure in Section 7.3.5 a potential of 2.0×10^{-20} J was applied to the spherocylinders to cause alignment, the potential was then removed and the change in structure of the system was monitored.

Snaphots of the field applied to the system at the two densities are shown in Figures 7.28 and 7.29. In the former, initial alignment of the spherocylinders occurs, followed by some formation of incomplete layers over a period of 1.425 ns as the system is allowed to equilibrate in the field. However, when the field is removed, some disorder occurs immediately and this is followed by the break-up of layers into the same multi-domain structure that was seen in the earlier simulations carried out in the absence of the applied field. In Figure 7.28d domains are more extensive than in the earlier simulations, but the same morphology of separate groups of orientationally ordered spherocylinders, with each "group director" pointing in a

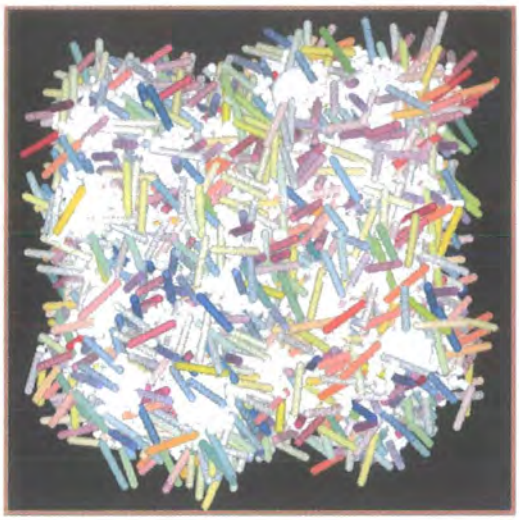

(a)

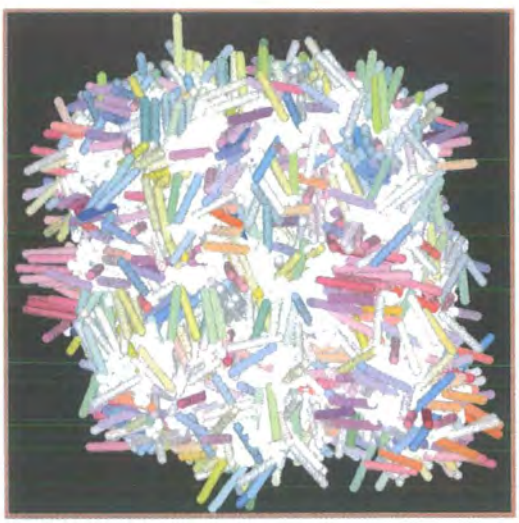

(b)

(c)

Figure 7.26: Snapshots at (a) 0.84 g cm^{-3}, (b) 1.09 g cm^{-3} and (a) 1.33 g cm^{-3}.

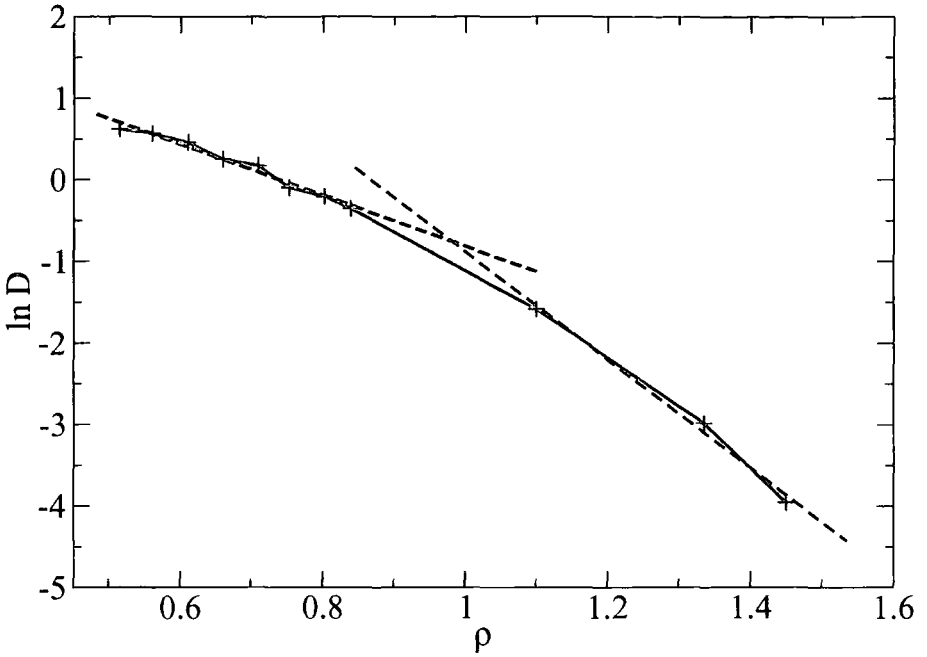

Figure 7.27: Plot indicating the change in the nature of translational diffusion with density, ρ.

different direction, is visible. The time evolution of the order parameter for the system is shown in Figure 7.30. The initial field causes a rise in S_2 to a value of approximately 0.8. The decay of S_2 is very slow, reordering to a value of 0.24 only after a further 6 ns. The behaviour for the higher density system of $\rho = 1.33$ g cm^{-3} seems to be similar. However, the timescale for the growth of S_2 with an external field applied and the loss of orientational order was longer (Figure 7.31). As before, incomplete layers appear to form in the field, but these layers break-up when the field is removed to leave groups of spherocylinders each aligned with a local director.

Distribution functions for the system at 1.09 g cm^{-3} with no field and with an external field applied for 1.425 ns are shown in Figure 7.32. It is evident from these that there is no major structural change taking place. There is little change in $g(r)$ with the application of a field. Some slight changes are seen in the perpendicular and parallel components. However, the magnitude of these changes is small. There is no evidence for smectic ordering in either $g_\perp(r)$ or $g_2(r)$, and there is none of the additional structure that was evident in the mesophases formed by the SCLCP in chapter 5.

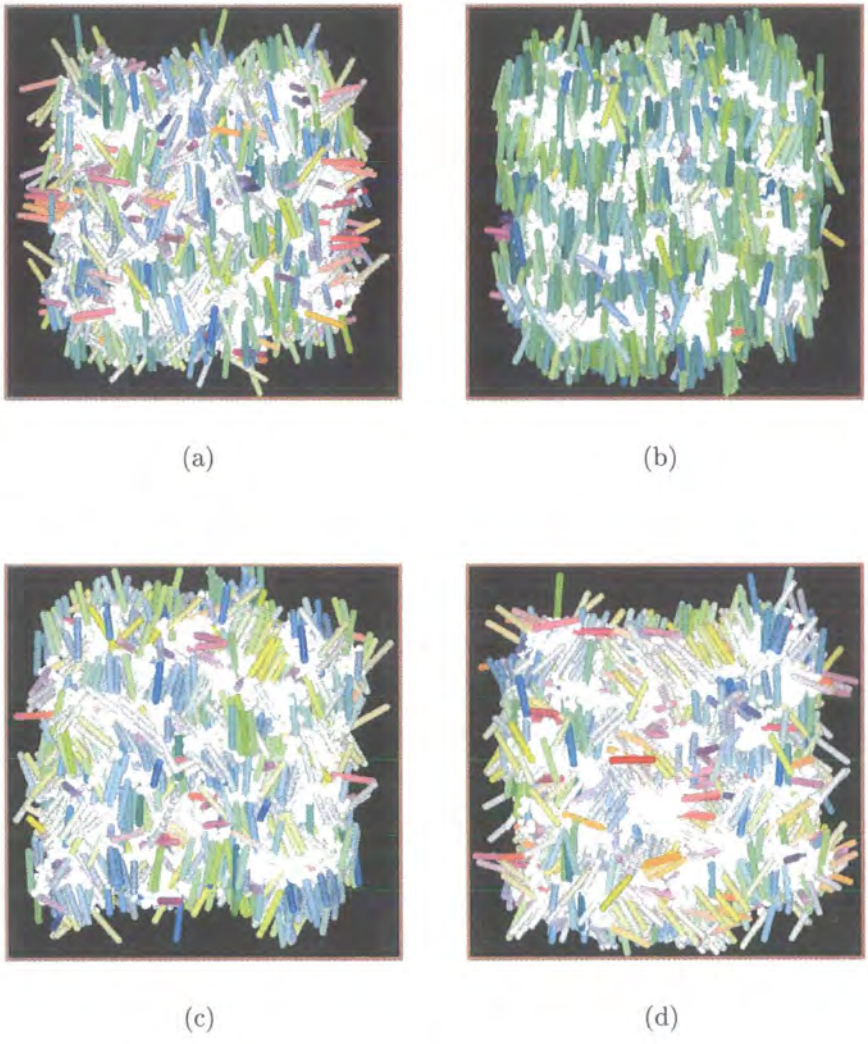

(a) (b)

(c) (d)

Figure 7.28: Snaphots of the system at a density of 1.09 g cm^{-3}.
(a) 0.075 ns after the field is applied, (b) 1.425 ns of applied field, (c) 1.425 ns after the field is removed and (d) 4.275 ns after the field is removed.

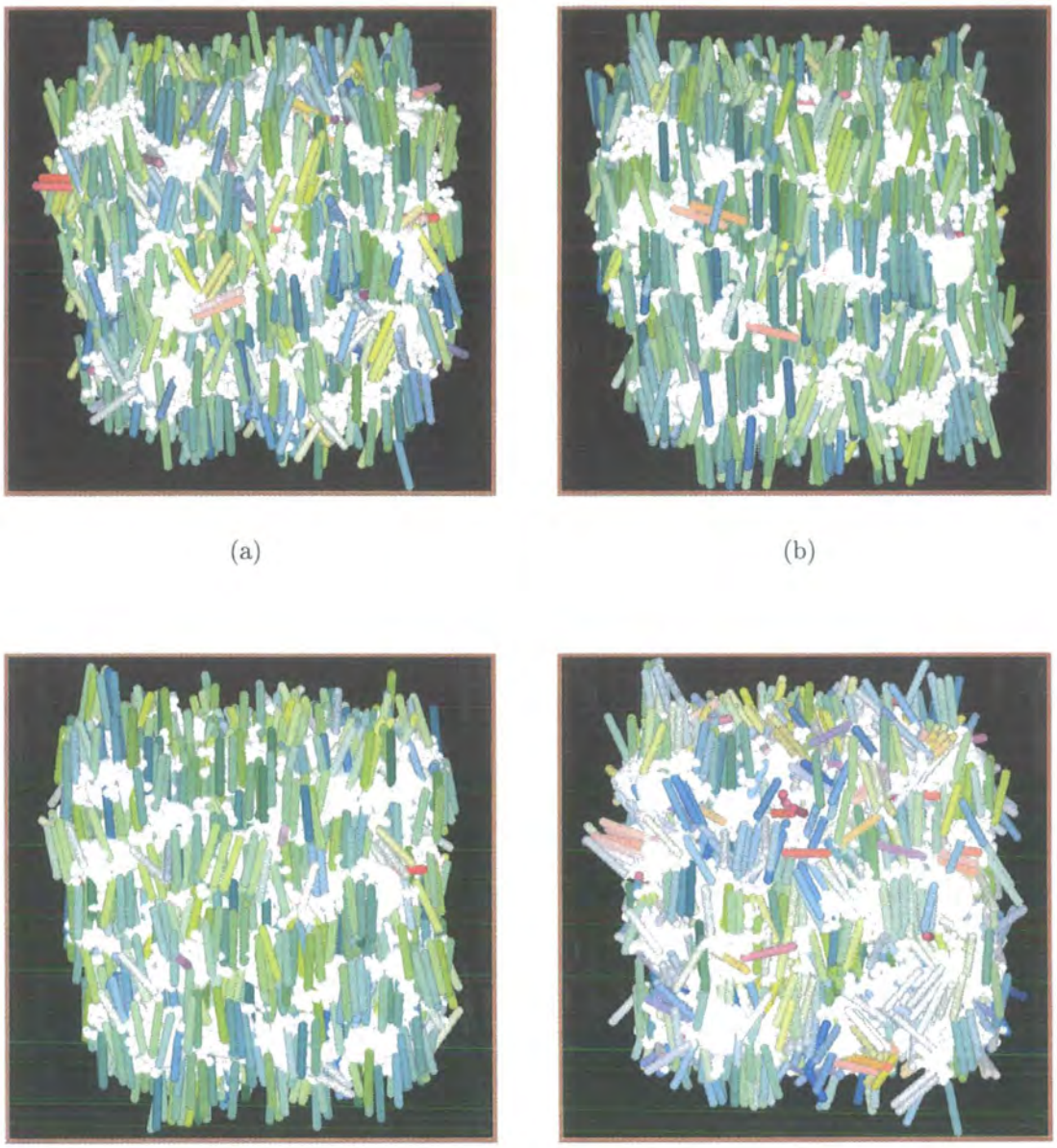

(a) (b)

(c) (d)

Figure 7.29: Snaphots of the system at a density of 1.33 g cm^{-3}.
(a) 2.175 ns after the field is applied, (b) 4.425 ns of applied field, (c) 5.925 ns of applied field (d) 1.35 ns after the field is removed from (a).

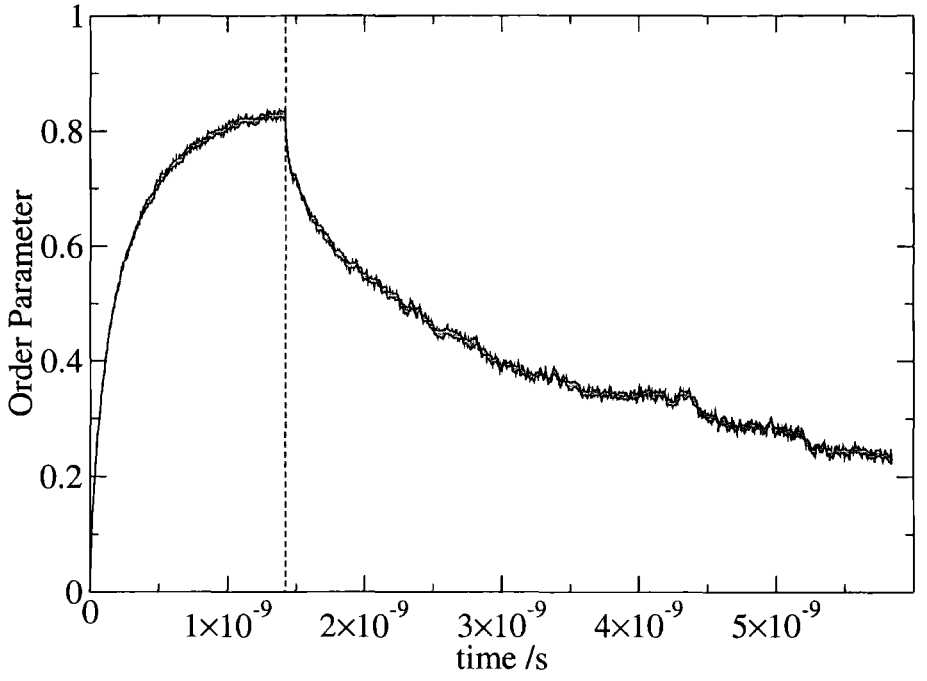

Figure 7.30: Order parameter evolution with time as a field is applied and then removed for the system at 1.09 g cm^{-3}.

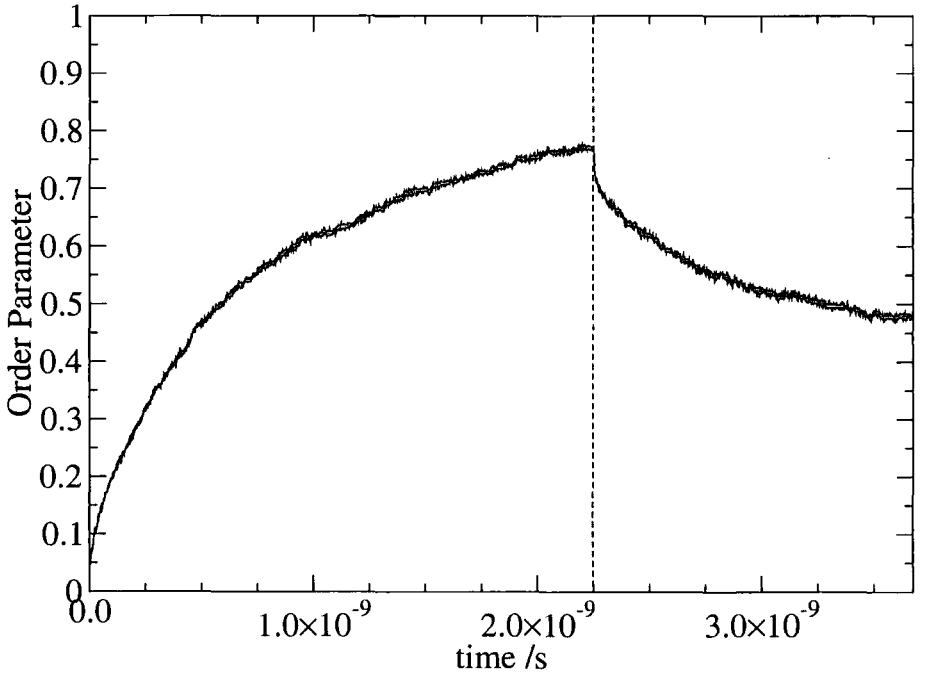

Figure 7.31: Order parameter evolution with time as a field is applied and then removed for the system at 1.33 g cm^{-3}.

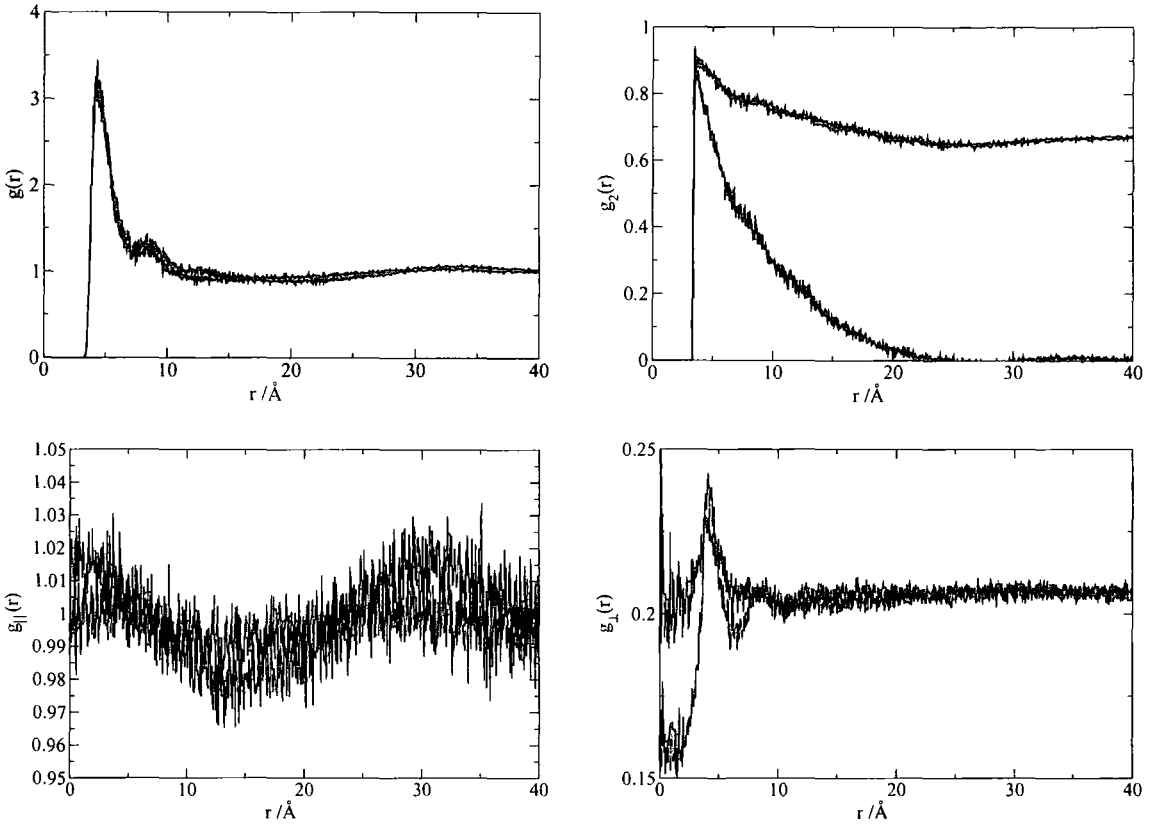

Figure 7.32: Distributions functions for the bulk dendrimer at 1.09 g cm^{-3}. Black represents the system with no aligning potential and blue, the system after exposure to an aligning potential for 1.425 ns.

7.4.6 Reducing Non-Bonding Potentials

There have been a number of previous studies in which equilibration was hastened by the modification of non-bonding interactions. Techniques such as dissipative particle dynamics allow particles to pass through each other during an initial equilibration period, then the non-bonding potentials are gradually switched on and an equilibrium structure often results.

In the study of this bulk dendrimer it was considered possible that equilibration was extremely slow. Hence, an equilibrium structure may not have been found. A set of simulations was undertaken in which the non-bonding contribution to the force field was changed by taking a tangent to the curve at a set distance, r_{trunc}, so that the repulsive part of the non-bonded interactions was truncated.[161] Figure 7.33 shows the form of these potentials plotted for the small sphere-small sphere interaction .

A series of simulations lasting 0.75 ns each were conducted with $U_{max} = 3\,\epsilon$, $5\,\epsilon$, $10\,\epsilon$, $20\,\epsilon$, $40\,\epsilon$, $80\,\epsilon$, $100\,\epsilon$ and $120\,\epsilon$. As an additional measure to allow full mixing the mass of the large core was reduced by 50% during the first five runs. Initial indications showed that the particles passed through each other for the tangent with $U_{max} = 3\,\epsilon$, then became less overlapped as the tangent gradient got steeper. However, the change in the form of the potential from the $U_{max} = 120\,\epsilon$ tangent to the cut and shifted Lennard-Jones was not achieved as it resulted in unmanageable repulsive forces. Some efforts to minimize the structure before changing to the LJ form proved fruitless. During these simulations no additional LC characteristics were observed.

7.5 Conclusions

7.5.1 Summary of Results

Simulations have been undertaken using two forms of a coarse-grained model of a carbosilane LC dendrimer. The first model used spherocylinders with $L/D = 3.2$. With this model no mesophases or evidence of a phase transition to a more ordered

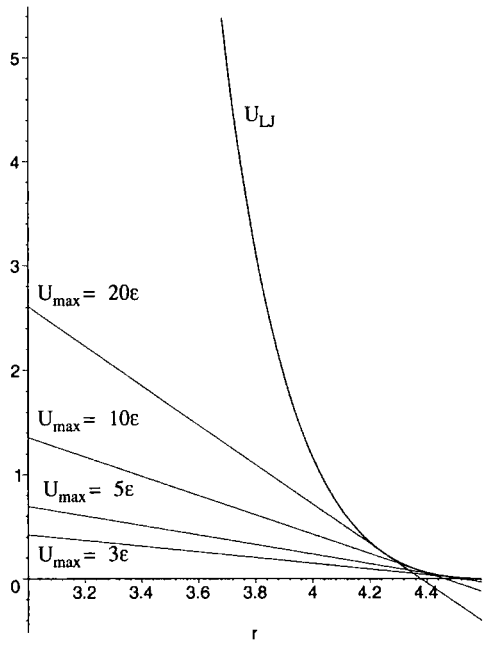

Figure 7.33: Comparison of the Lennard-Jones potential and truncated potentials with $U_{max} = 3\,\epsilon,\ 5\,\epsilon,\ 10\,\epsilon,\ 20\,\epsilon$.

structure were seen. The application of a field caused the SCs to align, but the alignment disappeared with rapid reorientation on removal of the field. There was no sign of microsegregation with this system.

The model with spherocylinders with $L/D = 6.0$ also showed no signs of a phase transition or the formation of stable mesophases. However, there were some signs that application of an external field induced some grouping and alignment of the spherocylinders. This effect was not strong enough to induce full microphase separation or stable ordered phases.

7.5.2 Entropic Effects in Spherocylinder Systems

The driving force for mesophase formation in purely repulsive spherocylinders is entropic. There is a competition between rotational and translational entropy. To illustrate this, two lines of equal length may be considered. When the two lines are forced to lie perpendicular to each other, as in Figure 7.34, one of them excludes the other from a square region of space. This is of no consequence at low density and perpendicular orientations are permissible. However, at higher densities this effect

begins to restrict the system. Eventually one expects a cross over where the loss in orientational entropy caused by alignment is less than the gain in translational entropy caused by the reduction in excluded area when alignment occurs. Hence as density increases alignment will eventually occur on purely entropic grounds. We therefore expect any microphase separation to occur with simultaneous alignment of the spherocylinders (which does occur), to be purely entropically driven.

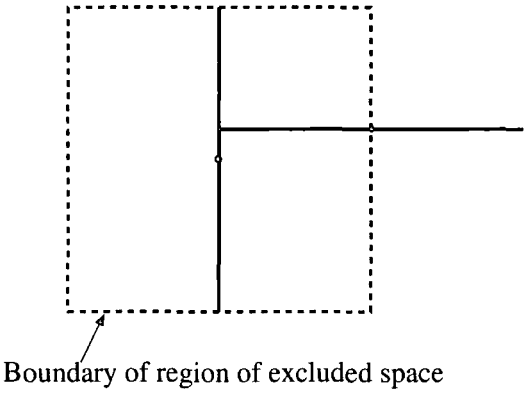

Figure 7.34: Schematic showing the excluded region of space created by two perpendicular lines.

7.5.3 Deficiencies in the Model

There are a number of adjustments that could be made to the model for further simulations.

Firstly, the inclusion of anisotropic attractive forces in the model would increase the driving force for microphase separation.

Next, the size of the large core particle could be reduced. In the snapshots it seems possible that these large spherical sites may be disrupting the alignment of spherocylinders in anything more than small groups. One possible solution would be to add an additional flexible spacer molecule to represent the $Si(Me)_2$ groups on the outside of the core.

Finally, the introduction of a spherocylinder angle that would reduce the flexibility of the mesogens may reduce the rapid reorientation of the SC sites that seems to impede alignment.

Chapter 8

Conclusions

The work presented in this thesis concentrates on methods of simulating macromolecular liquid crystalline materials on a molecular scale.

In Chapter 5, the first study investigated the phase behaviour of a side chain liquid crystal polymer. This study used a hybrid model in which united-atom Lennard-Jones sites represented the polymer backbone and flexible alkyl spacer and the mesogenic moieties were represented by Gay-Berne sites. Using molecular dynamics simulations this SCLCP was gradually cooled from an isotropic melt. Some microphase separation into mesogen rich and polymer rich domains was observed, although the order parameter remained low. In subsequent simulations an aligning potential was applied to represent the effect of an external magnetic field. In these simulations the mesogenic domains aligned and a layered structure was seen. At higher temperatures, the order within these layers was nematic. However, further cooling resulted in a smectic phase with mesogenic bilayers between polymer rich regions. These liquid crystal phases were characterized using radial and orientational distribution functions, diffusion data and order parameters. This work represents the first off-lattice simulation of a SCLCP.

Chapters 6 and 7 describe simulations of a second system, a third generation carbosilane dendrimer with mesogenic terminal groups. This LCDr has been investigated on three scales. Firstly, Monte Carlo simulations of a single molecule in the gas phase showed that the alkyl chains that separate the mesogens and the core allow extensive conformational flexibility. In a nematic mean field the mesogenic units

were able to align by altering their conformation, but rapid movement in the periphery of the molecule was still seen. Long time-scale fluctuations between slightly oblate and prolate structures were observed. These fluctuations mean that much longer simulations would be required to extract average semi-axis lengths. The rod shape conformation with mesogenic units in two groups either side of the core, that have been suggested as responsible for smectic layer formation, were not observed.

A semi-atomistic model, analogous to that of the SCLCP, was used in molecular dynamics simulations of the LCDr in solution. A single dendromesogen molecule was placed in isotropic, nematic and smectic solvents, represented by Gay-Berne sites. In liquid crystal solvents, the overall shape of the LCDr became rod-like and the mesogenic groups aligned. Penetration of the solvent molecules into the LCDr was observed for the outer layers but not the core.

Finally, a coarse grained model was designed incorporating information gained from the results of the earlier studies including atomic, bond length, angular and torsional distribution functions from atomistic simulations. Molecular Dynamics simulations at a range of densities were conducted. Using orientational correlation functions and diffusion data a density range in which mesophase formation was most likely was identified. In this range a magnetic field was applied. The mesogens aligned in the field, but relaxed to random orientations when the field was removed. Although no bulk mesophases were observed, at higher densities, using a spherocylinder with L/D = 6 to represent the mesogenic groups, the application of the field induced some microphase separation and small domains of typically < 10 mesogens formed. As a result of these findings suggestions have been made for the improvement of the model.

Bibliography

[1] P. Collings, *Liquid Crystals.* (IOP publishing Ltd, 1990).

[2] P. Collings and M. Hird, *Introduction to liquid crystals.* (Taylor & Francis, 1997).

[3] McBride C., *Computer simulation of liquid crystals.* Ph.D. thesis, University of Durham. (1999).

[4] F. Reinitzer, Monatshefte fur Chemie **9**, 421 (1888).

[5] F. Reinitzer, Liq. Cryst **5**, 7 (1989).

[6] O. Lehmann, Z. Phys. Chem. **4**, 462 (1889).

[7] H. Kelker and P. Knoll, Liq. Cryst. **5**, 19 (1989).

[8] J. Alejandre, J. W. Emsley, and D. J. Tildesley, J. Chem. Phys. **101**, 7027 (1994).

[9] G. Friedel, Anales Physique **18**, 273 (1922).

[10] J. W. Goodby, In *Handbook of Liquid Crystals*, edited by D. Demus, J. Goodby, G. W. Gray, H.-W. Spiess, and V. Vill, volume 1, chapter V.5 (Wiley-VCH, Weinheim, 1998).

[11] J. Goodby, G. Mehl, I. Saez, R. Tuffin, G. Mackenzie, R. Auzely-Velty, T. Benvegnu, and D. Plusquellec, Chem. Comm. **19**, 2057 (1998).

[12] V. Pisipati and S. Rananavare, Liq. Cryst. **13**, 747 (1993).

[13] K. Toyne, In *Thermotropic liquid crystals*, edited by G. Gray, chapter 2, 28.

[14] D. Demus, In *Handbook of liquid crystals*, edited by D. Demus, J. Goodby, G. Gray, H.-W. Spiess, and V. Vill, volume 1, chapter 6, 133 (Wiley-VCH, Weinheim, 1998).

[15] G. W. Gray and J. W. Goodby, *Smectic liquid crystals: Textures and Structures* (Leonard Hill, 1984).

[16] P. J. Collings and M. Hird, *Introduction to liquid crystals*, chapter 7 (Taylor & Francis, 1997).

[17] P. J. Collings and M. Hird, *Introduction to Liquid Crystals*, chapter 5 (Taylor & Francis, 1997).

[18] M. Engel, B. Hisgen, R. Keller, W. Kreuder, B. Reck, H. Ringsdorf, H.-W. Schmidt, and P. Tschirner, Pure & Appl. Chem. **57**, 1009 (1985).

[19] N. Ardoin and D. Astruc, Bull. Soc. Chim. Fr. **132**, 875 (1995).

[20] S. Friberg, M. Podimek, D. Tomalia, and D. Hedstrand, Mol. Cryst. Liq. Cryst. **164**, 157 (1988).

[21] V. Percec, C.-H. Ahn, T. K. Bera, G. Ungar, and D. J. P. Yeardley, Chem. Eur. J. **5**, 1070 (1999).

[22] G. Ungar, V. Percec, M. N. Holerca, and G. Johansson, Chem. Eur. J. **6**, 1258 (2000).

[23] J. Cameron, A. Facher, G. Latterman, and S. Diele, Adv. Mater. **9**, 398 (1997).

[24] J. Barbera, M. Marcos, and J. Serrano, Chem. Eur. J. **5**, 1834 (1999).

[25] F. Leslie, *Physical Properties of Liquid Crystals.*, chapter I-3, 25–71 (Wiley-VCH, 1999).

[26] P. A. Lebwhol and G. Lasher, Phys. Rev. A **6**, 426 (1972).

[27] D. J. Cleaver and M. P. Allen, Mol. Phys. **80**, 253 (1993).

[28] M. A. Bates, Phys. Rev. E **65**, art. no. 041706 (2002).

[29] C. Zannoni, J. Mat. Chem. **11**, 2637 (2001).

[30] M. R. Wilson, J. Chem. Phys. **107**, 8654 (1997).

[31] E. de Miguel and C. Vega, J. Chem. Phys. **117**, 6313 (2002).

[32] A. Cuetos, B. Martinez-Haya, L. F. Rull, and S. Lago, J. Chem. Phys. **117**, 2934 (2002).

[33] M. Al-Barwani and M. P. Allen, Phys. Rev. E **62**, 6706 (2000).

[34] M. P. Neal and A. J. Parker, Phys. Rev. E **6301**, art. no. 011706 (2001).

[35] S. J. Johnston, R. J. Low, and M. P. Neal, Phys. Rev. E **65**, art. no. 051706 (2002).

[36] D. J. Earl, J. Ilnytskyi, and M. R. Wilson, Mol. Phys. **99**, 1719 (2001).

[37] C. McBride, M. R. Wilson, and J. A. K. Howard, Mol. Phys. **93**, 955 (1998).

[38] D. L. Cheung, S. J. Clark, and M. R. Wilson, Chem. Phys. Lett. **356**, 140 (2002).

[39] W. G. Jang, M. A. Glaser, C. S. Park, K. H. Kim, Y. Lansac, and N. A. Clark, Phys. Rev. E **6405**, art. no. 051712 (2001).

[40] Y. Lansac, M. A. Glaser, and N. A. Clark, Phys. Rev. E **6405**, art. no. 051703 (2001).

[41] M. J. Cook and M. R. Wilson, Mol. Cryst. Liq. Cryst. **363**, 181 (2001).

[42] H. Ringsdorf and A. Schneller, British Polym. J. **13**, 43 (1981).

[43] Roviello A, J. Polym. Sci., Polym. Lett. Ed. **13**, 455 (1975).

[44] W. Jackson, J. Polym. Sci., Polym. Chem. Ed. **14**, 2043 (1976).

[45] R. Centore and P. Inaelli, In *Liquid crystal polymers*, edited by C. Carfagna, chapter 3, 31–45 (Elssevier Science Ltd,, 1994).

[46] J. W. Goodby, In *Handbook of Liquid Crystals*, edited by D. Demus, J. Goodby, G. W. Gray, H.-W. Spiess, and V. Vill, volume 3 (Wiley-VCH, Weinheim, 1998).

[47] J.-L. Jin, S. Antoun, C. Ober, and R. W. Lenz, British Polym. J. 132 (1980).

[48] J. Majnusz, J. M. Catala, and R. W. Lenz, Eur. Polym. J. **19**, 1043 (1983).

[49] W. R. Krigbaum, H. Hakemi, and R. Kotek, Macromolecules **18**, 965 (1985).

[50] H. Finkelmann, H. Ringsdorf, and J. Wendorff, Makromol. Chem. **179**, 273 (1978).

[51] H.-G. Noh, H.-K. Shim, J.-H. Chang, and J.-I. Jin, **30**, 1521 (1997).

[52] J. M. G. Cowie, *Polymers:Chemistry and Physics of Modern Materials.* 2nd edition (Blackie, 1994).

[53] M. Portugall, H. Ringsdorff, and R. Zentel, Makromol. Chem. **183**, 2311 (1982).

[54] C. B. McArdle, editor: *Side Chain Liquid Crystal Polymers.* (Blackie, 1989).

[55] B. Hahn, J. Wendorff, M. Portugall, and H. Ringsdorf, Coll. Polym. Sci. **259**, 875 (1981).

[56] B. Reck and H. Ringsdorf, Makromol. chem., Rapid Commun. **6**, 291 (1985).

[57] R. Zentel, G. F. Schmidt, J. Meyer, and M. Benalia, Liq. Cryst. **2**, 651 (1987).

[58] K. Kohlhammer, G. Kothe, R. Reck, and H. Ringsdorf, Ber. Bungsenges. Phys. Chem. **93**, 1323 (1989).

[59] R. Zentel, *Handbook of Liquid Crystals. High Molecular Weight Liquid Crystals*, volume 3, chapter I-3, 42–65 (Wiley-VCH, 1998).

[60] D. Demus, J. Goodby, G. W. Gray, H.-W. Spiess, and V. Vill, editors: *Handbook of Liquid Crystals. High Molecular Weight Liquid Crystals.* volume 3 (Wiley-VCH, 1998).

[61] H. Frey and C. Schlenk, Topics in Current Chemistry **210**, 69 (2000).

[62] G. R. Newkome, C. N. Moorefield, and F. Vögtle, *Dendrimers and Dendrons.* (Wiley-VCH, 2001).

[63] J. W. Goodby, D. W. Bruce, M. Hird, C. Imrie, and M. Neal, J. Mater. Chem. **11**, 2631 (2001).

[64] H. Melville, Trans Faraday Soc **40**, 217 (1944).

[65] F. Vögtle and E. Weber, Angew. Chem. Int. Ed. Engl. **18**, 753 (1979).

[66] E. Buhleier, W. Wehner, and F. Vögtle, Synthesis 155 (1978).

[67] O. A. Matthews, A. N. Shipway, and J. F. Stoddart, Prog. Polym. Sci. **23**, 1 (1998).

[68] A. W. Bosman, H. M. Janssen, and E. W. Meijer, Chem. Rev. **99**, 1665 (1999).

[69] D. Tomalia, A. Naylor, and W. Goddard, Angew. Chem. Int. Ed. Eng. **29**, 138 (1990).

[70] G. R. Newkome, Z.-Q. Yao, G. R. Baker, and V. P. Gupta, J. Org. Chem. **50**, 2003 (1985).

[71] H. Meier and M. Lehmann, Angew. Chem. Int. Ed. **37**, 643 (1998).

[72] D. J. Pesak and J. S. Moore, Angew. Chem. Int. Ed. Engl. **36**, 1636 (1997).

[73] J. Issberner, R. Moors, and F. Vögtle, Angew. Chem. Int. Ed. **33**, 2413 (1994).

[74] S. Bauer, H. Fischer, and H. Ringsdorf, Angew. Chem. Int. Ed. Engl. **32**, 1589 (1993).

[75] V. Percec, C. Peihwei, G. Ungar, and J. Zhou, J. Am. Chem. Soc. **117**, 11441 (1995).

[76] Y. Kim, Marcomol. Symp. **77**, 21 (1994).

[77] J. Barbera, B. Donnio, R. Gimenez, D. Guilllon, M. Marcos, A. Omenat, and J. Serrano, J. Mater. Chem. **11**, 2808 (2001).

[78] S. A. Ponomarenko, N. I. Boiko, V. P. Shibaev, R. Richardson, I. Whitehouse, E. Rebrov, and A. Muzafarov, Macromolecules **22**, 5549 (2000).

[79] S. A. Ponomarenko, N. I. Boiko, and V. P. Shibaev, Langmuir **16**, 5487 (2000).

[80] R. M. Richardson, I. J. Whitehouse, S. A. Ponomarenko, N. I. Boiko, and V. P. Shibaev, Mol. Cryst. Liq. Cryst. **330**, 176 (1999).

[81] S. A. Ponomarenko, N. I. Boiko, E. Rebrov, A. Muzafarov, I. J. Whitehouse, R. M. Richardson, and V. P. Shibaev, Mol. Cryst. Liq. Cryst. **332**, 43 (1999).

[82] S. A. Ponomarenko, E. A. Rebrov, A. Y. Bobrovsky, N. I. Boiko, A. M. Muzafarov, and V. P. Shibaev, Liq. Cryst. **21**, 1 (1996).

[83] K. Lorenz, D. Hoter, B. Stuhn, R. Mulhaupt, and H. Frey, Adv. Mat. **8**, 414 (1996).

[84] V. Percec, W.-D. Cho, G. Ungar, and D. J. P. Yeardley, Angew. Chem. Int. Ed. **39**, 1597 (2000).

[85] V. S. K. Balagurusamy, G. Ungar, V. Percec, and G. Johansson, J. Am. Chem. Soc. **119**, 1539 (1997).

[86] C. Tschierske, J. Mater. Chem. **11**, 2647 (2001).

[87] C. Tschierske, Nature **419**, 681 (2002).

[88] C. Tschierske, Curr. Opin. Colloid Interface Sci. **7**, 69 (2002).

[89] D. Fazio, C. Mongin, B. Donnio, Y. Galerne, D. Guillon, and D. W. Bruce, J. Mater. Chem. **11**, 2852 (2001).

[90] I. Saez and J. Goodby, Liq. Cryst. **26**, 1101 (1999).

[91] V. Percec, C. H. Ahn, W. D. Cho, A. M. Jamieson, J. Kim, T. Leman, M. Schmidt, M. Gerle, M. Moller, S. A. Prokhorova, S. S. Sheiko, S. Z. D.

Cheng, A. Zhang, G. Ungar, and D. J. P. Yeardley, J. Am. Chem. Soc. **120**, 8619 (1998).

[92] C. B. Gorman and J. C. Smith, Polymer **41**, 675 (2000).

[93] A. M. Naylor, W. A. Goddard, G. E. Kiefer, and D. A. Tomalia, J. Am. Chem. Soc. **111**, 2339 (1989).

[94] T. Cagin, G. F. Wang, R. Martin, G. Zamanakos, N. Vaidehi, D. T. Mainz, and W. A. Goddard, Comput. Theor. Polym. Sci. **11**, 345 (2001).

[95] K. Karatasos, D. B. Adolf, and G. R. Davies, J. Chem. Phys. **115**, 5310 (2001).

[96] M. A. Perez, E. Longo, and C. A. Taft, Theochem-J. Mol. Struct. **507**, 97 (2000).

[97] W. Carl, J. Chem. Soc.-Faraday Trans. **92**, 4151 (1996).

[98] M. L. Mansfield and L. I. Klushin, Macromolecules **26**, 4262 (1993).

[99] M. L. Mansfield, Macromolecules **33**, 8043 (2000).

[100] A. Terzis, A. Vanakaras, and D. Photinos, Mol. Cryst. Liq. Cryst. **330**, 517 (1999).

[101] A. G. Vanakaras and D. J. Photinos, J. Mater. Chem. **11**, 2832 (2001).

[102] R. Car and M. Parinello, Phys. Rev. Lett. **55**, 2471 (1985).

[103] A. Hinchcliffe, *Chemical Modeling From Atoms to Liquids.* (Wiley, 1999).

[104] B. J. Berne and P. Peckukas, J. Chem. Phys. **64**, 4213 (1972).

[105] J. G. Gay and B. J. Berne, J. Chem. Phys. **74**, 3316 (1981).

[106] J. Stelzer, H. R. Trebin, and L. Longa, J. Chem. Phys. **103**, 3098 (1995).

[107] J. Stelzer, H. Trebin, and L. Longa, J. Chem. Phys. **107**, 1295 (1997).

[108] C. Bacchiocchi and C. Zannoni, Phys. Rev. E **58**, 3237 (1998).

[109] D. J. Cleaver, C. M. Care, M. P. Allen, and M. P. Neal, Phys. Rev. E **54**, 559 (1996).

[110] E. de Miguel, L. F. Rull, M. K. Chalam, and K. E. Gubbins, Mol. Phys. **74**, 405 (1991).

[111] A. P. J. Emerson, G. R. Luckhurst, and S. G. Whatling, Mol. Phys. **82**, 113 (1994).

[112] G. R. Luckhurst, R. A. Stephens, and R. W. Phippen, Liq. Cryst. **8**, 451 (1990).

[113] C. Zannoni, *Physical Properties of Liquid Crystals: Nematics*, chapter 12, 624–634. Number 25 in EMIS DataReviews Series (INSPEC, The Institution of Electrical Engineers, London, UK, 2001).

[114] F. Ercolessi: *A Molecular Dynamics Primer* (1997). This on-line book can be found at http://www.sissa.it/furio.

[115] H. Andersen, J. Chem. Phys. **72**, 2384 (1980).

[116] W. Tschöp, K. Kremer, J. Batoulis, T. Bürger, and O. Hahn, Acta. Polym. **49**, 61 (1998).

[117] M. Murat and K. Kremer, J. Chem. Phys. **108**, 4340 (1998).

[118] M. Laso, H. C. Öttinger, and U. W. Suter, J. Chem. Phys. **95**, 2178 (1991).

[119] H. Fukunga, T. Aoyagi, J.-i. Takimoto, and M. Doi, Comp. Phys. Comm. **142**, 224 (2001).

[120] W. Tschöp, K. Kremer, O. Hahn, J. Batoulis, and T. Bürger, Acta. Polym. **49**, 75 (1998).

[121] J. Baschangel, K. Binder, W. Paul, M. Laso, U. W. Suter, I. Batoulis, W. Jilge, and T. Bürger, J. Chem. Phys. **95**, 6014 (1991).

[122] B. Alder and T. Wainwright, J. Chem. Phys. **27**, 1208 (1957).

[123] A. Rahman, Phys. Rev. **136**, A405 (1964).

[124] L. Verlet, Phys. Rev. **159**, 98 (1967).

[125] L. Verlet, Phys. Rev. **165**, 201 (1968).

[126] J.-P. Hansen and L. Verlet, Phys. Rev. **184**, 151 (1969).

[127] M. Allen and D. Tildesley, *Computer Simulation of Liquids.* (Oxford University Press, 1989).

[128] D. Frenkel and B. Smit, *Understanding Molecular Simulation, From Algorithms to Applications.* volume 1 of *Computational Science Series.* 2nd edition (The Academic Press, 2002).

[129] S. Nosé, J. Chem. Phys. **53**, 255 (1984).

[130] N. Metropolis and S. Ulam, J. Am. stat. Ass. **44**, 335 (1949).

[131] N. Metropolis, A. W. Rosenbluth, M. N. Rosenbluth, A. H. Teller, and E. Teller, J. Chem. Phys. **21**, 1087 (1953).

[132] B. J. Alder, S. P. Frankel, and V. A. Lewinson, J. Chem. Phys. **23**, 417 (1955).

[133] M. I. Manousiouthakis and M. W. Deem, J. Chem. Phys. **110**, 2753 (1999).

[134] P.-Y. Lui, N. Yao, and A. M. Jamieson, Macromolecules **32**, 6587 (1999).

[135] P. Martinoty, L. Hillilou, M. Mauzac, L. Benguigui, and D. Collin, Macromolecules **32**, 1746 (1999).

[136] R. J. Sarna, G. P. Simon, G. Day, H.-J. Kim, and W. R. Jackson, Macromolecules **27**, 1603 (1994).

[137] S. H. Lee, V. Surendranath, Y. C. Kim, and E. Gelerinter, Liq. Cryst. **18**, 495 (1995).

[138] Z. X. Fan, S. Buchner, W. Haase, and H. G. Zachmann, J. Chem. Phys. **92**, 5099 (1990).

[139] J. Ebbutt, R. M. Richardson, J. Blackmore, D. G. McDonnell, and M. Verral, Mol. Cryst. Liq. Cryst. **261**, 549 (1995).

[140] C. McBride and M. R. Wilson, Mol. Phys. **97**, 511 (1999).

[141] M. G. Martin and J. I. Siepmann, J. Phys. Chem. B **103**, 4508 (1999).

[142] S. K. Nath and R. Khare, J. Chem. Phys. **115**, 10827 (2001).

[143] N. L. Allinger, **99**, 8127 (1977).

[144] S. T. Cui, P. T. Cummings, and H. D. Cochran, Fluid Phase Equilibria **141**, 45 (1997).

[145] J.-P. Ryckaert and A. Bellemans, Farad. DIscuss. Chem. Scoc. **66**, 95 (1978).

[146] J. P. Ryckaert, Mol. Phys. **55**, 549 (1985).

[147] G. R. Luckhurst and G. Saielli, J. Chem. Phys. **112**, 4342 (2000).

[148] *AVS5 & AVS Express* (1998). Advanced Visual Systems Inc., Waltham, U.S.A.

[149] W. L. Jorgensen, J. D. Madura, and C. J. Swenson, J. Am. Chem. Soc. **106**, 6638 (1984).

[150] D. S. Maxwell, J. Tirado-Rives, and W. L. Jorgensen, J. Comput. Chem. **16**, 984 (1995).

[151] M. J. Cook and M. R. Wilson, Mol. Cryst. Liq. Cryst. **357**, 149 (2001).

[152] M. Wilson, Liq. Cryst. **21**, 437 (1996).

[153] J. W. Emsley, G. R. Luckhurst, and C. P. Stockley, Proc. R. Soc. Lond. A **381**, 117 (1982).

[154] M. R. Wilson, J. Mol. Liq. **68**, 23 (1996).

[155] T. J. H. Vlugt, R. Krishna, and B. Smit, J. Phys. Chem. B **103**, 1102 (1999).

[156] J. M. Ilnytskyi and M. R. Wilson, Comp. Phys. Comm **134**, 23 (2001).

[157] K. Kremer and G. S. Grest, J. Chem. Phys. **92**, 5057 (1989).

[158] O. Hahn, L. D. Site, and K. Kremer, Macromol. Theory Simul. **10**, 288 (2001).

[159] Y. N. Vorobjev and J. Hermans, Biophysical J. **73**, 722 (1997).

[160] A. Bondi, J. Phys. Chem. **68**, 441 (1964).

[161] J. H. R. Clarke, Unpublished.